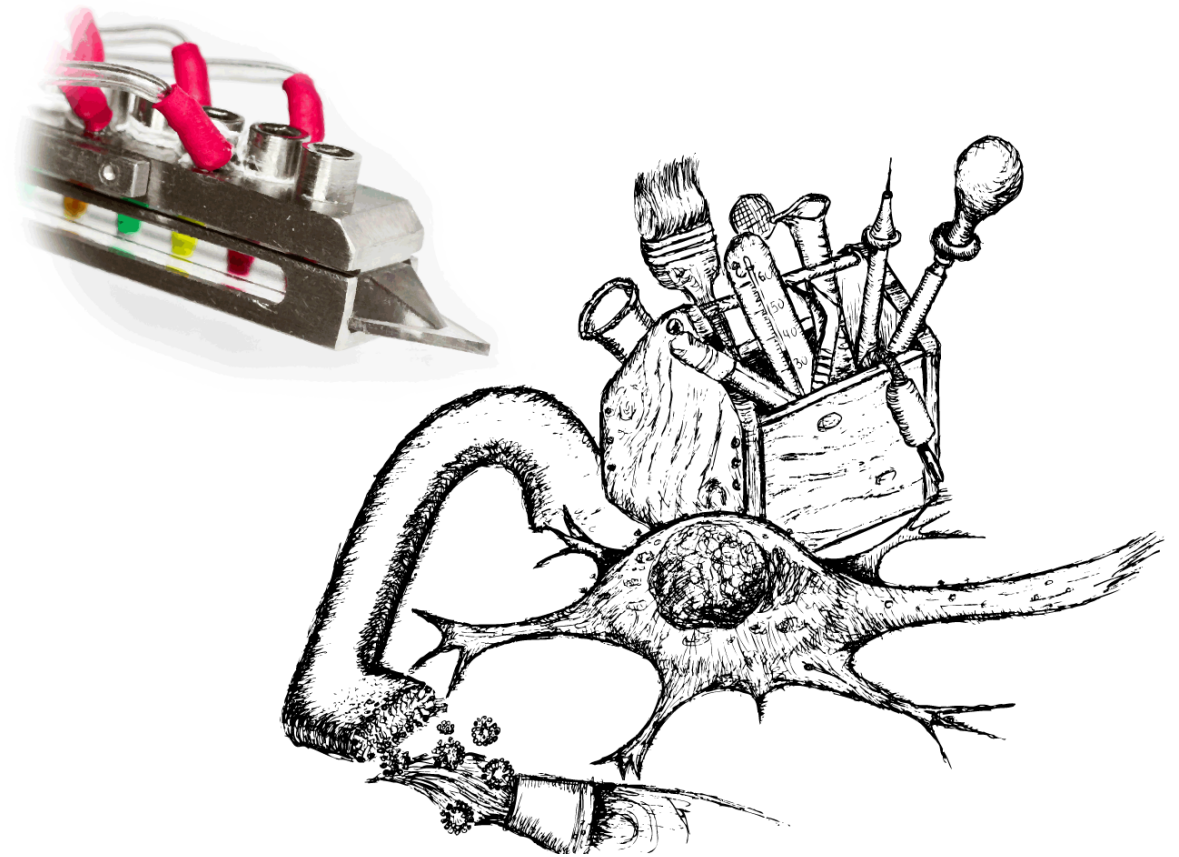




Alar Ainla

The Multifunctional Pipette



The Multifunctional Pipette

A Microfluidic Technology for the Biosciences

ALAR AINLA

Department of Chemical and Biological Engineering
CHALMERS UNIVERSITY OF TECHNOLOGY
Gothenburg, Sweden 2013



2013

THESIS FOR THE DEGREE OF DOCTOR OF PHILOSOPHY

THE MULTIFUNCTIONAL PIPETTE

A MICROFLUIDIC TECHNOLOGY FOR THE BIOSCIENCES

ALAR AINLA



Department of Chemical and Biological Engineering
CHALMERS UNIVERSITY OF TECHNOLOGY

Göteborg, Sweden 2013

The Multifunctional Pipette

A Microfluidic Technology for the Biosciences

ALAR AINLA

ISBN: 978-91-7385-818-2

Doktorsavhandlingar vid Chalmers tekniska högskola

Ny serie nr: 3499

ISSN: 0346-718X

©Alar Ainla, 2013

Department of Chemical and Biological Engineering

Chalmers University of Technology

SE-412 96 Göteborg

Sweden

Telephone: +46-(0)31 772 1000

Front cover image: Multifunctional pipette -- a toolbox for single-cell and biomembrane studies. You may guess which tool represents which experiment in the papers!

Back cover photo by Viktoria Gusak

Printed by Chalmers reproservice

Göteborg, Sweden 2013

The Multifunctional Pipette

A Microfluidic Technology for the Biosciences

ALAR AINLA

Department of Chemical and Biological Engineering

Chalmers University of Technology

ABSTRACT

The theme of the work described in this thesis is the generation and application of liquid microenvironments in chemistry and bioscience using microfluidic devices. First, a computer controlled multi-stage dilution system to generate time-dependent chemical waves was developed, and its application was demonstrated on model biomembranes. Thereafter the focus was shifted towards spatial control of chemistry. Using a hydrodynamic flow confinement concept in an open liquid volume, we created a device coined "*Multifunctional Pipette*". It features localized liquid handling at single-cell size scales together with fast solution exchange. The technology has been refined and optimized to provide a feature-rich tool for biologists working with cells and tissues in microscopy experiments. Application examples include cell zeiosis, single-cell dose-response determination and ion-channel stimulation. Subsequent studies cover modifications and applications of this device, such as on-chip electrodes and electroporation, as well as uses in cell cultures, on tissue slices, and as an optofluidic thermometer. Finally, localized liquid handling has been applied to assemble 2-dimensional fluidic networks consisting of directly written supported lipid bilayers. This "*Lab on a Membrane*" toolbox allows rapid prototyping of 2D-fluidic circuits, modify their chemistry and connectivity on-demand and apply them in studies of molecular interactions.

Keywords: Microfluidics, microfabrication, PDMS, microfluidic dilution, microfluidic mixer, hydrodynamic flow confinement, microfluidic superfusion, single-cell analysis, supported lipid membranes, microfluidic temperature sensing.

LIST OF PUBLICATIONS

- I A Microfluidic Diluter Based on Pulse Width Flow Modulation**
Alar Ainla, Irep Gözen, Owe Orwar & Aldo Jesorka
Analytical Chemistry 2009, 81(13), 5549-5556.
- II A Microfluidic Pipette for Single-Cell Pharmacology**
Alar Ainla, Erik T. Jansson, Natalia Stepanyants, Owe Orwar & Aldo Jesorka
Analytical Chemistry, 2010, 82(11), 4529-4536.
- III A multifunctional pipette**
Alar Ainla, Gavin D. M. Jeffries, Ralf Brune, Owe Orwar & Aldo Jesorka
Lab on a Chip, 2012, 12(7), 1255-1261.
- IV Single-Cell Electroporation Using a Multifunctional Pipette**
Alar Ainla, Shijun Xu, Nicolas Sanchez, Gavin D. M. Jeffries & Aldo Jesorka
Lab on a Chip, 2012, 12(22), 4605-4609.
- V A multifunctional pipette for local administration of drugs to brain slices**
Aikeremu Ahemaiti, Alar Ainla, Gavin D. M. Jeffries, Holger Wigström, Owe Orwar, Aldo Jesorka & Kent Jardemark
Manuscript
- VI An optofluidic temperature probe**
Ilona Węgrzyn, Alar Ainla, Gavin D. M. Jeffries & Aldo Jesorka
Submitted manuscript
- VII Lab on a Membrane: a Toolbox for Reconfigurable 2D fluidic networks**
Alar Ainla, Irep Gözen, Bodil Hakonen & Aldo Jesorka
Submitted manuscript

CONTRIBUTION REPORT

- I Proposed concept for the diluter. Designed and fabricated microfluidic devices. Designed pneumatic and electronic control system and software. Performed calibration and testing. Analyzed data and developed models. Participated in lipid spreading experiments. Designed figures. Contributed to the writing of the paper.
- II Proposed the pipette concept. Designed and fabricated all microfluidic devices. Designed control mechanism and software. Performed calibrations and testing. Performed finite element modeling. Analyzed data. Participated in all biological experiments. Designed figures. Contributed to the writing of the paper.
- III Contributed to the design of the pipette shape and interfacing. Designed and characterized microfluidic circuitries. Participated in switching speed experiments. Performed calculations and developed models. Performed biological experiments. Wrote the paper.
- IV Participated and supervised electrode development. Designed electrical interface. Participated in all biological experiments. Performed calculations and developed models. Designed figures. Contributed to the writing of the paper.
- V Participated in intracellular recording experiments. Designed figures. Contributed to the writing of the paper.
- VI Proposed concept of dye multiplexing. Developed models and performed simulations. Participated in experimental planning. Participated in all experiments. Contributed to data analysis. Designed figures. Contributed to the writing of the paper.
- VII Proposed concepts of writing and erasing lipids using multifunctional pipette. Participated in experimental planning. Wrote control software. Participated in all experiments. Performed simulations. Analyzed and interpreted all data. Designed figures. Contributed to the writing of the paper.

PUBLICATIONS NOT INCLUDED IN THIS THESIS

Thermal Migration of Molecular Lipid Films as Contactless Fabrication Strategy for Lipid Nanotube Network

Irep Gozen, Mehrnaz Shaali, Alar Ainla, Bahatur Ortmen, Inga Pöldsalu, Kiryl Kustanovich, Gavin D. M. Jeffries, Paul Dommersnes, Zoran Konkoli & Aldo Jesorka

Submitted manuscript

Calibrated On-chip Dilution Module for the Multifunctional Pipette

Andreas Genner, Alar Ainla & Aldo Jesorka

Proceedings of the 3rd International Workshop on Soft Matter Physics & Complex Flows. Ed.: Jon Otto Fossum and Elisabeth Bouchaud. Lofoten, Norway

Influence of Temperature on Enzyme Activity in Single Cells

Shijun Xu, Alar Ainla, Gavin D. M. Jeffries, Kent Jardemark, Owe Orwar & Aldo Jesorka

Manuscript

Book chapter:

Hydrodynamically Confined Flow Devices

Alar Ainla, Gavin D. M. Jeffries & Aldo Jesorka

*In book "Hydrodynamics - Theory and Model", by Jinhai Zheng, InTech, 2012
ISBN 978-953-51-0130-7*

Review article:

Hydrodynamic Flow Confinement Technology in Microfluidic Perfusion Devices

Alar Ainla, Gavin D. M. Jeffries & Aldo Jesorka

Micromachines 2012, 3(2), 442-461.

RELATED PATENT APPLICATIONS

PIPETTES, METHODS OF USE, AND METHODS OF STIMULATING AN OBJECT OF INTEREST

Alar Ainla, Owe Orwar & Aldo Jesorka

PCT/IB2010/003307. Priority: Dec 3rd 2009.

MICROFLUIDIC DEVICE WITH HOLDING INTERFACE AND METHODS OF USE

Alar Ainla, Gavin D. M. Jeffries, Owe Orwar & Aldo Jesorka

PCT/US12/36758. Priority: May 6th, 2011.

METHOD OF HYDRODYNAMIC MANIPULATION OF OBJECTS ATTACHED TO A TWO-DIMENSIONAL FLUID

Alar Ainla, Bodil Hakonen, Irep Gözen, Owe Orwar & Aldo Jesorka

US Provisional Patent Application. Priority: July 30th, 2012.

METHOD TO FABRICATE, MODIFY, REMOVE AND UTILIZE FLUID MEMBRANES

Alar Ainla, Irep Gözen & Aldo Jesorka

US Provisional Patent Application. Priority: January 19th, 2013.

NOTATIONS & ABBREVIATIONS

ABBREVIATIONS

AFM	<i><u>A</u>tom<u>i</u>c fo<u>r</u>ce <u>m</u>icrosco<u>p</u>y</i>
AMPA	<i>2-amino-3-(3-hydroxy-5-methyl-isoxazol-4-yl) propanoic acid</i>
AOBS	<i><u>A</u>cousto-<u>o</u>ptical <u>b</u>eam <u>s</u>plitter</i>
APD	<i><u>A</u>valanche <u>p</u>hoto<u>d</u>iode</i>
APTES	<i>3-<u>a</u>minopropyl triethoxy <u>s</u>ilane</i>
CE	<i><u>C</u>apillary <u>e</u>lectrophoresis</i>
CLSM	<i><u>C</u>onfocal <u>l</u>aser scanning <u>m</u>icrosco<u>p</u>y</i>
COC	<i><u>C</u>yclic <u>o</u>lefin copolymer</i>
COP	<i><u>C</u>yclic <u>o</u>lefin polymers</i>
DNA	<i><u>D</u>eoxyribo<u>n</u>ucleic acid</i>
DPN	<i><u>D</u>ip-<u>p</u>en <u>n</u>anolithography</i>
DQN	<i><u>D</u>iazoquinone</i>
DRIE	<i><u>D</u>eep <u>r</u>eactive-<u>i</u>on <u>e</u>tching</i>
FCS	<i><u>F</u>luorescence <u>c</u>orrelation spectroscopy</i>
FDP	<i><u>F</u>luorescein <u>d</u>iphosphate</i>
FEM	<i><u>F</u>inite <u>e</u>lement <u>m</u>ethod</i>
FRAP	<i><u>F</u>luorescence <u>r</u>ecovery <u>a</u>fter <u>p</u>hotobleaching</i>
FRET	<i><u>F</u>örster <u>r</u>esonance <u>e</u>nergy transfer</i>
GABA	<i>γ-<u>A</u>mino<u>b</u>utyric acid</i>
GFP	<i><u>G</u>reen <u>f</u>luorescent <u>p</u>rotein</i>
HCF	<i><u>H</u>ydrodynamic <u>c</u>onfined <u>f</u>low</i>
HF	<i><u>H</u>ydrofluoric acid</i>
LTI	<i><u>L</u>inear <u>t</u>ime <u>i</u>nvariant</i>
MEMS	<i><u>M</u>icro<u>e</u>lectro<u>m</u>echanical <u>s</u>ystem</i>
NA	<i><u>N</u>umerical <u>a</u>perture</i>
PC	<i><u>P</u>olycarbonate</i>
PDE	<i><u>P</u>artial <u>d</u>ifferential <u>e</u>quation</i>
PDMS	<i><u>P</u>oly<u>d</u>imethylsiloxane</i>
PMMA	<i><u>P</u>oly(<u>m</u>ethyl <u>m</u>ethacrylate)</i>
PMT	<i><u>P</u>hoto<u>m</u>ultiplier tube</i>
PWFM	<i><u>P</u>ulse-<u>w</u>idth <u>f</u>low <u>m</u>odulation</i>
PWM	<i><u>P</u>ulse-<u>w</u>idth <u>m</u>odulation</i>
SICM	<i><u>S</u>canning <u>i</u>on-<u>c</u>onductance <u>m</u>icrosco<u>p</u>y</i>
SOI	<i><u>S</u>ilicon <u>o</u>n <u>i</u>nsulator</i>
TEOS	<i><u>T</u>etraethyl orthosilicate</i>
TIRF	<i><u>T</u>otal <u>i</u>nternal <u>r</u>eflection <u>f</u>luorescence</i>
TPE	<i><u>T</u>hermoplastic <u>e</u>lastomer</i>
TRPV1	<i><u>T</u>ransient <u>r</u>eceptor potential <u>v</u>anilloid</i>

PHYSICAL NOTATIONS

Re	<i>Reynolds number</i>
Pe	<i>Peclet number</i>
St	<i>Strouhal number</i>
p	<i>Pressure</i>
Q	<i>Flow rate</i>
R	<i>Flow resistance</i>
G	<i>Flow conductance</i>
C	<i>Compliance</i>
c	<i>Concentration</i>

MATHEMATICAL NOTATIONS

\oint_S	<i>Integral over closed surface</i>
\iiint_V	<i>Integral over volume</i>
\otimes	<i>Convolution</i>
∇	<i>Nabla operator</i>

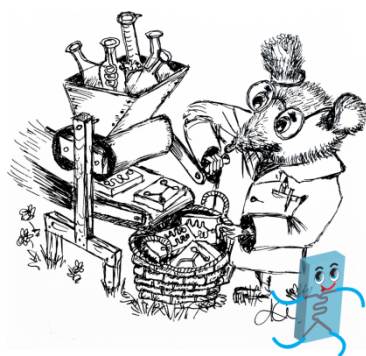
CONTENTS

1. Introduction	3
2. Fundamentals of Microfluidics	6
2.1 Fluid Physics	6
2.1.1 Flow.....	6
2.1.2 Mass Transport & Diffusion	12
2.1.3 Temperature	19
2.2 Microfluidics <i>versus</i> Microelectronics	20
2.2.1 Analogies.....	20
2.2.2 Circuits	22
2.2.3 Differences.....	25
3. Methods	27
3.1 Fabrication of Microfluidic Devices.....	27
3.1.1 Additive techniques.....	28
3.1.2 Subtractive techniques.....	29
3.1.3 Forming techniques.....	31
3.1.4 channel Sealing.....	33
3.1.5 other methods.....	34
3.1.6 Materials.....	34
3.1.7 Photolithography.....	36
3.1.8 PDMS Microfluidics	39
3.2 Microscopy.....	42
3.3 Simulations.....	47
4. Technology.....	49
4.1 Microfluidic dilution	49

4.2 Localized Delivery of Chemicals	53
4.2.1 Hydrodynamic flow confinement	53
4.2.2 Solution Exchange - need for speed.....	58
4.2.2 Other Methods to deliver chemicals.....	59
4.3 Functional BioMembranes	61
4.3.1 Structure of the Biomembrane	61
4.3.2 Properties of the Biomembranes.....	62
4.3.3 Supported lipid membrane technologies.....	62
Summary	64
Acknowledgements	68
References	70

Appendix

Papers I-VII



1. INTRODUCTION

Squeezing flasks and tubes from chemistry labs into small chips filled with networks of channels, valves, mixers and reaction chambers is a goal of the new and rapidly blooming field of Microfluidics. These so called 'Lab on a Chip' devices may eventually revolutionize medical diagnostics as well as chemical and biological analysis and research.

-- In the 23rd century, interplanetary travel has become as common as flights from London to Paris a few centuries ago. Of course, mankind hasn't made progress only in rocket science. A traveler has great need for protection, while wandering in the vastness of space. That's why Starfleet is equipped with Tricorders[1]- handheld devices which can help, while scouting on an alien planet or examining the health of a person, to detect infections by space bugs. -- With this vision of the future depicted in the 1960's cult movie Star Trek, director Gene Roddenberry was decades ahead of his time. It was in the 1980s, when a microfabricated gas-chromatography column was actually putting forward the first steps towards miniaturization in chemical analysis[2]. And it took yet another decade, until 1991, before the Swedish company Pharmacia Biosensor AB (later Biacore AB, now part of GE Healthcare) coined the name 'Microfluidics' in one of their scientific papers[3]. Despite of this little known origin, the term 'Microfluidics' has now become synonymous with an entire field of science and technology, which is focusing on liquid manipulation and chemistry inside microscale devices. The field has exploded during the last decade, which is indicted by a doubling of the number of scientific publications and patent applications in less than every three years (Figure 1.1 A). Of course, such intensive research has resulted in a multitude of achievements, including deeper understanding of fluid physics at small scales, different means of fabrication and control, numerous applications and already more than a hundred companies making microfluidics-related products. Still, when looking at the typical technology lifecycle model (Figure 1.1 B), microfluidics is in its puberty, undergoing rapid development toward maturation[4], which includes improvements in manufacturing as well as identification of new applications. This shall pave the way for the wide-scale use of the technology, eventually bringing benefits for the society in general, such as faster, cheaper and more comprehensive diagnostics[5]. While the interplanetary spaceships from the Star Trek world are still a matter of science fiction, the medical Tricorder, helping to tackle "earth bugs", is actually almost within our reach. In 2012 Qualcomm was announcing a Tricorder X Prize of 10 million USD for the first team to successfully build a portable device which is able to detect autonomously 15 distinct and common diseases, and does it better or at least as good as a trained physician[6]. This device would allow to keep better track of personal health, prevent diseases, and reduce queues in front of doctors' doors. All

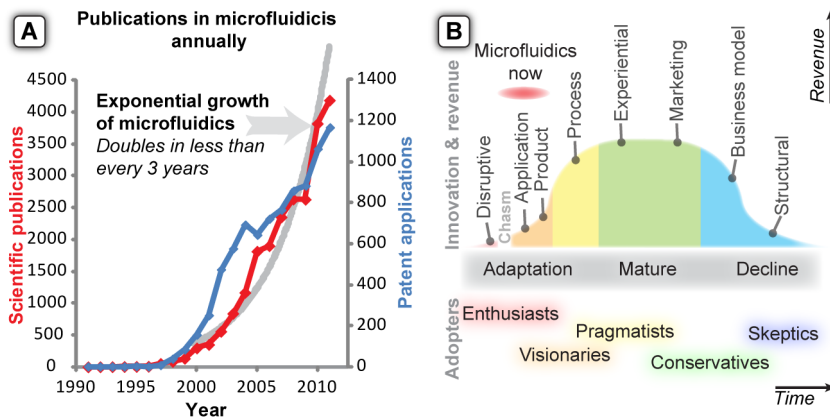


Figure 1.1. Development of microfluidics technology. **(A)** Growth of microfluidics during last two decades. Based on scientific (ISI Web of Knowledge) and patent (espacenet) databases. **(B)** Microfluidics in technology life cycle. Different phases of innovation, adaptation and economic impact[7-8].

of these points are of critical importance in the future, since the aging population will inevitably increase the social burden of healthcare needs.

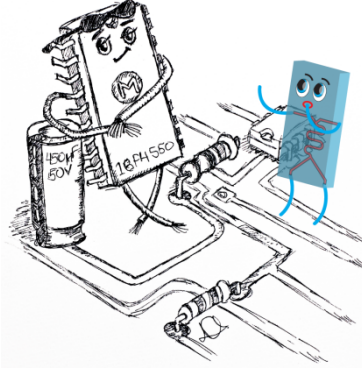
Microfluidics is not only holding promises in diagnostics, but can also extend the technical possibilities in our chemical, biological and medical research laboratories, for example by increasing efficiency and throughput, or by providing equipment in size scales specifically fitted to address single cells or their parts.

The backbone of this thesis is indeed the development of microfluidics based research tools and components, providing biophysicist and biologist with new means to control the chemical environment around single-cells. The PhD project started with a computer controlled, general purpose microfluidic dilution device, designed to generate chemical waves with desired parameters (Paper I). When it turned out to be cumbersome to apply this initial device in real biological experiments, it inspired the development of the next concept, which we termed a microfluidics pipette (Paper II). This device allowed localized delivery of solutions with precision at the size scale of single cells in open volumes. This concept was reshaped for improved usability, turning it into a multifunctional tool for bioscience research (Paper III). We have explored diverse uses of the device for single cell electroporation (Paper IV), delivery of neurochemicals to brain slices (Paper V), and temperature measurement (Paper VI), and finally made a leap into new application areas and established a general method for the printing and manipulation of 2D nanofluidic circuits - a "lab on a membrane" (Paper VII).

The thesis provides the background and context for the research described in the included papers. First relevant fluid physics, transport process are discussed, followed by practical instructions and considerations for designing microfluidics systems, and the finally the methods relevant for the thesis, such as microfabrication, imaging with different microscopy tools, and modeling are listed. The final chapter provides an in-depth overview, and

comparison of the specific technologies studied and developed in this thesis, which are dilution, delivery of chemicals to adherent cells, and trapping of micro-objects.

The author hopes that the thesis would not only earn him an advanced degree, but will also provide some inspiration for new students who are starting to explore the field of microfluidics, as well as some useful hints and guidance to consider before designing chips. Unfortunately, the relevance of the thesis could potentially be short lived, due to the rapid development of the field. On the other hand, that is exactly what is making it so exciting to work with!



2. FUNDAMENTALS OF MICROFLUIDICS

Microfluidics and its big brother Microelectronics. Microelectronics has provided a plentitude of inspiration, also tools for fabricating Microfluidics. Both have similarities even when it comes to physical laws. Yet why has Microfluidics not been able to repeat the glory of its older sibling? Why it has been so difficult to fully mimic electronic systems? These questions will be addressed in the following chapter, along with a brief exploration of the physical principles of microfluidics.

2.1 FLUID PHYSICS

2.1.1 FLOW

Transport of liquid in microscale channels is central for most microfluidic systems, including the ones described in this thesis. Therefore it is important to understand the basic driving forces, mechanisms and properties of microflows. The mechanical aspect of the flow, which is the motion of liquid, is described by classical mechanics and hydrodynamics. In order to derive such a flow equation, one can actually start from basic principles of mechanics known as Newton's laws, named after Sir Isaac Newton, who formulated them in his work *Philosophiae Naturalis Principia Mathematica* at 1687. Most important are his 2nd and 3rd law (Eq 2.1 and Eq 2.2) relating acceleration and force acting on a body, and defining mutuality of interactions.

$$\vec{a} = \frac{\vec{F}}{m} \quad (2.1)$$

Where \vec{F} is the force acting on a body, m is its mass and \vec{a} the acceleration caused by the force.

$$\vec{F}_2 = -\vec{F}_1 \quad (2.2)$$

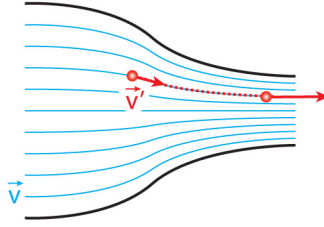


Figure 2.1. Steady flow in a tube with shrinking diameter. The concept of a velocity field \vec{v} (blue) and the velocity of a particular fluid particle \vec{v}' (red). Even though the velocity field is steady, the particular fluid particle can accelerate during its journey.

Which implies, that if one body affects another with force \vec{F}_1 , then the second body affects the first back with force \vec{F}_2 , which has the same magnitude, but acts in opposite direction.

While the original notion of Newton's 2nd law is well suited for describing falling apples and the motion of other solid objects, it is less convenient for handling liquid streams. For solid objects their coordinate and velocity is used to describe motion, while for fluids the **velocity field** becomes handier. It means that we are not looking at the velocity of one particular "fluid particle", but instead at the velocity of the fluid in a certain place in space. The important difference can be understood, if we imagine a constant flow rate in a tube, which means that the velocity field should be also constant. However, if the tube has a narrower region, the liquid needs to accelerate to pass it, since the flow velocity must be higher in the narrower region in order to maintain an overall constant flow rate. This means, that a particular fluid particle, which would always be a subject to the Newton's 2nd equation, may experience acceleration, even if the velocity field is steady. This is illustrated in figure 2.1.

Lets express the acceleration of fluid particle \vec{a}' from the velocity field \vec{v} during an infinitely small time step dt . This acceleration would contain then two parts; one due to the change in the velocity field, and another due to the changing position of the particle in the steady field.

$$\vec{a}' = \frac{d\vec{v}'}{dt} = \underbrace{\frac{\vec{v}(t+dt) - \vec{v}(t)}{dt}}_{\text{temporal}} + \underbrace{\frac{\vec{v}(\vec{r}(t+dt)) - \vec{v}(\vec{r}(t))}{dt}}_{\text{spatial}} \quad (2.3)$$

Using the chain rule of differentiation on a spatial component, eq. 2.3 becomes

$$\vec{a}' = \frac{d\vec{v}(t)}{dt} + \underbrace{\frac{d\vec{r}(t)}{dt}}_{\vec{v}} \frac{d\vec{v}(\vec{r})}{d\vec{r}} \quad (2.4)$$

Since $\vec{v} = \vec{v}(t, \vec{r})$, the partial derivative notation shall be used here, giving

$$\vec{a}' = \frac{\partial \vec{v}(t, \vec{r})}{\partial t} + \vec{v} \frac{\partial \vec{v}(\vec{r})}{\partial \vec{r}} = \frac{\partial \vec{v}}{\partial t} + \vec{v} \cdot \nabla \vec{v} \quad (2.5)$$

From the acceleration of the fluid particle and its mass dm , we calculate the force $d\vec{F}'$

$$d\vec{F}'_{net} = dm\vec{a}' \quad (2.6)$$

In contrast to solid objects, the density ρ would be a more suitable descriptor of a fluid than the mass of some arbitrarily chosen particle:

$$d\vec{F}'_{net} = \rho dV \vec{a}' = \rho dV \left(\frac{\partial \vec{v}}{\partial t} + \vec{v} \cdot \nabla \vec{v} \right) \quad (2.7)$$

In most microfluidic systems where water solutions are used, it is safe to assume that the fluid is incompressible, which means that the density is a constant

$$\text{div}(\vec{v}) = 0 \text{ and } \rho = \text{const} \quad (2.8)$$

As seen from eq. 2.7, even a steady flow of a liquid features acceleration, and therefore forces acting between the fluid particles. The most common forces, which are always present, are caused by pressure and the viscosity of the fluids.

Liquid pressure acts on all surfaces and exerts a force in perpendicular direction to them. In order to derive the force exerted to a liquid particle with volume V we need to integrate the pressure over the surface of this particle, where dS denotes a small surface element and \vec{n} points to its normal direction.

$$\vec{F}'_{pres.} = - \oint \oint_{\text{surface of particle}} P \cdot \vec{n} dS \quad (2.9)$$

By using Ostrogradsky's divergence theorem, this integral over the surface can be turned into an integral over volume

$$\vec{F}'_{pres.} = - \iiint_{\text{volume of particle}} \nabla P dV \quad (2.10)$$

If the volume V is infinitely small, we will have a differential form of the equation

$$d\vec{F}'_{pres.} = -\nabla P dV \quad (2.11)$$

Where ∇P is the pressure gradient (also denoted $\text{grad}(P)$)

Another important force is friction inside fluid flow, which happens when different parts of the liquid move at different velocity. This was also studied by Newton, who found that the force F required to overcome the friction and move two parallel plates relative to each

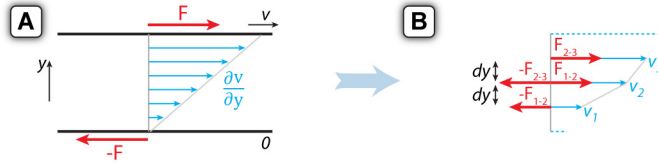


Figure 2.2. Viscosity. **(A)** Two parallel plates separated by a Newtonian fluid and moving relative to each other (also known as Couette flow). **(B)** Relating viscous forces and velocity field.

other, when both are separated by a fluid, is proportional to the velocity gradient (also called shear rate) $\partial v / \partial y$ and the area of the plates S (Figure 2.2A)

$$F = \eta S \frac{\partial v}{\partial y} \quad (2.12)$$

with a proportionality constant η , called **dynamic viscosity**, which is a characteristic property of the fluid, depending also on the temperature. However, this relation is correct only for some simple substances, called Newtonian fluids. In non-Newtonian fluids, like polymer solutions, η depends also on shear rate, making the behavior much more complex. Fortunately water and most dilute aqueous solutions used in microfluidics behave as Newtonian fluids, therefore we focus in following only on them.

Starting from Newton's law of viscosity we can derive how the viscous force inside the fluid is related to the velocity field. First let's imagine three close layers of fluid, which move with different speeds v_1 , v_2 and v_3 . If the layers are separated by distance dy , the forces acting between them can be calculated using Newton's viscosity law (2.12)

$$\begin{aligned} F_{2-3} &= \eta S \frac{v_3 - v_2}{dy} \\ F_{1-2} &= \eta S \frac{v_2 - v_1}{dy} \end{aligned} \quad (2.13)$$

Taking into account Newton's 3rd law about the mutuality of interactions (Eq. 2.2) and the summing forces from both sides we can calculate the net force acting on the middle layer of the fluid

$$F = F_{1-2} - F_{2-3} = \eta S \left(\frac{v_2 - v_1}{dy} - \frac{v_3 - v_2}{dy} \right) \quad (2.14)$$

As seen from this equation the force acting on the fluid layer does not depend on the velocity gradient, but on its change, which can be described through the derivative of the gradient in case of infinitely small dy .

$$F = \eta S \frac{\partial}{\partial y} \left(\frac{\partial v}{\partial y} \right) dy = \eta \frac{\partial}{\partial y} \left(\frac{\partial v}{\partial y} \right) \underbrace{S dy}_{dv} \quad (2.15)$$

where dV is the volume of the layer. In order to generalize the equation, we calculate the force, considering infinitely small layers (dS), and three dimensions:

$$d\vec{F}'_{visc.} = \eta \nabla^2 \vec{v} dV \quad (2.16)$$

Now the different forces can be combined, and the net force is proportional to the acceleration

$$\begin{aligned} d\vec{F}'_{net} &= d\vec{F}'_{pres.} + d\vec{F}'_{visc.} \\ \rho dV \left(\frac{\partial \vec{v}}{\partial t} + \vec{v} \cdot \nabla \vec{v} \right) &= -\nabla P dV + \eta \nabla^2 \vec{v} dV \end{aligned} \quad (2.17)$$

After dividing both sides by dV we obtain the following differential equation

$$\rho \left(\frac{\partial \vec{v}}{\partial t} + \vec{v} \cdot \nabla \vec{v} \right) = -\nabla P + \eta \nabla^2 \vec{v} \quad (2.18)$$

This equation, named after 19th century French and British scientists Claude-Louis Navier and Sir George Gabriel Stokes (**Navier-Stokes' equation**) relates the velocity field of the flow with the pressure distribution and viscosity. It is a central concept in all flow calculations. Unfortunately, this non-linear partial differential equation is almost never analytically solvable. In fact, understanding Navier-Stokes' equation is considered one of the greatest unsolved problems in mathematics, with a million dollar price promised to someone who can elucidate its properties[9].

But some qualitative insight into the flow behavior and its dependence on the size scales can be obtained by using scaling laws. For that purpose eq. 2.18 can be re-written in a dimensionless form, using the following replacements

$$\vec{r} = L_0 \vec{\tilde{r}}, \nabla = \frac{1}{L_0} \vec{\tilde{\nabla}}, \vec{v} = v_0 \vec{\tilde{v}}, t = \frac{L_0}{v_0} \tilde{t} \text{ and } P = \frac{\eta v_0}{L_0} \tilde{P} \quad (2.19)$$

Where \sim denotes dimensionless analogues. L_0 and v_0 are characteristic size and velocity scales.

$$\rho \left(\frac{v_0}{L_0} \frac{\partial \vec{\tilde{v}}}{\partial \tilde{t}} + v_0 \vec{\tilde{v}} \cdot \left(\frac{v_0}{L_0} \right) \vec{\tilde{\nabla}} \vec{\tilde{v}} \right) = - \left(\frac{\eta v_0}{L_0^2} \right) \vec{\tilde{\nabla}} \tilde{P} + \eta \left(\frac{v_0}{L_0^2} \right) \vec{\tilde{\nabla}}^2 \vec{\tilde{v}} \quad (2.20)$$

Re-arrangements lead to

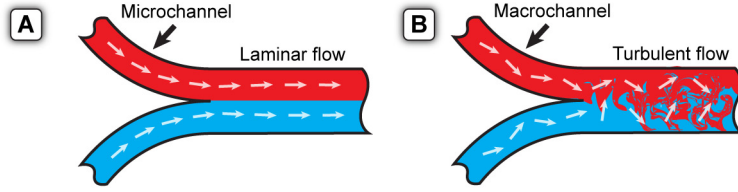


Figure 2.3. Velocity field. **(A)** Laminar flow. **(B)** Turbulent flow

$$\underbrace{\frac{\rho v_0 L_0}{\eta}}_{Re} \left(\frac{\partial \vec{v}}{\partial t} + \vec{v} \cdot \nabla \vec{v} \right) = -\nabla \tilde{P} + \nabla^2 \vec{v} \quad (2.21)$$

demonstrating that the dimensionless Navier-Stokes' equation depends only on one scaling parameter, known as **Reynolds number** (Re)

$$Re = \frac{\rho v_0 L_0}{\eta} \quad (2.22)$$

If Re is large ($Re \gg 1$), the equation is dominated by the left side, which describes inertia. Due to the non-linear term $\vec{v} \cdot \nabla \vec{v}$ the behavior of flow in a "high Reynolds number mode" is chaotic (**turbulent flow**). Alternatively, if Re is low ($Re \ll 1$), the inertial side can be neglected and the equation is dominated by pressure and viscosity terms. This linear equation, known as **Stokes' equation** (Eq 2.23) has a well defined solution, which corresponds to the **laminar flow** regime. In typical microfluidic systems, where the channel sizes are small and the flow is slow, the Reynolds number is low and the flow is laminar.

Stokes' equation

$$\nabla P = \eta \nabla^2 \vec{v} \quad (2.23)$$

This equation has analytical solutions for a variety of simple geometries like cylindrical and rectangular tubes. Due to fabrication constraints, microfluidic channels have most commonly rectangular geometry. In a long rectangular channel the flow field is [10]

$$v_x(y, z) = \frac{4h^2 \Delta p}{\pi^3 \eta L} \sum_{n, \text{odd}} \frac{1}{n^3} \left[1 - \frac{\cosh\left(n\pi \frac{y}{h}\right)}{\cosh\left(n\pi \frac{w}{2h}\right)} \right] \sin\left(n\pi \frac{z}{h}\right) \quad (2.24)$$

$$v_y = v_z = 0$$

Where L is the channel length along the x axis, h is the channel height along the z axis, w is the channel width along the y axis and Δp is the pressure difference between the channel ends. If the velocity is integrated over the cross section, the total flow rate can be found as

$$\begin{aligned}
 Q &= \int_0^h \int_{-w/2}^{w/2} v_x(y, z) dy dz \\
 &= \frac{h^3 w \Delta p}{12 \eta L} \left[1 - \sum_{n, odd}^{\infty} \frac{1}{n^5} \frac{192}{\pi^5} \frac{h}{w} \tanh\left(n\pi \frac{w}{2h}\right) \right]
 \end{aligned} \tag{2.25}$$

For practical purposes, this infinite series is still hard to calculate, therefore an approximation can be used

$$Q = \Delta p \frac{h^3 w}{12 \eta L} \left[1 - 0.630 \frac{h}{w} \right] \tag{2.26}$$

where $h < w$. In worst case, when the channel has a square cross-section, the error generated by using this approximation is actually only 13%.

2.1.2 MASS TRANSPORT & DIFFUSION

From a chemical point of view, it would be boring to pump just water. Therefore, most of the microfluidic systems handle a variety of solutions and reagents, are able to mix and switch between them, and carry out chemical reactions. This introduces a new dimension into the equations - the chemical composition. In case there is no reactivity between different fluids and no strong interaction between composition and flow, the composition can be split into independent concentrations of molecules and each of them can be considered separately. An example for a case where composition and flow behavior are not independent would be sugar solution and water, where the sugar concentration determines viscosity and therefore flow, which would then again influence concentration. This type of coupling makes calculations significantly more complex. In contrast, the research presented in this thesis involved only dilute solutions, where the chemical composition has no major effect on the flow properties. In this case the concentration of a substance can be described by the **convection-diffusion equation** (Eq. 2.27)

$$\frac{\partial c}{\partial t} = -\vec{v} \cdot \nabla c + D \nabla^2 c \tag{2.27}$$

where the left-hand side describes the temporal change of the concentration, which depends on the convective transport by the flow ($-\vec{v} \cdot \nabla c$), and on diffusion ($D \nabla^2 c$). This equation has a striking similarity to the Navier-Stokes equation, where just c has been replaced by \vec{v} . Therefore, the Navier-Stokes equation can be considered as the transport equation of momentum, where viscosity acts as diffusivity of momentum.

If we convert the convection-diffusion equation into a dimensionless form, as we did previously with Navier-Stokes (Eq. 2.21), the resulting equation depends on two scaling parameters St and Pe

$$St \frac{\partial \tilde{c}}{\partial \tilde{t}} = -\tilde{\mathbf{v}} \cdot \tilde{\nabla} \tilde{c} + \frac{1}{Pe} \tilde{\nabla}^2 \tilde{c} \quad (2.28)$$

where St stands for the Strouhal number, describing unsteadiness, and Pe for **Peclet number**, describing the ratio between convective and diffusive mass transport. Pe is analogous to the Reynolds number, which describes the same for momentum.

$$St = \frac{L_0}{\tau v_0} \quad \text{and} \quad Pe = \frac{v_0 L_0}{D} \quad (2.29)$$

where τ is the unsteady time.

In the following we consider two important cases, which are both also relevant for the research presented in this thesis. First, a steady flow and concentration pattern, where $St = 0$, and second, transient propagation of concentration pulses in a pressure driven flow.

Steady flow

Our macro-world experience tells us that putting together two miscible liquids, for example syrup and water, will eventually result in their complete mixing. Microfluidics, on the other hand, offers an easy way to form and even maintain spatially constant concentration gradients. This requires that diffusion, which always mixes substances until the differences have faded, is compensated by the convective flow, which replaces mixed liquids. The dimensionless convection-diffusion equation (Eq. 2.28) shows that the stationary equation ($St=0$) depends only one parameter, which is the Peclet number. Here, a higher Peclet number implies dominance of convection over diffusion, therefore less mixing and sharper concentration gradients, and vice versa. This is illustrated in figure 2.4, showing a typical T- or Y-channel, where two solutions enter a common channel, co-flow, and mix diffusively. The further we go from the junction point, the more diffusion has progressed, and the smoother is the gradient. A detailed description of the concentration profile is complex and requires numerical simulations. However, if we can assume a 2-dimensional channel with constant velocity, an analytical solution is possible (Eq. 2.30)

$$c(x, w, t/T_0) = \frac{c_0}{2} \sum_{n \in \pm \mathbb{N}} \left(\operatorname{erf} \left(\frac{x/w - (2n+1)}{\sqrt{t/T_0}} \right) - \operatorname{erf} \left(\frac{x/w - 2n}{\sqrt{t/T_0}} \right) \right) \quad (2.30)$$

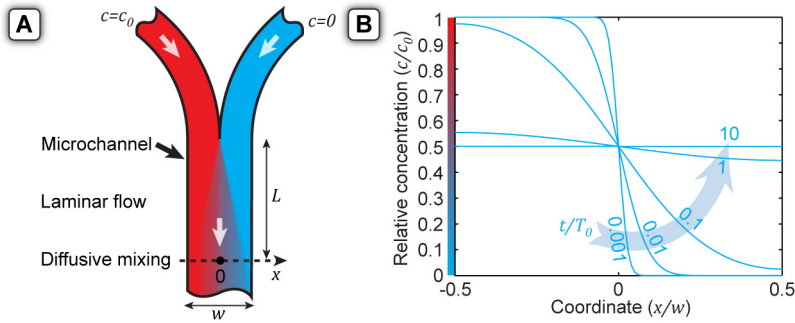


Figure 2.4. Stationary concentration gradients in microchannels. **(A)** A Y-shaped channel, fed by two flows, where one is carrying a solution of a substance with concentration c_0 and the other one is the pure solvent ($c=0$). Due to the lack of turbulence, these two flows mix only due to molecular diffusion, which smoothens the concentration difference between the flows. On the other hand this diffusive mixing is compensated by a replenishing supply of liquids. The balance between diffusion and convective replacement is establishing a stationary concentration distribution **(B)**. The concentration profile in this kind of channel depends only on one dimensionless time ratio t/T_0 . The greater the ratio, the smoother is the gradient.

where $T_0 = w^2/4D$ is characteristic time-scale of the system, and $t = L/v_{aver}$ is the time, during which diffusion has occurred. In reality this assumption is well suitable for high aspect ratio channels.

This principle has been used in a variety of devices, for example to generate concentration gradients for cell migration studies[11]. There is a class of separation techniques, based on devices called H-filters, where these two flows are split apart again at the end of the common channel [12]. The separation of the substances is based on their different diffusion properties. Even more efficient separation is achieved when active transport can be included and the selected substance can be dragged to one edge of the channel, for example by magnetic force[13], which is used to remove pathogens from blood. The transport mode can be even biological. For example, similar filters have been used to separate live and dead sperms to improve *in vitro* fertilization[14]. Besides separation, this kind of dispersion in microchannels has to be considered when designing microfluidic mixers, to make sure that two fluids have been become well blended at the end of a mixing channel.

The same principle of convection competing with diffusion has found an application in hydrodynamic flow confinement (HCF), allowing localized delivery of chemicals. HCF is a key element of the multifunctional pipette, studied in this thesis.

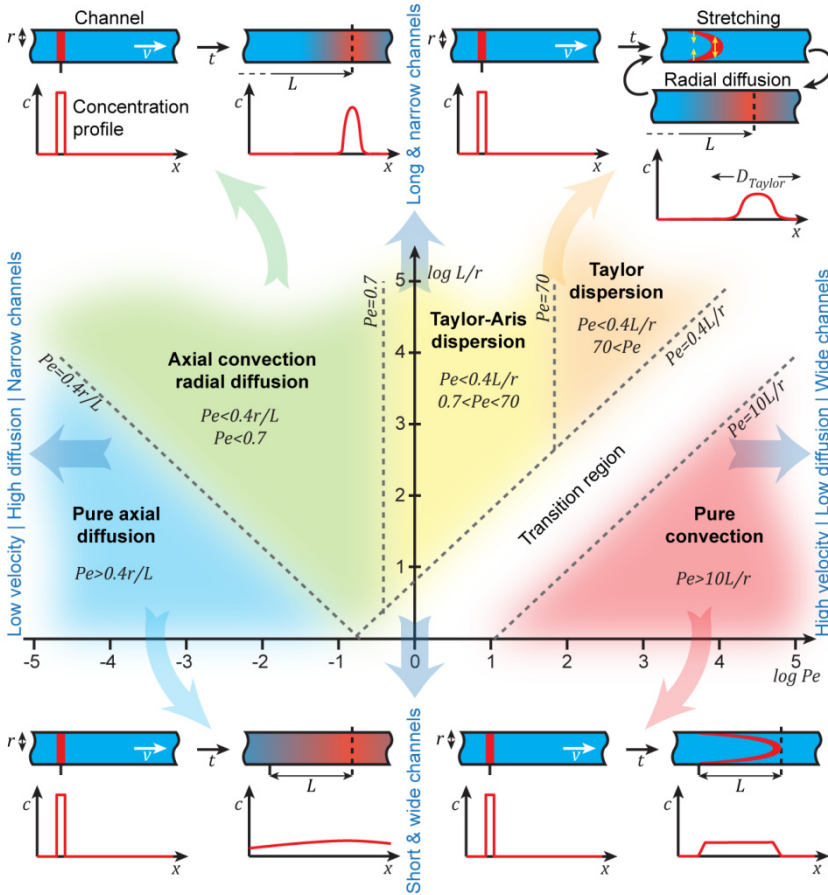


Figure 2.5. Dispersion models and their regions of applicability depending on Pe number and channel geometries (L/r). (According to Probstein “Physiochemical Hydrodynamics”[15]). The colors used to shade the regions have blurry edges to emphasis that the transitions between these modes are not sharp. The illustrations show how a short plug of a substance is dispersed in case of different transport modes.

Transient flow

But how will a fluid stream with unsteady composition be affected when it is transported in microfluidic channels? If we switch between different solutions? These questions can be answered by analyzing the transient propagation of concentration pulses. The convection-diffusion equation (Eq. 2.28) shows that in this case all three terms contribute to the equation, and an exact solution would depend on two dimensionless parameters, St and Pe . This makes it more complicated to formulate a universal description. However, depending on which phenomena are dominating it is possible to separate different transport modes, and provide simpler models to describe each of them[15]. This depends on two aspects,

the Peclet number and the ratio of channel length and radius L/r (Figure 2.5). Here the Peclet number represents the ratio of convection along the channel axis (axial) and diffusion across its cross section (radial). But since the convection ($\propto t$) and diffusion ($\propto \sqrt{t}$) are scaling differently, channel length has to be also considered in order to determine the right transport model.

Let's look first at the case of a low Pe number, where the flow is slow and the diffusion is fast. If the channels are relatively short, the output is primarily dominated by diffusion (**Pure axial diffusion**). However, when the channel length is increased, the convection will eventually catch-up with diffusion, due to their different scaling. In this case, the convection dominates the axial transport, but the radial transport is still ruled by the diffusion, which means that the concentration over the cross-section of the channel is constant. (**Axial convection, radial diffusion**). the border between these modes is approximately at $Pe \approx 0.4 r/L$.

If we increase the flow and Peclet number, the radial diffusion cannot keep up with convection. In case of very fast flow and short channels, the pressure driven fluid stream is stretching the substance pulse into a parabolic shape, while diffusion does not have time for any significant action. Then the dispersion is only due to **Pure convection**. When the channels are made sufficiently long, both diffusion and convection are entering the process. Convection is stretching the concentration pulse and diffusion is mixing it in radial direction. This was studied by the British physicist Sir G. I. Taylor in the 1950's[16], who found that the interplay between axial stretching and radial diffusion causes the injected fluid plug to be smeared in the same way as diffusion does, but with a very much higher diffusion coefficient. This dispersion mode has been coined after him as **Taylor dispersion**. The effectively increased axial diffusion coefficient D_{eff} is called a Taylor dispersion coefficient (Eq. 2.31)

$$D_{eff} = \frac{r^2 v_{aver}^2}{48D} \quad (2.31)$$

In contrast to the molecular diffusion coefficient D , the Taylor dispersion coefficient is not a materials property, but depends on the geometries and flow rates in the tube. It is interesting to note that molecular diffusion has an inverse effect on the Taylor dispersion (Eq. 2.31). A higher D corresponds to lower dispersion. Pure Taylor dispersion neglects the axial diffusion, but when the Pe numbers are lower, both the contribution of Taylor dispersion and of molecular diffusion should be considered (**Taylor-Aris dispersion**), with the dispersion coefficient given by eq. 2.32.

$$D_{eff} = D + \frac{r^2 v_{aver}^2}{48D} \quad (2.32)$$

When it comes to practical calculations, it is important to notices that the above given coefficients (Eq. 2.31, 2.32) and boundaries between the dispersion modes are for circular capillaries. In case of other channel shapes, geometry specific correction coefficients have

to be used, while the scaling laws still hold universally. For example, for high aspect ratio channels with width w , the Taylor-Aris dispersion becomes (Eq. 2.33)[17].

$$D_{eff} = D + \frac{w^2 v_{aver}^2}{210D} \quad (2.33)$$

In case of more complex geometries and transition region between the dispersion modes, it is often most efficient to use numerical computer simulations (discussed in a later chapter).

In all transport models (Figure 2.5) other than pure convection and the transition region neighboring it, the concentration can be considered constant across the channel cross-section (radially), and varies only along the channel axis, i.e., dispersion and transport can be described as a one dimensional system.

This simplifies the mathematical representation. In all these cases, dispersion is described as diffusion, whether molecular or Taylor's.

If we want to calculate how a solution of variable composition is affected by the transport through a channel, the notion of signals and system, where time dependent concentration takes the role of a signal, and diffusion in the channel takes the role of a system, can become useful. In this notion a system acts on the input signal, turning it into an output signal. The diffusion process is a linear-time invariant (LTI) system, meaning that i) changing concentration at the input would change the concentration at the output proportionally, and ii) the channel behaves exactly the same at different times. LTI systems have several useful properties. They can be described entirely by their impulse response function, which reflects how the system transforms an infinitely narrow input pulse (delta impulse). In case of diffusion, or Taylor dispersion, such a pulse would spread and evolve into a Gaussian (Eq. 2.34).

$$C_{sys}(x, t) = \frac{1}{\sqrt{4\pi Dt}} \exp\left(-\frac{x^2}{4Dt}\right) \quad (2.34)$$

where D is the dispersion coefficient and t is time. If we consider a channel with length L and average velocity v_{aver} , the spatial coordinate can be turned into a time delay. $t = (L - x)/v_{aver}$, giving eq. 2.35.

$$C_{sys}(t) = \frac{1}{\sqrt{4\pi Dt}} \exp\left(-\frac{(L - tv_{aver})^2}{4Dt}\right) \quad (2.35)$$

LTI implies that in this case the output signal of the system is a convolution of input signal and impulse response of the system (Eq. 2.36).

$$c_{out}(t) = c_{inp}(t) \otimes C_{sys}(t) = \int_{-\infty}^{\infty} c_{inp}(\tau) C_{sys}(t - \tau) d\tau \quad (2.36)$$

LTI systems can be represented also in a frequency (Fourier) domain, where the convolution integral turns into a simple multiplication of the two spectra of the input signal and the impulse response (Eq. 2.37).

$$c_{out}(\omega) = c_{inp}(\omega) \cdot \mathbf{C}_{sys}(\omega) \quad (2.37)$$

Each spectrum can be found using the Fourier transform (2.38).

$$c(\omega) = \int_{-\infty}^{\infty} c(\tau) e^{-i\omega\tau} d\tau \quad (2.38)$$

If we assume that axial convection is larger than dispersion, as it usually is, the impulse response of the channel would become (Eq. 2.39)

$$\mathbf{C}_{sys}(t) \approx \frac{1}{\sqrt{4\pi DL/v_{aver}}} \exp\left(-\frac{(L - tv_{aver})^2}{4DL/v_{aver}}\right) \quad (2.39)$$

which has Fourier transform (Eq. 2.40)

$$\mathbf{C}_{sys}(\omega) \approx \frac{1}{v_{aver}\sqrt{2\pi}} \exp\left(-\frac{DL}{v_{aver}^3} \omega^2\right) \exp\left(-i\frac{L}{v_{aver}} \omega\right) \quad (2.40)$$

The magnitude of this spectrum is (Eq. 2.41)

$$|\mathbf{C}_{sys}(\omega)| \propto \exp\left(-\frac{DL}{v_{aver}^3} \omega^2\right) = \exp\left(-\frac{\omega^2}{\omega_p^2}\right) \quad (2.41)$$

This function has larger values in case of low frequencies (ω) and low values in case of higher, which means also that the channel acts as a **chemical low-pass filter** for concentration signals, letting to pass slow concentration waves, while damping sharp changes. Parameter ω_p (Eq. 2.42) can be referred as a **cut-off frequency** of the filter[18].

$$\omega_p = \sqrt{\frac{v_{aver}^3}{DL}} \quad (2.42)$$

The cut-off frequency is higher with fast flow (no time for dispersion) and is lower with a higher dispersion coefficient and longer channels.

In the context of the research of this thesis, the chemical low-pass filter has been used in a microfluidic diluter (Paper I), where it smoothens fast pulses to a constant concentration level. Note that if fast solution exchange is desirable (Multifunctional pipette (Paper III)), the dispersion effects are a limiting factor.

2.1.3 TEMPERATURE

Temperature is also affecting chemical and physical processes. It describes the motional energy of molecules, which affects their diffusion and reaction rate (Arrhenius law), as well as the chemical equilibria. Thermal transport is very similar to the convection-diffusion equation (Eq. 2.27 and 2.43)

$$c_p \frac{\partial T}{\partial t} = -c_p \vec{v} \cdot \nabla T + \frac{k}{\rho} \nabla^2 T + P \quad (2.43)$$

where c_p is specific heat capacity, k is thermal conductivity, ρ is density and P is spatial heating power. Re-arranging the equation gives (Eq. 2.44)

$$\frac{\partial T}{\partial t} = -\vec{v} \cdot \nabla T + \frac{k}{\rho c_p} \nabla^2 T + \frac{P}{c_p} \quad (2.44)$$

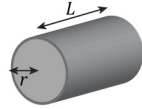
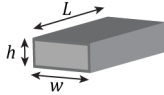
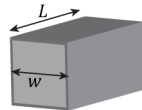
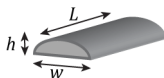
where $D_T = k/\rho c_p$ is the thermal diffusivity. Even though the thermal convection-diffusion equation is exactly the same as for the concentration case, there is one significant dissimilarity, which is especially important in the microfluidics realm: the difference of the diffusion constants between different materials. Molecules diffuse readily in liquids, but they do not enter into most of the solids (their diffusion constant is close to zero). Therefore we can consider that molecular diffusion occurs only inside channels, while , on the other hand, temperature is very similarly conducted by solids and liquids. For example, the thermal diffusivities in water and glass are $1.4 \cdot 10^{-7} m^2/s$ and $3.4 \cdot 10^{-7} m^2/s$, respectively. This means that both the liquid and the device have to be considered when calculating heat transport in microfluidics. For practical purposes this is mostly done by using finite-element modeling (FEM). In comparison to molecular diffusion, thermal diffusion is much faster. This is favorable in case precise temperature control is needed, due to the fast thermal equilibration of the liquid to the device temperature. Fast diffusion makes it, on the other hand, harder to generate thermal gradients (Figure 2.4). In order to achieve a sufficiently high Pe number, the channels have to be larger and flow faster. Nevertheless, thermal gradients established in microfluidic devices have been exploited to study, for example, developmental control mechanisms in fly embryos[19].

2.2 MICROFLUIDICS *VERSUS* MICROELECTRONICS

2.2.1 ANALOGIES

Microfluidic and microelectronic device are not only fabricated in a similar way, they also hold similarities in the circuit theories used to describe them. With slight modifications, this analogy provides a variety of useful tools for designing and analyzing microfluidic circuits. Equation 2.26 describes the flow rate dependence in a microfluidic channel, where the flow rate is proportional to the pressure difference at the channel ends and to a parameter depending on channel geometry and viscosity. This is corresponding to Ohm's law in electronics, which describes the proportionality between current and a voltage difference. Fluidic analogies for voltage, current, current density and charge would be pressure, flow rate, flow velocity and fluid volume, respectively. The channel geometry and viscosity dependent proportionality parameter is called "hydrodynamic resistance". Similar analogies exist also for the passive circuit elements capacitor and inductor (Figure 2.6). Hydrodynamic capacitance describes which volume of a liquid can be placed into a "liquid capacitor" per unit of pressure increase. In physical terms, the "liquid capacitor" can correspond to an elastic tube, which is enlarged in volume when pressurized, or to air-bubbles in a channel, which can be compressed. Inductance corresponds to mechanical inertia of the flow.

Table 2.1. Most common channel and tube geometries for microfluidics and their respective hydrodynamic resistances[10].

Geometry	Channel resistance	Figure
Circular	$R = \frac{8}{\pi} \eta L \frac{1}{r^4}$	
Rectangular	$R \approx \frac{12}{1 - 0.63(h/w)} \eta L \frac{1}{h^3 w}$	
Square	$R = 28.4 \eta L \frac{1}{w^4}$	
Parabolic	$R = \frac{105}{4} \eta L \frac{1}{h^3 w}$	

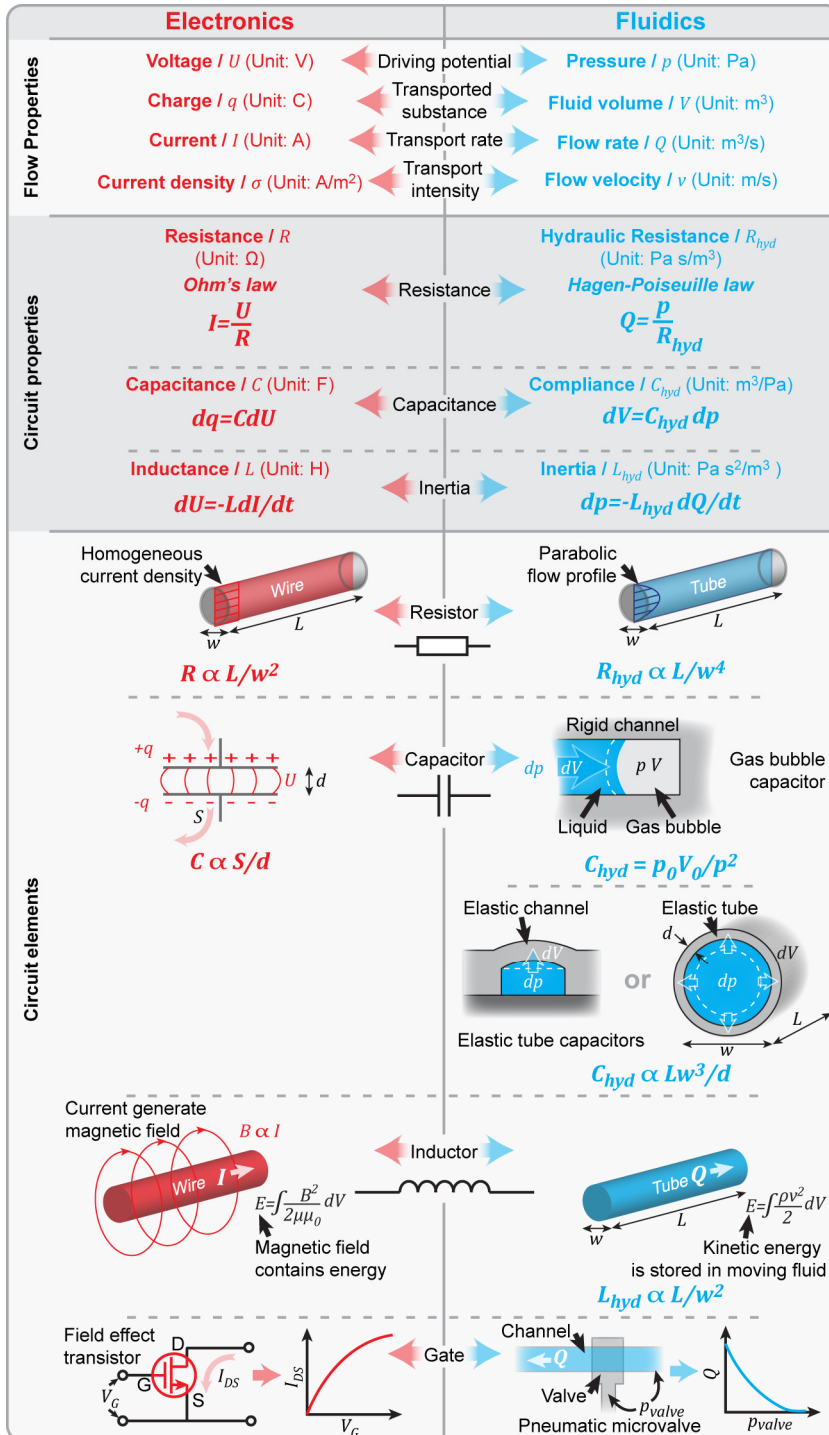


Figure 2.6. (On previous page) Analogies between electronics and fluidics.

Besides passive components, also active components, like valves are commonly found in microfluidic systems, allowing modulation of the fluid flow. Pneumatic analogs for digital logics, latches and even fluidic processors have been reported[20-22].

2.2.2 CIRCUITS

Similar to electronics, these microfluidic elements can be combined to circuits with different properties. The most common of such circuits is a simple network of channels, which corresponds to a network of flow resistors, where pressures are applied to the inlets. In order to find the flow rates in such a system, Kirchoff's rule, stating that the sum of flows to every circuit node has to be zero (incompressible fluid and channel), can be applied. For practical calculations we can first redraw the system in the way shown in figure 2.8., by grouping inlets/outlets and internal nodes of the circuits. The resistances of each flow resistor, and the pressures at the inlets, are known, thus the complete flow pattern can be calculated after the pressures at the internal nodes have also been found. This requires solving a linear equation system. To compose such an equation we consider linearity, which means that the flow in every resistor can be expressed as a superposition of two flows, each starting from a different end of the resistor. For mathematical simplicity we can replace the resistances by conductivities $G = 1/R$, then $Q = G \cdot p$. Now we can write the equation for an internal node i , using Kirchoff's current rule: the sum of the outflows from the node to every other node, and the inflows from every other node to the node has to be zero. For the node i this can be written as eq. 2.45.

$$\underbrace{-\left(\sum_{j=1}^m g_{ji} + \sum_{j=1}^n G_{j1}\right) p_i}_{\text{outflow from the node } i} + \underbrace{\sum_{j=1}^m g_{ji} p_j}_{\text{inflow from other internal nodes to node } i} + \underbrace{\sum_{j=1}^n G_{ji} P_j}_{\text{inflow from input nodes to node } i} = 0 \quad (2.45)$$

This system of m linear equations can be re-arranged into a matrix form (Eq. 2.46),

$$\underbrace{\begin{pmatrix} -\sum_{i=1}^m g_{i1} - \sum_{j=1}^n G_{j1} & \cdots & g_{1m} \\ \vdots & \ddots & \vdots \\ g_{m1} & \cdots & -\sum_{i=1}^m g_{im} - \sum_{j=1}^n G_{jm} \end{pmatrix}}_g \underbrace{\begin{pmatrix} p_1 \\ \vdots \\ p_m \end{pmatrix}}_{\vec{p}} = - \underbrace{\begin{pmatrix} G_{11} & \cdots & G_{n1} \\ \vdots & \ddots & \vdots \\ G_{1m} & \cdots & G_{nm} \end{pmatrix}}_G \underbrace{\begin{pmatrix} P_1 \\ \vdots \\ P_n \end{pmatrix}}_{\vec{P}} \quad (2.46)$$

which makes it convenient to solve (Eq. 2.47)

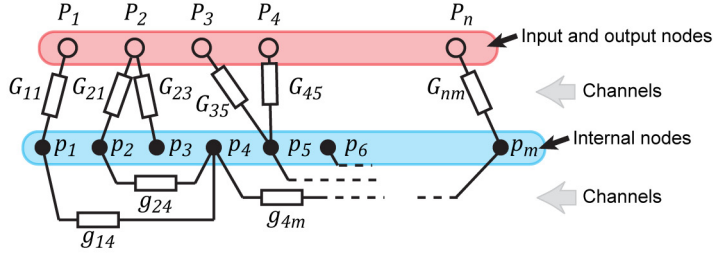


Figure 2.8. Calculating flows in arbitrary channel networks. The network has n inlets and outlets, with defined pressures P_i , and m internal nodes with pressures p_j which shall be found. Each internal node i can be connected with another internal node j through a resistor with conductance g_{ij} , or with inlet k through a resistor with conductance G_{ik} . Nodes that are not connected have zero conductances between them. Also $g_{ii} = 0$.

$$\vec{p} = -\mathbf{g}^{-1}\mathbf{G}\vec{P} \quad (2.47)$$

Other circuit elements, such as fluidic capacitors and inductors can be also incorporated to the calculation by replacing resistances by impedances with complex values.

In the following we consider a few important circuits for microfluidics design, where multiple different types of elements have been combined (Figure 2.9). Since these are not just resistor networks, their response has also a temporal component, which shall be considered while designing the fluidic switching systems. The first example is a tube or a channel, with elastic walls, or with a compressible fluid in it. Such a tube act as a series of resistors and capacitors (Figure 2.9A), known also as a RC-line, which slows and delays any pressure signal applied through it. Pressure propagation in such a tube is described by the differential equation (Eq. 2.48)

$$\frac{L^2}{RC} \frac{d^2 p}{dx^2} = \frac{dp}{dt} \quad (2.48)$$

If we turn it into a dimensionless form, as we did before with other equations, we can see that the equation depend only on one dimensionless parameter $\tau = RC$. The higher the RC constant the longer and slower is the response. This is an important consideration in fluidic switching systems, such as the multifunctional pipette presented in paper III. Similar RC circuits are involved in pneumatic valves (Figure 2.9B), since deflecting the valve will require a certain volume of fluid (capacitance), which is transported through the channel (resistance).

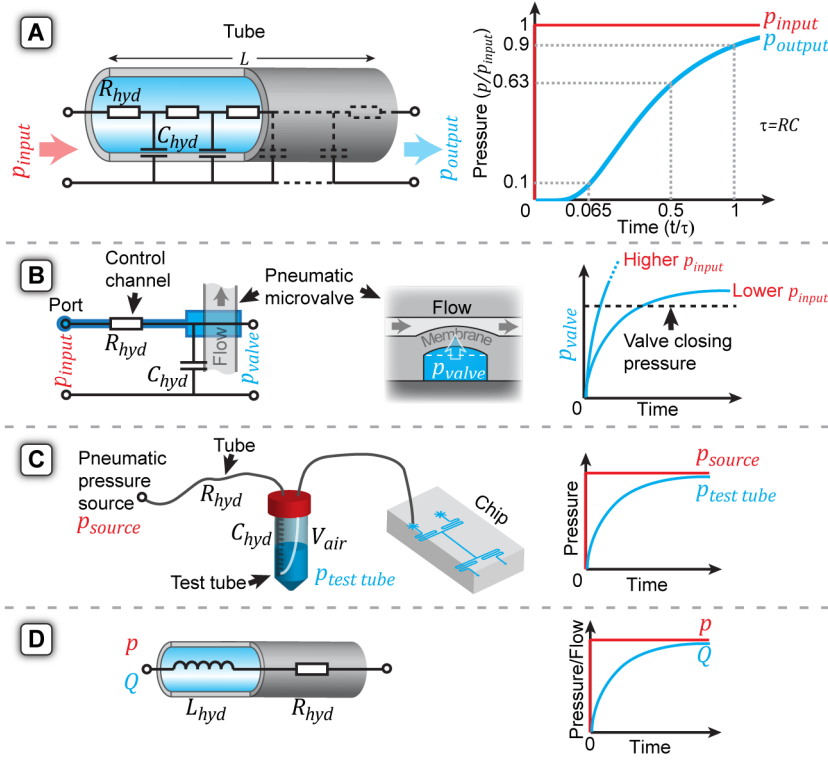


Figure 2.9. Circuit elements in microfluidic design. **(A)** Pressure propagation in elastic tube. **(B)** Control of microvalves. **(C)** Controlling pressures in supply tube. **(D)** Hydrodynamic inductance.

$$p_{out} = p_{inp} \left(1 - e^{-\frac{t}{\tau}} \right) \quad (2.49)$$

RC constant ($\tau = RC$) determines, how fast these valves can be actuated.

Here however, faster valve closure can be achieved by using higher control pressure, since the necessary pressure level would be reached sooner. The RC constant itself, however, is independent of pressure. This has been a consideration in the design of the microfluidic diluter (Paper I). The third example involves pressure driven flow from a test tube (Figure 2.9C). In order to establish a flow, the test tube has to be pressurized, which involves a gas flow from the supply. In case of small pressures, $C \approx V_0/p_0$. The last example shows a microfluidic analogue to an RL circuit, which is describing the inertia of the flow (Figure 2.9D). Hydraulic inductance can be expressed as $L = 2E_{kin}/Q^2$, which in case of a circular tube would be $L = 4\rho l/3\pi r^2$. the time constant of such a circuit is $\tau = L/R$, and it scales

with the channel size as $\propto r^2$, meaning that the significance of inertia is dropping rapidly with shrinking dimensions.

2.2.3 DIFFERENCES

Even though there are many analogies, fluidics is so far having difficulties to fully mimic highly integrated electronic circuits. This is due to few, but essential differences between these two domains of technology (Figure 2.10). The most important one is the way how information is carried and processed. In electronics, it is electric potential and current, carried by a single particle: the electron. In fluidics it is the pressure and the fluid flow, but with the exception of some micropneumatic control systems[22], interesting information is usually carried neither by the flow nor by the pressure, but by the chemical composition. Differently from the electron, there are nearly infinite numbers of molecules and mixtures possible. This has an implication: in fluidics it is not enough to convey information by waves of potential, but liquid has to actually travel through the system, which is much more time consuming and makes it hard to efficiently connect different chips with macroscopic tubing. The ease of interconnectivity has been the foundation for applicability of microelectronics. Microchips, which contain many microscopic transistors and require complex and expensive manufacturing are universal building blocks that are easily connected by macroscopic wires and circuit boards to create a particular functionality. Therefore great applications emerged (literally) from garage projects, for example the personal computer. Modular microfluidic constructors have been also developed, but

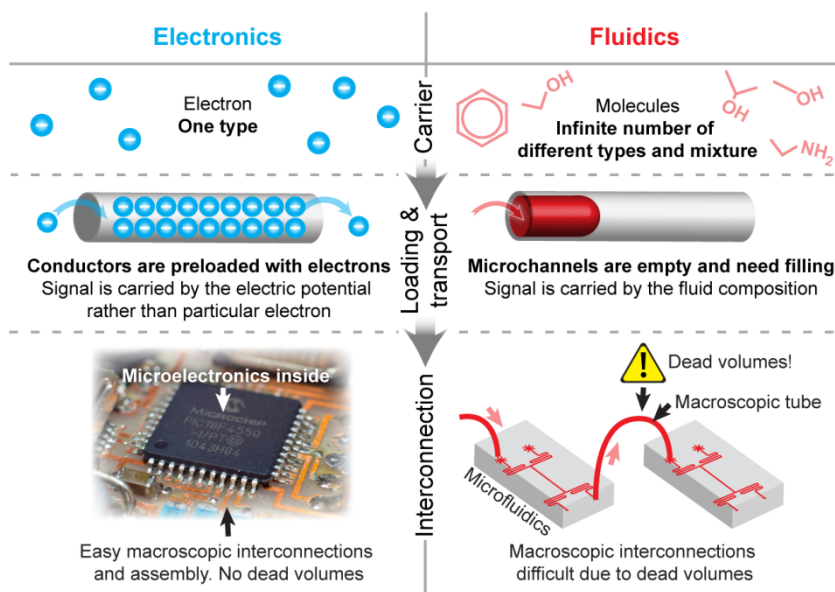


Figure 2.10. Differences between microelectronics and microfluidics

comprised circuits with significantly larger channels (several 100s of μm)[23-24].

Another important difference is that the function of electronic circuits usually does not depend on the length of the interconnections (except very high frequency electronics), while in fluidics, the interconnections are also entangled with the properties of the circuit - their length, volume and fluidic resistance has to be considered. This restricts flexibility of assembly. It is typically needed that all functions of the system are incorporated into one chip, specifically created for a desired purpose. Therefore facile and low-cost methods to prototype and fabricate chips are needed to promote the development of new devices for various applications. Closest to this ideal is PDMS microfluidics, which has gained huge popularity among developers [25]. PDMS microfluidics is more thoroughly described in the second chapter. Hopefully, currently emerging rapid prototyping techniques (e.g. 3D printing) will lead to even simpler methods to design and create microfluidic systems.



3. METHODS

Dust particles, common in our ambient atmosphere, can be significantly larger than microstructures, therefore microfabrication has to be performed in a highly clean environment - in a cleanroom. Special overalls are required for operators to protect the samples from the biggest source of contamination - us. The photo shows the author in the MC2 cleanroom at Chalmers, holding a silicon master used to manufacture PDMS multifunctional pipettes.

3.1 FABRICATION OF MICROFLUIDIC DEVICES

Most typical microfluidic devices are containing features that vary in size over 3-to-7 orders of magnitude: a cm scale chip, mm scale solution reservoirs and interface ports, and 100-10 μm scale channels. However, microfluidics can also bridge with nanofluidics, bringing the channel size down to the nanometer scale. It is hard to fabricate all of them with a single technique. Therefore, combinations of various tooling technologies are required[26]. For example, the main device in this work, the multifunctional pipette, has been fabricated using a mold which consists of two parts - a microfabricated master to define the microchannels, and a milled cavity to give the device its shape and define the solution reservoirs (Figure 3.1). The following section gives an brief overview of fabrication technologies for microfluidic devices.

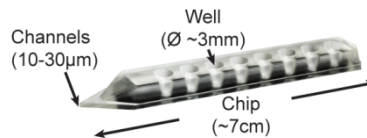


Figure 3.1. Size scales of a microfluidic device, applied on the example of the multifunctional pipette.

Key element of most current microfluidic devices is a network of small channels, where liquid handling occurs. Notable exceptions are droplets on surfaces, paper and thread microfluidics. Apart from rare techniques, which allow for generation of channels directly[27], most approaches to form close channels involve two common steps -

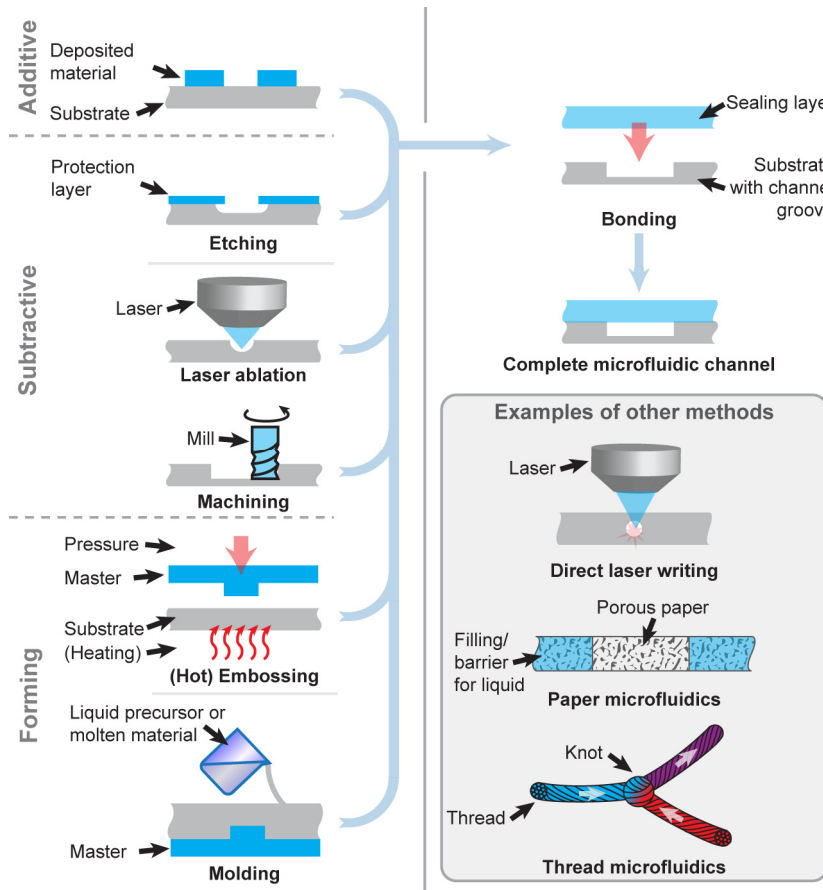


Figure 3.2. Fabrication of microfluidics devices.

fabrication of a channel groove and subsequent sealing of its opened side with another layer of material (Figure 3.2). This procedure can be repeated to build multilayered channel structures. A large variety of techniques has been developed to fabricate channels and seal them in numerous different materials.

In general, fabrication techniques can be divided into three groups: **additive**, where materials are selectively added and gaps between them form channels; **subtractive**, where materials are selectively removed, and **forming**, where materials are shaped with the help of a template ("master").

3.1.1 ADDITIVE TECHNIQUES

The most common and well established way to define microstructures is through a photolithographic process (described in details later), where a thin film of a light sensitive

polymer (photoresist) is applied on a flat surface. A pattern is created by illuminating the photoresist through a photomask, followed by selective removal (development) of either exposed or unexposed parts of the resist. In most photolithographic applications, the forming resist pattern is used as a physical mask for further processing, such as deposition or etching. In microfluidics, the resist layers can be used directly as building material to define the device. Especially popular is the negative epoxy photoresist SU-8. Multiple SU-8 layers can be fabricated on top of each other, and also bonded thermally[28]. This method allows fabrication of high precision, chemically resistant devices. Shortcomings are the expensive materials and instrumentation required. While typical lithography is limited to thin solid coatings of photoresists, stereolithography, a related technique, (patented 1984 by C.W. Hull)[29], works in a liquid bath of photopolymer. This allows the sample to be moved vertically, while the strong optical absorption of the polymer ensures that the photoreaction occurs only in a very thin layer on the surface, which is scanned by laser. By this layer by layer approach it is possible to build large 3D structures. This technology was expensive and accessible only for industrial prototyping, until recently, when affordable 3D printers have become available [30]. Stereolithography has been also used to make high precision (about $\sim 40\mu\text{m}$) objects composed of multiple materials[31]. Similarly, multiphoton lithography is a technique to build 3D structures optically, but with significantly smaller feature size ($< 1\mu\text{m}$)[32]. This very sharp point is achieved by non-linear absorption of a focused femtosecond laser. Other, inkjet like 3D printing techniques, have found applications to build hydrogels for tissue scaffolds[33] and even assemble multiple cell types, which can be used in the future for regeneration of tissues[34]. Lately, customized low-cost 3D printed reactionware has been used for chemical synthesis[35]. It is a visionary example, showing the transition of 3D printing technology from model making to low-cost prototyping and manufacturing of functional scientific instrumentation. Similar developments would be highly desirable also for microfluidics. So far, low-cost methods lack the resolution, while high resolution multiphoton lithography is expensive, slow and restricted to small structures. However, affordable 3D printing is already available to make the somewhat larger 'microfluidics', which can be applied to create interfaces to microfluidic devices[36]. It can be expected that 3D printing and related techniques will revolutionize fabrication of microfluidic devices, as it anticipated in other areas of manufacturing. In some people's opinion, the third industrial revolution will be based on 3D printing and mass customization[37].

3.1.2 SUBTRACTIVE TECHNIQUES

The most commonly used subtractive technique in microfabrication is **etching** - a chemical removal of material. In order to define features, the substrate is typically patterned, using a photoresist. Development creates openings in the resist layer, which define where the etching takes place. Depending on the chemical environment, etching procedures are divided into **wet etching** in solutions and **dry etching** using gases and plasmas[38]. The materials most commonly etched are inorganic, such as oxides, silicon and glass, the latter two being the most significant for practical microfluidic applications[39].

Glass is usually wet etched, using concentrated hydrofluoric acid (HF). With 48% HF, the isotropic etch rate at room temperature is about $8\mu\text{m}/\text{min}$ [40]. Since glass is a attractive

material for microfluidics, and there is a lack of alternative fabrication processes, HF etching is used widely. It has serious disadvantages, though, such as health risks, but also the isotropic etching profile, which can only produce shallow, wide channels with round edges. Since photoresists do not withstand HF, a sacrificial evaporated metal layer (eg. Cr/Au) must be used as etching masks. This is an additional expensive process step.

Silicon has been long a standard material for the electronics industry. Numerous processing techniques are well established for microelectronics fabrication. From the microfluidics and MEMS prospective, the most interesting technique is **deep reactive-ion etching (DRIE)**. This process was patented by Robert Bosch GmbH 1992[41]. It allows etching of very high aspect ratio structures with nearly vertical side walls. This dry plasma etching process uses two steps, nearly isotropic chemical etching with SF_6 , followed by surface passivation with an inert plasma deposited fluoropolymer, this cycle is repeated[42]. In order to introduce directionality, the substrate is biased, which causes vertical bombardment of the passivation layer by ions. This removes the polymer layer selectively from the bottom of the structure, while having less effect on the side walls. In this way etching proceeds only from the bottom. Number and length of cycles is determining overall etch speed and smoothness of the side walls. DRIE can produce deep (100s of μm), high aspect ratio (>25), uniform ($\sim 5\%$) structures at moderate speed ($\sim 6 \mu\text{m}/\text{min}$) and with good selectivity on silicon over the photoresist etch mask ($>50:1$)[42]. If higher uniformity is needed, DRIE can be performed on silicon on insulator (SOI) wafers, where the silicon layer can better uniformity ($<1\%$). In this case the etching proceeds until it reaches a buried oxide layer, which defines the final etch depth. Disadvantage of SOI wafers is their very high cost (almost 10x as high as regular Si wafers[43]), but it can be an option to fabricate precision masters used for replica molding[44]. The DRIE process has been adopted also for glass, using CHF_3 as etching gas, but suffers from poor selectivity, and requires an anodically bonded silicon wafer as an etching mask[45]. The aspect ratio is also much lower compared to silicon (wall angle of about 85°). Therefore, efforts to perform DRIE on glass are only justified in specific cases.

Laser ablation is a technique, where high power laser radiation is used to remove material[46-47]. The exact ablation mechanism depends on laser and substrate material, but in general it can be photochemical (UV lasers) or thermal (IR laser). Depending on the instrument, ablation can occur as a parallel process, where the entire structure is illuminated through a mask, or as a serial process, where the beam is scanned over the pattern to be written. Typical substrates are polymers, but also glass has been laser ablated, even though it requires more care, to avoid thermal stress and cracking[48]. Laser processing can be combined with post processing, such as wet etching. Laser ablation has been used for both fabrication of channel networks as well as for additional process steps, such as creation of interconnects in multilayered PDMS devices[49]. Low-cost commercial cutters are based on CO_2 lasers. They can produce $\sim 100 \mu\text{m}$ channels with a surface roughness of few μm in PMMA. Higher resolutions can be obtained with pulsed excimer, Nd:YAG or Ti:sapphire lasers, which can ablate in sub- μm steps [50]. Disadvantages of laser processing are channel roughness, and uncontrollable surface properties due to radiation damage and debris, which is deposited around the ablation site. Main advantage is the single-step fabrication of channel structures from design to finished chip, without a need

for photolithography. This makes laser ablation a good candidate for rapid prototyping of microfluidic devices.

Mechanical machining is mostly associated with manufacturing of macroscopic goods, but micromilling can be equally competitive for microfluidic purposes[51-52]. For example, a high performance milling machine with 1 μm movement precision and 50-400 μm diameter carbide milling bits has been used to machine a brass molding master, featuring 20 μm wide and 400 μm high channel structures (aspect ratio 20), with vertical side walls having an average roughness of <100nm. PMMA CE chips produced from this master had a similar separation performance compare to the ones fabricated with a LIGA-made master. If needed, the machined metal structures can be further smoothened, for example, with electrochemical polishing[53]. For engraving of channels, milling bits with a diameter down to 5 μm exists, even though for economical reasons their high price (>1'000kr/pcs) and wear rate should be considered[54]. Examples of milled microfluidic devices in aluminum with channel sizes ranging from 100 to 700 μm , have found use in, for example, chemical synthesis of polymers[55] and fluorescent microparticles[56]. Like with laser ablation, the advantage of milling is that the structures can be created from the design in a single process. Furthermore, one machine can produce features with greatly different heights, which is rarely possible with other techniques. Disadvantages are the low throughput, high cost of machinery, and rapid wear of tools.

3.1.3 FORMING TECHNIQUES

The world of low cost disposable microfluidic devices is ruled by the different forming techniques for polymers. All of them share a common feature: a template, also called master, or mold, is used to define the shape of a soft, or softened polymeric material, which is thereafter hardened, and released from the template. The molds themselves have to be manufactured using other techniques.

Casting (also reactive injection molding, or replica molding) is the simplest method, with minimal capital investment required to start. This is the reason why it has become popular for microfluidic chip fabrication in academic laboratories. Casting is used to create devices in thermosetting and elastomeric materials, starting with a liquid pre-polymer, which is poured onto the master or injected into mould cavity, followed by curing. Heat or UV-light cross-links the pre-polymer, turning it into hard plastics or rubber, which is then removed from the mold. A great advantage of casting is that it requires no special equipment other than the mold, which can be easily fabricated with high precision using lithographic patterning of photoresists (eg. SU-8). Since the pre-polymer mixture is of low viscosity, it usually fills the mold without problems. The relatively long setting time makes the process robust and easy to reproduce manually. However, this last aspect turns into a major disadvantage when trying to use the technique for high throughput production, since the curing time can be on the order of hours, compared to injection molding, which can complete a cycle in seconds. All devices in the present work have been made using casting or reactive injection molding of PDMS.

Injection molding is a well established industrial method to manufacture macroscopic parts in thermoplastic materials. Similar to casting, a soft polymer mass is injected into a mold

where it solidifies, adopting the shape of the mold. Instead of by a chemical reaction, the liquid/solid state of thermoplastics is controlled by heating and cooling it around its glass transition temperature (T_g). Since the required temperature change is relatively small, injection molding can have very short production cycles, limited only by thermal diffusion. Due to the viscosity of molten polymers, high injection pressures (~ 1000 bars) are required[57]. Many other aspects have to be considered when adopting injection molding for a new design, such as the temperatures of plastic and mold, injection rate and pressure, cooling times and holding pressures [58-59]. The design has to also consider the release of the final solid part. Thermal and flow "memory" of high molecular weight polymers can cause uneven shrinkage, stress and bending. In order to cope with this multi-dimensional optimization problem, specific softwares exist to model the injection molding process. Compared to "classical" injection molding on the macro scale, microinjection molding has its own additional requirements, like the use of an evacuated mold, cycling of the mold temperature (the VarioTherm process), used to avoid cooling of the polymer before it has managed to fill the small features. On one hand, very high costs for capital equipment, the fabrication of the mold cavity, and the required process optimization have rendered injection molding essentially inaccessible to academic researchers. On the other hand, low maintenance and material costs, high throughput and automated manufacturing, as well as a wide variety of different material, has made injection molding the method of choice for larger-scale industrial production of microfluidic devices.

Embossing (also nanoimprint) is like injection molding used to shape thermoplastic materials, but the extent of geometrical transformation of the material is less [60]. The process starts with the insertion of a plastics piece between two mold plates, where it is heated until softening (around T_g). Thereafter the plates are pressed together, shaping the softened material, which is then cooled to solidify. Microstructure imprinting can be performed in vacuum to avoid defects by trapped air. The material flow is in this case much smaller compared to injection molding, therefore it causes less stress. In general, hot embossing is significantly simpler than injection molding, but also with lower throughput and a more restricted range of usable geometries. Since high stress is involved due to pressing, the masters have to be stronger (typically DRIE etched silicon or electroplated metal), than the photoresist patterns used for PDMS casting. This additional difficulty makes embossing less common for prototyping. Nevertheless, hot-embossing is an excellent choice for relatively easy reproduction of fine (sub μm) and high aspect ratios structures in thermoplastics.

In conclusion, which choice to make from the above mentioned techniques, depends on geometrical and material requirements. It is also an economic decision determined by the scale of production. Casting is suited for small series (up to 100s of pieces), followed by embossing and injection molding for large scale (in the $>10'000$ pcs range)[50]. From the material perspective, casting is limited to curable polymers, while embossing and injection molding can be used with wider variety of thermoplastics. From the aspect of geometry, casting and injection molding have high flexibility to replicate 3D structures at different size scales in single process step, being only limited by release-related restrictions. Embossing is suited only for 2D layouts.

3.1.4 CHANNEL SEALING

All of above-mentioned methods can only produce channel grooves. In order to form closed channels, they have to be sealed. Some techniques are reviewed below.

A **Conformal** seal is formed when two flat and smooth surfaces are pressed against each other[61]. This method is very simple, but the resulting devices have generally lower pressure resistance and mechanical integrity. Advantages are the reversibility, which allows the device to be reused, or the ability to chemically or biologically pattern a surface with material from the channels[62-63]. Also, since no pre-bonding treatment is needed, it is easier to integrate microfluidics with a surface which is already covered with a (potentially sensitive) pattern.

Gluing is another well known way to bind surfaces together. In microfluidics, gluing requires precautions to avoid that the channels are contaminated, or even filled, by the glue. An efficient way to transfer liquid glue is stamping from a thin spin-coated layer. For example, a combination of a UV-curable adhesive and PDMS has been used for sealing[64].

Plasma bonding is a technique to achieve chemical bonding between surfaces after activation with plasma, an ionized gas, which due to its high energy state is extremely reactive. Plasma bonding is a "clean" technique, without the risk of clogging. However, for bond formation to occur between two solid surfaces, smoothness is required to allow molecular level contact. Typically, plasma bonding is used with soft materials. The most widely applied example is oxygen plasma bonding of PDMS to PDMS and PDMS to glass[25], which has also been also used to fabricate all devices in the current work. However, plasma treatment is sometimes not sufficient, and the activated surfaces have to be treated further to form a molecular monolayer with suitable bonding chemistry. For example, 3-aminopropyl triethoxy silane (APTES) can be used to assist the bonding of PDMS and PMMA[65] or PDMS and various metals, PP, PE and even Teflon[66]. Tetraethyl orthosilicate (TEOS) has been used for plasma bonding of PMMA-PMMA at low-temperatures[67].

Thermal bonding is used to bond thermoplastic polymers, which are heated slightly above T_g , and pressed together[50, 68]. Care must be taken to avoid deformation of the channel structures. The relatively narrow process window (combination of temperature, pressure, time) is the main disadvantage of this bonding technique, which is otherwise clean, i.e., it neither introduces additional material, such as glue, nor does it cause surface damage like the plasma bonding technique.

Solvent bonding is similar to thermal bonding, but instead of high temperature, a small amount of a suitable solvent is used to soften polymer surfaces, which are then pressed together for contact. The solvent then diffuses into the bulk material and the bonded polymer hardens again[69-70]. One of the most common examples is ethanol or DMSO/water bonding of PMMA. As with thermal bonding, attention must be paid to avoid excessive softening of the surface, which would deform the channels.

Anodic bonding is used to bond silicon and glass surfaces, which are pressed together under vacuum at elevated temperature (200-450 °C). High voltages (200-1200 V) are applied over the assembly[71], and bonding takes place in about 10-30 min. An alternative way to bond glass without adhesive involves the use of Ca^{2+} ions[72].

3.1.5 OTHER METHODS

In addition to previously described common routes to make microfluidic chips, other method exists, mostly developed for particular purposes. A few examples are mentioned here.

Exciting for rapid prototyping is the direct laser writing into mesoporous glass, using focused pulses of a femtosecond laser [27]. ~40% of the volume of this material consists of pores. Since the method is based on non-linear absorption of light, which locally destroys the material structure, changing the focus height allows to create truly three-dimensional channel networks inside the substrate. The diameter of the circular channels, which is in the range between 10-50 μm , can be controlled by the NA of the objective and the laser power. After writing, the channels are consolidated by high temperature annealing (>1000 °C). This is a rare method by which closed channels are created in a single process step, without need for sealing.

In contrast to all those methods requiring complex machines and materials, some microfluidic devices can be fabricated even at home, using materials as common as paper[73] and yarn[74-75]. Both are functioning based on capillary driven transport in a porous hydrophilic matrix, where circuits can be defined by introducing (printing) hydrophobic wax barriers, or by making knots. These devices do not have high enough precision for most modern laboratory uses, but their almost negligible cost makes them attractive for disposable diagnostics, especially for those whose resources are limited.

3.1.6 MATERIALS

Silicon has well established, but expensive, manufacturing schemes, which involve mainly photolithography and wet and dry etching (DRIE). Since Si is also a substrate for semiconductor electronics, it is attractive for hybrid electronic-fluidic devices, sensors and MEMS. The advantages of silicon are its high thermal and chemical stability; disadvantages are opaqueness and the planar device geometry, which often requires additional interfacing components.

Glass and quartz are in a many ways similar to silicon, but feature optical transparency without auto-fluorescence. Typical fabrication methods are wet etching, which is isotropic compared to the anisotropic DRIE used for silicon. Direct photo-patterning is also possible[76], using pulsed laser treatment, which changes amorphouse/crystalline structure of the material and increases the subsequent etch rate. This in combination with very stable surface chemistry has made glass prominent for electrically driven (electrokinetic) microfluidics[77-78], in particular for capillary electrophoresis (CE) chips with optical readout.

Thermoplastics are molten by heat and can be then reshaped by injection molding or hot embossing. They are favorable over other many other materials, as they are really cheap, optically transparent and easily moldable with minimal geometry restrictions. As biological lab-ware is typically made of thermoplastics, their use and chemical compatibility in biology is well established. All of them are fine in aqueous solutions, but have generally low organic solvent compatibility, different plastics being dissolved by different solvents, especially by hydrocarbons[50]. Most commonly used for microfluidics are PMMA, PC, COP and COC.

Thermoset polymers are solidified by cross-linking, which can be induced by heat or UV-radiation. Once cross-linked these materials will not melt. Therefore channels have to be molded either before curing[79], or by using photo-patterning (eg. SU-8) or can be etched later using photolithography (eg. polyimide/Kapton®)[80]. An advantages of thermoset polymers is their high chemical stability (eg. SU-8, Kapton).

Elastomers, as is evident from the name, are elastic and easily deformable materials. Since elastomers are composed of polymer chains above T_g , they can reflow, but cross-linking limits their overall fluidity. In general, elastomers are favorable, since they are easy to interface, due to their "build in gaskets". They also provide an easy route to fabricate miniature pneumatic valves, invented by Unger & Quake 2001[81]. The most famous elastomer for microfluidics is PDMS, to which a separate chapter is devoted. Another interesting type of related materials are thermoplastic elastomers (TPEs)[82], which are block-co-polymers (eg. styrene and butadiene), where one is amorphous and above T_g , and another crystalline acting as a physical cross-linker. Once heated above the melting temperature of crystalline polymer, the entire material melts and acts as thermoplastic, allowing it be processed as such. After melting, TPEs can have significantly lower viscosity than typical thermoplastics, making their forming easier[82].

Table 3.1. Examples of material costs (Polymer chips are assumed to be 5 mm thick)

Material	Approximate cost	Cost of cm ²
Si	200 SEK/4" wafer[83]	2.5 SEK
PDMS	500 SEK/kg	0.25 SEK
Polypropylen	130 SEK/kg[36]	0.06 SEK
Versaflex TPE	36 SEK/kg[82]	0.02 SEK

3.1.7 PHOTOLITHOGRAPHY

Photolithography is the main patterning technique in the top-down microelectronics industry. This important application has driven research in optics and photo-chemicals. Its main results, integrated circuits with more and more transistors (most notably reflected in Moore's law) have been defined by a photolithographic technique). The procedure of photolithography is depicted in figure 3.3. First, a substrate is covered with photoresist. This is typically performed by spin-coating, where photoresist is dispensed onto the substrate, and then thinned by spinning. The final thickness depends on viscosity, spin speed & time, and the rate of evaporation. Alternatives to spin-coating are spray-coating and lamination. After this coating step, the substrate is heated and the solvent evaporated, forming a flat polymer layer, which can be patterned optically, either through a photomask (a parallel process) or by direct writing with a laser scanner[63] (a serial process). Laser scanning is most suitable for rapid prototyping, and masks are superior when multiple substrates need to be processed. For mask-based photolithography there are also several options, depending on quality and feature size required: quartz and deep UV exposure for finest (~ 500 nm feature size), soda lime for intermediate (>1 μm) and polyester films for larger structures (features: >10 μm). The latter is often sufficient for microfluidics, where the channels are several tens of micrometers in size. For comparison, the cost per area of quartz and soda lime masks is about 30, and 20 times higher, respectively, than the polyester film mask[84]. After exposure, the photoresists are developed, meaning that the polymer is selectively removed either from the exposed areas (positive resist) or unexposed areas (negative resist). In the following, the negative SU-8 and positive AZ4562 photoresists, which were used in this work, are more thoroughly discussed.

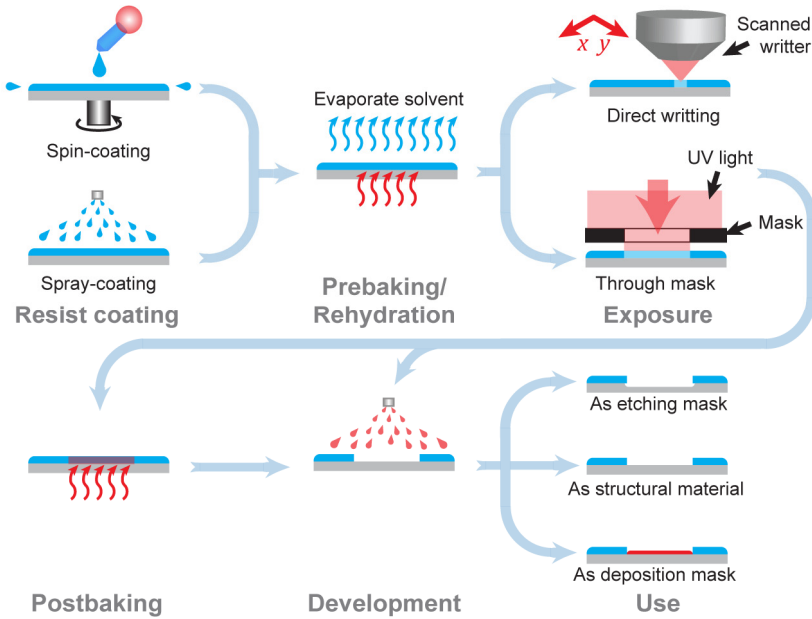


Figure 3.3. Typical photolithographic process

Chemistry of photoresists

SU-8 is a negative, chemically amplified photoresist, originally invented by IBM in the 1980's[85], which is now developed and produced mostly by MicroChem Inc. The key components of the resist are epoxy resin, a photo catalyst and solvent (Figure 3.4). During exposure, the photocatalysts fragments, forming a Lewis acid, which during the post baking step catalyzes epoxy group opening and cross-linking reactions, which eventually renders the exposed part of polymer insoluble in developer (an organic solvent). In fact, hard baked SU-8 becomes completely insoluble in all organic solvents, and can be only slowly removed by oxidation in a plasma or piranha solution. Therefore, SU-8 is primarily a permanent resist, which due to its mechanical strength, optical transparency and excellent adhesion has become widely used as photo-patternable construction material for MEMS and microfluidic devices, as well as for the fabrication of masters for soft-lithography. All microfluidic device in this work have been made with SU-8 masters. Different resist film thicknesses can be achieved with different formulations of SU-8 in combination with spin speed variations. Film thicknesses in the range of 0.5 to >200 μm are thus obtained in a single-coating cycle[86]. Optimized formulations also exist for improved adhesion (SU-8 3000 series) and highest aspect ratios (SU-8 2000 series).

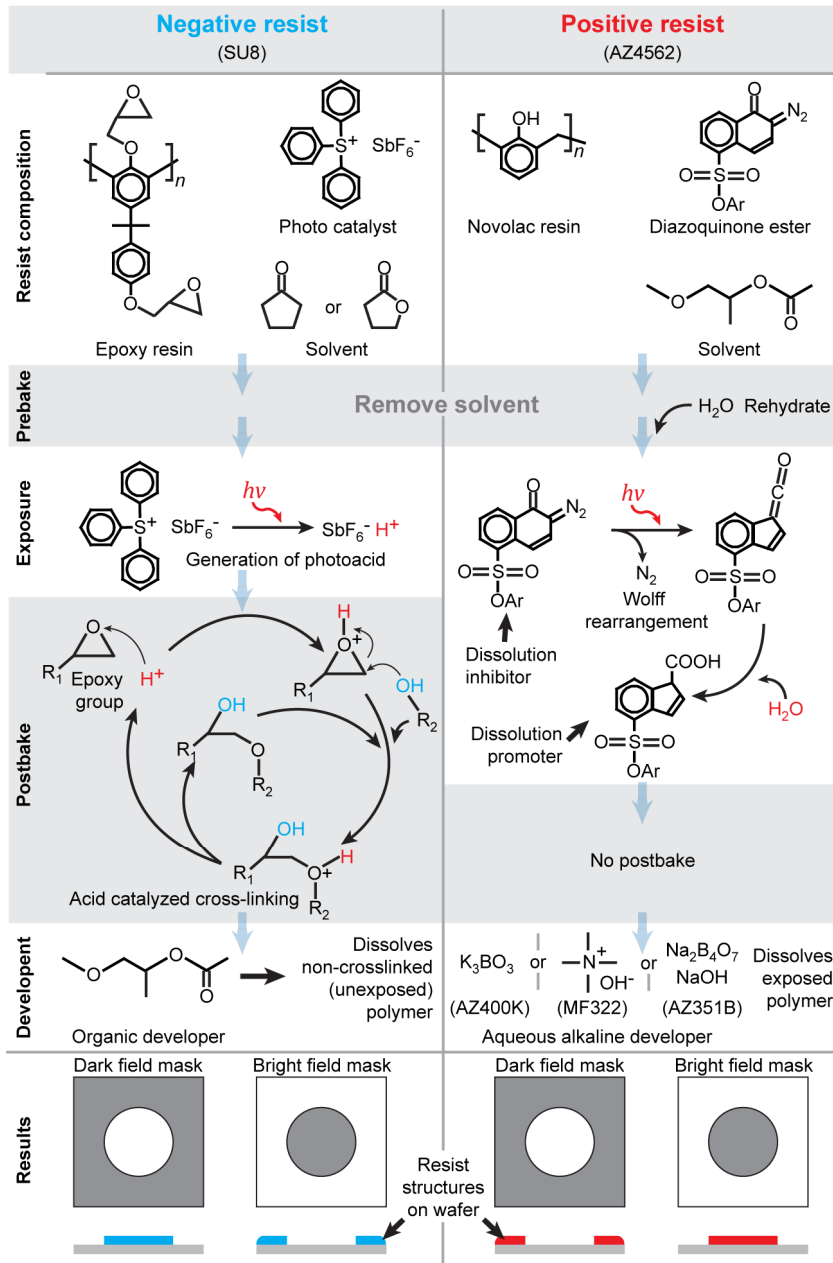


Figure 3.4. Chemistry of photolithography. Examples of negative (SU-8) and positive (AZ4562) photoresists used in the presented research work.

AZ4562 is a positive resist by AZ Electronic Materials GmbH. It is based on a phenolic novolak resin and diazoquinone (DQN resists), where the latter is forming a complex with phenolic OH groups. This hydrophobic complex renders photoresist insoluble in the aqueous developer. Exposure to UV cleaves the diazo group, and in a rearrangement reaction the compound is transformed into a carboxylic acid, which dissociates from the resin and allows it be removed with alkaline aqueous developer. It must be noted that UV-induced re-arrangement reactions require water to complete. Therefore rehydration, which allows water to diffuse back into the resist after pre-baking is a critical processes step. It happens on negligible time scales in case of thin resists (few μm), but requires up to several hours for thick coatings (tens of μm). DQN resists are suitable for near UV, but not suitable for deep UV exposure, due to strong absorption, which would not allow uniform exposure. This resist is favorable, due to the aqueous development, which pose less health hazards compared to organic solvents (e.g. SU-8 developer). However, it is mechanically much weaker than cross-linked SU-8 and could not be used as constructional material. In microfluidics, positive resists are used for rounded surface elements. since they are not cross-linked. The rectangular structures melt above glass transition temperature, and the liquid resist curves due to surface tension. Rounded channels are the key components in pneumatically actuated microvalves[81], also used in this work (Paper I).

3.1.8 PDMS MICROFLUIDICS

Polydimethylsiloxane (PDMS) is a polymer with silicon based backbone (-Si-O-) decorated with organic side groups (-CH₃). It has a wide range of uses as a surfactant and anti-foaming agent in food processing, cosmetics and herbicides[87], as structural material for medical devices, as sealant and as lubricant.

The use of PDMS in chemical microsystems emerged in the mid 1990s, when Xia & Whitesides introduced the concept of 'Soft-Lithography' as a micro/nano patterning method based on a molded PDMS stamp[88-89]. Just a few years later, the same replica molded PDMS stamps started a revolution in microfluidics, when Duffy & Whitesides described the plasma bonding of PDMS-PDMS and PDMS-glass[25]. By this, the full fabrication process of microfluidic devices was established, using relatively cheap and simple means (Figure 3.5). After a master is made photolithographically (typically a single layer of SU-8 on a Si-wafer, which is also the most basic lithography step possible), the remaining process is easily accomplishable in every chemistry lab. PDMS is mixed from two components, degassed to remove air bubbles and casted onto the master simply by pouring. After curing in an oven, a rubbery PDMS slab can be peeled off the master. Since the material is soft, fluidic interfaces can be easily punched out with hollow punch tools made from syringe needles. Finally the slab, and another piece of PDMS or glass, are treated with an oxygen plasma (a low-cost plasma cleaner is sufficient) and bonded, by simply placing them together. This procedure was quickly adopted by many labs, and PDMS became the dominant polymer material in the field of microfluidics research, with several hundreds of publications produced each year[50, 69].

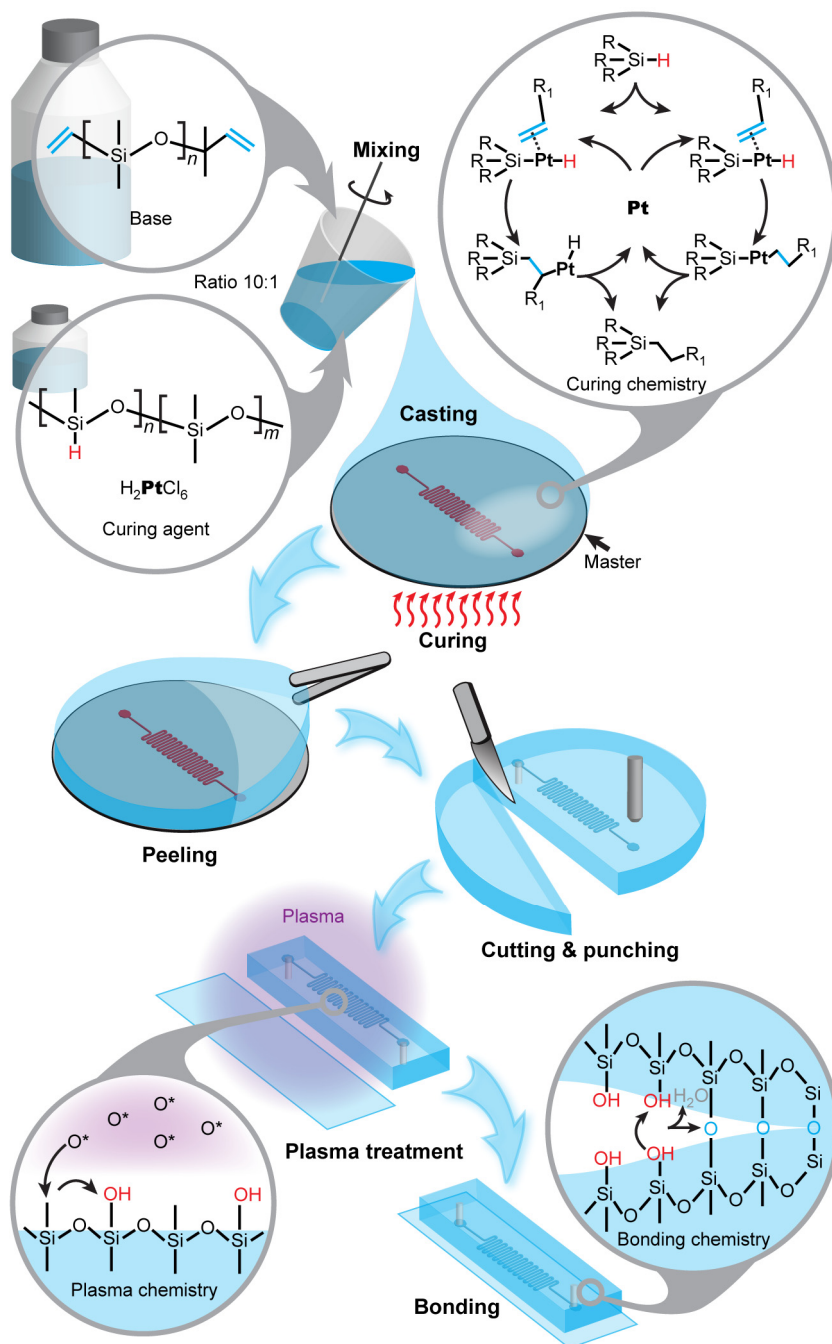


Figure 3.5. Fabrication of PDMS microfluidic devices, with chemistry of curing[90-91] and bonding.

In addition to facile fabrication, several other favorable properties of PDMS have contributed to this success. Most important is the optical transparency with low auto-fluorescence, which allows these devices to be used in microscopy - one of the easiest means of detection and visualization. PDMS also has good biocompatibility, as it is non-toxic and gas permeable. Not less important is the elasticity, which contributes to fabrication but also to reliable interfacing, since a tight seal is formed when supply and control tubing is pressed into the punched out conduits. PDMS elasticity is also the foundation of the simple, but powerful valve concept invented by Unger & Quake[81]. Lately, mechanics and microfluidics have been combined to create soft-actuators and robotics[92].

Disadvantages of PDMS are low solvent compatibility[93], in some applications also deformability, as it introduces compliance (Paper III) and non-linear resistance. In some applications, another limiting factor is the unstable surface chemistry after oxygen bonding, which gradually returns from the hydrophilic ($\sim 5^\circ$) to the hydrophobic state(109°)[94-95]. From the manufacturing point of view, 30min-1h curing time is much longer than the injection molding cycle, which can be completed within seconds. Regardless of these few shortcomings, PDMS with its well-established prototyping schemes, is most likely to remain for years to come a important material in this field. All microfluidic devices described in this thesis were fabricated from PDMS, using soft-lithography.

3.2 MICROSCOPY

As the well known idiom says, “*Seeing is believing*”. For working with small structures and objects, microscopy is an essential tool. It makes microscopic features visible, which cannot not be resolved by the human eye. The work presented in this thesis has been tightly intertwined with the use of microscopes, starting from the simplest inspection of microstructures to the most sensitive quantitative measurements of single cell chemistry. One can go even further and state that all microfluidic instruments and devices presented in this thesis can be considered to be tools or accessories for biological microscopy.

The history of optical microscopy dates back to 16th century, where Dutch spectacle-makers Hans and Zacharias Janssen assembled the first compound microscope[96]. The next, and even more important, milestones were set by Robert Hook and Antonie van Leeuwenhoek, who used simple microscopes to describe for the first time the small-scale world, and introduced this technique to the biological society[97]. This was followed by a long list of inventions, including Köhler’s homogeneous illumination mode in 1893, Zernike’s phase contrast[98] and Nomarski’s differential interference contrast[99] methods, which allowed imaging of transparent samples, such as cells. However, for molecular and cell biology the biggest breakthrough came with the development of fluorescence microscopy, which with its multitude of variations allows high resolution imaging of sub-cellular components. nowadays it can have the sensitivity to visualize single molecules, and makes quantitative characterization of chemical composition, reaction rates, diffusion and more possible. Fluorescence microscopy techniques have been used extensively in this work to characterize the fluidic circuits and the kinetics of cellular chemistry.

Fluorescence microscopy techniques are used for visualizing fluorescent molecules, which are characterized by absorption and subsequent re-emission of light, where the emitted photon has a longer wavelength (lower energy) than the absorbed. The energy difference is dissipated as heat. This phenomenon is best explained with the help of the Jablonski diagram[100] (Figure 3.6 B). While fluorescence phenomena were already observed in the 16th century, and the name “fluorescence” was coined in the mid 19th century by G. G. Stokes[101], the same Stokes who developed hydrodynamics, its use in biological microscopy emerged not before the beginning of the 20th century (Carl Zeiss’ UV microscope in 1904 and Oskar Heimstädt’s first successful fluorescence microscope in 1911)[96]. A rapid development phase followed, and by the 1930th various producers and commercial ultraviolet microscopes were already on the market. Another important contribution to fluorescence microscopy was brought about by the emergence of synthetic dyes in the mid 19th century[102]. In 1871, Adolf von Bayer created a first fluorescent dye, fluorescein, soon followed by many others[96] (e.g. rhodamine B by Ceresole in 1887). For the biologist, the true power of fluorescent dyes arose from the possibility to couple them to biomolecules, and most notably to antibodies (Albert Coons, 1941)[103], which allows them to be used for highly selective staining of molecular

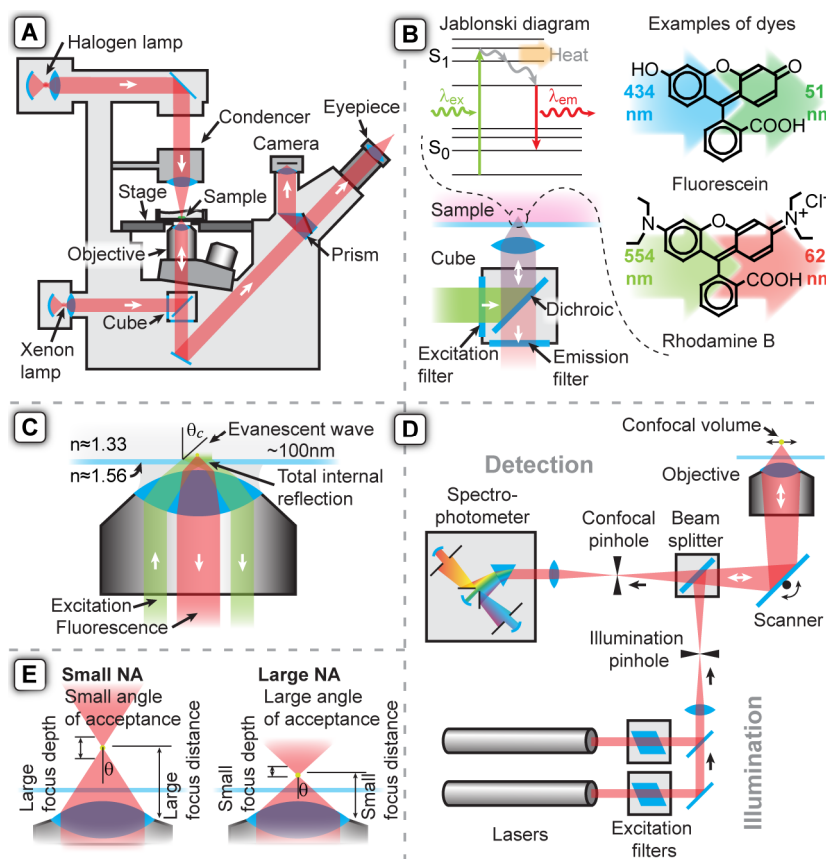


Figure 3.6. Essentials of optical microscopy. **(A)** Schematics of a common inverted epifluorescence microscope. **(B)** Principles of fluorescence microscopy and examples of fluorophores (dyes)[104-105] **(C)** Principles of total internal reflection fluorescence (TIRF) microscopy. **(D)** Schematics of a scanning confocal microscope. **(E)** Choosing the objective – the meaning of numerical aperture (NA).

components of cells. A large contribution to the nowadays widespread use of fluorescent microscopes came from the invention of dichromatic mirrors (Johan Sebastiaan Ploem, 1967). By now, fluorescence microscopy has developed into many branches, making use of specific molecular and spectroscopic phenomena. Examples are: fluorescence correlation spectroscopy (FCS)[106] & recovery after photobleaching (FRAP)[107], allowing to study reactions and molecular transport; Förster resonance energy transfer (FRET)[108], which can elucidate structures of molecular assemblies, dyes whose fluorescence is altered by binding to other chemical species and can be used to study cell physiology, two-photon excitation[109] etc.

The principle of fluorescence microscope (Figure 3.6 A-B) is to illuminate the sample with light at the excitation wavelength of a fluorophore or dye, while collecting at the emission

wavelength. The key component of the microscope is a filtering system called **beam splitter**, which in most microscopes contains three parts: the **dichroic** mirror and two band pass filters for excitation and emission. the function of the dichroic mirror is to be reflective to a certain wavelength range, and transmissive to another. This allows separating excitation light, which is focused through the objective onto the sample, from emission light, which emanates from the excited sample. Since different dyes have different excitation and emission spectra, filters and dichroics have to be exchanged to match this. Therefore, for the convenience of use, filters and mirror are usually combined into small assemblies commonly called a “**cube**”.

Total internal reflection fluorescence (TIRF) microscopy is a modification of common fluorescence microscopy in order to image in very thin layers on a surface (Figure 3.6 C). This technique, invented by Daniel Axelrod in 1981[110], is based on total internal reflection of light occurring at the interface of two media with different optical densities (n). When a beam, coming from a higher refractive index material and hitting the surface at an angle which is larger than a critical angle θ_c (Eq 3.1), all light is reflected back. However, this reflection occurs in a finite layer near the surface, where the electromagnetic field reaches somewhat into the medium of lower refractive index. This **evanescent wave** is confined in a thin layer, about 100nm in thickness. It decays exponentially with distance from the surface[111]. Using the evanescent wave for exciting molecules allows to confine the illumination to the nm scale layer. This eliminates background fluorescence, which would otherwise complicate sensitive measurements. TIRF enabled imaging of single molecules.

$$\theta_c = \arcsin \frac{n_{low}}{n_{high}} \quad (3.1)$$

The refractive index of glass is about 1.56, that if water is 1.33, giving a critical angle of 58°. In this work, we have used TIRF to characterize solution exchange near surfaces, in order to mimic the flow around adherent cells, while eliminating light from higher layers. This was necessary, since faster solution exchange higher above the surface could give incorrectly shorter values for the exchange times (Paper III).

Confocal laser scanning microscopy (CLSM) is another technique based on fluorescence microscopy with high vertical (depth) resolution (Figure 3.6 D). The principle of confocal microscopy was patented by Marvin Minsky in 1957[112]. Compared to wide-field fluorescent microscopes, which illuminate and accept light from various focal planes of the sample, confocal microscopes exploit small pinholes, which are defining a sharp focus point, while illumination intensity and acceptance of light from outside the focal plane drop rapidly. While the simplest configuration of the confocal microscope allows collection of light from just a single point (point confocal), all modern confocal microscopes contain a scanning mechanism. The scanning action is typically based on deflected mirrors or a perforated spinning disk (Nipkow disk), which sweeps the focus point in the xy plane. The light intensities collected from each point are then reconstructed into an image. If the focus point is also scanned vertically (z-axis), three dimensional images can be created. Nowadays, commercial confocal microscopes integrate additional advanced optical instrumentation. Tunable excitation filters allow to adjust the power of the different excitation lights. The

dichroic mirrors can be replaced by an acousto-optic beam splitter (AOBS), which similarly use the interference principle to separate wavelengths to be reflected or transmitted. Instead of fixed thin film coatings, a layered structure is effectively formed when high frequency sound waves are compressing and expanding a piece of glass, changing locally its refractive index (interaction of phonons and photons). The great advantage of the AOBS is that all filtering properties can be instantaneously and electronically changed by synthesizing an appropriate signal for the piezoelectric transducer, which excites the glass. Similarly flexible is the processing of the emission light, where tunable spectrometers can isolate multiple wavelength ranges, which can be simultaneously collected with highly sensitive sensors, typically photomultiplier tubes (PMT) or avalanche photodiodes (APD). This flexibility has made confocal microscopes indispensable for biologists. A multitude of fluorophores can be monitored simultaneously, helping to elucidate intracellular structures and phenomena.

Fluorophores (dyes) are molecules with fluorescent properties. However, modern fluorophores have more advanced duties than simple shining. They can be conjugated to molecules such as antibodies and lipids, which are binding to particular biomolecules and cell parts, allowing them to be visualized. Another important type of fluorescent dyes are those which change their fluorescent properties after a particular modification, or environmental change. For example, temperature dependant fluorescence (eg. Rhodamine B[113], molecular beacons[114]) can be utilized for temperature measurements. The fluorescence of some dyes, such as Calcium GreenTM[115], Fluo-3, or Fluo-4 [116], increases upon binding to Ca^{2+} , which is one of the most important regulators of cellular processes. Therefore, these dyes allow physiological monitoring of calcium levels in cells. YO-PRO-1TM, another example, displays similar fluorescence changes when binding to DNA[117]. Other dyes need modifications in their molecular structure to become fluorescent. For example, fluorescein diphosphate (FDP) becomes fluorescent when its phosphate groups are removed by alkaline phosphatases. Therefore it can be used to monitor enzyme activity in cells[118]. The portfolio of methods used in cell biology has been redefined by fluorescent proteins, first green (GFP)[119], and now also many other colors. GFP genes can be inserted in particular places of the genome, and the resulting fusion can reveal the expression of otherwise invisible proteins. Another important aspect is the chemical stability of the fluorophore. Many classical fluorescent dyes, in particular fluorescein, are prone to degradation (photobleaching) due to the excitation light. A large selection of advanced dyes, featuring superior photostability, high fluorescence quantum yield, and a wide range of excitation wavelengths, is available today. Further developments concern the engineering of interactions of dyes with biological matter, such as specific transport across the boundary of cells or organelles, and deposition in selected locations. This allow for accumulating them inside cells (e.g. acetoxymethyl ester conjugates [Paper III]) or their use for probing ion-channel function (eg. YO-PRO-1 passing through TRPV1 channels [Paper II]). Thus, fluorophores provide biological microscopy with a great advantage - processes inside living cells can be followed under physiological conditions in real-time with very high spatial and temporal resolution. However, caution has to be taken, as electronically excited dyes in cells are reactive molecules. They may also pose unwanted side-effects on cellular processes. Establishing a fluorescent probing scheme for a new experiment can be a serious challenge.

Limits of microscopy. Resolution of optical imaging techniques has fundamental limits caused by the diffraction of light. This diffraction limit was studied by Ernst Karl Abbe 1873, who found that light cannot be focused to an infinitely sharp spot, but to a minimum spot size d , as defined by eq. 3.2 (known as **Abbe diffraction limit**).

$$d = \frac{\lambda}{2NA} \quad (3.2)$$

where λ is wavelength of the light and $NA = n \sin(\theta)$ is the numerical aperture, describing the capacity of the optical system to collect light. n is the refractive index of the working medium and θ is the maximum acceptance angle as shown on figure 3.6 E. The larger the maximum angle of acceptance, the higher is the NA , and the better the resolution. However, a high NA has also other advantages, like the collection of a larger fraction of photons of fluorescence, which are emitted equally in all directions (Table 3.2). Difficulties with high NA objectives are a shallower depth of focus and shorter focus (working) distance. High NA objectives require an immersion liquid (water or oil), otherwise the light coming in a high angle could never leave the sample, due to the total internal reflection in the cover slip. Therefore the NA of the optical system cannot be larger than the smallest refractive index present in the medium separating sample and objective. Air objectives therefore have a $NA < 1$. Last, but not least, manufacturing lenses which can focus light equally at a larger range of angles requires higher precision and quality, resulting in a high price tag on high NA objectives. (For example, 40x microscope objectives with 0.65 and 1.3 NA would cost about 7'000 and 50'000 kr respectively.[120])

Table 3.2. Illustration of light harvesting efficiencies of objectives with different NA s, working with an aqueous sample ($n = 1.33$). For isotropic fluorescence, the fraction of light collected by the cone of acceptance would be $(1 - \cos(\theta))/2$.

NA	$\theta(^{\circ})$	% of light collected
0.3	13	1.3
0.7	32	7.6
1.3	78	35

3.3 SIMULATIONS

As discussed before, many physical processes are described by partial differential equation (PDE) systems, like the Navier-Stokes (Eq. 2.18) or convection-diffusion (Eq. 2.27) equations, which are describing fluid flow and transport of chemicals. Unfortunately, solving these equation is often challenging, even in case of extremely simple geometries, and is completely impossible in almost all real-life settings, where multiple physical phenomena, different materials and objects with complex shapes are combined. This problem has been greatly alleviated by the emergence of simulation methods, which together with the rapidly developing high power personal computers, have become commonplace in all branches of engineering.

To make computer representations of PDEs describing spatially and temporally continuous physical fields (eg. pressure, temperature, concentration etc.), these fields have to be discretized by slicing space and time into finite numbers of elements, which is represented by the name **finite element method (FEM)**. In contrast, a continuum, can be thought of as made from an infinite number of elements. All values themselves can only be represented with limited precision. (e.g. the 64-bit double precision floating point data type can hold values from about $\pm 10^{-300}$ to $\pm 10^{+300}$, with a precision of 15 decimal points. It sounds like an enormous range and precision, but when small and big numbers are added and subtracted from each other, the rounding errors can lead easily to numerical chaos). After dividing the complex object into small, simple shapes, which can be described by algebraic equations, these elements are joined into a network, called **mesh**, with connected nodes. Some values in some nodes will be defined by boundary conditions, others will be unknown. In a similar way, as described in section 2.2.2 for pressures and flows in microfluidic channel networks, all relations between the mesh nodes can be encompassed into large algebraic equation systems. Solving the equation systems with the help of matrix algebra gives the unknown values in each mesh node (simulation results).

Modern finite element software packages have become convenient tools with easy graphical user interfaces, allowing engineers and scientists from various disciplines to perform simulations, while requiring neither any programming skill nor understanding of the complex mathematics behind the solver algorithms. Nevertheless, it is essential that the user knows the system and physics behind it, otherwise resulting graphs may look beautiful, but have little touch with reality.

The typical workflow of finite element modeling is depicted in figure 3.7, using a microfluidic mixer as an example. The first essential step is to split the system into parts and eliminate unimportant details and those parts which can be calculated analytically. This matters greatly, since the total number of elements in the model is finite and limited by the available working memory. A well chosen simulation region allocates computation resource to the regions in the geometry where they are needed. For example, the flow rates in the supply channels of the microfluidic mixer can be calculated using analytical expressions (Table 2.1), therefore the interesting region is only around the point, where the two flows meet. Thereafter the geometry of the selected part of the device is drawn, followed by assigning the physics (eg. Stoke's equation and convection-diffusion equation), materials

properties and the relations between all these phenomena. In the example, the convection-diffusion depends on the flow velocities calculated from Stoke's equation, but it can also have the opposite relation if the fluid viscosity depends on the substrate concentration. Determining these relations properly is an essential part of model building. Failing to do it, can waste computation power or result in errors. Proper boundary conditions must be selected and finally, the geometry should be meshed into a network of finite elements. Even though the mesh is a purely computational construct, creating it requires physical consideration. As the mesh discretely samples the continuum space, its density has to correspond to the variations, such that the regions with rapid change have the highest, while the more homogenous parts can have a lower density. Mesh density has to be finer than size of the features it tries to reveal. This is analogous to the Nyquists-Shannon theorem for signal sampling. Once an actual simulation succeeds, the results have to be verified - are they physical and realistic? For example, are inflow and outflow of liquids equal, is total amount of substance conserved, or how do simulations correspond to experiences from experiments? If profiles, which are expected to be smooth, oscillate, the reason is most likely a numerical instability - the consequence of poor meshing. In general, a good mesh has been achieved when further increase of its density does not change the results significantly (convergence).

The use of simulations can serve two purposes - to understanding nuances and mechanisms in experiments, which are hard to measure directly, or to evaluate performances of device designs before fabricating them, which can save significant time and resources. In the presented work, the FEM modeling package COMSOL (Founded 1986 by students of the Royal Institute of Technology in Stockholm) has been used extensively for both purposes[63].

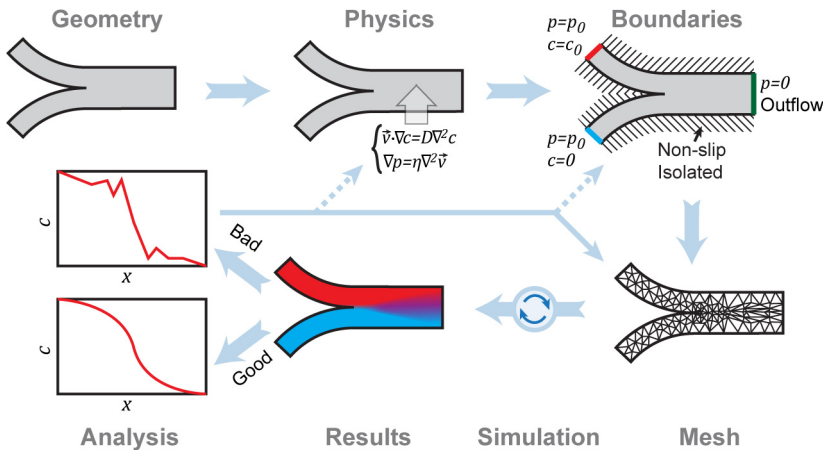
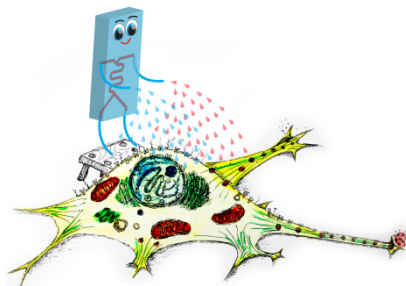


Figure 3.7. A typical process of finite element modeling.



4. TECHNOLOGY

For a living organism to function, constant exchange of information is required on the cellular level, where the messengers are different chemicals. In order to study the machinery of the cell, it is important to be able to control and adjust its surrounding. The central theme of this work is the development of advanced tools to handle chemical environments at the size scales of the cell with the help of microfluidic technology.

4.1 MICROFLUIDIC DILUTION

The preparation of mixtures and dilutions is a common experimental procedure in most areas of chemistry and molecular biology. Since a significant amount of research involves optimization of concentrations and mixing of reagents by trial and error, automation is very desirable. The use of a microfluidic format for mixing gives additional benefits, such as low reagent consumption and low device cost, as compared to liquid handling robots. In the following chapter a number of microfluidic mixing concepts are presented and compared.

In principle, dilutions in microfluidics require the same steps as in a macro-scale lab, metering reagents and mixing them. If the dilution factor is required to be large, it is usually not practical to dilute in a single step, but rather in several steps, starting from a concentrated stock solution (Figure 4.1).

Metering is most crucial step, as it determines the accuracy of the final concentration. In microfluidics, various principles exist to determine the ratios of supplied fluids. Metering can be based on a ratio of input flows, or it can be defined by known volumes of reservoirs. Figure 4.1 depicts four of these concepts. In the first example, the mixing ratio in a continuous flow device is set by the ratio of external pumping rates (e.g. syringe pumps), by the ratio of pressures on liquid reservoirs, or by hard-wired differences in fluidic resistance of the channels. These diluters can be sequentially combined into networks in order to generate spatial gradients, whose shapes are controlled by the inflows[121]. Such gradients were, for example, used to dynamically regulate the nutrient levels of yeast and elucidate its metabolic regulation mechanisms [122]. The second type is also based on the ratio of flow rates, but here the flows are generated by on-chip peristaltic pumps, which are controlled by a pneumatic pulse sequence, whose frequency is proportional to the flow[123].

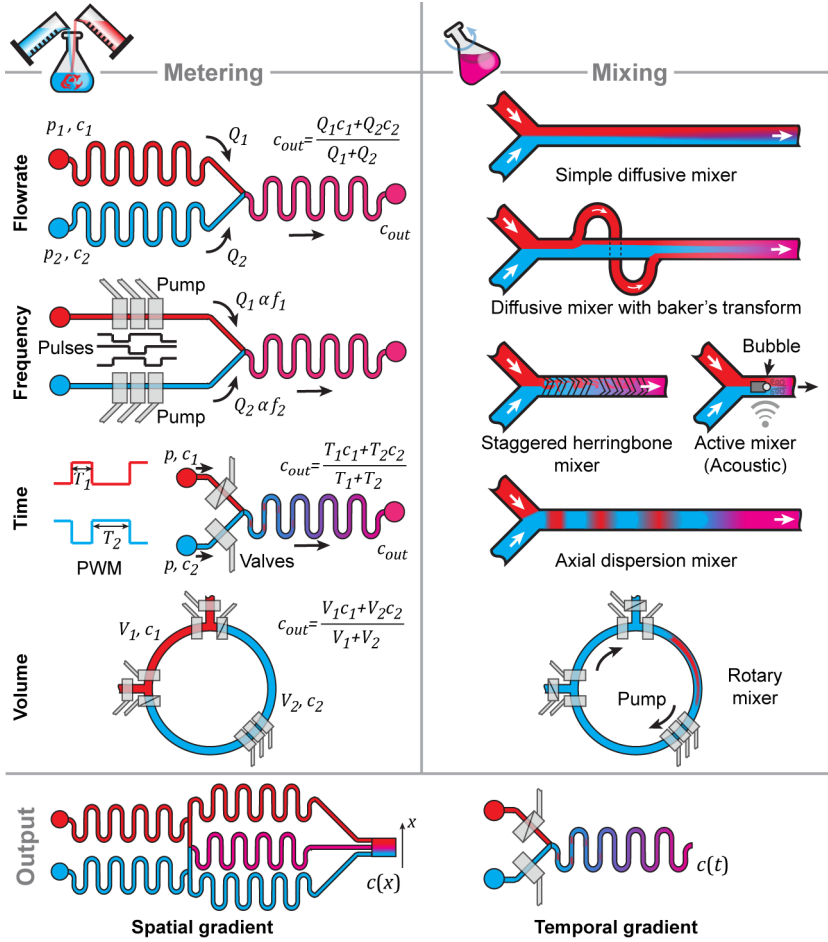


Figure 4.1. Generation of dilutions in microfluidics.

Peristaltic metering can be also used for volumetric injections. In this case the number of cycles is more important than the frequency [124]. In the third method the concentration is equally controlled by flow rate, but in a time averaging way, where the contribution are determined by the length of flow pulses emerging from supply channels. Concentration control with variable pulse lengths is the fluidic counterpart to pulse width flow modulation (PWM), commonly used in electronics to convert digital codes into analog signals[18] (Paper I). In the fourth example, the metering is based on the volume of defined channel segment[125-126].

An important analytical merit is, of course, precision, where many factors can contribute to practical results. If we put aside possible clogging by dirt particles etc. (gross error), then there are two major contributions, the precision of the chip and the precision of the control signal. In microfabricated devices, the channel length is normally much larger than the

width, and all fabrication techniques allow it to be produced with negligible variance. Much harder is to control the uniformity of the channel cross-section, in particular height. Neither spin-coating nor etching produce exactly uniform structures. Thick (30 μ m) SU8 has about $\sim 10\%$ or more height variation, [127], glass etching[128] and DRIE[42] about $\sim 5\%$, and SOI wafers[43] $\sim 1\%$. Size variation can have different effects on precision (Table 4.1). For example, the hydrodynamic resistance depends on the 4-th power of the cross-sectional size (Table 2.1), while the volume only on the 2-nd, which means that pressure driven metering (flow rate based and PWM) is twice as sensitive on geometry variations compared to the channel volume-based ones (peristaltic pumping and reservoirs). Higher precisions in the control signals are typically easier to achieve. Typical electronic pressure regulators have an accuracy of $\sim 1\%$ [129]). Peristaltic and PWM metering relies on timing precision, which is easily achieved with electronic control, but since they involve also pneumatic actuation by solenoid valves, which requires a switching time of a few to 10 ms, the maximum frequency becomes limited.

Mixing is the next step in making dilutions. Mixing speed and efficiency determine time response and stability of the diluter. It is desirable to have a precisely determined output concentration with no spatial or temporal variations. The simplest mixer is the T-junction, where two flows meet and co-flow until molecular diffusion eradicates the concentration differences. Since there are no turbulences, this processes is slow. It can be boosted by increasing the contact area, where liquid sheets are pressed wider and thinner. However the contact area can be increased even more efficiently by using the so called baker's transform (due to the dough making analogy), where a fluid stream is split and rejoined such that opposite sides will be connected. The problem with the baker's transform circuits is that they requires either crossing channels (multilayered design) or 3D channel geometries[27, 130]. Both are complicated to achieve with most of the common fabrication methods. While in intermediate Re number flows mixing eddies can be generated by various pumps and sharp edges, passive stirring at low Re is more challenging [131]. An elegant solution is a staggered herringbone mixer (invented by Stroock & Whitesides, 2002), where small diagonal grooves at the bottom of the channel guide the liquid and give its flow field a non-zero component in the y-z plane (Eq. 2.24). This leads to general rotation, which can efficiently mix substrates in about 1cm of the channel length[132]. Some other micro-stirring concepts introduce radial velocities by electric fields or sonication. An interesting example is an acoustic micromixer using a trapped bubble, which can achieve complete mixing in a few milliseconds[133]. Pulsed flows, like the one produced by PWM flow metering, are favorable, since flow segmentation together with Taylor dispersion helps to improve mixing efficiency (Paper I). A similar process happens also in rotary mixers, where one pulse is circularly pumped in the channel, where it spreads due to the Taylor dispersion[124-125].

The choice of the mixing concept depends on the required features. Should there be a continuous outflow, or should the mixtures be made in portions? What are the required response time, precision and dynamic range? Can it be made in one stage, or need multiple diluters be connected in series? Shall the output be a spatial or temporal gradient? Compromises are generally needed and a higher dynamic range and precision requires longer preparation (response) time (Table 4.1).

Table 4.1. Comparison and key features of dilution concepts in microfluidics.

	Flow rate	Peristaltic	PWM	Volume (reservoirs)
Continuous outflow	Yes	Yes	Yes	No
Geometry dependence	$\propto r^4$	$\propto r^2$	$\propto r^4$	$\propto r^2$
Continuously adjustable output	Yes, Pressures	Yes, Frequency	Yes, Pulse length	No, Discrete steps
Output	Proportional	Proportional	Proportional	Exponential Nr of dilutions
Increasing dynamic range	Multiple stages	Multiple stages	Multiple stages	-

4.2 LOCALIZED DELIVERY OF CHEMICALS

4.2.1 HYDRODYNAMIC FLOW CONFINEMENT

In a stereotypic view, microfluidic devices are confined laboratories on chips, into which materials and samples are introduced, and all the magic of the experiment occurs inside channels surrounded by walls. Instead, this work describes another, younger and less explored paradigm in microfluidics: useful properties of micro-scale fluid-flows are projected beyond the boundaries of the device, and into an open volume. This allows for easy integration with existing instrumentation and experimental environments, and lowers the acceptance barrier for the new technology.

One of the useful properties of microflows is their stability, which has allowed to develop devices to address biological cells with high spatial[11] and temporal[134] resolution. To use this feature, the cells have to be brought or even grown inside the devices, which can be unfavorable. For example, adherent cells or cells extracted from tissues lose their spatial organization when suspended. Free-floating cells in suspensions may also increase the risks of clogging of smaller channels. The alternative approach of culturing cells inside the device can be challenging, too, due to different rates of oxygen and nutrient transport, requiring additional optimization. Most of these concerns can be alleviated by separating cells and fluidics. Biologists can prepare their cell cultures and tissue slices in conventional Petri dishes, using well established protocols, and the fluidic functions can be brought in when and where needed. The simplest device of this kind is a glass capillary injecting a liquid. Though widely used, its capacity to define the exposed area is very limited due to diffusion. As described before (Ch 2.1.2), microfluidics offers means to combat diffusion by convective flow and therefore allows to maintain inhomogeneous concentration distributions steadily. This principle is not limited to closed channels. If fluid leaves into the open volume, it can be still captured and circulated back into the device by sufficient neighboring inflow. Such circulation forms a small reservoir, whose boundaries are defined by hydrodynamic flow-lines and the content by the outflow. In the following we call this circulation a **hydrodynamically confined flow (HCF)**.

The general, the concept of using simultaneous out- and inflows (circulation) in liquid delivery is not new, it has in several incarnations found use in different devices (Figure 4.2). One of the earliest is the **push-pull cannulae** (developed by J. H. Gaddum, 1961)[135], used to sample neurotransmitters in brain. This early device suffered from the risk of damage of the tissue by the liquid, got frequently clogged and became contaminated by cells and blood. An improvement, the dialytrode (by Delgado et al, 1972)[136], was introduced, separating the liquid flow from the cells by a semi-permeable polysulfone membrane. The chemitrode, a similar probe, was reported around the same time [137]. The practical construction and efficiency of this sampling device was improved by U. Ungerstedt (Karolinska Institute) in 1974, using a hollow membrane tube[138]. This method, known as **microdialysis**, has become widely used to sample neurochemicals in both research[139] and clinical settings[140]. Although related, microdialysis is not using hydrodynamic confinement, since the flow is separated by the membrane, and coupling happens only by diffusion.

In 1996, semi-open volume confinement of liquid has been patented by Mitsumori et al. for a wet cleaning nozzle, invented for processing of large substrates of the kind used for solar cells and LCD displays [141]. Confinement occurs on a dry surface, where a precise flow balance allows to avoid leaks from the close gap between substrate and flow chamber, such that it required no seal or mechanical connection. This device is a gigantic, several orders of magnitude larger relative of the HCF systems discussed in this thesis. In a same year, another microscopic flow confinement system emerged, used as a **fast local superfusion** technique for the stimulation of adherent neurons[142]. Here, two glass capillaries (\varnothing about 10 μm) are positioned in close vicinity ($\sim 20 \mu\text{m}$) around the cell, one used for injection, other for aspiration. This setup formed a HCF about 30 μm in size, and pressure switching allowed solution exchange on the ms time scales. This tool has been an essential component, in studies of the motility of dendritic filopodia[143] and potentiation of synapses[144]. However, it suffered from many practical shortcomings. It was hard to control the exact geometries of the capillaries, which effected the flow-rates. It was also tedious to position them repeatedly, since already slight variations in distance can cause a significant change in the flow field and exposure profile. The aspect of positioning has been simplified by combining two needles into one coaxial superfusion pipette (**Picoliter fountain-pen**)[145], where a smaller injection pipette is placed through the orifice of another, larger one, for aspiration. Even though it reduced the positioning difficulties of two separate pipettes, it introduced much more complex assembly and interfacing requirements. Somewhat simpler to handle is the dual pipette pulled from the theta-tube[146]. An important limitation of both of these dual-capillary systems is that they do not allow fast exchange of perfusion solution. As with all glass pipettes, they also are extremely fragile, making their handling cumbersome. In any case, dual-pipettes have made an important contribution to research, where they have been used, for example, to stimulate artificial neural networks[147] and measure signal propagation in them[148], as well as for stimulation of cardiac myocytes[149] and collection of mRNA[146].

Most of the problems associated with glass pipettes can be overcome by using microtechnology, which allows repeated fabrication of channels with well defined geometries and positions, as well as to design circuits that allow fast solution exchange, dilution and other liquid processing functions.

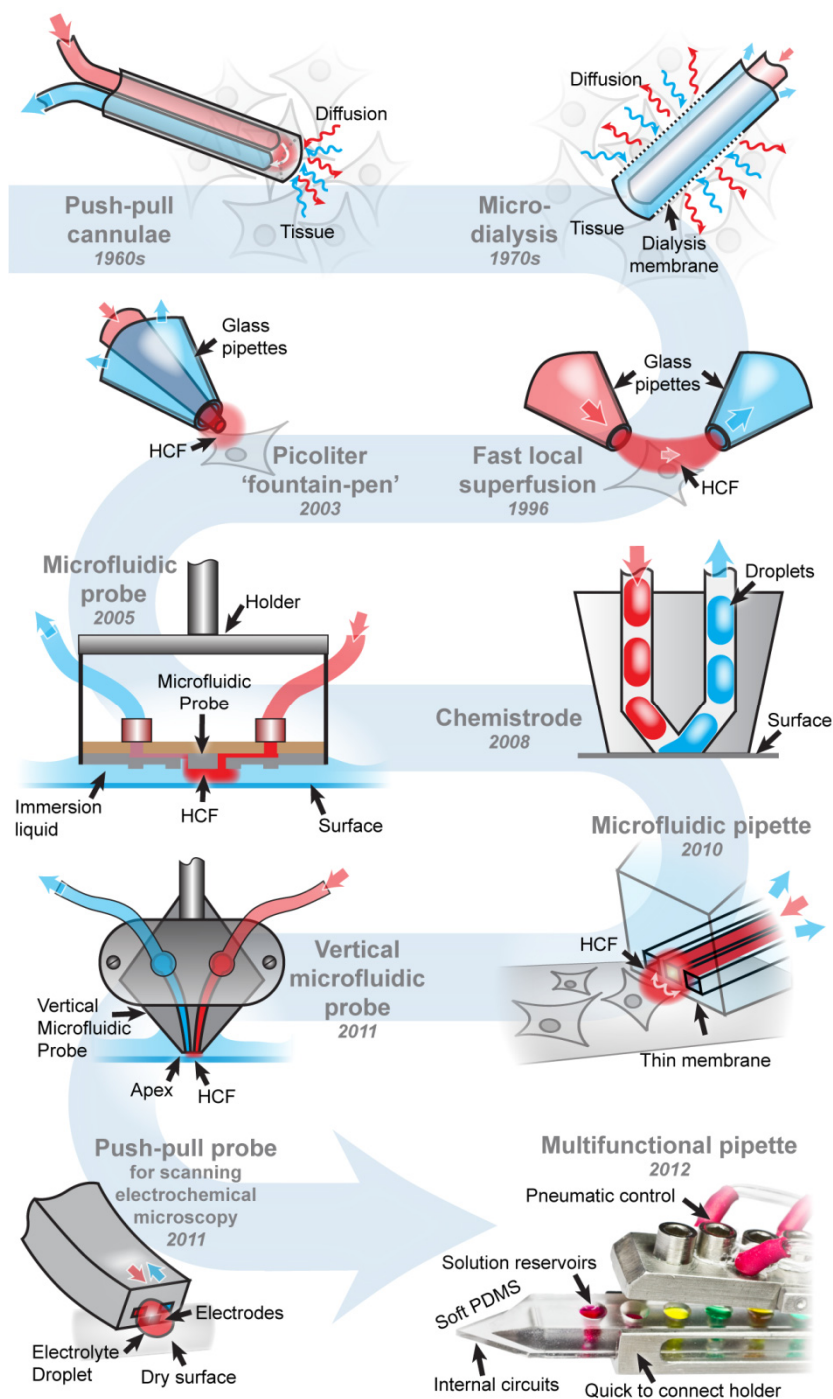


Figure 4.2. History and examples of hydrodynamically confined flow devices and related concepts.

First microfabricated HCF device was the **Microfluidic probe** (by D. Juncker & E. Delamarche in 2005) which has been inspired by inkjet and spotting technologies, but was crafted to provide superior spot-quality for surface processing in liquid environments[150-151]. This device resembles a print head, brought into close vicinity of the surface such that the channels point towards it. The first practical difficulty associated with this design was the alignment of the large head, which has to be parallel to the surface in order to avoid contact and damage, and to be close enough to deliver solutions. Another shortcoming was the rather complicated fabrication, which consisted of three lithography steps, HF etching, two DRIE processes, dicing and bonding. These aspects were somewhat improved in a later vertical design by the same inventor[152-153]. The microfluidic probe was used to pick up cells, pattern antibodies[150], and stain adherent cells and tissues[150, 153-154]. From a biologists perspective, many practical limits remained, such as the apex, which covers the processed area and restrain the use of upright microscopes and limits access by other probes such as glass pipettes, microelectrodes or optical fibers, used in various biological experiments. These restrictions are particularly severe for neuroscientists, who would like to combine solution exchange with electrophysiological recordings.

We, initially unaware of the microfluidic probe, were driven to build our **Pipette** by the need of biologists and biophysicists to exchange the solution environment around cells (superfusion), to stimulate them or to create gradients in order to drive membrane migration. Knowing that glass pipettes are widely used for these purposes, we saw our device as a modern variant of the classical pipette with extended functionality and more convenient use - and named it multifunctional pipette. In contrast to the microfluidic probe, it is applied under an angle, just like glass needles in typical biological experiments. The combination with other probes, e.g., electrophysiological recording pipettes, and upright microscopes, remains unrestricted. Our device worked well in conjunction with micromanipulators, and needed no specific station to position and align it[155]. Furthermore, as biological experiments can require series of multiple reagents to be applied to a cell, our device had the functionality to switch solutions and create dilution series through a single HCF. In order to perform switching, no physical movement of probe or sample is required, another advantage for the biologist, since motion could hinder the use of other probes or even disturb sensitive imaging or recording.

Table 4.2. Comparison and key features of microfluidic probes and multifunctional pipette.

Features	Microfluidic probes	Multifunctional pipette
Alignment	Apex parallel to surface	Variable application angle
Angle sensitivity	Sensitive around 2 axes Large (mm scale) apex would collide with surface	Insensitive Application angle flexible Low sensitivity to rotation around tip axis due to sharp tip
Vertical height sensitivity	Identical	
Confinement boundary	Sharper	Smoother
Shear stress on the sample	Higher	Lower
Microscope compatibility		
- Inverted	Yes	Yes
- Upright	No	Yes
- Transmission	No	Yes
Compatibility with additional probes	No	Yes
Solution exchange	No	Yes (4 solutions ~ 50 - 100ms)
1D gradients	Yes	Yes
2D gradients	Yes	No
Chemical compatibility	High	Limited to aqueous solutions
Supply	External through tubing (cleaning needed)	Integrated wells (cleaning not needed)
Flow driving	Syringe pumps	Air pressure from computer controlled pneumatics
Materials	hard Si/glass (mostly)	Soft (PDMS)
Fabrication	Complex Multistep photolithography	Simple One step soft-lithography. Most limiting step is individual tip punching
Fabrication infrastructure requirements	High	Low
Device usage	Most likely multiple use	Most likely disposable use
Optimal for	Chemical surface processing	Single-cell manipulations

Other, similar and related devices exist. For example, the **Chemisthode** (not to be confused with the aforementioned Chemitrode, which is a different concept) by Chen & Ismagilov[156], is used for both stimulating and collecting responses from local areas on a surface, using droplet microfluidics. This probe is not a HCF device, since conformal contact with the surface is required during operation. Very similar is also a PDMS spotter used for fabrication of protein chips[157], but instead of droplet flow, continuous flow was used there. Some other device are applied to deliver, maintain and refresh microscale droplets on dry surfaces. One example is a microfluidic probe, which used a hydrophobic/-philic apex region to define the flow chamber[158]. A similar approach had been shown before, also for liquid guidance inside channels[159]. A different open volume push-pull probe was reported for the delivery of fresh electrolyte in scanning electrochemical microscopy[160-161].

It is interesting to note that chemical circulation is actually used in nature for the same purpose: to stimulate cells. Nature's probe is called **synapse** (more precisely chemical synapse), where one nerve cell stimulates the other by the release of neurotransmitters. In order to avoid contamination and to control the stimulation, neurotransmitters can be pumped back by transporter proteins[162]. Differently from the above described liquid handling devices, this circulation is not hydrodynamic but molecular, and occurs on significantly smaller size scales.

4.2.2 SOLUTION EXCHANGE - NEED FOR SPEED

As mentioned in the preface to this chapter (Ch. 4), all communication between cells is mediated by exchange of chemical species - ions, small and large molecules. In order to study this communication, we need tools, both for detecting and for stimulating. The processes themselves can occur on various timescales. Pathways involving regulation of gene expression have slow response times (minutes to hours)[122, 163]. Neural communication, on the other hand, is fast - for example seeing or feeling something is separated from the perception in the brain by mere milliseconds, even though it requires multiple steps of cell-to-cell information exchange. Even higher, microsecond scale time resolution, is needed for signals arriving from either ear to enable us to locate the origin of the sound (stereo effect)[163]. This is owed to the fast ion-channels in the membranes of nerve cells, which receive and carry signals. **Ligand-gated ion-channels** in the synapse of a receiving cell are sensing the release of neurotransmitters from another cell. Some of these receptors can have gating constants of only a few tens to hundreds of microseconds (eg. Acetylcholine and AMPA receptors)[164-165]. Fortunately, as ion channels are conducting charged ions, electrical current through them can be relatively easily measured by the patch-clamp technique and high sensitivity amplifiers[166]. Using small membrane patches extracted from cells and immobilized at the tip of a glass pipette allows measurements of current, even through individual ion-channels (single-channel recording). In order to study kinetic and different steps of the gating process of these channels, it is also important to apply a stimulus, the chemical ligand, with time resolution higher than the opening and closing of the channel. This is not trivial and has been the subject of many studies. The

performance of solution exchange is highly dependent on the instrumentation and the nature of the sample. The shortest solution-exchange times can be achieved by switching flows on the tip of a glass pipette (~ 10 - 20 ms)[167], by steering the streams from a theta-tube ($200\text{ }\mu\text{s}$)[168], or by using piezo driven scanning of fluid streams ($<100\text{ }\mu\text{m}$)[165]. More complicated is the situation around cells, which can vary in size, and be either suspended on a pipette or adherent to a surface. For suspended cells, microfluidic open volume superfusion can produce exchange times of about ~ 30 ms[169]. With glass capillaries and special flow chambers, exchange time of ~ 10 ms were reported for small cells[170] and 200 - 400 ms for large *Xenopus oocytes*.

Solution exchange times have often been characterized by liquid junction potential measurements in the tip of glass pipettes, which represent well the settings of single-cell recordings, but not those of actual cells. V. Pidoplichko [171] characterized the relationship between sample size and solution-exchange times as nearly linear: ~ 0.8 ms per μm of cell diameter. Theoretical models suggest that $20\text{ }\mu\text{s}$ exchange times are possible for small patches[172].

Fast timescales can not only be found in gating of ion-channels, but also in other cellular processes. Some, such as electron-transfer processes or passage of ions through ion-channels[162] are much faster than the technically possible solution exchange times. More relevant are the timescales found in enzymatic reactions[173] and in conformational changes of large protein complexes, where characteristic time constants can easily be on the order of tens of milliseconds to several seconds[174].

4.2.2 OTHER METHODS TO DELIVER CHEMICALS

While hydrodynamic flow confinement is a relatively universal method to control the chemical environment at size scales in the area of 10 - $100\text{ }\mu\text{m}$, other techniques exist, which can beat a HCF device in speed and size, but are more limited for specific applications.

Photolysis can be used to generate active molecules by optically releasing them from biologically inactive caged pre-cursors. As the method is extremely fast and localized ($<1\text{ }\mu\text{m}/<1\text{ }\mu\text{s}$)[175], it has gained popularity to stimulate neuronal networks, where the use of lasers and acousto-optic scanning allows to define spatial exposure patterns. This method has also its limitation, in particular the need for caged substances. Currently there are caged forms of acetylcholine, glutamate, calcium, GABA, glycine, and IP_3 available[176]. Control of the exact concentration, the inability to remove released substances by other means than diffusion, and the complex experimental setup are other difficulties.

Iontophoresis is analogous to pressure drive injection through capillaries, only that electrical current is used instead. A problem that this technique shares with other electrokinetic mechanisms is that this transport mode is more substance-specific than the pressure driven counterpart [177]. **Organic ion pumps**[178] are somewhat similar to iontophoresis. Here, ion-conducting polymer materials are used to eject ions by means of current. A related technique is **nanopipette** based delivery[179], where electrical pulses are

used to eject single-fluorescent molecules from a $\sim 100\text{nm}$ pipette tip in a scanning ion-conductance microscopy (SICM) setup.

Nanoliter patterns[180] based on two phase aqueous polymer solutions have been used to reduce diffusion and maintain the chemical composition in artificial cellular microenvironments. An advantage of this technique is that a large number of chemical environments can be created and maintained without continuous active intervention. It is, however, limited to experiment where a steady environments is sufficient, since the polymer hull around the cell does not support fast changes in composition.

Dip-Pen nanolithography (DPN)[181] is a surface patterning technique for features on size scale of 1-100 nm, using an AFM tip. It cannot be used for maintaining a compositionally defined liquid environment around cells. An enhancement of DPN is the **nanofountain probe**[182-183] featuring a molecular-ink feeding mechanism. **FluidFM**[184], is another variant of AFM, where the injection aperture is milled into the tip by using a focused ion beam. It can work as a regular AFM, but also penetrate the cell membrane and inject femtoliter amounts of liquids.

4.3 FUNCTIONAL BIOMEMBRANES

Biomebranes are forming the reaction vessels for the chemical machinery of life. Universally from small bacteria to human cells, they are confining all necessary components and nutrients. Material and information transport can occur controllably and selectively through exo- and endocytosis, transmembrane proteins or sometimes just by diffusion. This vital role of membrane proteins in orchestrating cellular processes, has made them also essential drug targets. Up to 70% percent of new drugs address membrane proteins[185]. In a different aspect, biomembranes represent an intriguing physical structure: a molecularly thin two-dimensional fluid, where molecular motion is restricted in normal direction of the membrane, while they can easily diffuse laterally.

The role of biomembranes in the context of this thesis is significant, as all example applications of the developed devices directly addressed biomembranes, either by activating ion-channels, inducing membrane vesiculation, or by creating or manipulating artificially assembled model membrane structures on solid supports.

purpose

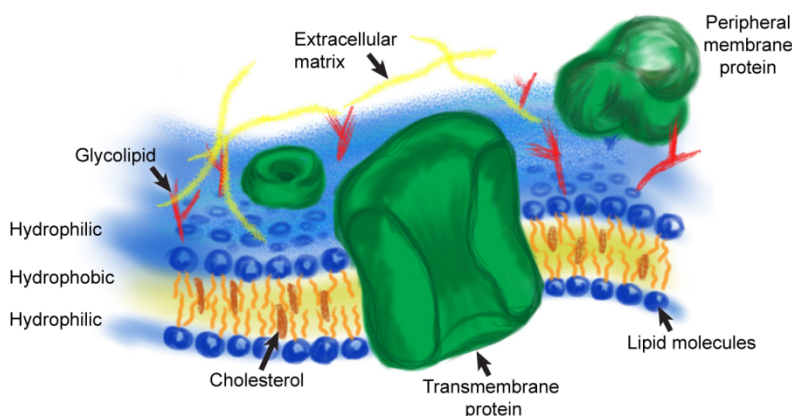


Figure 4.3. A cell membrane and its components

4.3.1 STRUCTURE OF THE BIOMEMBRANE

The biomembrane is a thin elastic sheet, self-assembled from various amphiphilic lipid molecules. Lipids have a hydrophobic tail, which is most commonly composed of two fatty acid chains, a hydrophilic head which often consists of a phosphate moiety (phospholipid), and a small organic headgroup, such as choline. Both parts of the molecule are linked together by a glycerol unit. When brought into water, the lipids spontaneously line up their hydrophobic tails and assemble into thin sheets, screening their nonpolar ends from the polar environment. The most efficient screening is obtained in an arrangement, where two molecularly thin sheets of lipid film orient their hydrophobic sides towards each other,

effectively forming a bilayer. The film remains fluidic, as the molecules are not covalently interconnected, but held together by weak interactions. Molecules other than lipids can populate the bilayer, either by dissolving into the hydrophobic inner part of the membrane (cholesterol and other sterols), by chemically conjugating to the lipid head group (sugars and small proteins, forming glycolipids and lipoproteins), or by embedding themselves into the membrane, often spanning it entirely. The last category is most important, since membrane-spanning proteins fulfill numerous transport, sensing, regulatory and other functions in the membrane. With this diverse composition, the membrane is no longer a passive layer of mixed molecules, separating the inside from the outside of a cell, but rather a highly functional active boundary, which controls and regulates the concentration of molecules on either side, establishes identity, and manages the connection to neighboring cells.

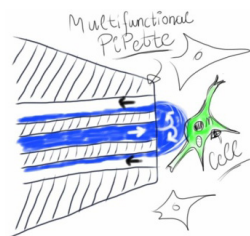
4.3.2 PROPERTIES OF THE BIOMEMBRANES

Major features of the biomembrane are elasticity and fluidity. The elasticity provides the cell with the ability to adapt its shape to environmental cues, such as changes in temperature, osmotic pressure or other sources of stress. Fluidity, on the other hand, serves various transport and interaction needs. Self-healing after rupture, distribution of different lipids to other regions of the membrane, and the ability to fuse and mix molecules are some of the beneficial consequences of membrane fluidity. Another major aspect is the need for insertion of lipids and proteins after their biosynthesis, which is also ensured by the high lateral mobility of the membrane. Finally, molecules can meet in the fluid lipid matrix, interact and generate chemical signals. Other biomembrane properties are high electrical resistance and limited ion permeability, while gases, lipid-soluble molecules and small amounts of water can pass the boundary almost unrestricted. Some of the beneficial properties, in particular the ability to host ion channels and other membrane proteins, have led to the desire to construct biomimetic membrane models. In this context it is desired to maintain the fluidic features of the membrane, while managing to stabilize and immobilize the nanometer-thin assemblies. A practical solution to this problem is the solid-supported lipid membrane.

4.3.3 SUPPORTED LIPID MEMBRANE TECHNOLOGIES

In order to facilitate scientific studies and technological use of biomembranes, a planar, fixed geometry is favorable[186]. Many probing techniques, microscopy and patterning techniques such as photolithography are constructed for planar substrates. Compatibility with these technologies has helped to investigate and exploit membrane features to a great extent. Supported lipid membranes can serve as biomimetic surface coating[187]. Moreover, selective transport can be investigated, for example in ion-channel based biosensors[188]. In some examples, fluidity is at the heart of use, by exploiting two-dimensional transport, either by diffusion, spreading[189], electric field[190], thermophoresis [Gözen et al, unpublished], hydrodynamic shearing[191] or surface

acoustic waves[192]. Others use biomembranes as a natural medium for handling membrane proteins, such as their accumulation[193] and separation[191]. In some cases, supported membrane are used as bulk coating, while in other instances micropatterns are needed. The lipid membrane can be patterned with the assistance of surface structures [189, 194], or lithographically, using soft-lithographic stamping[195], or even by microfluidic flow chambers[196].



SUMMARY

This work describes the development of microfluidic technology for spatial and temporal manipulation of chemical microenvironments at the size scale of a single cell.

In **Paper I** a microfluidic dilution system is presented. Dilution is based on pulse width flow modulation (PWFM), where fluid streams are multiplexed using pneumatically actuated microvalves made in PDMS. By balancing the accuracy of the shortest pulse lengths and response time, we found that up to 10-fold dilution per dilution stage and about 5s response time is feasible. In order to achieve a wider range of dilutions, multiple stages can be combined in series (two in this paper and three in a follow up-study). Since PDMS channels deform under pressure, which causes non-linear resistance and compliance effects, the circuits were made to maintain, ideally, the same pressure and flow in every switching state. The main features and advantages of this diluter are the low-cost PDMS fabrication, fast response time, time-dependent output through a single channel, continuously variable concentration settings, minimal number of control channels (serial control signal), and a simple control system, where no pressure regulation is needed, only digital valves. Some drawbacks are the required calibration and the limited dynamic range. In the paper the diluter was characterized using fluorescence and electrochemical measurements, and finally applied to control the spreading of supported lipid-double bilayers. In a follow up study, which is not included in this thesis, a three stage diluter was fabricated, and a fully automated calibration and deployment system was developed [Genner, Ainla and Jesorka]. This diluter was eventually modified to allow liquid exchange in front of its outlet. This gave rise to concept of the microfluidic pipette.

Paper II introduces the microfluidic pipette. Compared to the diluter shown in paper I, which also features an open volume outlet, the channel exits are here concentrated in the sharp tip of the device. This allows to position them next to objects of interest on a surface, i.e., a free standing device. Another aspect is the simultaneously applied inflow, which allows the outflowing liquid to be confined into a small volume - a hydrodynamically confined flow (HCF). In this paper the properties of the HCF were studied and device was combined with a simple one-stage PWFM diluter, which used a valveless switching principle based on hydrodynamic flow steering. The microfluidic pipette was used in

several single-cell applications, to induce membrane zeiosis (blebbing), stimulate ion-channels in electrophysiology experiments and to perform dose-response measurements.

Paper III describes the redefining of the initial pipette into a real multifunctional research tool. Major practical inconveniences associated with its use were removed. Most importantly, shape and interfacing were improved, adjusting the device to the environment of biological microscopy, which is, typically, crowded by the objective, condenser lens, dish edge and other needles and probes. Therefore, a narrow and elongated design with a sharp tip has been chosen. Another important aspect was efficient interfacing, which is required to facilitate quick set-up, to prevent leaks and contamination and to reduce cleaning needs. This has been achieved by using integrated wells, which preserve solutions and have no dead volumes to fill. Since the simple, low-cost pipette tip can be considered to be disposable, there is also no need for cleaning and no risk of contamination. The first presented function of this new pipette was fast switching between three solution environments, which yielded about 200 ms exchange time. The switching process and the contributing factors were analyzed theoretically, and by means of computational models. This theoretical insight has been used later (Xu et al. unpublished manuscript and Paper VI & VII) to further improve the circuitry, now being capable of switching between four solutions in 50-100 ms. Further improvements and novel functions are easy to introduce, due to the modularity of the design. New circuits are integrated at the cost and effort of fabricating a channel structure on a silicon wafer - the molding tools as well as the holders are reused without modifications. The efforts were rewarded by the editors of *Lab on a Chip*, who elected our technology into the top 10% technologies!

Paper IV extends the capabilities of the multifunctional pipette by integrating electrodes into the PDMS device. It is difficult to use conventional metal patterning techniques on PDMS, owed to the poor adhesion between the materials. Therefore, our approach was to fill the channels with the low-melting Field's metal. This method is favorable, as high conductivity electrodes can be post processed by means of a simple hot-plate and a pump. The modified pipettes were used to combine localized solution delivery and electroporation of single adherent cells. A shortcoming of this approach is the brittleness of Field's metal structures. The otherwise robust tip became fragile and sensitive to bending. More flexible future alternatives could involve conductive polymer composites, but they exhibit lower conductivity and require larger channels, as the materials are more viscous and coarse.

Paper V explores the applications of the pipette on rat brain slices. As discussed already in previous chapter, neuroscience is in great need for fast superfusion, while the high spatial organization of the brain requires confined stimulation. Microfluidics is generally well suited for these tasks, but harder to apply in tissues. Specific chambers to hold tissue in the device are required[197]. The pipette provides an easier alternative, allowing

electrophysiological experiments to be performed in their conventional environments (e.g. oxygenation). A distinct benefit of the pipette is faster solution exchange time compared to the conventionally used whole-slice perfusion. Localized stimulation can not only allow new types of experiments to be performed, it also aids in the economic use of resources, as more data sets per slice can be collected, increasing efficiency and saving the lives of animals.

In **Paper VI**, the advantages of solution exchange and confinement are harnessed in a fluorescence based optofluidic thermometer, where the HCF allows contamination-free delivery of dyes, used for direct temperature measurement in the physiological temperature range. Switching between two fluorophores of different temperature dependent fluorescence is used to create a reference system capable of eliminating microscope and alignment specific variability. This measurement technique was used together with a fiber optic microheater, to observe heat activation of temperature sensitive ion-channel (*hTRPV1*), monitored as an uptake of YO-PRO-1 to the channels.

Finally, **Paper VII** is engaging the pipette to implement a unique rapid prototyping platform for 2D nanofluidic circuits based upon supported lipid bilayers. The lipid material is locally deposited from small unilamellar vesicles, which are fusing into a continuous membrane, where molecules can be transported by diffusion and, and in some cases, by capillary or shear forces. The geometry and composition of the circuitry is defined by synchronous computer controlled switching between membrane sources and scanning of the microscope stage. In addition to writing such compositionally diverse networks, they can be at any point removed, repaired or functionalized in a single experiment. This large variety of possibilities to manipulate lipid films and attached compounds constitutes a **lab on a membrane**, useful to controllably and conveniently study transport of membrane components and their interactions.

Conclusion and remarks

My research described in this thesis has been focused on the development of a microfluidic liquid handling tool, starting from basic principles and finishing with a refined instrument, which has been diversely applied in studies on cell cultures, tissue slices and biomimetic membranes. Locally controlled liquid handling can also be the foundation for other independent techniques, such as microthermometry and most notably: the writing of two-dimensional nanofluidic networks.

All the functions presented here are based on the concept of localized solution exchange. This is, however, just one possible aspect of the use of this device. Perhaps more desirable, but also more challenging is the opposite: collection and analysis of cellular content or release. Proteins are expressed in really tiny quantities: amounts in the 200 zmol range are

typical according to [198], which correspond to just 100'000 molecules, yet many rare proteins are even less abundant.

Another exciting area for future studies is the *Lab on a Membrane* and its applications in investigations of molecules confined in 2D liquids. On one hand, direct analysis of membrane proteins and their behavior is central to fundamental understanding of cell biology and aids in the development of new drugs. On the another hand, 2D fluidity represents a fundamentally different transport mode and a special environment for chemistry. Simplicity and robustness of our method may render 2D chemistry practically useable. Particularly fascinating is the combination of 2D fluidic and 2D electronics. One can envision connecting molecularly thin flows and graphene sensors to create new analytical techniques, able to detect few molecules extracted from just a single cell. Even if the multifunctional pipette, will be not an active part of membrane based detection devices, it may become a development tool as indispensable as the oscilloscope is for the development of electronics.

I believe that this technology, being functional, robust and simple to use, will find its way into many bioscience labs. It will enable new kinds of experiments, will improve data quality and ensure the efficient use of reagents, cell cultures and tissues. But after all, most of the exciting journey is still ahead of us: to discover new applications and abilities and solve questions and problems which we, at this point, are not even aware of.



ACKNOWLEDGEMENTS

These last five years, I have been working on my PhD has been greatest fun! And the biggest contributors to this joy are, you, wonderful people, from all over the world, whom I have had opportunity to meet here, work together, gain ideas and inspiration, share struggles, excitement and celebrate successes, both between the lab walls and during free times! You have made it a memorable journey of my life!

Thanks ...

Owe: for accepting me as a PhD student in your lab and for believing in my work and the choices and for your vision and motivating passion towards the research.

Aldo: for being the best mentor, colleague and friend, a great scientist, who is always filled with curiosity and limitless enthusiasm to try even the wildest ideas! For always being helpful and opened to share your diverse knowledge and expertise - these thousands of hours of discussions about science, technology and philosophy has taught me a lot and also brought up many interesting ideas! Not to mention your immense contribution to all these developments and writing our papers, but also for proof reading my thesis, suggestions and improvements.

My co-authors:

Gavin: for all the work which we have done together to develop the pipette, most of all, for your mastery of design and fine mechanics, which has given our pipette its elegant shape and look. And for always rescuing us, when we got into trouble with optics and microscopes, as well as with challenges in English grammar. Not less important, for all the coffee-corner discussions, which although killed a bit of time, were always keeping me updated about the latest and coolest tech news!

Irep: for skipping the last trams and sleeping time, to sit after midnight in the confocal lab and pursue both our coolest (the very first tests of the pipette and the lab on a membrane) and sometimes most challenging experiments - that's the spirit! For keeping up enthusiasm and positive attitude, but also for the other fun outside of the confocal lab! ...and for all the help in this final thesis rush!

Kent: for the introduction to the interesting field of neuroscience, and rats and brains and electrophysiology. For being such a great host and having good times in Stockholm and at Karolinska.

Erik: for being able to watch over your shoulder, and learn about all the struggles and 'black magic' of patch-clamp. And of course, for your great company in all the conferences and being my Trans-Atlantic Swedish teacher!

Natasha: For handling cell blebbs and being a good snowboard teacher.

Also **Ilona, Bodil, Shijun, Aikram, Ralf, Holger & Nicolas** - for your great contributions to make all these different developments and experiments possible.

Our young, enthusiastic and driven microfluidics team, featuring:

Anna, Kiryl, Anil, Davood & Fredrik: for all the new ideas and for trying them out to bring about the next generations of devices! A pity that lately, in my thesis rush, I haven't had enough time to discuss with you, as much as I wish I would have.

OrwarLab:

For creating a nice, friendly, cooperative and warm atmosphere, that coming to the lab is almost like coming home. For our present (**Mehrnaz, Celine, Carolina, Haijiang**) & former (**Brigitte, Maria, Ilja, Johan, Tanya, Helen, Ludvig, Martin, Jian, Jessica, Lidiya, Inga**) members.

Andreas for taking the challenge of further developing the microfluidic diluter. **Paul** for your great knowledge and compelling discussions about different field of sciences.

The Collectricon team:

Christer, Fredrik, Glenn & Mattias for sharing your expertise and helping us to develop the production of high-quality pipettes, which have allowed us to do a large part of the research presented here. Big thanks also to the **Chalmers NanoInitiative**, whose financial support made this collaboration possible.

Collaborators & contributors:

Jelena, Carina, Ann-Sofie, Andy (Chalmers/GU), **Joseph Bruton** and **Håkan Westerblad** (Karolinska Institute), **Claudio Rivera** (University of Helsinki), **Olivier Curet** (Sanofi, Paris): for teaching me some new techniques, contributing to experiments, having interesting discussions, shearing insight into your exciting research and testing our devices in your projects. I have learned a lot!

The MC2 crew: **John, Johan, Hendrik, Ulf, Göran**: for teaching and helping with all the cleanroom machines.

My other friends:

Beer Club members: you made my Thursdays! Fortunately you were far too many (98!) to be listed here. But one of the spirits of the BC has been, of course, **Michal** - who besides other fun, is a master of delicious smoked fishes and bbq's.

Important people on the way, without whom I wouldn't be here: my high-school teacher **Ene**, who inspired me to study physics; my mentor in Estonia, **Alvo**, who inspired me to work in science; my friend **Triinu**, from whom I heard about Chalmers; **Alfred Ots' Scholarship Foundation**, which made my MSc. studies here possible; **Göran Wendin & Zoran**, thank to whom I met Aldo, and rest you already know ...

My Estonian friends both here in Sweden and in Estonia! Especially **Mart**, the greatest friend of all Estonian Chalmers students, for your cheerfulness and care in arranging the delightful series of student symposia and many memorable dinners.

Annemarie: for the experience to have cats, and wonderful midsummers.

Our International Hiking Team: **Ludo, Toma, Masha, Gaizka**: for the reason to wait for the summers and the next adventures!

Vika: For many-many nice times together, great hikes and explorations, patience, kindness, support and good spirit toward science.

My family: **Mom, Dad & Tanel**: for unconditional love and support for all my endeavors. At first, for home, guidance and environment, where my young scientific curiosity has been nourished (including the sacrifice of numerous domestic gadgets). Later always encouraging my educational and scientific pursuits. Tanel: also for his advices and help in technology development. *Kallid Mammid ja Papi! Suur aitähh kõige eest ja vabandused, kui mul viimastel aegadel nii vähe aega on olnud, aga nüüd on see siis tehtud!*

Tack så Mycket! Suur Aitähh! Big Thanks!

REFERENCES

1. Tricorder. Wikipedia. (<http://en.wikipedia.org/wiki/Tricorder>)
2. Terry SC, Jerman JH, & Angell JB (1979) GAS-CHROMATOGRAPHIC AIR ANALYZER FABRICATED ON A SILICON-WAFER. *IEEE Transactions on Electron Devices* 26(12):1880-1886.
3. Karlsson R, Michaelsson A, & Mattsson L (1991) KINETIC-ANALYSIS OF MONOCLONAL ANTIBODY-ANTIGEN INTERACTIONS WITH A NEW BIOSENSOR BASED ANALYTICAL SYSTEM. *Journal of Immunological Methods* 145(1-2):229-240.
4. Becker H (2009) Hype, hope and hubris: the quest for the killer application in microfluidics. *Lab Chip* 9(15):2119-2122.
5. Chin CD, Linder V, & Sia SK (2012) Commercialization of microfluidic point-of-care diagnostic devices. *Lab Chip* 12(12):2118-2134.
6. Waters H (2011) New \$10 million X Prize launched for tricorder-style medical device. *Nat Med* 17(7):754-754.
7. Moore GA (1991) *Crossing the Chasm* (Harper Business Essentials).
8. Rogers EM (1962) *Diffusion of innovations* (Free Press., New York).
9. Existence and Smoothness of the Navier-Stokes Equation. Clay Mathematics Institute. (http://www.claymath.org/millennium/Navier-Stokes_Equations/)
10. Bruus H (2007) *Theoretical Microfluidics* (Oxford University Press).
11. Jeon NL, *et al.* (2002) Neutrophil chemotaxis in linear and complex gradients of interleukin-8 formed in a microfabricated device. *Nat. Biotechnol.* 20(8):826-830.
12. Weigl BH & Yager P (1999) Microfluidics - Microfluidic diffusion-based separation and detection. *Science* 283(5400):346-347.
13. Yung CW, Fiering J, Mueller AJ, & Ingber DE (2009) Micromagnetic-microfluidic blood cleansing device. *Lab Chip* 9(9):1171-1177.
14. Cho BS, *et al.* (2003) Passively driven integrated microfluidic system for separation of motile sperm. *Analytical Chemistry* 75(7):1671-1675.
15. Probstein RF (2003) *Physiochemical Hydrodynamics* (Wiley-Interscience).
16. Taylor G (1953) DISPERSION OF SOLUBLE MATTER IN SOLVENT FLOWING SLOWLY THROUGH A TUBE. *Proceedings of the Royal Society of London Series a-Mathematical and Physical Sciences* 219(1137):186-203.
17. Aris R (1956) ON THE DISPERSION OF A SOLUTE IN A FLUID FLOWING THROUGH A TUBE. *Proceedings of the Royal Society of London Series a-Mathematical and Physical Sciences* 235(1200):67-77.

18. Azizi F & Mastrangelo CH (2008) Generation of dynamic chemical signals with pulse code modulators. *Lab Chip* 8(6):907-912.
19. Lucchetta EM, Lee JH, Fu LA, Patel NH, & Ismagilov RF (2005) Dynamics of *Drosophila* embryonic patterning network perturbed in space and time using microfluidics. *Nature* 434(7037):1134-1138.
20. Mosadegh B, *et al.* (2010) Integrated elastomeric components for autonomous regulation of sequential and oscillatory flow switching in microfluidic devices. *Nature Physics* 6(6):433-437.
21. Nguyen TV, Duncan PN, Ahrar S, & Hui EE (2012) Semi-autonomous liquid handling via on-chip pneumatic digital logic. *Lab Chip* 12(20):3991-3994.
22. Rhee M & Burns MA (2009) Microfluidic pneumatic logic circuits and digital pneumatic microprocessors for integrated microfluidic systems. *Lab Chip* 9(21):3131-3143.
23. Langelier SM, *et al.* (2011) Flexible casting of modular self-aligning microfluidic assembly blocks. *Lab Chip* 11(9):1679-1687.
24. Yuen PK (2008) SmartBuild - A truly plug-n-play modular microfluidic system. *Lab Chip* 8(8):1374-1378.
25. Duffy DC, McDonald JC, Schueller OJA, & Whitesides GM (1998) Rapid prototyping of microfluidic systems in poly(dimethylsiloxane). *Analytical Chemistry* 70(23):4974-4984.
26. Becker H, Beckert E, & Gartner C (2010) Hybrid tooling technologies for injection molded and hot embossed polymeric microfluidic devices. *Microfluidics, Biomems, and Medical Microsystems VIII*, Proceedings of SPIE, eds Becker H & Wang W (Spie-Int Soc Optical Engineering, Bellingham), Vol 7593.
27. Liao Y, *et al.* (2012) Rapid prototyping of three-dimensional microfluidic mixers in glass by femtosecond laser direct writing. *Lab Chip* 12(4):746-749.
28. Agirregabiria M, *et al.* (2005) Fabrication of SU-8 multilayer microstructures based on successive CMOS compatible adhesive bonding and releasing steps. *Lab Chip* 5(5):545-552.
29. Hull CW (1984) US 4,575,330.
30. THE FORM 1. 3D PRINTER. FormLabs. (<http://formlabs.com>)
31. Choi J-W, MacDonald E, & Wicker R (2010) Multi-material microstereolithography. *International Journal of Advanced Manufacturing Technology* 49(5-8):543-551.
32. LaFratta CN, Fourkas JT, Baldacchini T, & Farrer RA (2007) Multiphoton fabrication. *Angew Chem Int Edit* 46(33):6238-6258.
33. Murphy SV, Skardal A, & Atala A (2013) Evaluation of hydrogels for bio-printing applications. *J. Biomed. Mater. Res. Part A* 101A(1):272-284.
34. Xu T, *et al.* (2013) Complex heterogeneous tissue constructs containing multiple cell types prepared by inkjet printing technology. *Biomaterials* 34(1):130-139.

35. Symes MD, *et al.* (2012) Integrated 3D-printed reactionware for chemical synthesis and analysis. *Nat. Chem.* 4(5):349-354.
36. Kitson PJ, Rosnes MH, Sans V, Dragone V, & Cronin L (2012) Configurable 3D-Printed millifluidic and microfluidic 'lab on a chip' reactionware devices. *Lab Chip* 12(18):3267-3271.
37. (2012) Manufacturing. The third industrial revolution *The Economist*
38. Madou MJ (2002) *Fundamentals of Microfabrication. The Science of Miniaturization. 2nd Ed.* (CRC Press).
39. Iliescu C, Taylor H, Avram M, Miao J, & Franssila S (2012) A practical guide for the fabrication of microfluidic devices using glass and silicon. *Biomicrofluidics* 6(1).
40. Bu MQ, Melvin T, Ensell GJ, Wilkinson JS, & Evans AGR (2004) A new masking technology for deep glass etching and its microfluidic application. *Sens. Actuator A-Phys.* 115(2-3):476-482.
41. Laermer F & Schilp A (WO9414187-A; DE4241045-C; EP625285-A; DE4241045-C2; DE4241045-A1; DE4241045-C1; WO9414187-A1; EP625285-A1; JP7503815-W; US5501893-A; EP625285-B1; JP2007129260-A; JP4090492-B2).
42. Richter K, Orfert M, Howitz S, & Thierbach S (1999) Deep plasma silicon etch for microfluidic applications. *Surf. Coat. Technol.* 116:461-467.
43. SOI Wafers. Virginia Semiconductor Inc. (<http://www.virginiasemi.com>)
44. Pihl J, *et al.* (2005) Microfluidic gradient-generating device for pharmacological profiling. *Analytical Chemistry* 77(13):3897-3903.
45. Akashi T & Yoshimura Y (2008) Profile control of a borosilicate-glass groove formed by deep reactive ion etching. *Journal of Micromechanics and Microengineering* 18(10).
46. Malek CGK (2006) Laser processing for bio-microfluidics applications (part I). *Analytical and Bioanalytical Chemistry* 385(8):1351-1361.
47. Malek CGK (2006) Laser processing for bio-microfluidics applications (part II). *Analytical and Bioanalytical Chemistry* 385(8):1362-1369.
48. Chung CK, *et al.* (2010) Water-assisted CO₂ laser ablated glass and modified thermal bonding for capillary-driven bio-fluidic application. *Biomedical Microdevices* 12(1):107-114.
49. Huft J, Da Costa DJ, Walker D, & Hansen CL (2010) Three-dimensional large-scale microfluidic integration by laser ablation of interlayer connections. *Lab Chip* 10(18):2358-2365.
50. Becker H & Gaertner C (2008) Polymer microfabrication technologies for microfluidic systems. *Analytical and Bioanalytical Chemistry* 390(1):89-111.
51. Hupert ML, *et al.* (2007) Evaluation of micromilled metal mold masters for the replication of microchip electrophoresis devices. *Microfluid. Nanofluid.* 3(1):1-11.

52. Hupert ML, *et al.* (2006) High-precision micromilling for low-cost fabrication of metal mold masters - art. no. 61120B. *Microfluidics, BioMEMs, and Medical Microsystems IV*, Proceedings of the Society of Photo-Optical Instrumentation Engineers (Spie), eds Papautsky I & Wang W (Spie-Int Soc Optical Engineering, Bellingham), Vol 6112, pp B1120-B1120.
53. Schaller T, Bohn L, Mayer J, & Schubert K (1999) Microstructure grooves with a width of less than 50 μm cut with ground hard metal micro end mills. *Precis. Eng.-J. Am. Soc. Precis. Eng.* 23(4):229-235.
54. Micron mills. Performance Microtools. (<http://www.pmtnow.com/>)
55. Iida K, *et al.* (2009) Living anionic polymerization using a microfluidic reactor. *Lab Chip* 9(2):339-345.
56. Lin YS, *et al.* (2012) An Aluminum Microfluidic Chip Fabrication Using a Convenient Micromilling Process for Fluorescent Poly(DL-lactide-co-glycolide) Microparticle Generation. *Sensors* 12(2):1455-1467.
57. Becker H & Gartner C (2000) Polymer microfabrication methods for microfluidic analytical applications. *Electrophoresis* 21(1):12-26.
58. Attia UM, Marson S, & Alcock JR (2009) Micro-injection moulding of polymer microfluidic devices. *Microfluid. Nanofluid.* 7(1):1-28.
59. Hecke M & Schomburg WK (2004) Review on micro molding of thermoplastic polymers. *Journal of Micromechanics and Microengineering* 14(3):R1-R14.
60. Becker H & Heim U (1999) Polymer hot embossing with silicon master structures. *Sens. Mater.* 11(5):297-304.
61. Anwar K, Han T, & Kim SM (2011) Reversible sealing techniques for microdevice applications. *Sensors and Actuators B-Chemical* 153(2):301-311.
62. Rhee SW, *et al.* (2005) Patterned cell culture inside microfluidic devices. *Lab Chip* 5(1):102-107.
63. COMSOL AB. (www.comsol.se)
64. Satyanarayana S, Karnik RN, & Majumdar A (2005) Stamp-and-stick room-temperature bonding technique for microdevices. *Journal of Microelectromechanical Systems* 14(2):392-399.
65. Kim K, Park SW, & Yang SS (2010) The optimization of PDMS-PMMA bonding process using silane primer. *BioChip J.* 4(2):148-154.
66. Sunkara V, Park DK, & Cho YK (2012) Versatile method for bonding hard and soft materials. *RSC Adv.* 2(24):9066-9070.
67. Tennico YH, Koesdjojo MT, Kondo S, Mandrell DT, & Remcho VT (2010) Surface modification-assisted bonding of polymer-based microfluidic devices. *Sensors and Actuators B-Chemical* 143(2):799-804.
68. Bhattacharyya A & Klapperich CM (2006) Thermoplastic microfluidic device for on-chip purification of nucleic acids for disposable diagnostics. *Analytical Chemistry* 78(3):788-792.

69. Tsao CW & DeVoe DL (2009) Bonding of thermoplastic polymer microfluidics. *Microfluid. Nanofluid.* 6(1):1-16.
70. Brown L, Koerner T, Horton JH, & Oleschuk RD (2006) Fabrication and characterization of poly(methylmethacrylate) microfluidic devices bonded using surface modifications and solvents. *Lab Chip* 6(1):66-73.
71. Wei J, Xie H, Nai ML, Wong CK, & Lee LC (2003) Low temperature wafer anodic bonding. *Journal of Micromechanics and Microengineering* 13(2):217-222.
72. Allen PB & Chiu DT (2008) Calcium-assisted glass-to-glass bonding for fabrication of glass microfluidic devices. *Analytical Chemistry* 80(18):7153-7157.
73. Martinez AW, Phillips ST, Whitesides GM, & Carrilho E (2010) Diagnostics for the Developing World: Microfluidic Paper-Based Analytical Devices. *Analytical Chemistry* 82(1):3-10.
74. Li X, Tian JF, & Shen W (2010) Thread as a Versatile Material for Low-Cost Microfluidic Diagnostics. *ACS Appl. Mater. Interfaces* 2(1):1-6.
75. Safavieh R, Zhou GZ, & Juncker D (2011) Microfluidics made of yarns and knots: from fundamental properties to simple networks and operations. *Lab Chip* 11(15):2618-2624.
76. Foturan Photosensitive Glass. Invenious. (<http://www.invenios.com/>)
77. Bruin GJM (2000) Recent developments in electrokinetically driven analysis on microfabricated devices. *Electrophoresis* 21(18):3931-3951.
78. Mellors JS, Gorbounov V, Ramsey RS, & Ramsey JM (2008) Fully integrated glass microfluidic device for performing high-efficiency capillary electrophoresis and electrospray ionization mass spectrometry. *Analytical Chemistry* 80(18):6881-6887.
79. Fiorini GS, Lorenz RM, Kuo JS, & Chiu DT (2004) Rapid prototyping of thermoset polyester microfluidic devices. *Analytical Chemistry* 76(16):4697-4704.
80. Metz S, Holzer R, & Renaud P (2001) Polyimide-based microfluidic devices. *Lab Chip* 1(1):29-34.
81. Unger MA, Chou HP, Thorsen T, Scherer A, & Quake SR (2000) Monolithic microfabricated valves and pumps by multilayer soft lithography. *Science* 288(5463):113-116.
82. Roy E, Geissler M, Galas JC, & Veres T (2011) Prototyping of microfluidic systems using a commercial thermoplastic elastomer. *Microfluid. Nanofluid.* 11(3):235-244.
83. Personal Communication with MC2 personal about costs of microfabrication.
84. The Photo-Mask Guide. JD Phototools. (<http://www.jdphoto.co.uk/>)
85. Gelorme JD, Cox RJ, & Gutierrez SAR (EP222187-A; JP62102242-A; BR8604549-A; US4882245-A; EP222187-B; DE3674340-G; ES2017615-B; CA1289803-C; JP95078628-B2).

86. SU-8 2000 Permanent Epoxy Resists. MicroChem Inc. (<http://www.microchem.com>)
87. Lecomte JP. Silicone in the Food Industries. Dow Corning. (<http://www.dowcorning.com/content/publishedlit/Chapter3.pdf>)
88. Xia YN & Whitesides GM (1998) Soft lithography. *Annual Review of Materials Science* 28:153-184.
89. Xia YN & Whitesides GM (1998) Soft lithography. *Angew Chem Int Edit* 37(5):551-575.
90. Lewis LN & Lewis N (1986) PLATINUM-CATALYZED HYDROSILYLATION - COLLOID FORMATION AS THE ESSENTIAL STEP. *J. Am. Chem. Soc.* 108(23):7228-7231.
91. Faglioni F, Blanco M, Goddard WA, & Saunders D (2002) Heterogeneous inhibition of homogeneous reactions: Karstedt catalyzed hydrosilylation. *J. Phys. Chem. B* 106(7):1714-1721.
92. Morin SA, *et al.* (2012) Camouflage and Display for Soft Machines. *Science* 337(6096):828-832.
93. Lee JN, Park C, & Whitesides GM (2003) Solvent compatibility of poly(dimethylsiloxane)-based microfluidic devices. *Analytical Chemistry* 75(23):6544-6554.
94. Jo BH, Van Lerberghe LM, Motsegood KM, & Beebe DJ (2000) Three-dimensional micro-channel fabrication in polydimethylsiloxane (PDMS) elastomer. *Journal of Microelectromechanical Systems* 9(1):76-81.
95. McDonald JC, *et al.* (2000) Fabrication of microfluidic systems in poly(dimethylsiloxane). *Electrophoresis* 21(1):27-40.
96. Rosenthal CK, *et al.* (2009) Milestones of Light Microscopy *Nature Milestones*
97. Hook R (1665) Micrographia: or Some Physiological Descriptions of Minute Bodies, Made by Magnifying Glasses with Observations and Inquiries Thereupon. (Project Gutenberg Literary Archive Foundation (<http://www.gutenberg.org>)).
98. Zernike F (1942) Phase contrast, a new method for the microscopic observation of transparent objects. *Physica* 9:686-698.
99. Allen RD, David GB, & Nomarski G (1969) The zeiss-Nomarski differential interference equipment for transmitted-light microscopy. *Z Wiss Mikrosk* 69(4):193-221.
100. Jablonski A (1933) Efficiency of anti-stokes fluorescence in dyes. *Nature* 131:839-840.
101. Stokes GG (1852) On the Change of Refrangibility of Light. *Philosophical Transactions of the Royal Society of London* 142:463-562.
102. Masters BR (2010) The Development of Fluorescence Microscopy. *ENCYCLOPEDIA OF LIFE SCIENCES*.

103. Coons AH, Creech HJ, & Jones RN (1941) Immunological properties of an antibody containing a fluorescent group. *Proceedings of the Society for Experimental Biology and Medicine* 47(2):200-202.
104. Martin MM & Lindqvist L (1975) PH-DEPENDENCE OF FLUORESCENCE. *Journal of Luminescence* 10(6):381-390.
105. Rhodamine B. Sigma-Aldrich. (<http://www.sigmaaldrich.com>)
106. Magde D, Webb WW, & Elson E (1972) THERMODYNAMIC FLUCTUATIONS IN A REACTING SYSTEM - MEASUREMENT BY FLUORESCENCE CORRELATION SPECTROSCOPY. *Phys Rev Lett* 29(11):705-&.
107. Peters R, Peters J, Tews KH, & Bahr W (1974) MICROFLUORIMETRIC STUDY OF TRANSLATIONAL DIFFUSION IN ERYTHROCYTE-MEMBRANES. *Biochim Biophys Acta* 367(3):282-294.
108. Stryer L & Haugland RP (1967) ENERGY TRANSFER - A SPECTROSCOPIC RULER. *Proceedings of the National Academy of Sciences of the United States of America* 58(2):719-&.
109. Denk W, Strickler JH, & Webb WW (1990) 2-PHOTON LASER SCANNING FLUORESCENCE MICROSCOPY. *Science* 248(4951):73-76.
110. Axelrod D (1981) CELL-SUBSTRATE CONTACTS ILLUMINATED BY TOTAL INTERNAL-REFLECTION FLUORESCENCE. *Journal of Cell Biology* 89(1):141-145.
111. Total Internal Reflection Fluorescence (TIRF) Microscopy. Nikon. MicroscopyU. (<http://www.microscopyu.com/>)
112. Minsky M (1957) US3013467.
113. Karstens T & Kobs K (1980) RHODAMINE-B AND RHODAMINE-101 AS REFERENCE SUBSTANCES FOR FLUORESCENCE QUANTUM YIELD MEASUREMENTS. *Journal of Physical Chemistry* 84(14):1871-1872.
114. Barilero T, Le Saux T, Gosse C, & Jullien L (2009) Fluorescent Thermometers for Dual-Emission-Wavelength Measurements: Molecular Engineering and Application to Thermal Imaging in a Microsystem. *Analytical Chemistry* 81(19):7988-8000.
115. Eberhard M & Erne P (1991) CALCIUM-BINDING TO FLUORESCENT CALCIUM INDICATORS - CALCIUM GREEN, CALCIUM ORANGE AND CALCIUM CRIMSON. *Biochemical and Biophysical Research Communications* 180(1):209-215.
116. Fluo-3 Calcium Indicator. Life Technologies. (<http://www.invitrogen.com>)
117. YO-PRO®-1 Iodide (491/509). Life Technologies. (<http://www.invitrogen.com>)
118. Nolkranz K, Farre C, Hurtig KJ, Rylander P, & Orwar O (2002) Functional screening of intracellular proteins in single cells and in patterned cell arrays using electroporation. *Analytical Chemistry* 74(16):4300-4305.

119. Prasher DC, Eckenrode VK, Ward WW, Prendergast FG, & Cormier MJ (1992) PRIMARY STRUCTURE OF THE AEQUOREA-VICTORIA GREEN-FLUORESCENT PROTEIN. *Gene* 111(2):229-233.
120. Thorlabs. (<http://www.thorlabs.com/>)
121. Dertinger SKW, Chiu DT, Jeon NL, & Whitesides GM (2001) Generation of gradients having complex shapes using microfluidic networks. *Analytical Chemistry* 73(6):1240-1246.
122. Bennett MR, *et al.* (2008) Metabolic gene regulation in a dynamically changing environment. *Nature* 454(7208):1119-1122.
123. Zhang X & Roper MG (2009) Microfluidic Perfusion System for Automated Delivery of Temporal Gradients to Islets of Langerhans. *Analytical Chemistry* 81(3):1162-1168.
124. Hansen CL, Sommer MOA, & Quake SR (2004) Systematic investigation of protein phase behavior with a microfluidic formulator. *Proceedings of the National Academy of Sciences of the United States of America* 101(40):14431-14436.
125. Paegel BM, Grover WH, Skelley AM, Mathies RA, & Joyce GF (2006) Microfluidic serial dilution circuit. *Analytical Chemistry* 78(21):7522-7527.
126. Hong JW, Chen Y, Anderson WF, & Quake SR (2006) Molecular biology on a microfluidic chip. *Journal of Physics-Condensed Matter* 18(18):S691-S701.
127. Chen RH & Cheng CM (2001) Study of spin coating properties of SU-8 thick-layer photoresist. *Advances in Resist Technology and Processing XVIII, Pts 1 and 2*, Proceedings of the Society of Photo-Optical Instrumentation Engineers (Spie), ed Houlihan FM, Vol 4345, pp 494-501.
128. Iliescu C, Chen B, & Miao J (2008) On the wet etching of Pyrex glass. *Sens. Actuator A-Phys.* 143(1):154-161.
129. Miniature Electronic Pressure Controllers. Parker Precision Fluidics. (<http://www.parker.com>)
130. Yasui T, *et al.* (2011) Microfluidic baker's transformation device for three-dimensional rapid mixing. *Lab Chip* 11(19):3356-3360.
131. Nguyen NT & Wu ZG (2005) Micromixers - a review. *Journal of Micromechanics and Microengineering* 15(2):R1-R16.
132. Stroock AD, *et al.* (2002) Chaotic mixer for microchannels. *Science* 295(5555):647-651.
133. Ahmed D, Mao XL, Shi JJ, Juluri BK, & Huang TJ (2009) A millisecond micromixer via single-bubble-based acoustic streaming. *Lab Chip* 9(18):2738-2741.
134. Olofsson J, *et al.* (2005) A chemical waveform synthesizer. *Proceedings of the National Academy of Sciences of the United States of America* 102(23):8097-8102.

135. Gaddum JH (1961) PUSH-PULL CANNULAE. *Journal of Physiology-London* 155(1):P1-&.
136. Delgado JMR, Defeudis FV, Roth RH, Ryugo DK, & Mitruka BM (1972) DIALYTRODE FOR LONG-TERM INTRACEREBRAL PERFUSION IN AWAKE MONKEYS. *Arch. Int. Pharmacodyn. Ther.* 198(1):9-&.
137. Kovacs DA, Zoll JG, & Erickson CK (1976) IMPROVED INTRACEREBRAL CHEMITRODE FOR CHEMICAL AND ELECTRICAL STUDIES OF BRAIN. *Pharmacol. Biochem. Behav.* 4(5):621-625.
138. Ungerste.U & Pycock C (1974) FUNCTIONAL CORRELATES OF DOPAMINE NEUROTRANSMISSION. *Bulletin Der Schweizerischen Akademie Der Medizinischen Wissenschaften* 30(1-3):44-55.
139. Elmquist WF & Sawchuk RJ (1997) Application of microdialysis in pharmacokinetic studies. *Pharm. Res.* 14(3):267-288.
140. Ungerstedt U (2009) Microdialysis in Neurointensive Care. ed 2nd (Stockholm).
141. Mitumori K, *et al.* (JP11033506-A; US6230722-B1; US2001037819-A1; US6517635-B2; US42566-E.
142. Veselovsky NS, Engert F, & Lux HD (1996) Fast local superfusion technique. *Pflügers Archiv-European Journal of Physiology* 432(2):351-354.
143. Lohmann C, Finski A, & Bonhoeffer T (2005) Local calcium transients regulate the spontaneous motility of dendritic filopodia. *Nat. Neurosci.* 8(3):305-312.
144. Engert F & Bonhoeffer T (1997) Synapse specificity of long-term potentiation breaks down at short distances. *Nature* 388(6639):279-284.
145. Feinerman O & Moses E (2003) A picoliter 'fountain-pen' using co-axial dual pipettes. *J Neurosci Meth* 127(1):75-84.
146. Shiku H, *et al.* (2009) A microfluidic dual capillary probe to collect messenger RNA from adherent cells and spheroids. *Anal. Biochem.* 385(1):138-142.
147. Feinerman O, Rotem A, & Moses E (2008) Reliable neuronal logic devices from patterned hippocampal cultures. *Nature Physics* 4(12):967-973.
148. Feinerman O, Segal M, & Moses E (2005) Signal propagation along unidimensional neuronal networks. *J. Neurophysiol.* 94(5):3406-3416.
149. Klauke N, Smith GL, & Cooper JM (2007) Microfluidic partitioning of the extracellular space around single cardiac myocytes. *Analytical Chemistry* 79(3):1205-1212.
150. Juncker D, Schmid H, & Delamarche E (2005) Multipurpose microfluidic probe. *Nat. Mater.* 4(8):622-628.
151. Lovchik RD, Drechsler U, & Delamarche E (2009) Multilayered microfluidic probe heads. *Journal of Micromechanics and Microengineering* 19(11).
152. Kaigala GV, Lovchik RD, Drechsler U, & Delamarche E (2011) A Vertical Microfluidic Probe. *Langmuir* 27(9):5686-5693.

153. Queval A, *et al.* (2010) Chamber and microfluidic probe for microperfusion of organotypic brain slices. *Lab Chip* 10(3):326-334.
154. Lovchik RD, Kaigala GV, Georgiadis M, & Delamarche E (2012) Micro-immunohistochemistry using a microfluidic probe. *Lab Chip* 12(6):1040-1043.
155. Perrault CM, *et al.* (2010) Integrated microfluidic probe station. *Rev. Sci. Instrum.* 81(11).
156. Chen D, *et al.* (2008) The chemistode: A droplet-based microfluidic device for stimulation and recording with high temporal, spatial, and chemical resolution. *Proceedings of the National Academy of Sciences of the United States of America* 105(44):16843-16848.
157. Chang-Yen DA, Myszka DG, & Gale BK (2006) A novel PDMS microfluidic spotter for fabrication of protein chips and microarrays. *Journal of Microelectromechanical Systems* 15(5):1145-1151.
158. Delamarche E, Juncker D, & Schmid H (2005) Microfluidics for processing surfaces and miniaturizing biological assays. *Adv. Mater.* 17(24):2911-2933.
159. Zhao B, Moore JS, & Beebe DJ (2001) Surface-directed liquid flow inside microchannels. *Science* 291(5506):1023-1026.
160. Momotenko D, Cortes-Salazar F, Lesch A, Wittstock G, & Girault HH (2011) Microfluidic Push-Pull Probe for Scanning Electrochemical Microscopy. *Analytical Chemistry* 83(13):5275-5282.
161. Cortes-Salazar F, Momotenko D, Girault HH, Lesch A, & Wittstock G (2011) Seeing Big with Scanning Electrochemical Microscopy. *Analytical Chemistry* 83(5):1493-1499.
162. Lodish H (2007) *Molecular Cell Biology* (Freeman & Co Ltd).
163. Buonomano DV (2007) The biology of time across different scales. *Nature Chemical Biology* 3(10):594-597.
164. Breitingner HG (2001) Fast kinetic analysis of ligand-gated ion channels. *Neuroscientist* 7(2):95-103.
165. Auzmendi J, Do Porto DF, Pallavicini C, & Moffatt L (2012) Achieving Maximal Speed of Solution Exchange for Patch Clamp Experiments. *PLoS One* 7(8).
166. Hamill OP, Marty A, Neher E, Sakmann B, & Sigworth FJ (1981) IMPROVED PATCH-CLAMP TECHNIQUES FOR HIGH-RESOLUTION CURRENT RECORDING FROM CELLS AND CELL-FREE MEMBRANE PATCHES. *Pflügers Archiv-European Journal of Physiology* 391(2):85-100.
167. Kakei M & Ashcroft FM (1987) A MICROFLOW SUPERFUSION SYSTEM FOR USE WITH EXCISED MEMBRANE PATCHES. *Pflügers Archiv-European Journal of Physiology* 409(3):337-341.
168. Maconochie DJ & Knight DE (1989) A METHOD FOR MAKING SOLUTION CHANGES IN THE SUB-MILLISECOND RANGE AT THE

- TIP OF A PATCH PIPETTE. *Pflügers Archiv-European Journal of Physiology* 414(5):589-596.
169. Sinclair J, *et al.* (2002) A cell-based bar code reader for high-throughput screening of ion channel-ligand interactions. *Analytical Chemistry* 74(24):6133-6138.
170. Hering S, Beech DJ, & Bolton TB (1987) A SIMPLE METHOD OF FAST EXTRACELLULAR SOLUTION EXCHANGE FOR THE STUDY OF WHOLE-CELL OR SINGLE CHANNEL CURRENTS USING PATCH-CLAMP TECHNIQUE. *Pflügers Archiv-European Journal of Physiology* 410(3):335-337.
171. Pidoplichko VI (1996) Dependence of solution exchange time on cell or patch linear dimensions in concentration jump experiments using patch-clamped sensory neurones. *Pflügers Archiv-European Journal of Physiology* 432(6):1074-1079.
172. Sachs F (1999) Practical limits on the maximal speed of solution exchange for patch clamp experiments. *Biophys. J.* 77(2):682-690.
173. Lu HP, Xun LY, & Xie XS (1998) Single-molecule enzymatic dynamics. *Science* 282(5395):1877-1882.
174. Zhuang XW, *et al.* (2000) A single-molecule study of RNA catalysis and folding. *Science* 288(5473):2048-+.
175. Losavio BE, Iyer V, Patel S, & Saggau P (2010) Acousto-optic laser scanning for multi-site photo-stimulation of single neurons in vitro. *J. Neural Eng.* 7(4).
176. Kramer RH, Fortin DL, & Trauner D (2009) New photochemical tools for controlling neuronal activity. *Curr. Opin. Neurobiol.* 19(5):544-552.
177. Herr NR, Belle AM, Daniel KB, Carelli RM, & Wightman RM (2010) Probing Presynaptic Regulation of Extracellular Dopamine with Iontophoresis. *ACS Chem. Neurosci.* 1(9):627-638.
178. Isaksson J, *et al.* (2007) Electronic control of Ca²⁺ signalling in neuronal cells using an organic electronic ion pump. *Nat. Mater.* 6(9):673-679.
179. Bruckbauer A, *et al.* (2007) Nanopipette delivery of individual molecules to cellular compartments for single-molecule fluorescence tracking. *Biophys. J.* 93(9):3120-3131.
180. Tavana H, *et al.* (2009) Nanolitre liquid patterning in aqueous environments for spatially defined reagent delivery to mammalian cells. *Nat. Mater.* 8(9):736-741.
181. Ginger DS, Zhang H, & Mirkin CA (2004) The evolution of dip-pen nanolithography. *Angew Chem Int Edit* 43(1):30-45.
182. Kim KH, Moldovan N, & Espinosa HD (2005) A nanofountain probe with sub-100 nm molecular writing resolution. *Small* 1(6):632-635.
183. Kim KH, *et al.* (2008) Direct delivery and submicrometer Patterning of DNA by a nanofountain probe. *Adv. Mater.* 20(2):330-+.

184. Meister A, *et al.* (2009) FluidFM: Combining Atomic Force Microscopy and Nanofluidics in a Universal Liquid Delivery System for Single Cell Applications and Beyond. *Nano Lett* 9(6):2501-2507.
185. Lundstrom K (2006) Structural genomics for membrane proteins. *Cell. Mol. Life Sci.* 63(22):2597-2607.
186. Castellana ET & Cremer PS (2006) Solid supported lipid bilayers: From biophysical studies to sensor design. *Surface Science Reports* 61(10):429-444.
187. Knoll W, *et al.* (2008) Solid supported lipid membranes: New concepts for the biomimetic functionalization of solid surfaces. *Biointerphases* 3(2):FA125-FA135.
188. Cornell BA, *et al.* (1997) A biosensor that uses ion-channel switches. *Nature* 387(6633):580-583.
189. Czolkos I, *et al.* (2009) Platform for Controlled Supramolecular Nanoassembly. *Nano Lett* 9(6):2482-2486.
190. Groves JT, Boxer SG, & McConnel HM (1997) Electric field-induced reorganization of two-component supported bilayer membranes. *Proceedings of the National Academy of Sciences of the United States of America* 94(25):13390-13395.
191. Jonsson P, Gunnarsson A, & Hook F (2011) Accumulation and Separation of Membrane-Bound Proteins Using Hydrodynamic Forces. *Analytical Chemistry* 83(2):604-611.
192. Hennig M, Neumann J, Wixforth A, Radler JO, & Schneider MF (2009) Dynamic patterns in a supported lipid bilayer driven by standing surface acoustic waves. *Lab Chip* 9(21):3050-3053.
193. Jonsson P, *et al.* (2012) Hydrodynamic trapping of molecules in lipid bilayers. *Proceedings of the National Academy of Sciences of the United States of America* 109(26):10328-10333.
194. Groves JT, Ulman N, & Boxer SG (1997) Micropatterning fluid lipid bilayers on solid supports. *Science* 275(5300):651-653.
195. Nafday OA, Lowry TW, & Lenhart S (2012) Multifunctional Lipid Multilayer Stamping. *Small* 8(7):1021-1028.
196. Smith KA, Gale BK, & Conboy JC (2008) Micropatterned Fluid Lipid Bilayer Arrays Created Using a Continuous Flow Microspotter. *Analytical Chemistry* 80(21):7980-7987.
197. Huang Y, Williams JC, & Johnson SM (2012) Brain slice on a chip: opportunities and challenges of applying microfluidic technology to intact tissues. *Lab Chip* 12(12):2103-2117.

PAPER

I

A Microfluidic Diluter Based on Pulse Width Flow Modulation

Alar Ainla, Irep Gözen, Owe Orwar, and Aldo Jesorka*

Department of Chemical and Biological Engineering, and Microtechnology Centre (MC2), Chalmers University of Technology, SE-412 96, Göteborg, Sweden

We demonstrate that pulse width flow modulation (PWF) can be used to design fast, accurate, and precise multi-stage dilution modules for microfluidic devices. The PWF stage unit presented here yields 10-fold dilution, but several PWF stages can be connected in series to yield higher-order dilutions. We have combined two stages in a device thus capable of diluting up to 100-fold, and we have experimentally determined a set of rules that can be conveniently utilized to design multistage diluters. Microfabrication with resist-based molds yielded geometrical channel height variances of 7% (22.9(16) μm) with corresponding hydraulic resistance variances of $\sim 20\%$. Pulsing frequencies, channel lengths, and flow pressures can be chosen within a wide range to establish the desired diluter properties. Finally, we illustrate the benefits of on-chip dilution in an example application where we investigate the effect of the Ca^{2+} concentration on a phospholipid bilayer spreading from a membrane reservoir onto a SiO_2 surface. This is one of many possible applications where flexible concentration control is desirable.

The preparation of solutions of different concentrations, with respect to, for example, a ligand or a substrate, is an essential and central part of many chemical and biological assays, and microfluidic devices that are capable of diluting solutions with high accuracy and precision are of great interest. The concept of dilution is simple, and it involves the precise metering of two or several solutions, followed by mixing. Microfluidic diluters can be divided into two major classes, based on their principle of operation. The first uses a central reactor, where components are metered and then mixed. Metering can be achieved by means of peristaltic micropumps¹ or via microinjection.² Mixing can be achieved with a rotary pump.^{1–3} To achieve concentrations over several orders of magnitude, serial dilution can be used.⁴ These types of devices can produce only small-volume elements of diluted solutions at a time, but not a continuous flow of solutions. Another

class of diluters is working in the continuous-flow regime, where flows are combined, and the final concentrations are defined by initial concentrations and flow rates. Continuous flow diluters are mostly based on ladders of channels and are used in devices to generate different gradients.^{5–9} In most of these devices, dilution is determined by design geometry. Redefining their functional properties can be achieved only by designing new circuitry. Lately, dilution ladders have been combined with flow multiplexing, enabling computer control of dilution for the generation of chemical signals.¹⁰ To enhance the mixing rate, sequential segmentation can be exploited¹¹ and, when combined with pulse-width modulation, different dilutions can be achieved.¹² The modulation can be conducted both inside¹² and outside the actual microfluidic device.¹³ The first method allows for faster exchange times and lower substrate consumption, whereas the second method offers greater simplicity on the microfabrication part.

Here, we demonstrate that multiple stages of pulse width flow modulation (PWF)-based diluters can be coupled in series to obtain a robust device with ~ 10 -fold dilution capability per single stage, high accuracy, speed, and full flexibility to adjust the concentration online. Each single dilution stage contains a flow modulator and a mixer (see Figure 1). The purpose of the flow modulator is to multiplex the output flow between the substrate and the solvent. The average substrate content in the output stream is determined by the duty cycle of the modulator, which is defined by the ratio of the substrate pulse length to the total switching period. The switching is driven in such a way that flow speed and pressure distribution in all channels remains constant, which is required for maximum accuracy. Therefore, a waste outlet is also continuously operated to avoid flow interruptions in the input channels. The modulator is followed by a mixer, which acts as a low-pass filter for the chemical concentration signal. Because of the Taylor dispersion, effective diffusion along the flow

* To whom correspondence should be addressed. Tel.: +46 31 772 6112. Fax: +46 31 772 6120. E-mail: aldo@chalmers.se.

- (1) Hansen, C. L.; Sommer, M. O. A.; Quake, S. R. *Proc. Natl. Acad. Sci. U.S.A.* **2004**, *101*, 14431–14436.
- (2) Hong, J. W.; Studer, V.; Hang, G.; Anderson, W. F.; Quake, S. R. *Nat. Biotechnol.* **2004**, *22*, 435–439.
- (3) Chou, H.-P.; Unger, M. A.; Quake, S. R. *Biomed. Microdev.* **2001**, *3*, 323–330.
- (4) Paegel, B. M.; Grover, W. H.; Skelley, A. M.; Mathies, R. A.; Joyce, G. F. *Anal. Chem.* **2006**, *78*, 7522–7527.

- (5) Dertinger, S. K. W.; Chiu, D. T.; Jeon, N. L.; Whitesides, G. M. *Anal. Chem.* **2001**, *73*, 1240–1246.
- (6) Holden, M. A.; Kumar, S.; Castellana, E. T.; Beskok, A.; Cremer, P. S. *Sens. Actuators, B* **2003**, *92*, 199–207.
- (7) Kim, C.; Lee, K.; Kim, J. H.; Shin, K. S.; Lee, K. J.; Kim, T. S.; Kang, J. Y. *Lab Chip* **2008**, *8*, 473–479.
- (8) Walker, G. M.; Monteiro-Riviere, N.; Rouse, J.; O'Neill, A. T. *Lab Chip* **2007**, *7*, 226–232.
- (9) Pihl, J.; Sinclair, J.; Sahlin, E.; Karlsson, M.; Pettersson, F.; Olofsson, J.; Orwar, O. *Anal. Chem.* **2005**, *77*, 3897–3903.
- (10) Chen, L.; Azizi, F.; Mastrangelo, C. H. *Lab Chip* **2007**, *7*, 850–855.
- (11) Nguyen, N. T.; Huang, X. Y. *Biomed. Microdev.* **2006**, *8*, 133–139.
- (12) Azizi, F.; Mastrangelo, C. H. *Lab Chip* **2008**, *8*, 907–912.
- (13) Bridle, H.; Olofsson, J.; Jesorka, A.; Orwar, O. *Anal. Chem.* **2007**, *79*, 9286–9293.

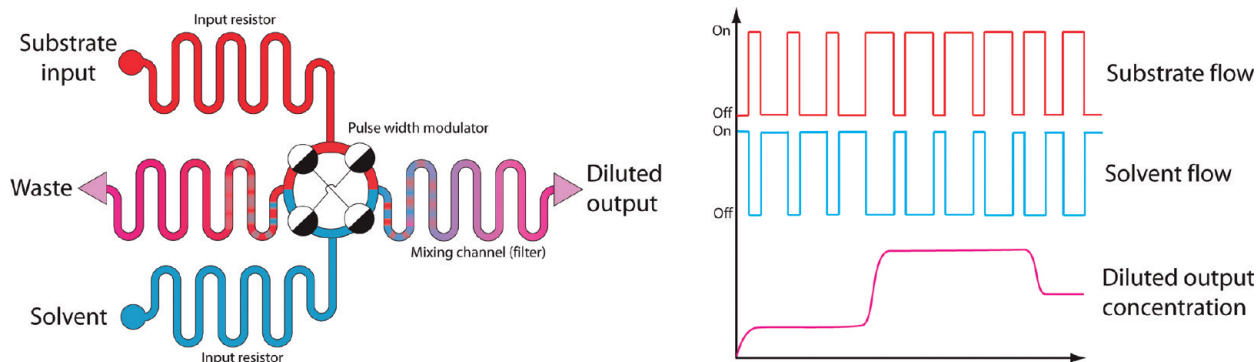


Figure 1. (Left) Schematic drawing showing a single dilution stage based on pulse width flow modulation (PWFM). (Right) Pulse code of flow switching and output concentration.

direction is significantly increased.¹⁴ The effective diffusion coefficient of a Taylor–Aris dispersion can be written as¹¹

$$D_{\text{effective}} = D + \frac{l^2 v^2}{210D} \approx \frac{l^2 v^2}{210D} \propto Pe^2 D \quad (1)$$

where D is the diffusion coefficient, l the channel width, v the mean velocity, and Pe the Peclet number. Thus, because of dispersion, substrate pulse boundaries are smoothed and the amplitude of the initial concentration fluctuation decreases until a constant output concentration is established. The system is, by principle, a chemical counterpart to the pulse width modulation-based digital-analog converters (DACs) that are common in electronics. PWFM is technologically favorable, because dilution information is transmitted as a serial code and only two control lines are required per dilution stage.

To construct and fabricate multilayer devices that were equipped with pneumatic valves,¹⁵ poly(dimethylsiloxane) (PDMS)-based soft lithography was applied. This is a well-established technique to rapidly produce microfluidic devices and it is a favorable technique, because of the simple microfabrication procedures and fast flow control (switching times of 10–20 ms). Here, we have characterized such a PWFM microfluidic device and, furthermore, developed a model that can be used to rapidly design circuits that are needed for a variety of applications. The design concept presented here can be used in various devices where computer-controlled dilution is favorable, and where the concentration of a solute can be rapidly changed on demand. Examples of such assays include feedback-controlled receptors and enzyme assays, as well as applications in stopped-flow analytical microdevices.

To demonstrate the benefits of our PWFM concept, we report an application example for studies of controlled spreading of phospholipids bilayers on silicon dioxide surfaces. These supported lipid bilayers are of considerable interest from both the fundamental and the practical point of view.¹⁶ Compared to conventional procedures (e.g., those using micropipets), the dilution chip reduces the time demand dramatically and shows greater flexibility and control which would be hardly attainable otherwise.

MATERIALS AND METHODS

Materials. Silicon wafers (n -type, with a size of 2 in.), HDMS primer, Clariant AZ4562 and Microchem SU8-10 photoresists, and AZ351 and SU8 developers were provided by the MC2 cleanroom facility at Chalmers University of Technology. A Dow Corning Sylgard 184 PDMS kit was obtained from GA Lindberg (Göteborg, Sweden). Dichlorodimethylsilane, fluorescein disodium salt, and hexamine ruthenium(III) chloride were obtained from Sigma–Aldrich. Soy bean polar extract (SPE) (which contained 22.1% phosphatidylethanolamine, 18.4% phosphatidylinositol, 45.7% phosphatidylcholine, and 6.9% phosphatidic acid, with other compounds comprising the remaining 6.9%) was obtained from Avanti Polar Lipids, Inc. (Alabaster, AL). Texas Red DHPE was obtained from Invitrogen. All solutions used in the study were prepared in Milli-Q grade deionized water. Polytetrafluoroethylene (PTFE) tubing was obtained from VWR Scientific. External valves (Pneumadyne, Inc.) for pneumatic control were ordered from H&H Export Inc. (Duluth, MN). All other electronic components were ordered from the Swedish companies ELFA A.B. or Farnell A.B.

Fabrication of the Microfluidic Chip. All molds for replica molding were prepared in the ISO100 cleanroom facility MC2 at Chalmers University of Technology, whereas PDMS casting and curing was conducted in an ambient environment in a standard laboratory. The layout was designed using Autodesk AutoCAD 2008 software (see Figure 2a). Mixing channels were designed to be 37 mm long, and the total length of all flow paths was 126.9(1.4) mm. Patterns for each layer were transferred to the E-beam lithography system (Model JBX-9300FS, JEOL, Tokyo, Japan) and written to chromium-coated soda-lime glass masks. Wafers were treated before use by means of an oxygen plasma in the Tepla 300PC microwave plasma processor (1 mbar, 250 W for 1 min, O_2 gas flow = 400 sccm). Resists were exposed on a Karl Süss MA6 contact mask aligner (G-line, 5–6 mW/cm²). For the control channel mold, SU8-10 was spin-coated at 2000 rpm for 30 s, soft baked at 65 °C for 2 min, ramped to 95 °C, baked 5 min (all on a hot plate) and left to cool to room temperature (RT). Subsequently, the wafers were exposed with 5 mW/cm² ultraviolet (UV) light for 40 s through a dark-field mask, post-baked for 1 min at 65 °C, ramped to 95 °C, baked for 2 min, and finally left to cool to RT. The resist was developed in SU8 developer for 3 min, rinsed with developer, and washed in deionized water (DIW). The mold then was blow-dried and cleaned in oxygen plasma (50 W, 250 mTorr, 1 min). The flow channel mold was fabricated using the positive photoresist

(14) Squires, T. M.; Quake, S. R. *Rev. Mod. Phys.* **2005**, *77*, 977–1026.

(15) Unger, M. A.; Chou, H. P.; Thorsen, T.; Scherer, A.; Quake, S. R. *Science* **2000**, *288*, 113–116.

(16) Sackmann, E. *Science* **1996**, *271*, 43–48.

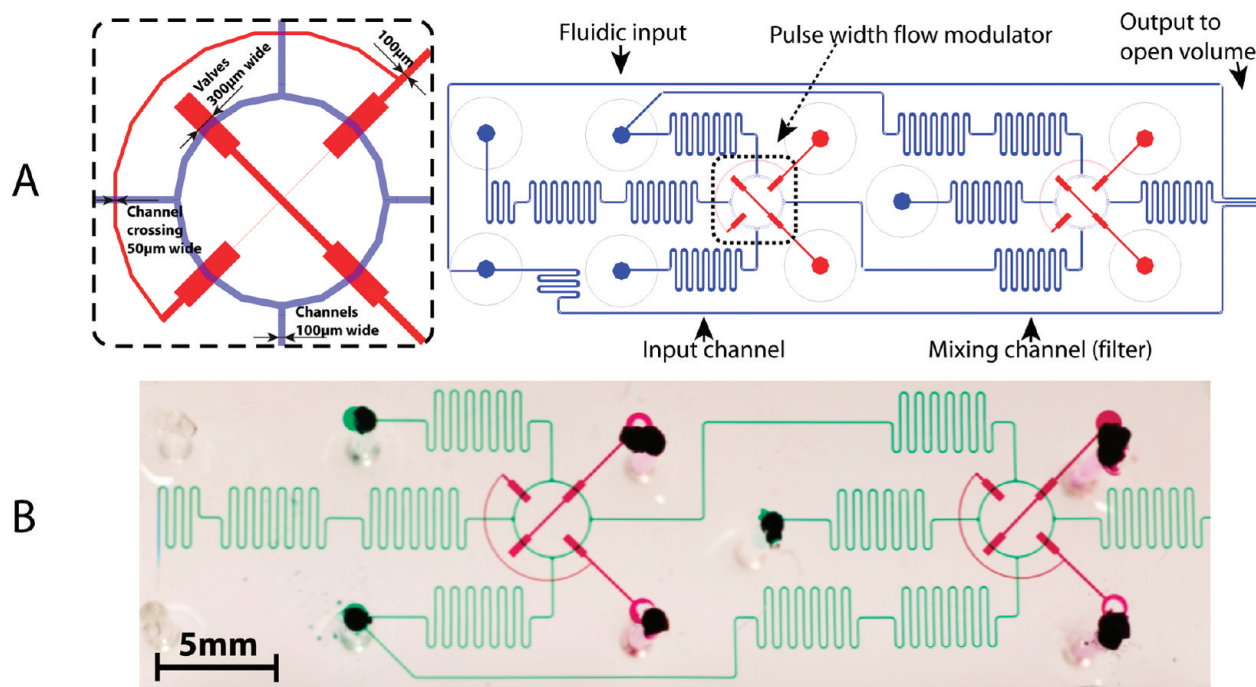


Figure 2. (A) Schematic layout and (B) photograph of the microfluidic two-stage diluter. Flow channels are blue, control channels are red, and interface holes are surrounded by black circles. In the photograph, the control channels are filled with a red dye solution, and the flow channels are filled with a green dye solution.

AZ4562. First, HDMS primer was applied to the wafer to remove water traces on the surface (a reaction time of 2 min, followed by the removal of liquid with spin-coating). The photoresist then was spin-coated onto the wafer at 1500 rpm for 30 s and baked for 3 min at 100 °C (hot plate), followed by the deposition of another resist layer, which was applied using the same procedure. Baking was continued for 1 h afterward. After cooling to RT, the resist was exposed through a bright-field mask for 11 min and developed in a AZ351:water (1:4) mixture for ~40 min (visual inspection until completeness); thereafter, the mold was rinsed with water and blow-dried. Finally, both molds were hard-baked at 200 °C (air circulation oven) for 30 min, with slow heating and cooling. The geometries of the molds were characterized with an Olympus Model MX40 microscope and a Tencor AS500 stylus profiler (the control and flow channel heights were 15 and 22.5 μm , respectively). Before use, the molds were anti-adhesion-treated with dichlorodimethylsilane by exposing the surfaces to the vapors under a Petri dish cover for 5 min. PDMS prepolymer was prepared by mixing parts A and B in a 10:1 ratio and degassed for 15 min in a desiccator. Subsequently, the flow channel mold was used to cast a 10-mm-thick PDMS slab, where fluid inputs were defined by syringe needles. To prepare the control channel membrane, PDMS was spin-coated onto the control channel mold at 1500 rpm for 60 s. Both PDMS structures were cured at 95 °C (using an air circulation oven) for 1 h. Thereafter the chip was assembled using oxygen plasma bonding in a Plasma Therm Batchtop PE/RIE at 250 mTorr, 85 W, 10 sccm O_2 for 10 s. Initially, the bottom surface of the thick PDMS slab and the thin PDMS membrane, which still adhered to the wafer, were treated, aligned, and bonded at 95 °C (in an air circulation oven) for 1 h. The composite then was peeled off, plasma-treated, and bonded with a glass

microscope coverslip. Finally, the chip was left to complete bonding overnight, reproducibly yielding a functional device.

Characterization Setup. Figure 3 shows the characterization setup. A liquid flow and control interface was assembled from syringe needles and 0.8-mm-ID PTFE tubing. This interface was proven to be leak-proof at pressures up to 4 bar. Liquids were stored in test tubes and pressure-driven to the chip. Pressures were controlled by reducers, and values were measured with a Pascolo EEx digital manometer (Keller AG). Control channels were filled with water to avoid air diffusion through the membrane and bubble formation. The valve control pressure was 3 bar (relative to ambient pressure). Control channel pressures were operated by solenoid valves (Pneumadyne, Inc.), which were accurately controlled (the time resolution of signals was 1 ms) by an electronic module, based on PIC18F1220 (Microchip, Inc.) and the interface through the COM port to a personal computer (PC).

The performance of the two diluter stages was evaluated by two different means: an indirect procedure (fluorescence intensity of a dye solution passing through the system) and a direct procedure (electrochemical detection of a redox active compound at the channel exit).

Diluter Characterization by Fluorescence Microscopy Imaging. One set of characterization experiments was performed with a Leica Model DM IRB fluorescence microscope. The substrate tube was loaded with a 1 mM fluorescein disodium salt solution in Milli-Q water. Measurements were performed on different pressures and pulsing frequencies. In the investigated dilution range (10 μM –1 mM), the fluorescence intensity was determined to be linearly dependent on fluorescein concentration (higher concentrations might yield quenching or reabsorption). The fluorescence intensity was determined from snapshots taken with a Nikon D200 digital SLR camera at ISO100 in the RAW

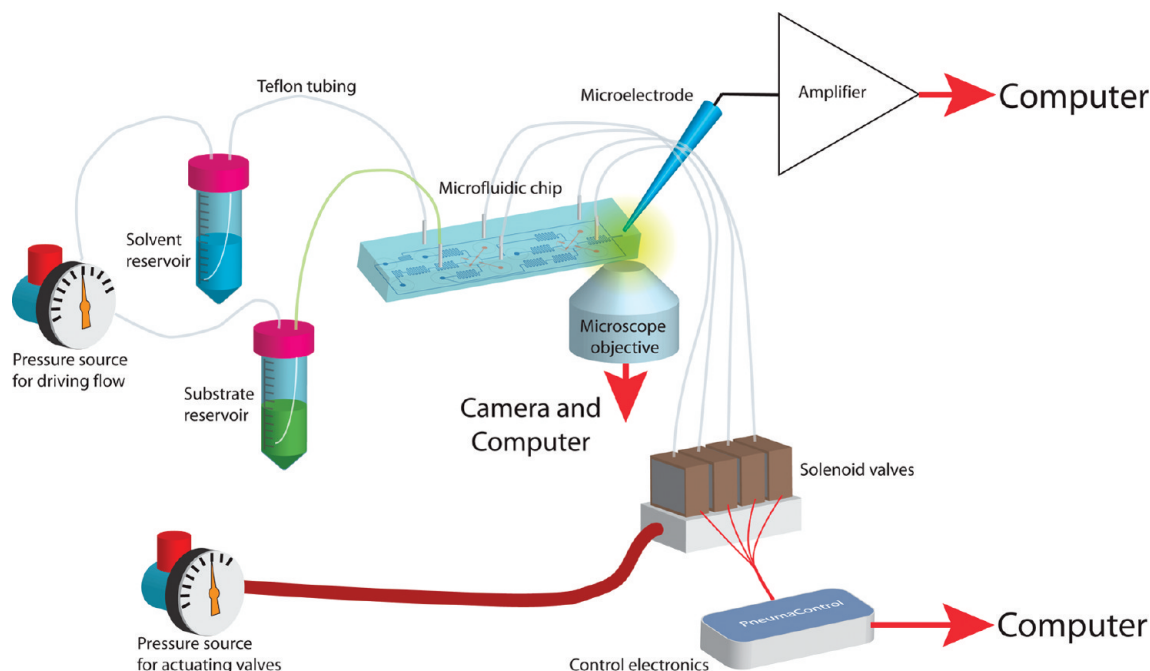


Figure 3. Experimental setup for the liquid supply, pneumatics, valve control, and electrochemical/optical characterization.

format. Because the profile of the channel is parabolic, a square polynomial fit was applied, which yielded accurate concentration values. Time-resolved properties were evaluated from recordings with the MotionPro HS-4 (RedLake Inc.) high-speed camera with adjustable frame rates up to 5000 fps.

Electrochemical Characterization. For direct electrochemical characterization of the diluter performance, the solvent tube was loaded with a buffer solution (25 mM KH_2PO_4 , 25 mM K_2HPO_4 , 1 M KCl) and the substrate tube was loaded with 10 mM hexamine ruthenium(III) chloride in the same buffer. Buffered solutions are generally required for electrophysiological studies and bioassays; therefore, the medium was chosen in the characterization. In the procedure, a carbon fiber microelectrode (ProCFE, Degan Corp., Minneapolis, MN) was positioned with a micromanipulator in the open volume in front of the diluter outlet. A platinum wire was used as a counter electrode, which also was immersed in the open volume. A cyclic voltammogram was recorded with a polarographic analyzer (Model POL150, Radiometer Analytical SAS), using a two-electrode setup in the potential range from -700 mV to -200 mV. After baseline subtraction, the saturation current was determined. The saturation current is a function of the flow speed and is proportional to solution concentration; because the flow speed was kept constant, the relative change in concentration could be monitored.

Data Fitting and Modeling. Data fitting and modeling was performed with MATLAB 7.6.0 software (MathWorks, Inc., Natick, MA). The mixing model was based on the analytical expression that defined the solution concentration in the channel at a distance x from the channel beginning at time moment t .¹¹

$$c(x, t) = \alpha + \sum_{n=1}^{\infty} \frac{2\sin(\alpha\pi n)}{\pi n} \times \text{Re}\left\{\exp\left[\frac{1}{2}(Pe - \sqrt{Pe^2 + 8\pi n Pe i})\left(\frac{x}{L}\right)\right] \exp\left[2\pi n\left(\frac{t}{T}\right)i\right]\right\} \quad (2)$$

where $\alpha \in [0, 1]$ is the PWFDM duty cycle, Pe the Peclet number ($Pe = v^2T/D_{\text{effective}}$, v the mean velocity, T the pulsing period, L the characteristic length scale ($L = vT$), and $D_{\text{effective}}$ the dispersion along the flow direction (as defined by eq 1). Concentration fluctuations were extracted from movies recorded at different points along the channel.

The deformation of the PDMS channels that results from pressure application was modeled with the COMSOL Femlab Structural Mechanics module at the following elastic modulus range: 750 kPa–3 MPa (specification by Dow Corning).

Lipid Spreading Experiment. For studies on lipid film spreading, the glass surface near the chip outlet was covered with an 80-nm-thick layer of silicon dioxide (SiO_2), using reactive sputtering on a FHR MS 150 system, (FHR Anlagenbau GmbH, Germany). The giant multilamellar lipid vesicles were prepared using a modified dehydration–rehydration technique, as described previously.^{17,18} For visualization, lipids from soy bean polar extract were stained with Texas Red DHPE (1%). Three microliters ($3 \mu\text{L}$) of a solution that contained small unilamellar vesicles was placed on a borosilicate coverslip and dehydrated in a vacuum desiccator for 15 min. The dry lipid film was then rehydrated with buffer solution (HEPES), which led to the formation of giant multilamellar vesicles. All buffers and liquids for the lipid spreading study were prepared based on the bivalent metal-ion-free HEPES buffer that contained HEPES (10 mM) and NaCl (100 mM) at pH 7.8.

The solvent reservoir on the PWFDM chip was loaded with pure buffer and the substrate reservoir with 1 mM CaCl_2 solution, dissolved in the same buffer. The substrate solution was stained with fluorescein solution ($10 \mu\text{M}$) for simultaneous monitoring of the dilution process. At the beginning of the experiment, the fluid flow from the chip was closed and a buffer that

(17) Karlsson, M.; Nollkrantz, K.; Davidson, M. J.; Stromberg, A.; Ryttsen, F.; Akerman, B.; Orwar, O. *Anal. Chem.* **2000**, *72*, 5857–5862.

(18) Karlsson, M.; Sott, K.; Cans, A. S.; Karlsson, A.; Karlsson, R.; Orwar, O. *Langmuir* **2001**, *17*, 6754–6758.

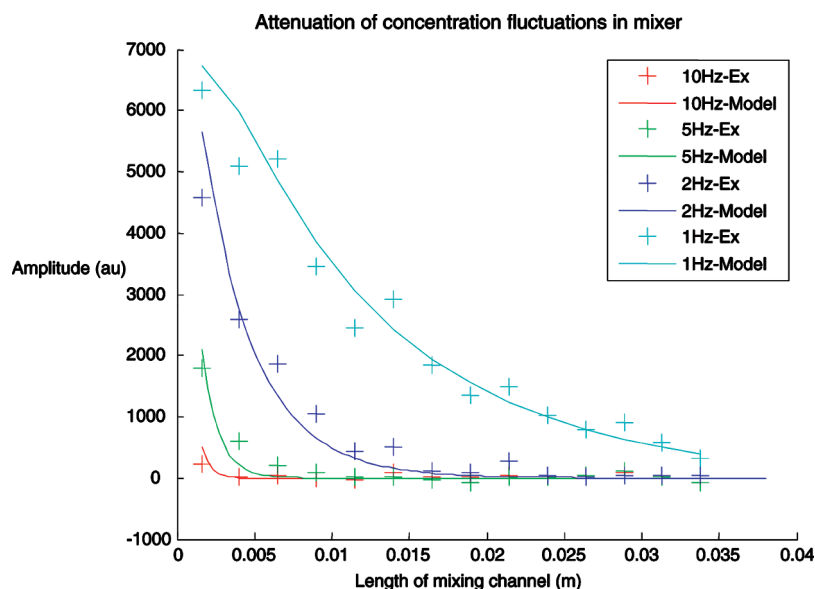


Figure 4. Attenuation of concentration fluctuation of a fluorescent dye (fluorescein) solution measured at different mixer lengths and pulsing frequencies (duty cycle = 0.5 and pressure = 0.5 bar). All data points are measured with a high-speed camera. Each solid line represents the respective simulated result.

contained suspended multilamellar vesicles was applied as a droplet near the mixer channel outlet. Vesicles were left to settle on the surface for 10 min and the experiment was started. The spreading response of the lipid reservoir (multilamellar vesicle) to stimuli of different Ca^{2+} concentrations was monitored and recorded under a Leica DM IRE2 confocal scanning microscope that was equipped with a Leica TCS SL scanner (Leica AG, Wetzlar, Germany). The following excitation/emission wavelengths/ranges were used: 595/610–645 nm for the lipid films (Texas Red) and 488/500–540 nm for fluorescein. Because of only minor spectral overlap, both signals can be easily separated from each other.

RESULTS AND DISCUSSION

Mixing Channel. Because the mixing channel is one of the major components of the device, it was more thoroughly characterized. The diffusion coefficient of fluorescein is $D = 1.8 \times 10^{-9} \text{ m}^2/\text{s}$.¹⁹ Maximum–minimum amplitude fluctuations were measured as a function of distance from the multiplexer junction. After normalization, the theoretical values simulated with eq 2, and the experimentally measured values agreed very well (see Figure 4).

The flow speed in the channel was evaluated with a high-speed camera, which was triggered by the valve controller. The intensity was measured at the end of the mixer channel. Because the length is known, the mean flow velocity could be evaluated. The mixer response (see Figure 5) was separated into two components: the translation of a step function and the smoothing of the sharp boundary due to dispersion. The translation time is inversely proportional to the driving pressure (see Figure S1 in the Supporting Information), and the dispersion can be well described as diffusion spreading (see Figure S2 in the Supporting Information), where the effective diffusion coefficient is expressed by eq 1. Moreover, we have observed that the fluorescence intensity of a fluorescein solution flowing through the system is dependent

on the driving pressure. The intensity change can be attributed to two physical reasons: pressure-induced expansion of (soft) PDMS channels^{20,21} and/or the growing rate of replacement of photobleached dye by flow. Measurements made in different locations of the chip suggest that the large intensity change at low pressures is due to the replacement of bleached fluorescein, because this effect is observed similarly over the entire chip, thus being not dependent on pressure at a particular point. The linear pressure–intensity relationship at higher pressure values, on the other hand, is dependent on the particular observation point along the channel and therefore is due to localized pressure and channel deformation. Channel deformation ($\sim 9 \mu\text{m}/\text{bar}$) agrees also well with the COMSOL simulation at a Young's modulus of 1.1 MPa, which is in the range specified by the manufacturer (Dow Corning). Because of the channel deflections, it is important to design circuitry in a highly symmetric fashion to maintain the same flow and pressure distribution at different switched states.

Performance. In concentration measurement, at output, the intensity was measured at the outlet with high precision, because, statistically, data were collected over a large ensemble (RAW format picture). However, the observed relationship between intensity and duty cycle was not linear, which can be due to unbalanced hydraulic input resistances. After accounting for those differences, the model still did not yield an acceptable improvement. An improved fit was yielded only after the valve response time was added to the model, which can be expressed as

$$c(x) = c_0 \left[\frac{a(x + \Delta x)}{1 + x(a - 1) + \Delta x(a + 1)} \right] \quad (3)$$

where x is the duty cycle, a the ratio between the flow resistances of two inputs, and Δx the ratio of valve response time and full pulsing period ($\Delta x = \tau/T$). The valve response time describes

(19) Huiqian, Y.; Nguyen, N. T.; Huang, X. Y. *J. Phys.: Conf. Ser. (Int. MEMS Conf.)* **2006**, *34*, 136–141.

(20) Holden, M. A.; Kumar, S.; Beskok, A.; Cremer, P. S. *J. Micromech. Microeng.* **2003**, *13*, 412–418.

(21) Gervais, T.; El-Ali, J.; Gunther, A.; Jensen, K. F. *Lab Chip* **2006**, *6*, 500–507.

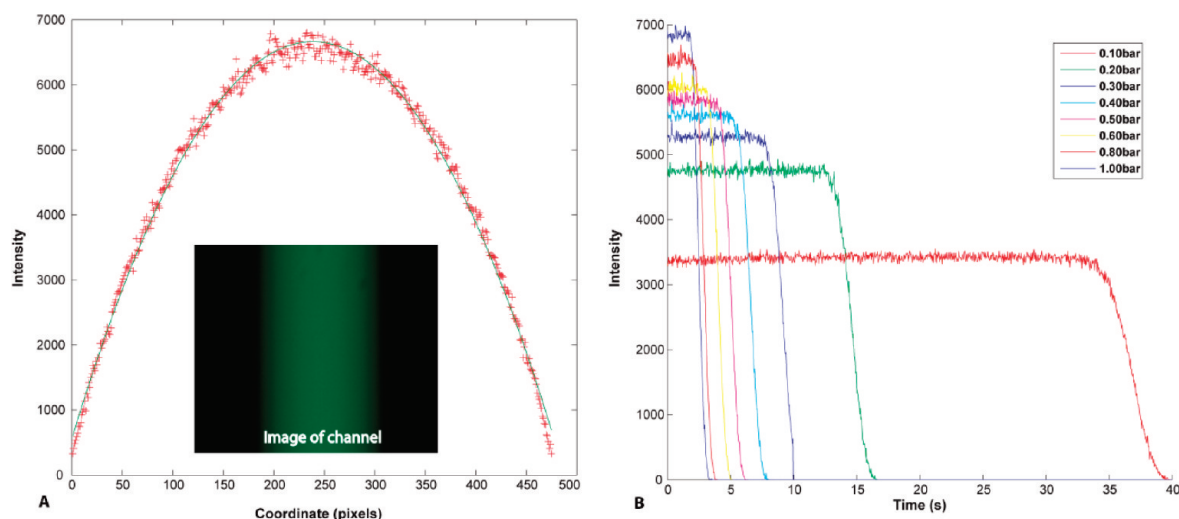


Figure 5. (A) The channel photographed through an inverted microscope. The dependence of the fluorescence intensity on the pixel coordinate can be fitted to a parabola, because of the parabolic cross section of the actual PDMS channel. (B) The response of the mixer channel to the fluorescein concentration step function measured at a distance of 40 mm from the multiplexer under different flow pressures. The flow is multiplexed at the time moment zero, and the intensity is recorded at the other end of the channel.

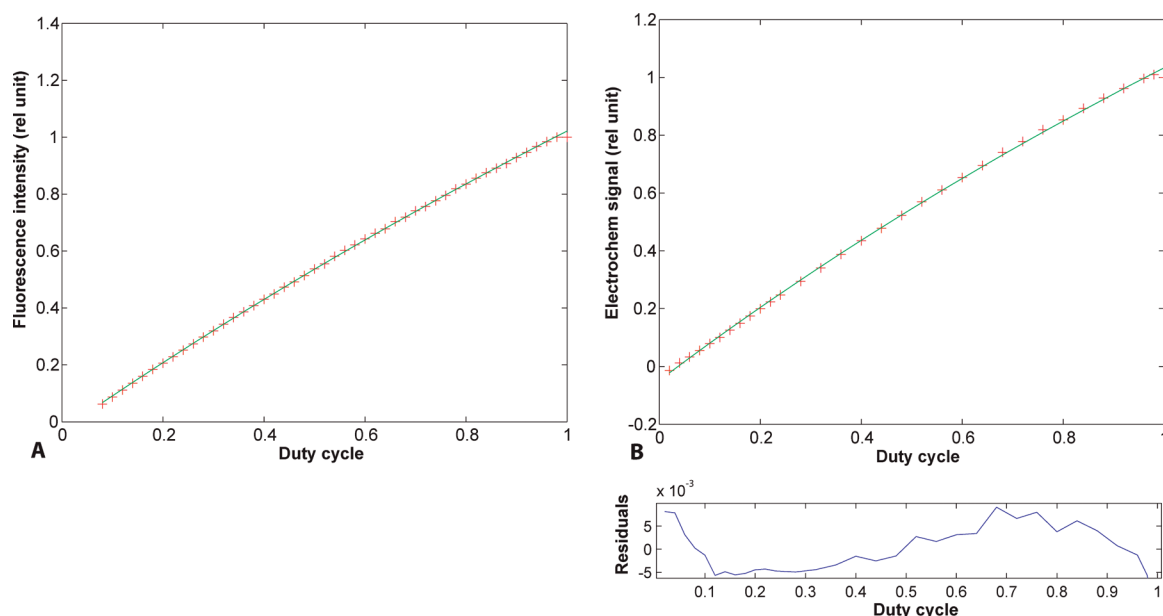


Figure 6. (A) Fluorescein concentration measured as the dependence of fluorescence intensity on the duty cycle of the two-stage diluter. Crosses represent experimental data and the line shows the fitted model. (B) Electrochemical measurement of the concentration up to 100-fold dilution.

how much the chemical pulse length differs from the electronic control pulse length. Introducing this parameter into the model yielded an excellent fit (see Figure 6a), with a maximum evaluated value of χ^2 of 0.201 per degree of freedom, which indicates the adequacy of the model. At duty cycles of >0.2 , the deviation of all experimental points from the model was $<1\%$; at duty cycle values between 0.1 and 0.2, the differences were $<5\%$. Fitted parameters were determined to be $a = 1.1562$, $\Delta x = -0.0240$, which means that the difference between input resistances is $\sim 16\%$ and the valve response time is 12 ms (with a full period of 500 ms). The high-speed camera revealed that the maximum frequency where the valve can open and close is 80 Hz, which agrees well with the 12-ms response time.

Because fluorescence measurements became too difficult to perform at high dilution ratios, we used an electrochemical

technique instead, which yielded a slightly different resistance ratio ($a = 1.16$, in the case of fluorescence measurement, and $a = 1.20$ for electrochemical case), but otherwise comparable results. These results are depicted in Figure 6b.

Ca²⁺-Induced Phospholipid Spreading on SiO₂. We applied the diluter to investigate lipid bilayer formation and spreading²² in the presence of Ca²⁺ ions^{23,24} held at different concentrations. Anionic lipids spread on SiO₂ surfaces only if Ca²⁺ ions are present,²⁵ because of Ca²⁺ ions bridging between negatively charged lipid head groups and the silica surface (also

(22) Radler, J.; Strey, H.; Sackmann, E. *Langmuir* **1995**, *11*, 4539–4548.

(23) Reviakine, I.; Simon, A.; Brisson, A. *Langmuir* **2000**, *16*, 1473–1477.

(24) Sinn, C. G.; Antonietti, M.; Dimova, R. *Colloid Surf. A* **2006**, *282*, 410–419.

(25) Stelzle, M.; Weissmuller, G.; Sackmann, E. *J. Phys. Chem.* **1993**, *97*, 2974–2981.

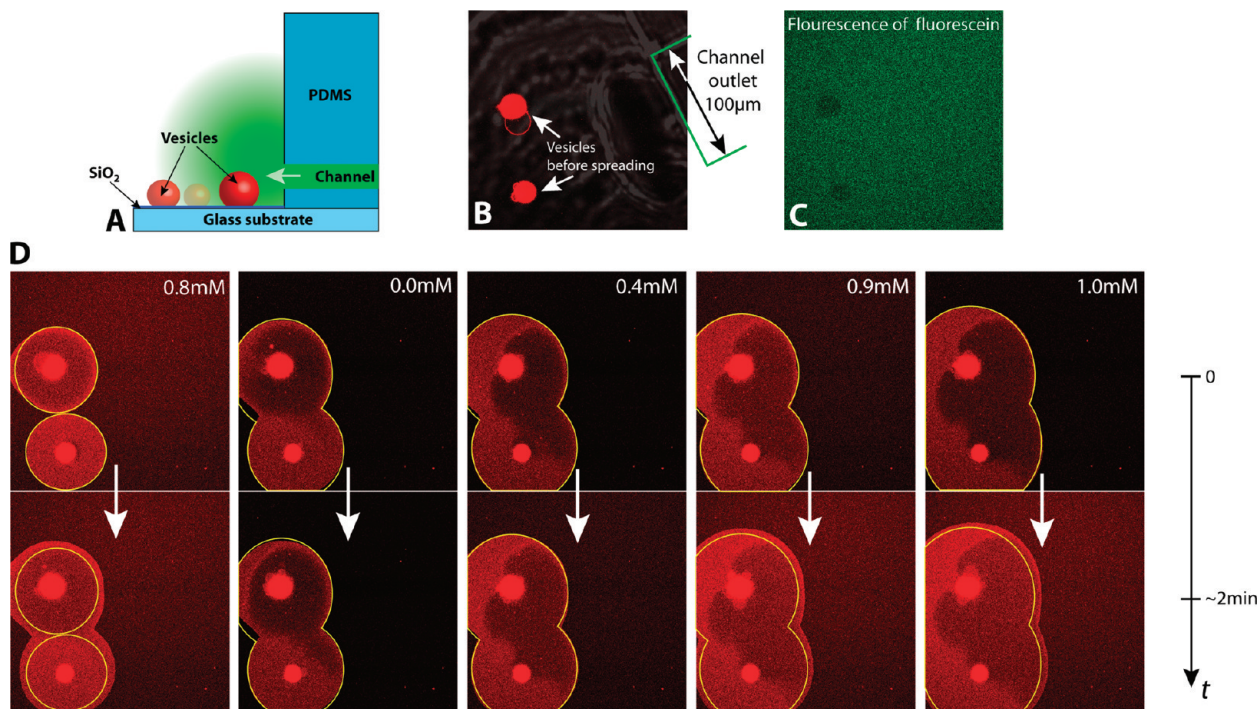


Figure 7. Dependence of lipid bilayer spreading on the Ca^{2+} concentration surrounding a lipid reservoir (multilamellar phospholipids vesicle). (A) Schematics of the experimental setup with vesicles in front of the open volume channel outlet. (B) Lipid vesicles in front of the channel outlet before reaching the effective concentration for spreading. (C) A trace of fluorescein enables simultaneous monitoring of substrate concentration, i.e. proper function of the PWFMC chip. The dark spots are the multilamellar vesicles, which have no affinity for the fluorescein. The image confirms that the area around the vesicle is homogeneously filled by the solution exiting the mixer channel. **D.** A series of spreading experiments: images in the upper row are corresponding to the lipid films at the beginning of the experiment, and in the lower row after two minutes at the end of the experiment, respectively. Yellow contours around lipid layers are added to visualize the extension of the spreading areas. The contours are of identical size in each pair of images.

negatively charged at neutral pH). Using traditional experimental techniques, such spreading experiments are quite laborious to perform, because every experiment with a given Ca^{2+} ion concentration would require replacement of a back-filled micropipet. Even conventional microfluidic solution exchangers, which are typically multichannel constant flow devices, do not easily allow for controlled initiation of spreading. Here, the Ca^{2+} concentration around lipid vesicles was controlled and the spreading behavior was monitored under a confocal microscope. Initially, in a single experiment with a duration of <30 min, we exposed the vesicles with a concentration range from 0.01 mM to 1 mM to determine the effective ion concentration (EC) of Ca^{2+} needed to induce film formation and spreading. This concentration was determined to be 0.6 mM. The onset of spreading was reliably observed within the chosen concentration step size of 0.1 mM. Thereafter, spreading experiments that were 2 min long were conducted (see Figure 7). Initially, we recorded the spreading at 0.8 mM Ca^{2+} , then reduced the concentration to 0.0 mM (pure buffer), which instantly stopped further spreading. When the concentration was increased to 0.4 mM, spreading was still almost imperceptible, while it increased rapidly when the Ca^{2+} concentration exceeded the effective limit at 1.0 mM.

In summary, this study demonstrates that the PWFMC microfluidic diluter is a versatile tool for studying a variety of concentration-dependent processes, such as controlling molecular film formation, which can eventually be combined with surface-based,

two-dimensional (2D) microfluidic systems.²⁶ Besides spreading, fine-tuning of the metal-ion concentration could be used to attach and release proteins to/from engineered lipid surfaces.²⁷ These techniques hold promise for applications in biosensor devices, bioelectronics or tools for molecular self-assembly, membrane protein studies, and fundamental biomembrane science.^{16,28–30}

CONCLUSION

We have shown that serial pulse-width flow modulation (PWFMC) stages are suitable for the design of fast and accurate dilution modules for microfluidic chips. It is favorable because of the easy control and compactness. To achieve higher dilutions than the 10-fold dilutions demonstrated herein, multiple PWFMC modules can be connected in series. Because of the currently unavoidable deformation of PDMS channels, it is suggested to use a highly symmetrical design to ensure constant pressure and flow distribution over time. The linearity of the device is determined by the equality of flow resistances of both channels. Microfabrication with resist-based molds, following slightly adapted literature procedures yielded a geometrical channel height variance of 7% (22.9(16) μm), which corresponds to a hydraulic

(26) Czolkos, I.; Erkan, Y.; Dommersnes, P.; Jesorka, A.; Orwar, O. *Nano Lett.* **2007**, *7*, 1980–1984.

(27) Schmitt, L.; Dietrich, C.; Tampe, R. *J. Am. Chem. Soc.* **1994**, *116*, 8485–8491.

(28) Nikolelis, D. P.; Hianik, T.; Krull, U. J. *Electroanal.* **1999**, *11*, 7–15.

(29) Oberholzer, T.; Luisi, P. L. *J. Biol. Phys.* **2002**, *28*, 733–744.

(30) Nissen, J.; Gritsch, S.; Wiegand, G.; Radler, J. O. *Eur. Phys. J. B* **1999**, *10*, 335–344.

resistance variance of $\sim 20\%$, because resistance is proportional to the third power of channel height. Therefore, the calibration of devices fabricated with different molds is required but are acceptable when compared to the high cost and equipment demands of molds fabricated from multilayered wafers. During the study, we have experimentally determined a set of valid rules that can be used to design microfluidic diluters at relatively low-cost and equipment complexity. Pulsing frequencies, channel lengths, and flow pressures must be chosen appropriately to meet the required properties of the diluter. The relationship between concentration (determined as fluorescence intensity and as electrochemically determined saturation current in a $\text{Ru}^{2+/3+}$ redox system) and a PWFDM duty cycle was determined to be strongly dependent on the valve response time, which must be taken into consideration when implementing a design. In conclusion, we have established that serialization of PWFDM diluter stages can be achieved with moderate complexity. All relevant performance parameters have been identified and adequately described for easy implementation. The device presented here is readily applicable as a building block in microfluidic analytical instrumentation, e.g., applications where the solution environment around a microscopic or nanoscopic sensor is desired to be automatically and systematically

changed over a wide concentration range (for example, in electrophysiology or single-cell studies aimed at obtaining binding isotherms, EC_{50} values, and kinetic information (e.g., on ion channels, enzymes, and receptors)). We applied the dilution chip to investigate Ca^{2+} -stimulated lipid membrane formation by spreading, in particular, to rapidly determine the lowest effective concentration of 0.6 mM, and we demonstrated that spreading of an anionic phospholipid bilayer membrane on SiO_2 can be reversibly controlled by modulating the Ca^{2+} concentration in the buffer surrounding the lipid reservoir.

ACKNOWLEDGMENT

The authors thank Ann-Sofie Cans for helpful discussions about electrochemical measurements and the Swedish Strategic Research Foundation (SSF) for financial support.

SUPPORTING INFORMATION AVAILABLE

This material is available free of charge via the Internet at <http://pubs.acs.org>.

Received for review May 8, 2009. Accepted May 11, 2009.
AC9010028

Supplementary information

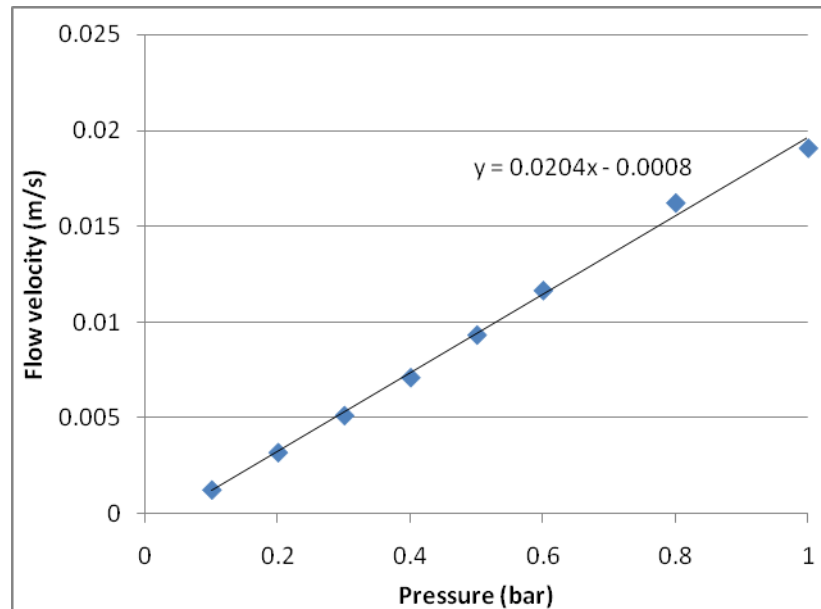


Figure S1. Mean flow velocity in channel measured under different flow pressures. Linear relation between pressure and flow velocity can be observed.

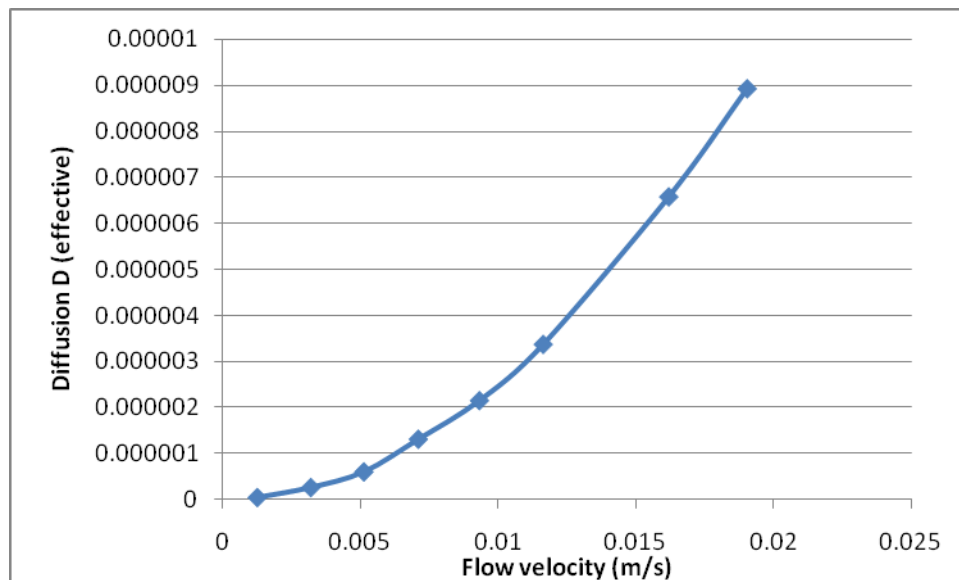
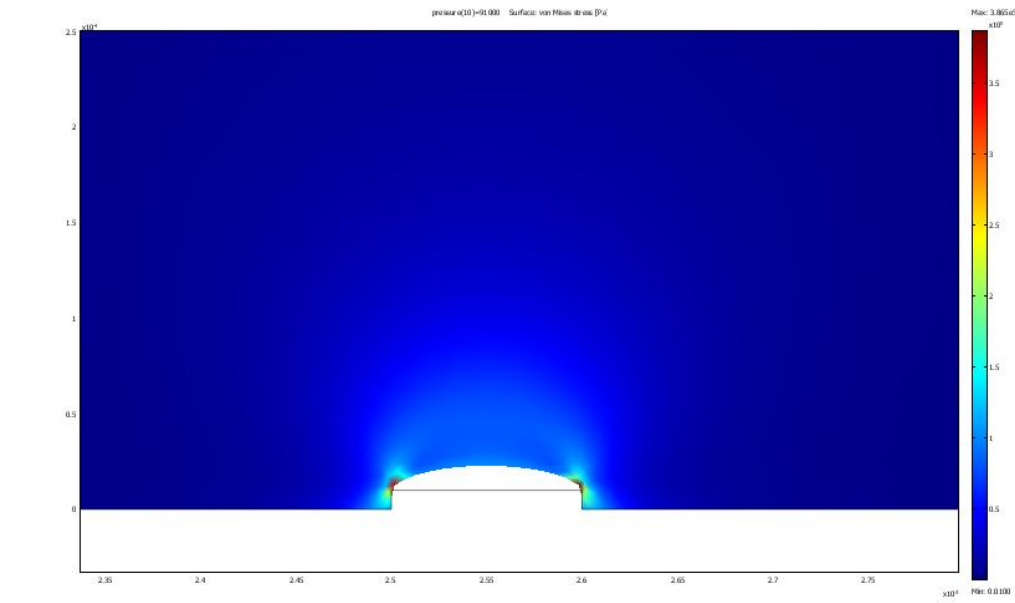
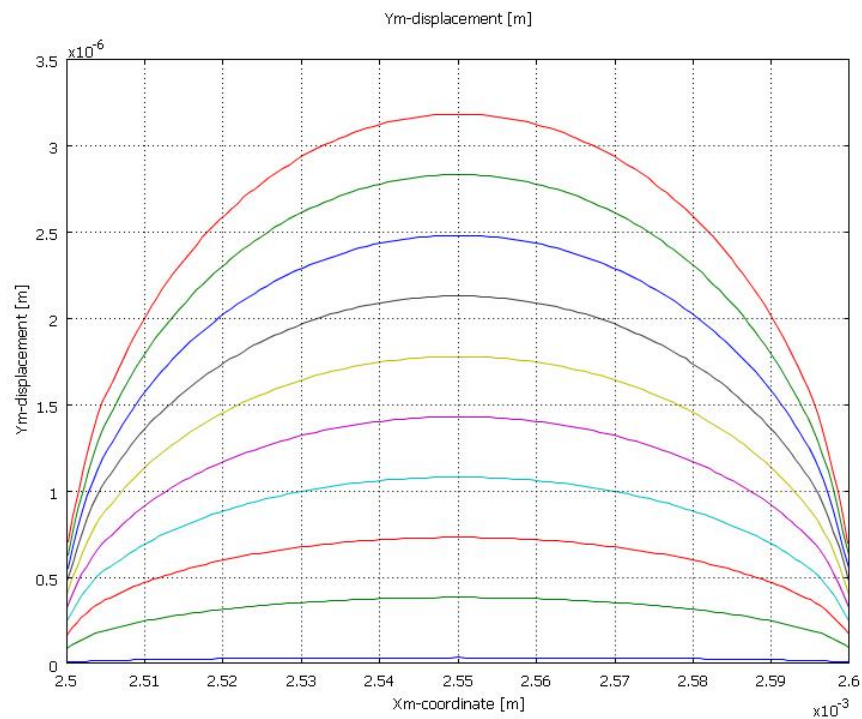


Figure S2. Effective diffusion coefficient measured from spreading of sharp concentration step during flow. Diffusion coefficient is proportional to square of mean velocity of flow, which is coherent with theoretical predictions (Equation 1)



A



B

Figure S3. COMSOL modeling of channel deformation under pressure. (Elastic modulus of PDMS 3MPa). **A)** Deformation of 100 μ m wide and 10 μ m high rectangular channel made in 5mm thick PDMS under pressure 1bar. **B)** Deformation of the ceiling of the channel under pressures 0.1bar to 1bar with 0.1bar step.

PAPER

II

A Microfluidic Pipette for Single-Cell Pharmacology

Alar Ainla, Erik T. Jansson, Natalia Stepanyants, Owe Orwar, and Aldo Jesorka*

Department of Chemical and Biological Engineering, Chalmers University of Technology, Kemivägen 10, SE-412 96 Göteborg, Sweden

We report on a free-standing microfluidic pipette made in poly(dimethylsiloxane) having a circulating liquid tip that generates a self-confining volume in front of the outlet channels. The method is flexible and scalable as the geometry and the size of the recirculation zone is defined by pressure, channel number, and geometry. The pipette is capable of carrying out a variety of complex fluid processing operations, such as mixing, multiplexing, or gradient generation at selected cells in cell and tissue cultures. Using an uptake assay, we show that it is possible to generate dose–response curves in situ from adherent Chinese hamster ovary cells expressing proton-activated human transient receptor potential vanilloid (hTRPV1) receptors. Using confined superfusion and cell stimulation, we could activate hTRPV1 receptors in single cells, measure the response by a patch-clamp pipette, and induce membrane bleb formation by exposing selected groups of cells to formaldehyde/dithiothreitol-containing solutions, respectively. In short, the microfluidic pipette allows for complex, contamination-free multiple-compound delivery for pharmacological screening of intact adherent cells.

A great number of methods for the probing and manipulation of the biochemical and physical properties of individual cells have emerged during the past few years.^{1,2} Single-cell studies may offer significant advantages compared to traditional biotechnological or bioanalytical methods^{2–5} because cellular and subcellular processes are revealed in greater detail and discrete and dynamic events are directly observable. Furthermore, single-cell methods may preserve the individuality of targeted subpopulations and reduce or eliminate artifacts arising from the averaging of measurements.³

In contrast, methods that can control the chemical environment around single intact cells in tissue or cell cultures are scarce but important because it would be of great interest to, for example, be able to obtain dose–response curves in situ in selected cells. In general, if dynamic and precise chemical stimulation protocols

can be applied to adherent cells displaying the native heterogeneity of receptor distributions, it would be a great advantage compared to today's superfusion techniques. So far, glass micropipettes have been indispensable tools in single-cell manipulations.^{6,7} If exposure to a chemical stimulus is desired, a glass micropipette can be used to deliver the active compound into the vicinity of the cell. However, glass pipettes are not suitable for maintaining localized superfusion because of the spreading of the active substrate outside the experimental region.

Recently, several new concepts to deliver small amounts of liquid to microscopic objects of interest have been reported. Examples include the chemistode,⁸ which uses a microfluidic flow cell to transport aqueous droplets in oil onto an area of interest. The microfluidic droplet dispenser for MALDI sample spotting,⁹ a concept utilizing slot pins for spatially defined reagent delivery to cells,¹⁰ flow photolysis,¹¹ and microsources positioned by optical tweezers¹² are other recent developments devised to control confined chemical environments. Another related concept is the silicon-based multipurpose microfluidic probe,¹³ where two channels generate a recirculating flow in a thin gap between the substrate and probe. However, practical use of this device is severely limited by complicated hard-material fabrication, positioning constraints of the coplanar layout, incompatibility of opaque silicon with bright-field microscopy, and inability to simultaneously apply other probing devices, such as a patch-clamp pipette, microelectrodes, or optical fibers.

Ideally, a pipette should allow for contamination-free, consecutive injections of different substrates or concentrations without the need to exchange the pipette needle. The pipette should be able to address individual cells, parts of adherent cells, individual cells within a tissue slice, or a primary cell culture. There are plenty of microfluidic devices that are based on the concept that the cell is brought to the device.^{14,15} In these situations, cells are detached from a surface using pipettes, thereby losing their spatial organization (i.e., retraction of dendrites and axons; all

* To whom correspondence should be addressed. Phone: +46 31 772 6112. Fax: +46 31 772 6120. E-mail: aldo@chalmers.se.

(1) Anselmetti, D. *Single Cell Analysis: Technologies and Applications*; Wiley-VCH Verlag GmbH: Weinheim, Germany, 2009.
(2) Brehm-Stecher, B. F.; Johnson, E. A. *Microbiol. Mol. Biol. Rev.* **2004**, *68*, 538.
(3) Niepel, M.; Spencer, S. L.; Sorger, P. K. *Curr. Opin. Chem. Biol.* **2009**, *13*, 556–561.
(4) Raser, J. M.; O'Shea, E. K. *Science* **2005**, *309*, 2010–2013.
(5) Perlman, Z. E.; Slack, M. D.; Feng, Y.; Mitchison, T. J.; Wu, L. F.; Altschuler, S. J. *Science* **2004**, *306*, 1194–1198.

(6) Ling, G.; Gerard, R. W. *J. Cell. Comp. Physiol.* **1949**, *34*, 383–396.
(7) Neher, E.; Sakmann, B. *Nature* **1976**, *260*, 799–802.
(8) Chen, D.; Du, W. B.; Liu, Y.; Liu, W. S.; Kuznetsov, A.; Mendez, F. E.; Philipson, L. H.; Ismagilov, R. F. *Proc. Natl. Acad. Sci. U.S.A.* **2008**, *105*, 16848–16843.
(9) Wang, J. B.; Zhou, Y.; Qiu, H. W.; Huang, H.; Sun, C. H.; Xi, J. Z.; Huang, Y. Y. *Lab Chip* **2009**, *9*, 1831–1835.
(10) Tavana, H.; Jovic, A.; Mosadegh, B.; Lee, Q. Y.; Liu, X.; Luker, K. E.; Luker, G. D.; Weiss, S. J.; Takayama, S. *Nat. Mater.* **2009**, *8*, 736–741.
(11) Beta, C.; Wyatt, D.; Rappel, W. J.; Bodenschatz, E. *Anal. Chem.* **2007**, *79*, 3940–3944.
(12) Kress, H.; Park, J. G.; Mejean, C. O.; Forster, J. D.; Park, J.; Walse, S. S.; Zhang, Y.; Wu, D. Q.; Weiner, O. D.; Fahmy, T. M.; Dufresne, E. R. *Nat. Methods* **2009**, *6*, 905–U963.
(13) Juncker, D.; Schmid, H.; Delamarche, E. *Nat. Mater.* **2005**, *4*, 622–628.

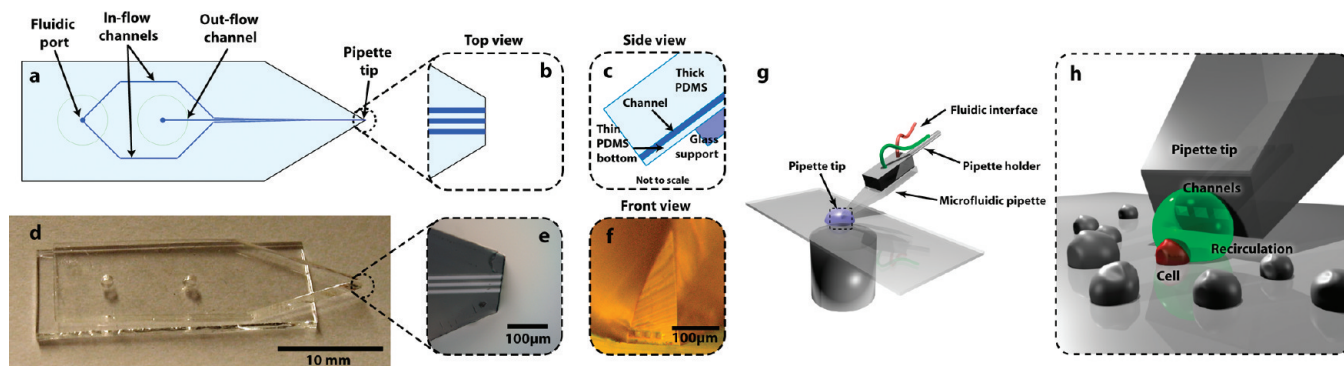


Figure 1. Construction and principle of the microfluidic pipette with a circulating liquid tip. (a–c) Schematic view and (b–f) photographic images of the microfluidic pipette in its simplest implementation. The magnification shows the three-channel tip (b, schematic; d–f, photographs of the top and front views) as well as a schematic side view (c). (g) Illustration of a microfluidic pipette in a typical experimental setup, selectively exposing surface-immobilized biological cells within a culture (h). Solution flowing from the channels is completely recirculated into the pipette by a pressure difference between the channels; contamination of the culture medium is thus efficiently avoided. The volume of the recirculation zone (green sphere in panel h) is comparable to the size of the single cell (red sphere in panel h). The diameter of the cell is approximately 10 μm , which is about equal to the channel width.

components end up in the cell soma because of the rounding up of the cell).

To meet these demands, we have developed a microfluidic pipette utilizing flow recirculation, initially reported using coaxial dual glass pipettes,¹⁶ to eliminate cross-contamination and contamination of the open volume and to enable high-resolution spatial control of the concentration very close to selected microscopic objects, such as single cells (Figure 1). The tip diameter is defined by the recirculating fluid and can be less than 10 μm in diameter, which is convenient for addressing single cells or parts of cells such as the somatic, dendritic, or axonal region of an adherent neuron. The point of exposure can be set freely by mechanical positioning devices in a three-dimensional environment. Because flow-switching and other fluid-processing functionalities can be conveniently incorporated in the soft-material microfluidic design, the device is capable of providing fast solution exchange, dilution, or other means of fluid manipulation. Importantly, the method allows for the direct pharmacological interrogation of single cells, as demonstrated here in an uptake assay, where we show that it is possible to generate dose–response curves in situ from adherent Chinese hamster ovary (CHO) cells expressing proton-activated human transient receptor potential vanilloid (*h*TRPV1) receptors.

MATERIALS AND METHODS

Materials. Two-inch n-type silicon wafers, photoresist Microchem SU-8-10 and SU-8 developer (1-methoxy-2-propyl acetate) were provided by the MC2 cleanroom facility at Chalmers. A Dow Corning Sylgard 184 poly(dimethylsiloxane) (PDMS) kit was obtained from GA Lindberg, Göteborg, Sweden. T-REX-CHO cells expressing the *h*TRPV1 were donated by AstraZeneca R&D CNS&P, Södertälje, Sweden. Fetal calf serum, a DMEM/F12 medium with glutamine, and Accutase were obtained from PAA GmbH, Pasching, Austria. Zeocin and YO-PRO-1 iodide (a DNA-binding propidium dye) were obtained from Invitrogen Ltd.,

Carlsbad, CA. All other chemicals were obtained from Sigma-Aldrich, Madison, WI. All solutions used in the study were prepared in Milli-Q-grade deionized water. Tubing was obtained from VWR International, Debrecen, Hungary. Pneumatic valves for pressure control were from Pneumadyne Inc. (Plymouth, MN) and Parker Hannifin Corp. (Columbus, OH). All electronic components were ordered from ELFA AB, Järfälla, Sweden.

Fabrication of Devices. We fabricated the microfluidic pipette by means of soft lithography.¹⁷ All molds for replica molding were prepared in the ISO100 cleanroom facility MC2 at Chalmers, whereas PDMS casting and curing was carried out in an ambient environment in a standard laboratory. Molds were prepared by using conventional techniques, and details can be found in the Supporting Information (Method S1). The PDMS prepolymer (Dow Corning Sylgard 184) was prepared by mixing parts A and B in a ratio of 10:1 (m/m) and degassing for 15 min in a desiccator. Subsequently, the mold was used to cast a PDMS slab. PDMS slabs of thickness >2 mm were cast using a molding template around the wafer; thinner slabs were prepared directly on the wafer by self-spreading (~1–2 mm) or spin-coating (<1 mm, Table S1 in the Supporting Information). For the thin membranes, PDMS was spin-coated onto the clean surface-treated wafer, using spin parameters, also listed in the table. PDMS structures were cured at 95 °C (air circulation oven) for 1 h. Thereafter, the chip was assembled by oxygen plasma bonding in a Plasma Therm Batchtop PE/RIE at 250 mTorr, 85 W, and 10 sccm O₂ for 10 s. At first, the bottom surface of the thick PDMS slab and the thin PDMS membrane, still adhered to the wafer, were treated and bonded at 95 °C for 1 h. Then the composite was peeled off, and 1-mm-diameter holes were punched through the slab. The pipette tip was shaped with a microtome blade. Then the composite slab and a borosilicate microscope glass coverslip were bonded together; an overhang of 5 mm with respect to the glass slide edge was left at the pipette tip edge. Finally, the chip was left to bond completely overnight, reproducibly (80%) yielding a functional device.

Interfaces and System Control. Devices were interfaced to the flow control unit by two techniques. Within the first,

(14) Bianchi, M. T.; Botzolakakis, E. J.; Haas, K. F.; Fisher, J. L.; Macdonald, R. L. *J. Physiol. (Oxford, U.K.)* **2007**, *584*, 769–787.

(15) Sinclair, J.; Pihl, J.; Olofsson, J.; Karlsson, M.; Jardemark, K.; Chiu, D. T.; Orwar, O. *Anal. Chem.* **2002**, *74*, 6133–6138.

(16) Feinerman, O.; Moses, E. J. *Neurosci. Methods* **2003**, *128*, 197–197.

(17) Xia, Y. N.; Whitesides, G. M. *Angew. Chem., Int. Ed.* **1998**, *37*, 551–575.

the microfluidic pipette was molded as a ~5-mm-thick PDMS slab, and ports were punched through the elastomer, using a flat, sharpened syringe needle (\varnothing 0.9 mm i.d.; Figure S1a in the Supporting Information, devices A and B). PTFE tubing was connected to these ports by means of slightly wider (\varnothing 1.1 mm o.d.) needles, establishing a tight seal (Figure S1c in the Supporting Information). Other possible interfacing concepts have been suggested.^{18–20}

Solutions were supplied from screw-cap laboratory test tubes. This technique is efficient when high flow rates or high pressures (up to 2–3 bar) are involved but also has shortcomings, such as the large volume of solution needed to fill the test tube as well as the interfacial tubing compared to the much smaller amounts of solution generally needed for microfluidic devices, causing further filling and purging of the tubes to remove air. Moreover, a minimum device thickness is needed to form tight seals, which limits miniaturization and requires more production material. Motivated, on the one hand, by the urge to remove these shortcomings and, on the other hand, the need to work in small Petri dishes under a confocal microscope, we devised another, miniaturized device interface. Here, the microfluidic device was fabricated as thin as possible (200 μ m to 1 mm) while still maintaining the mechanical integrity required for fabrication (Figure S1a in the Supporting Information, devices C and D). Fluid ports (\varnothing 1.6 mm) were punched into the device, where each of them served as a reservoir (2 μ L volume at 1 mm device thickness). To use the pipette, each reservoir was filled with a droplet of solution and closed by a manifold, providing pneumatic access for each port (Figure S1d in the Supporting Information). As long as the flow rates are small (\sim 1 nL s⁻¹), these reservoirs are large enough to supply solution for \sim 30 min experiments. This concept allowed for smaller devices and more efficient usage of valuable sample solution. There were no specific filling problems because the external tubing was only used for supplying the driving pressures. The pneumatic manifold was also fabricated from PDMS. Two smooth PDMS surfaces adhere sufficiently to each other to withstand up to \sim 10 kPa pressure. To apply higher pressures, the device and manifold can be supported by a metal clamp.

With a thickness of \sim 1 mm, the pipettes, are very compact and allow access to confined spaces, yet feature excellent stability (Figure S1e in the Supporting Information). Very thin devices (\sim 200 μ m thickness) have sufficient integrity but are highly flexible and are bent by surface tension when brought into contact with the open-volume solution (Figure S1b,f in the Supporting Information). They are therefore more difficult to position.

Pressure and vacuum were created with membrane pumps and controlled with electrically actuated valves (Pneumadyne Inc. and Parker Hannifin Corp.). All pressures were monitored and controlled with a Microchip PIC18F4550 microcontroller, interfaced via USB to a personal computer. Pressures and valve actuation were controlled with software written in-house in Visual C++ .NET, running under Windows Vista.

The pipette was attached to a water hydraulic micromanipulator Narishige MH-5, which allows three-dimensional positioning of

the pipette in order to bring the recirculation zone to the desired place (Figure S1c in the Supporting Information).

Device Testing. Liquid recirculation was investigated with a fluorescence microscope Leica DM IRB. As a substrate, a 1 mM fluorescein disodium salt solution in Milli-Q water was used. Still images were recorded with a Point Gray Chameleon USB camera, videos with a Hamamatsu C6157 3CCD camera, and high-speed videos with a RedLake MotionPro HS-4 BW camera.

Cell Culture. Adherent CHO cells expressing the *hTRPV1* protein (utilizing doxycycline, a tetracycline antibiotic, for induction of the T-REx expression system from Invitrogen Ltd.) were cultivated in Petri dishes for 2–6 days in Dulbecco's modified eagle medium/nutrient mixture F-12 (DMEM/F12 with glutamine) supplemented with fetal calf serum (10%), Zeocin (350 μ g mL⁻¹), and Blastidicin (5 μ g mL⁻¹). About 18–24 h prior to the experiments, the cells were incubated in a DMEM/F12 medium with glutamine, supplemented with fetal calf serum (10%) and doxycycline (1 μ g mL⁻¹) in order to induce expression of the TRPV1 protein. Before the experiments, the cells were washed with an extracellular buffer (see below) and incubated for 5 min with Accutase at 37 °C.

Cell Blebbing. The culturing medium was removed, and the cells were washed twice with a *N*-(2-hydroxyethyl)piperazine-*N'*-2-ethanesulfonic acid (HEPES) buffer, containing 140 mM NaCl, 1 mM CaCl₂, 5 mM KCl, 1 mM MgCl₂, 10 mM D-glucose, and 10 mM HEPES at pH 7.4. Afterward the cells were covered with 2 mL of a HEPES buffer, and the dish was placed on a confocal microscope stage. The pipette was loaded with a blebbing solution, containing 25 mM formaldehyde, 20 mM dithiothreitol (DTT), 2 mM CaCl₂, 10 mM HEPES, 0.15 M NaCl at pH 7.4, and 10 μ M disodium fluorescein for fluorescence monitoring purposes. After placing the pipette into the open volume, it was aligned to surface-immobilized single cells or cell groups. Fluorescein emission was used to control the size and shape of the recirculation zone to completely cover the cells but not the environment around them. The cells were exposed to the recirculation zone for 15 min, and the growth of membrane blebs was recorded. Control recordings were carried out outside the recirculation zone, confirming that no blebbing occurred on these unexposed cells. Several successive experiments were carried out in the same open volume, confirming the absence of contamination from the pipette.

Electrophysiology. The whole-cell patch-clamp method was used in all experiments. Patch-clamp pipettes were pulled with a laser-based pipette puller P-2000 (Sutter Instruments Co., Novato, CA). The resistance of the pulled patch-clamp pipettes was 2–10 M Ω . All data were recorded with a HEKA EPC10 patch-clamp amplifier and *Patchmaster* software (HEKA Elektronik, Lambrecht/Pfalz, Germany). The cells were clamped at -60 mV, and series resistance compensation was performed to 80%. Current signals were recorded at a sampling frequency of 5 kHz, low-pass-filtered at 1 kHz, and further digitally filtered at 10 Hz to reduce noise. The cell bath solution (extracellular buffer, ECB) contained 140 mM NaCl, 5 mM KCl, 1 mM CaCl₂, 1 mM MgCl₂, 10 mM HEPES, and 10 mM D-glucose; the pH was adjusted to 7.4 with NaOH. The patch-clamp electrode solution (intracellular buffer) contained 120 mM KCl, 1 mM CaCl₂, 2 mM MgCl₂, 11 mM ethylene glycol bis(2-aminoethyl ether)-*N,N,N',N'*-tetraacetic

(18) Fredrickson, C. K.; Fan, Z. H. *Lab Chip* **2004**, *4*, 526–533.

(19) Cooksey, G. A.; Plant, A. L.; Atencia, J. *Lab Chip* **2009**, *9*, 1298–1300.

(20) Chen, C. F.; Liu, J.; Hromada, L. P.; Tsao, C. W.; Chang, C. C.; DeVoe, D. L. *Lab Chip* **2009**, *9*, 50–55.

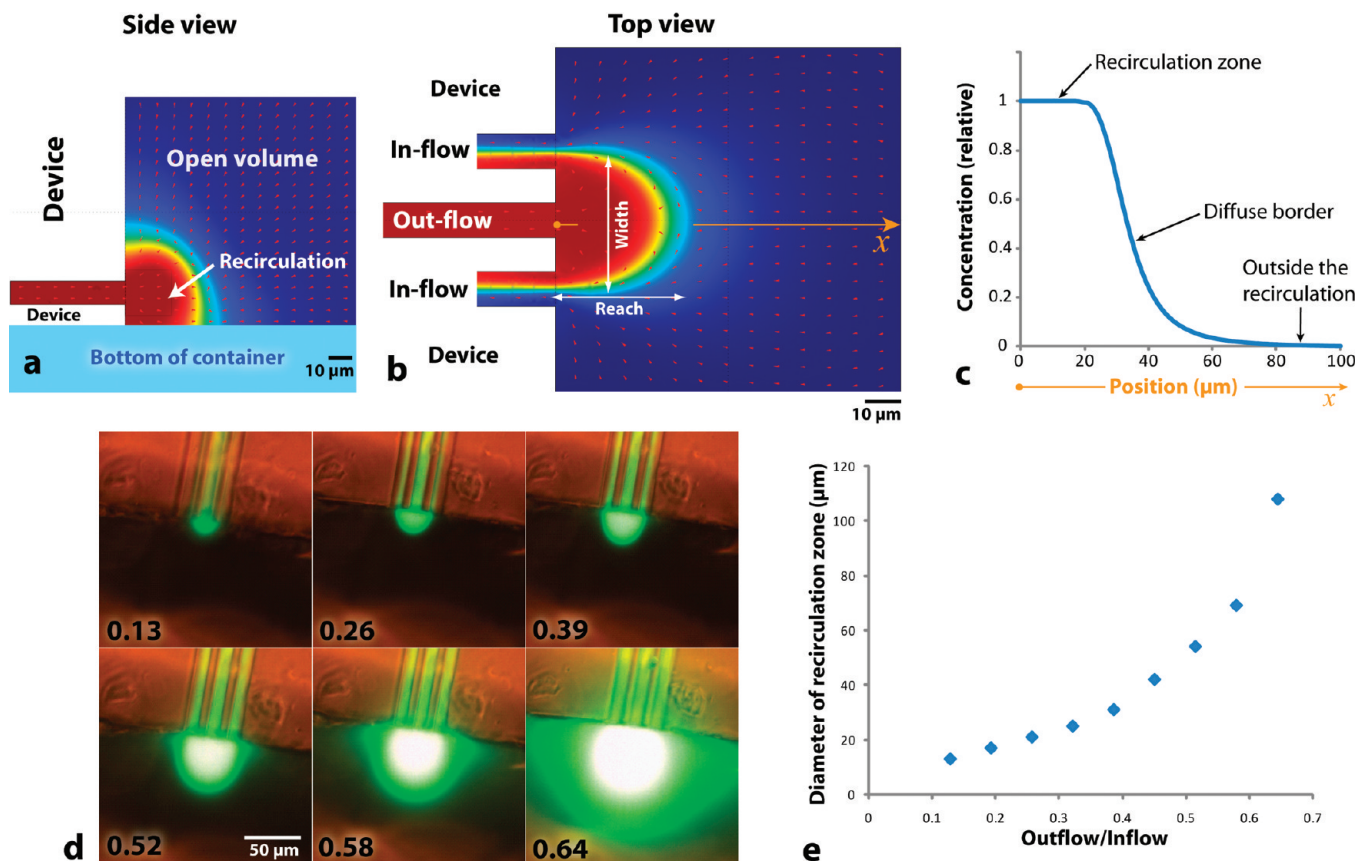


Figure 2. Concept of flow recirculation: (a and b) finite-element model and (d) microphotographic images of flow recirculation in front of the microfluidic channels. Side (a) and top (b) views show the flow field (red arrows) and the substrate concentration distribution as a color gradient (blue, 0% substrate; red, 100% substrate). The outflow/inflow ratio used for the simulation is 0.5. The orange arrow represents the distance from the channel outlet along the channel axis x . Panel c shows the concentration distribution as a function of the distance x . The size of the recirculation zone can be varied over 1 order of magnitude by adjusting the ratio between the pressures driving the flows (d and e). The inflow rate used in simulations and experiments is $\sim 16 \text{ nL s}^{-1}$, and the outflow rate is varied correspondingly.

acid, and 10 mM HEPES; the pH was adjusted to 7.2 with KOH. For pH stimulations, the pH of the ECB solution was set to 5.5, using HCl or NaOH. For the solution exchange, either the pipette was moved with a micromanipulator or the solution was exchanged by on-chip switching. Flow rates were in the range of $1\text{--}5 \text{ mm s}^{-1}$.

YO-PRO-1 Uptake Fluorescence Assay. Fluorescence was measured with a Leica IRE2 confocal microscope equipped with a Leica TCS SP confocal scanner, an oil-immersion $40\times$ Leica objective, and Leica confocal software. Fluorescence was measured from single cells, with excitation at 488 nm and emission at 505–600 nm, and images were captured at 0.6 Hz. YO-PRO-1, dissolved to $1 \mu\text{M}$ in Ca-free ECB with BAPTA in all three stock solutions (pH 7.4, 5.5, and 4.5) in the reservoir wells of the microfluidic pipette. The mixing ratios needed to obtain solutions of pH 6.4 and 5.1 from the three stock solutions were established by bulk experiments using a standard pH meter.

Simulations. Simulations were performed with COMSOL Multiphysics, combining Navier–Stokes and convection–diffusion equations. The simulations were based on an open volume of $100 \times 100 \times 100 \mu\text{m}^3$, which has four opened boundary sides and two nonslip boundaries serving as a microscope coverslip and a pipette tip. The pipette tip has three rectangular channels with dimensions $10 \times 10 \times 100 \mu\text{m}$, which are separated by $10 \mu\text{m}$ walls and a $10 \mu\text{m}$ bottom membrane. The pipette is

positioned such that the tip is in contact with the bottom surface. The water viscosity was 10^{-3} Pa s , and the diffusivity of the small molecules was $10^{-9} \text{ m}^2 \text{ s}^{-1}$. The simulation mesh was defined with $>30\,000$ elements. Flows were driven by pressure differences applied to the channels.

RESULTS AND DISCUSSION

Devices. We developed a soft-material pipetting device that fully utilizes flow recirculation, which is essentially a construction of a flow chamber with virtual boundaries that are hydrodynamically defined. A laminar fluid stream exiting from one channel is fully recirculated into neighboring channels, and a small circulating volume is created at the chip-to-open-volume interface, where the injected solution reaches a certain distance into the open volume. Flow recirculation provides a means to maintain a stationary concentration pattern, which would otherwise rapidly fade by spreading.

The recirculation volume itself is defined by the size, number, and spacing of the channel outlets as well as the flow rates (Figure 2). A stationary recirculation volume can be generated by two adjacent channels, where the inflow rate is higher than the outflow rate, such that all fluid leaving the outlet will flow entirely into the neighboring inlet (Figure S2 in the Supporting Information). Previously reported two-channel approaches required the substrate surface as an additional stabilizing boundary.¹³ However,

both the stability and homogeneity of the recirculation zone significantly improve in a three-channel configuration, where the outflow channel is situated between two inflow channels in the same plane. This design results in nearly spherical recirculation in the open volume (Figure 2a,b), where the reach of the recirculation zone can be controlled by device fabrication and by variation of the outflow/inflow ratio q (Figure 2d,e). For recirculating flow mode, the q must be lower than a critical value q_{critical} (~ 0.65 in our devices). Through electronic regulation of the driving pressures, it is easy and fast to control the q ratio (Video S1 in the Supporting Information) and therefore also the reach of the recirculation that can vary over an order of magnitude (Figure 2e). An important aspect of the virtual flow chamber is also the boundary between the open volume and recirculation zone. Because both are aqueous solutions, the boundary is diffusive and the width is determined by the exchange time and diffusivity, which finally sets the limit for miniaturization.

An important aspect of the virtual recirculation flow chamber is the fluidic boundary between the open volume and the recirculation zone. Because both are aqueous solutions, the boundary is diffusive and the width w is determined by the exchange time t and diffusivity D , such that $w \approx (2Dt)^{1/2}$. The exchange time is related to the outflow rate Q and the volume of the recirculation zone V . Flow rate $Q = vl^2$ and volume $V = \pi d^3/6$ define exchange time $\tau = V/Q = \pi d^3/6vl^2$, where v is the average flow velocity, l is the dimension of a square-shaped channel, and d is the diameter of the nearly spherical exchange volume. Example conditions suitable for biological cell studies, $d = 20 \mu\text{m}$, $v = 2 \text{ mm s}^{-1}$, and $l = 10 \mu\text{m}$, yield an exchange time of approximately 20 ms. The exchange time also influences the width of the diffusive boundary, which in the case of the previous example would be $\sim 6.5 \mu\text{m}$ ($D = 10^{-9} \text{ m}^2 \text{ s}^{-1}$ is a good estimate for small-molecule diffusion in water).

Another question regards the scalability of recirculation, or how small it can become. Because the pipette is intended for controlling a solution environment within an open volume, the exchange time has to be faster than the time needed for diffusion to cause the zone to become diluted with open-volume content $(d/2)^2/2D > \pi d^3/6vl^2$. In other words, the recirculation zone has to maintain its composition and counteract diffusion. This sets the limit on the smallest possible recirculation zone diameter. Geometrically, the recirculation volume has to be larger than the outflow channel, $d \geq l$, and for practical purposes, the flow velocity is rather limited because excessive flow rates certainly detach cells from their support. Consequently, $d > 4\pi D/2v$ leads to a critical diameter $d > 2 \mu\text{m}$, meaning that the fundamental diffusion limit of the technique is in the subcellular size range and does not affect application of the pipette to biological cell environments. Objects smaller than cells, such as lipid patches, surface-immobilized microparticles, etc., allow for an extension of this limit because higher flow rates could be applied. From a fabrication point of view, these dimensions are still much larger than the fundamental limits of lithography.

The microfluidic pipette is implemented as a PDMS microfluidic device, fabricated using the standard replica molding technique of soft lithography.¹⁷ In order to function as a pipette, it has channel exits on the tapered tip, which can be brought into

close proximity to, for example, a biological cell. With respect to the device layout, the simplest microfluidic recirculation pipette has only two fluidic connection ports (Figure 1a,d); one is pressurized for providing the substrate solution that leads to the outlet of the pipette tip and the other is of reduced pressure and connected to two inflow channels for recirculating the outflow. The pipette tip features three $10 \times 10 \mu\text{m}^2$ channels, separated by $10 \mu\text{m}$ walls, where the outlet channel is between two inlets (Figure 1b,e and Table S2 in the Supporting Information). Because most eukaryotic animal cells are in the size range of $10\text{--}30 \mu\text{m}$ diameter, we fabricated the channel geometry on a similar scale. Significantly smaller channel sizes are conceivable: limitations are imposed only by fabrication constraints and physical laws, most importantly, diffusion and flow velocity.

The flow-switching pipette (Figure 3 and Table S3 in the Supporting Information) has a more complex structure, which allows fast switching between three different solutions, for example, for fast pulsing of cells with chemical signals (Video S1 in the Supporting Information) or for use as a diluter based on pulse-width flow modulation (PWFM).²¹ For greatest simplicity, we have devised an on-chip flow switch without mechanical valves (Figure 3c). In addition to a pressure source, two external three-way solenoid valves are used to switch between elevated and atmospheric pressure on the switching ports 1 and 2. When switch 1 is pressurized, the flow direction in this channel is reversed and the laminar stream of solution 1 is pushed into the output channel. Solutions 2 and 3 move into the waste and switching channels (Figure 3d). In order to push solution 3 into the outlet, switch 2 is pressurized instead (Figure 3e). We measured the switching times, and they were found to be faster than 100 ms (Figure 3f); fluid exchange at the outlet featured a solution exchange time of $<500 \text{ ms}$ and a delay of $<1 \text{ s}$ (Figure 3g), depending on the driving pressure. When pulsing is intentionally faster, the solution plugs will completely mix before they reach the outlet, and the concentration of the solutions at the output will depend on the duty cycle of the pulsing sequence (PWFM²¹). This dependence can be calibrated by fluorescence measurement. For simple PWFM, it is recommended to switch between solutions 1 and 3, and then the output is approximately linearly dependent on the duty cycle (Figure 3h). This switching pipette demonstrates the complex, rapid fluid-handling modes of our microfluidic pipette, an impossible endeavor with conventional glass micropipettes, even if they possess flow-recirculation capability.

Single-Cell Applications. *Cell Blebbing.* Cell blebbing refers to the stimulated growth of phospholipid membrane buds out of a native living cell.²² The stimulant is typically an agent that breaks the cytoskeleton adhesion to the plasma membrane. Because the membrane blebs contain membrane protein, chemically induced blebbing is an attractive technique for membrane protein sampling because in some protocols the blebs can be released from the cells as vesicles that can be collected for proteomic analysis.²³

We employed 20 mM DTT and 25 mM formaldehyde as a bleb-inducing composition, which acts as protein disulfide bond

(21) Ainla, A.; Gozen, I.; Orwar, O.; Jesorka, A. *Anal. Chem.* **2009**, *81*, 5549–5556.

(22) Scott, R. E. *Science* **1976**, *194*, 743–745.

(23) Bauer, B.; Davidson, M.; Orwar, O. *Angew. Chem., Int. Ed.* **2009**, *48*, 1656–1659.

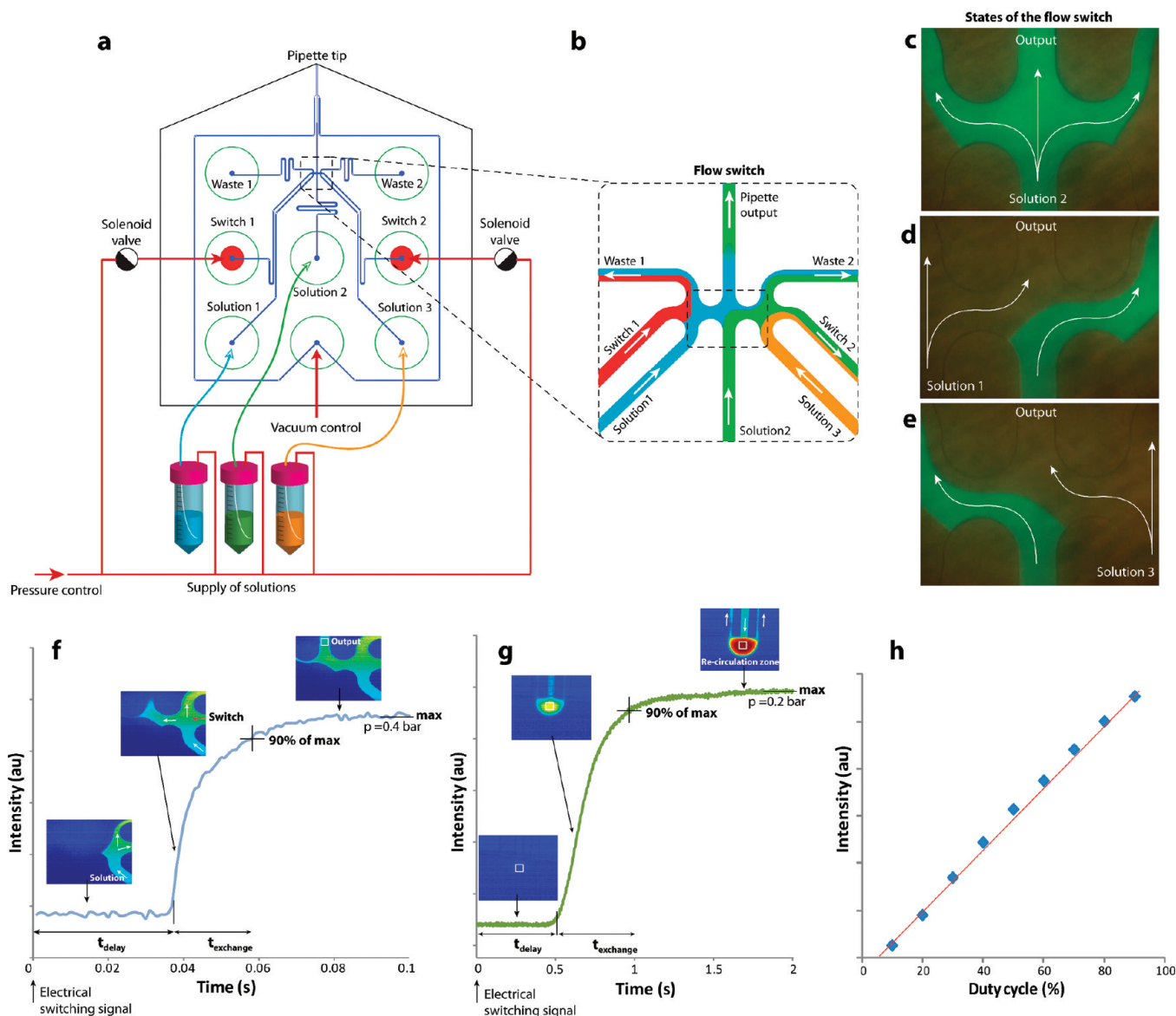


Figure 3. Schematic view of a microfluidic recirculation pipette with embedded three-component flow-switching capability: (a) design with associated experimental setup; (b) magnification showing the eight-channel flow-switching chamber; (c–e) fluorescence micrograph series of the switching between three different solutions [the content of the middle channel (c), or alternatively of the left (d)/right channel (e), is pushed into the outlet channel by actuation of support flows]; (f) typical response characteristics (~ 50 ms response time as a combination of switching delay and exchange time) of the flow-switching device, measured directly inside the switching node by means of a fluorescein solution; (g) typical response characteristics of the flow-recirculation zone (the typical response time for this layout of ~ 1 s arises from the channel length of the diffusive mixer); (h) on-chip PWFDM dilution of a fluorescein-containing buffer depending on the pulsing duty cycle.

reducing and thiol group blocking reagent.²⁴ Our microfluidic pipette was used to selectively deliver this blebbing solution to a small group of cells (Figure 4a). After a period of exposure in the recirculation volume (~ 20 min), blebs formed on the cell surface (Figure 4b,c). Unexposed cells outside the recirculation zone remained completely unaffected because the blebbing reagents cannot escape the recirculation zone (Figure 4d and Video S2 in the Supporting Information).

This example demonstrates that single cells can be exposed to bleb-inducing agents while preventing the spread of the compound to other cells in the same volume. This allows for use of the same cell culture in multiple successive experiments.

Because the recirculation flow can be finely controlled by adjustment of the channel pressures, it is possible to use it even for solution exchange in the presence of fragile structures such as membrane blebs and giant unilamellar vesicles.

Electrophysiology. Ion channel activity in single cells can be measured using patch-clamp recordings.²⁵ Recordings of channel activation or deactivation require exposure of the patch-clamped cells to solutions containing agonist or antagonists, respectively, which with the current micropipettes affects nearby cells because ligand concentrations will build up in the extracellular bath during prolonged stimulation. This will affect the response of the exposed

(24) Holowka, D.; Baird, B. *J. Biol. Chem.* **1984**, *259*, 3720–3728.

(25) Hamill, O. P.; Marty, A.; Neher, E.; Sakmann, B.; Sigworth, F. J. *Pflügers Arch.* **1981**, *391*, 85–100.

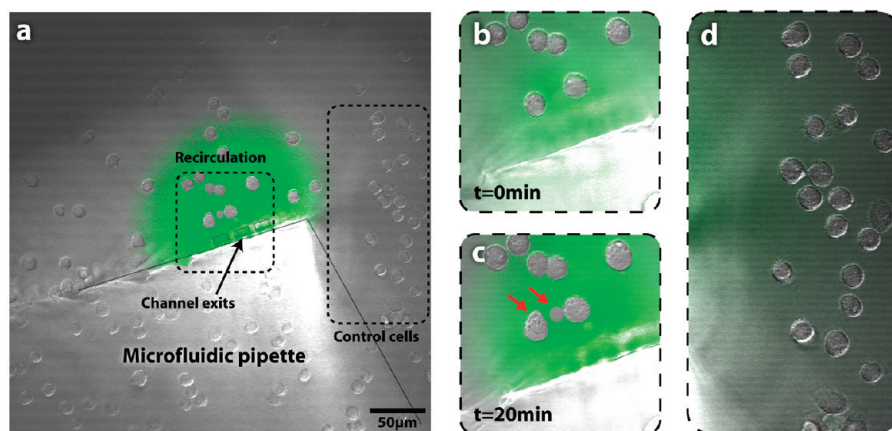


Figure 4. Application of the microfluidic recirculation pipette to selectively expose single cells in a collective to a chemical membrane blebbing solution, containing 25 mM formaldehyde and 20 mM DTT as active ingredients. The shape and extent of the recirculation zone are visualized by the green emission of 10 μ M fluorescein in the same solution. Fluorescence and bright-field micrographs have been overlaid in the panels for comparison: (a) interface between microfluidic pipette and cell culture plate under an inverted microscope (two distinct regions are highlighted and magnified); (b–d) magnifications showing cells inside the recirculation zone before (b) and after 20 min of exposure to the blebbing solution (c) as well as a large control region outside the recirculation zone (d) after exposure.

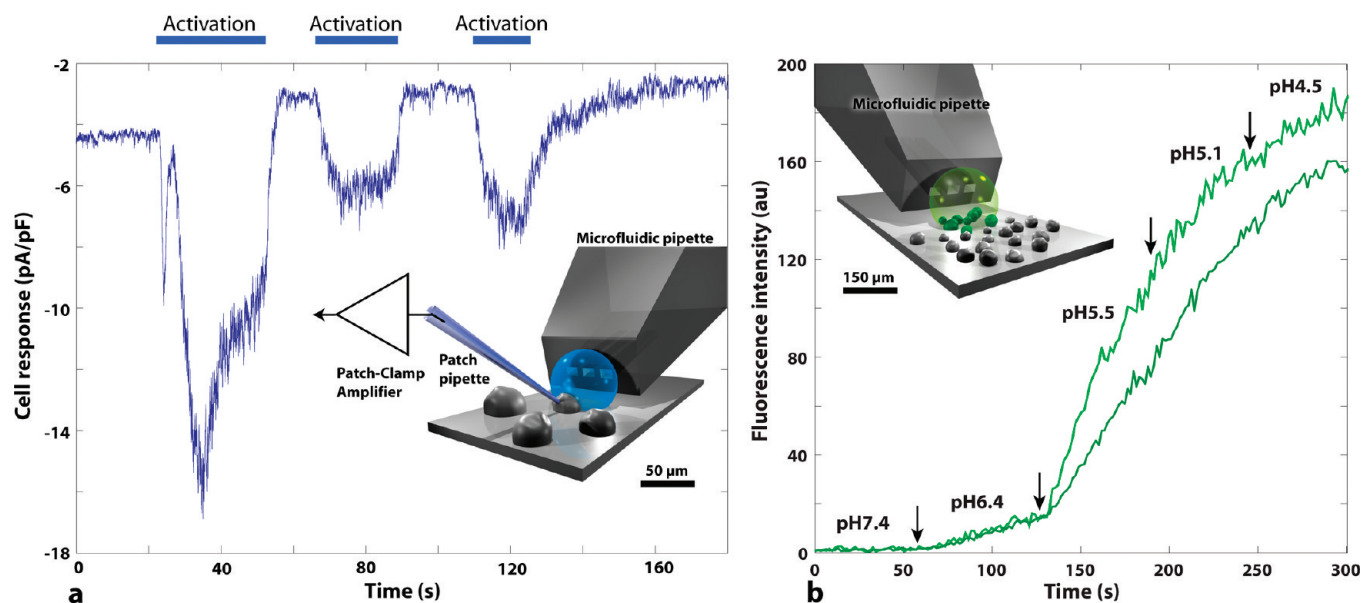


Figure 5. Single-cell patch-clamp and cell group fluorescence uptake assay supported by the microfluidic pipette. (a) Trace of the recorded current response versus time from repeated activation of TRPV1 ion channels from CHO cells by low pH, recorded during a single-cell patch-clamp experiment in front of the microfluidic pipette. A cell is selectively exposed to a pH 5.5 chemical stimulus provided by the pipette. The inset illustrates the experimental setup, with the cell subjected to the recirculation zone. The current response (~ -10 pA/pF) and its decrease in magnitude upon repeated stimulation are typical for the cell type expressing TRPV1. (b) Graphic time series of the dependency of the intracellular fluorescence intensity on the proton concentration (in pH units), obtained by selective exposure of colonies of the same CHO cells to a pH dilution series. The two traces represent fluorescence intensities measured from two independent cells. The arrows indicate the points in time when concentration switching occurs. The plateaus noticeable in both traces at pH 4.5 arise from saturation of the cell's nuclei with the applied dye. The insets show schematic pictures of the respective experimental setups at the length scales of the objects of interest.

cells because they experience a low level of tonic activation before the measurements start. Recent microfluidic approaches have managed to decrease the exposure of ligands to nonclamped cells during recording¹⁵ but never eliminated it completely. Here, the microfluidic pipette is utilized to resolve this situation. TRPV1-expressing CHO cells were used to show how currents from voltage-clamped cells can be evoked when exposed to agonist utilizing the pipette. TRPV1 is a nociceptive ion channel expressed in trigeminal and dorsal root sensory ganglia and is, among others, activated by noxious heat (>43 °C), capsaicin ($EC_{50} = 0.1$ μ M),

and reduced pH (5.4).^{26,27} Figure 5a shows a current recording, obtained from patch-clamped CHO cells under acidic (pH 5.5) stimulation. The inset is an illustration of the microfluidic pipette, exposing a patch-clamped cell to the stimulant contained in the recirculation zone.

(26) Caterina, M. J.; Schumacher, M. A.; Tominaga, M.; Rosen, T. A.; Levine, J. D.; Julius, D. *Nature* **1997**, *389*, 816–824.

(27) Tominaga, M.; Caterina, M. J.; Malmberg, A. B.; Rosen, T. A.; Gilbert, H.; Skinner, K.; Raumann, B. E.; Basbaum, A. I.; Julius, D. *Neuron* **1998**, *21*, 531–543.

Under these conditions, contamination of the open volume by the active compound is efficiently eliminated. In this example, the microfluidic pipette is positioned above the surface, so that translation of the pipette rapidly introduces the cell to or removes it from the recirculation zone. In this setup, cells can be detached or remain on the surface while connected to the patch-clamp pipette.

Single-Cell Uptake Assay. In order to demonstrate on-chip functionalities in connection with the microfluidic pipette, we monitored YO-PRO-1 uptake in TRPV1-expressing CHO cells during stimulation with calcium-free ECB with varying pH as the agonist. The microfluidic pipette served as an automatic solution-switching and dilution device in order to supply a sequence of buffer solutions of decreasing pH to the cells. The solutions were generated by means of flow switching and PWF. ²¹ Activation of TRPV1 by low pH under calcium-free conditions promotes pore dilation ²⁸ and thus allows for entry of the bulky YO-PRO-1 through the ion channel. The pore size increases with decreasing pH, and the intracellular fluorescence intensity can be plotted versus pH to construct dose–response relationships (Figure 5b). Dilution experiments of this kind, performed on uncharacterized ion channel/agonist systems, are thus useful to rapidly determine the effective concentration (EC₅₀) as well as the inhibitory concentration (IC₅₀) values.

CONCLUSION

Our microfluidic pipette is a multipurpose device that can be utilized in single-cell studies under a large variety of operation

conditions, also in conjunction with or supporting other experimental procedures simultaneously. It neither requires contact with a surface nor uses multiple-phase flows. It is compatible with ordinary bright-field fluorescence imaging and confocal microscopy stations. Because of its small footprint and uncomplicated control interface, it is applicable to almost all experimental environments in the life sciences. The simple fabrication protocol and interfacing as well as contamination-free solution delivery make it attractive as a routine research tool, particularly in pharmacological and physiological studies of isolated biological cells.

ACKNOWLEDGMENT

This research was funded by the European Research Council (ERC grant), the Knut & Alice Wallenberg Foundation, and the Swedish Strategic Research Foundation. We thank AstraZeneca R&D CNS&P Södertälje for the cell line stably expressing the *h*TRPV1 ion channel.

SUPPORTING INFORMATION AVAILABLE

Fabrication of molds, spin-coating parameters, photographs of the devices and interfaces, finite-element simulations, and specifications of single-solution and flow-switching pipettes. This material is available free of charge via the Internet at <http://pubs.acs.org>.

Received for review February 22, 2010. Accepted April 8, 2010.

AC100480F

(28) Chung, M. K.; Guler, A. D.; Caterina, M. J. *Nat. Neurosci.* **2008**, *11*, 555–564.

Supporting Information

A Microfluidic Pipette for Single-Cell Pharmacology

Alar Ainla, Erik T. Jansson, Natalia Stepanyants, Owe Orwar and Aldo Jesorka*

Department of Chemical and Biological Engineering, Chalmers University of Technology
Kemivägen 10, SE-412 96 Göteborg, Sweden.

Contents

Method S1. Fabrication of molds	2
Table S1. Spin coating parameters for thin PDMS (Dow Corning Sylgard 184) films	2
Figure S1. Photographs of the devices and interfaces.....	3
Figure S2. Finite element simulation of a two channel flow circulation (Channel width: 50 μm)	4
Table S2. Specification of single solution pipette	5
Table S3. Specification of flow switching pipette	5

Method S1. Fabrication of molds.

The layout was designed in Autodesk AutoCAD 2008. Patterns for each layer were transferred to the E-beam lithography system JEOL JBX-9300FS and written to chromium coated soda-lime glass masks. Wafers were treated before use by means of oxygen plasma in a microwave plasma processor (Tepla 300PC, 1 mbar, 250 W for 1 min, O₂ gas flow 400 sccm). Resists were exposed on a Karl Süss MA6 contact mask aligner (G-line, 5-6 mW cm⁻²). For the mold (10 µm resist thickness), SU8-10 was spin-coated at 3000 rpm for 30 s, soft baked at 65 °C for 2 min, ramped to 95 °C, baked 5 min (all on a hot plate) and left to cool to RT. Subsequently, the wafers were exposed with 5 mW cm⁻² UV-Light for 20 s through a dark field mask, post-baked 1 min at 65 °C, ramped to 95 °C, baked for 2 min and finally left to cool to RT. The resist was developed in SU8 developer for 2 min., rinsed with developer and washed in de-ionized water (DIW). The mould was blow dried and cleaned in oxygen plasma (50 W, 250 mTorr, 1 min). Finally, the mould was hard-baked at 200 °C (air circulation oven) for 30 min, with slow heating and cooling. The geometries of the moulds were characterized with an Olympus MX40 microscope and a stylus profiler Tencor AS500. Before use, the mould and a clean Si wafer were anti-adhesion-treated with dichloro dimethyl silane by exposing the surfaces to the vapors under a Petri dish cover for 5 min, and baked subsequently for 10 min at 95 °C.

Table S1. Spin coating parameters for thin PDMS (Dow Corning Sylgard 184) films.

Rotation speed (rpm)	Spin time (s)	Membrane thickness (µm)
<i>Thin membranes</i>		
1500	60	40
2000	300	12
2500	600	7
<i>Thick PDMS</i>		
500	60	190

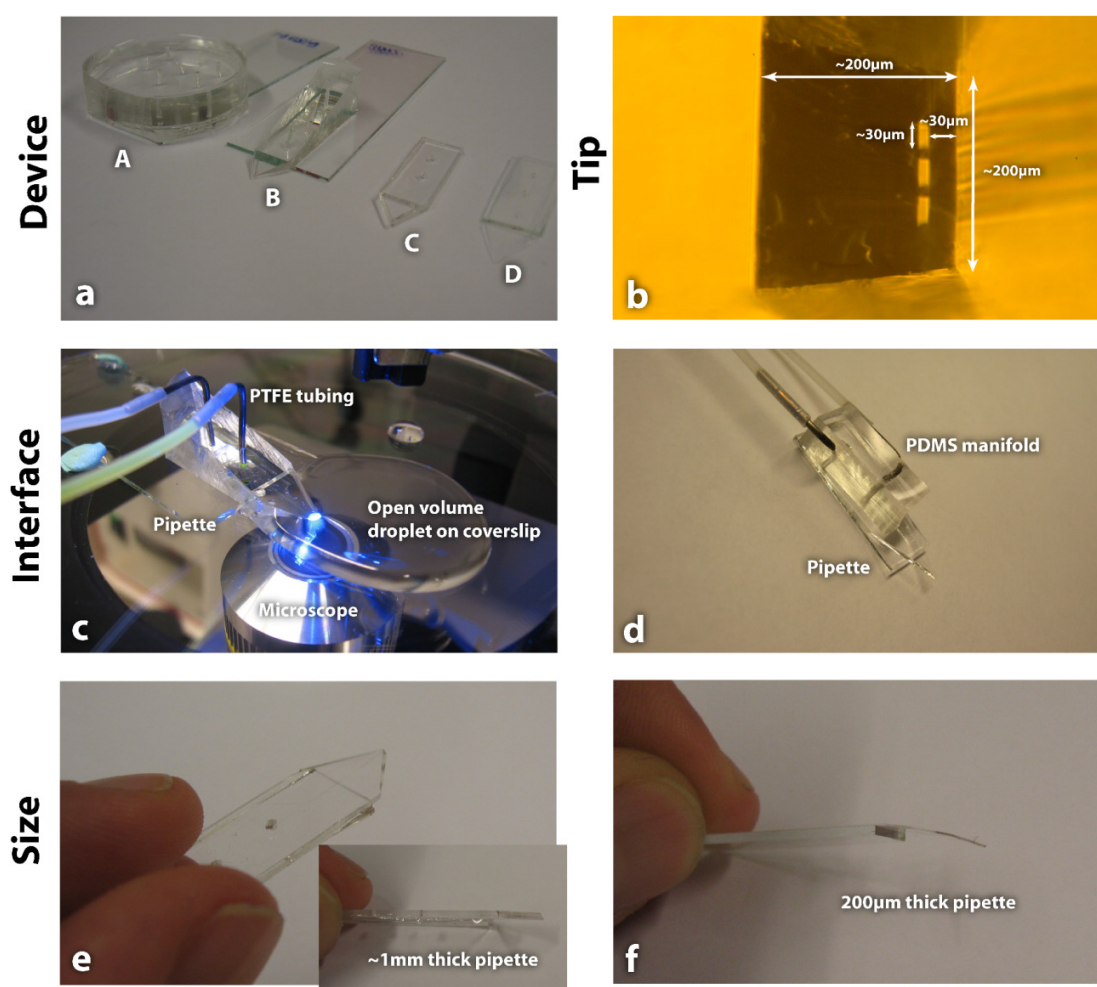


Figure S1. Photographs of the devices and interfaces.

(a) Different shapes of fabricated devices; devices A and B have a thick PDMS body to support direct interfacing by means of tubing; C and D have a thin body, requiring a manifold for interfacing. (b) The tip of the fluid switching pipette with 30 µm wide channel exits. (c) A pipette using the tubing interface in a typical experimental setup. (d) A thin pipette attached to the PDMS manifold. To increase pressure resistance both sides can be supported by a clamp. (e-f) Pipettes with 1 mm (e) and 200 µm (f) thick PDMS bodies.

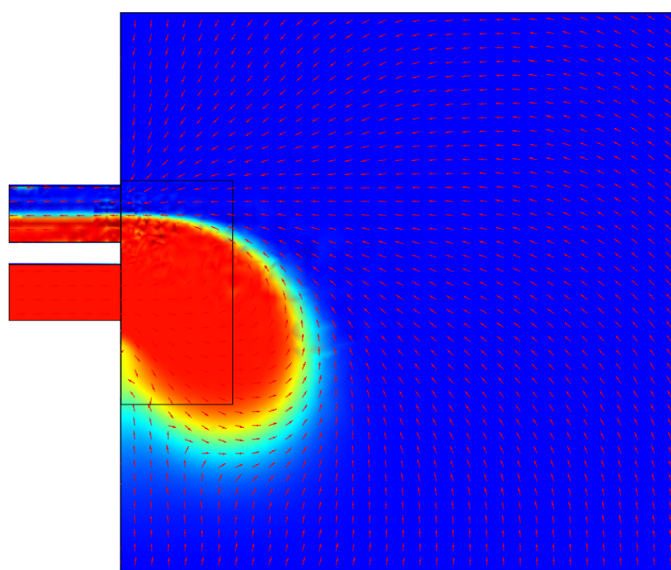


Figure S2. Finite element simulation of a two channel flow circulation (Channel width: 50 μm).

Table S2. Specification of a single solution pipette.

This device features compact overall size; it requires only a simple setup and allows contamination free exposure of one or a few single cells. However it is limited to one active solution. The exposure can be turned on/off by adjusting the driving pressures, thus enlarging or reducing the re-circulation zone. Alternatively, the pipette can be micromanipulated away from the cells.

Parameter	Value
Channel height	10 μm
Channel width	10 μm
Channel separation	10 μm
Fluid conductance	0.2 $\text{nL s}^{-1} \text{kPa}^{-1}$
Flow rate at 10kPa driving pressure	2 nL s^{-1}
Average flow velocity at the same pressure	20 mm s^{-1}
Bottom membrane thickness	10-40 μm
Critical flow ratio q_{critical}	0.65
Extend range of re-circulation	$\sim 10\text{-}100 \mu\text{m}$

Table S3. Specification of a flow switching pipette.

This device features capability to switch re-circulation content between 3 different solutions. The long spatial separation between the switching point and the channel outlets is leading to longer delay and solution exchange times. On the other hand, when pulsing is intentionally faster, the plugs will completely mix before they reach the outlet, and the concentration of the solutions at the output will depend on the duty cycle of the pulsing sequence (pulse width flow modulation).

Parameter	Value
Channel height	30 μm
Channel width	30 μm
Channel separation	30 μm
Flow rate from tubing (at 10kPa driving pressure)	$\sim 75 \text{ nL s}^{-1}$
Flow rate at outlet (10kPa pressure)	$\sim 15 \text{ nL s}^{-1}$
Average flow velocity (10kPa pressure)	$\sim 17 \text{ mm s}^{-1}$
Pneumatic switching time	<100ms
Solution exchange time at outlet (t_{exchange})	<500ms
Delay of solution exchange at outlet (t_{delay})	<1s

PAPER

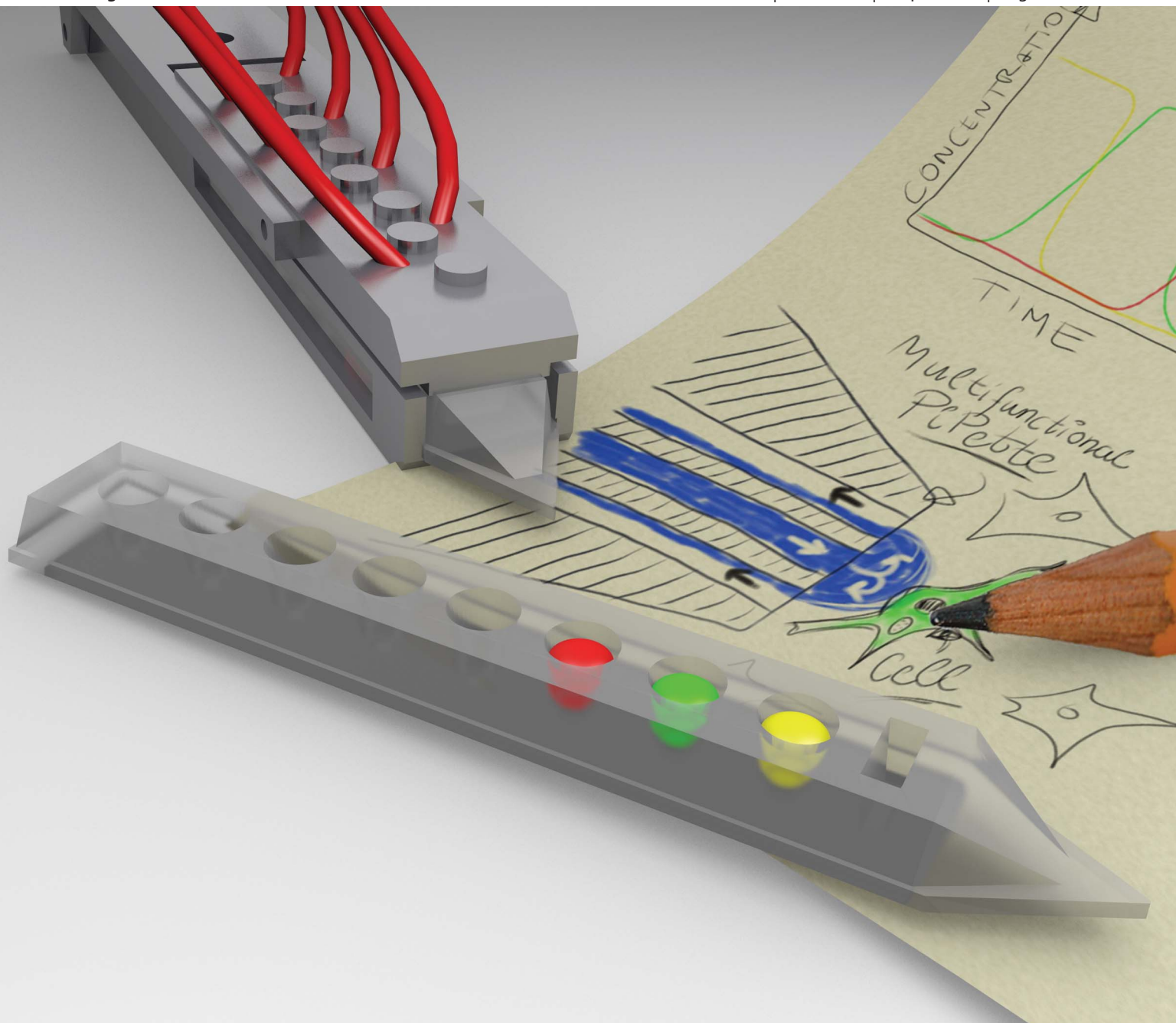
III

Lab on a Chip

Miniaturisation for chemistry, physics, biology, materials science and bioengineering

www.rsc.org/loc

Volume 12 | Number 7 | 7 April 2012 | Pages 1193–1396



ISSN 1473-0197

RSC Publishing

PAPER
Jesorka *et al.*
A multifunctional pipette



1473-0197 (2012) 12:7;1-2

Cite this: *Lab Chip*, 2012, **12**, 1255

www.rsc.org/loc

PAPER

A multifunctional pipette†

Alar Ainla, Gavin D. M. Jeffries, Ralf Brune, Owe Orwar and Aldo Jesorka*

Received 19th September 2011, Accepted 8th December 2011

DOI: 10.1039/c2lc20906c

Microfluidics has emerged as a powerful laboratory toolbox for biologists, allowing manipulation and analysis of processes at a cellular and sub-cellular level, through utilization of microfabricated features at size-scales relevant to that of a single cell. In the majority of microfluidic devices, sample processing and analysis occur within closed microchannels, imposing restrictions on sample preparation and use. We present an optimized non-contact open-volume microfluidic tool to overcome these and other restrictions, through the use of a hydrodynamically confined microflow pipette, serving as a multifunctional solution handling and dispensing tool. The geometries of the tool have been optimised for use in optical microscopy, with integrated solution reservoirs to reduce reagent use, contamination risks and cleaning requirements. Device performance was characterised using both epifluorescence and total internal reflection fluorescence (TIRF) microscopy, resulting in ~200 ms and ~130 ms exchange times at ~100 nm and ~30 μ m distances to the surface respectively.

Introduction

Microfluidics has opened a multitude of possibilities for the control of chemical environments at small length scales, enabling functionality and precision which were previously unattainable. The laminar flow regime of microfluidic devices allows the formation and maintenance of spatial concentration gradients,¹ while the introduction of on-chip valves in combination with low dead volumes made possible quick switching between different solutions.² To take advantage of this fluidic control using conventional techniques, the sample has to be introduced into the microchannels of the device, which in the context of biological applications is well suited for cell suspensions, but hard to apply when working with adherent cells and tissues.

Recently, several research groups have reported a new class of devices, which can deliver liquid into an open volume while simultaneously rerouting the liquid back into the chip. This is achieved by means of closely spaced adjacent channels under positive and negative pressure, respectively, creating a hydrodynamically confined flow (HCF) volume.^{3–5} This volume, fluidically connected to the device tip, can be positioned to stimulate and analyse a single cell or other object of interest, without affecting the surrounding liquid.

Hydrodynamic confinement of one miscible solution inside another is possible due to convective recirculation, counteracting diffusion, which otherwise would mix the two solutions. The balance of convection and diffusion in such an arrangement is

described by the dimensionless Péclet number (Pe). A larger Pe leads to a greater level of confinement, establishing a sharper, more defined boundary between the two liquids.

The idea of recirculation probes originates from physiology, where push–pull cannulae have been used for *in vivo* sampling since 1961.⁶ These probes remain popular for sampling of neurotransmitters.^{7,8} Hydrodynamic confinement within an open volume was first demonstrated in a picolitre ‘fountain-pen’ made of two co-axial pipettes, where the inner capillary is used for injection of reagent, and the outer one for aspirating the reagent back into the pipette.⁹ Similarly, theta tube capillaries have been applied for recirculation to stimulate cells with lysis buffer and collect the lysate for analysis.¹⁰ Both types of delivery require fragile tips that can be costly and difficult to fabricate.

Later, microfabrication in silicon and polydimethylsiloxane (PDMS) was used to create microfluidic probes, which circulate the liquid in a thin cleft, formed between the face of the probe tip and the surface under investigation.^{3,5,11–13} A similar principle has been exploited for use in an electrochemical probe, fabricated from polyethylene terephthalate (PET) and used to analyse dry surfaces.¹⁴ In this case the recirculation provides and refreshes an electrolyte droplet in front of the working electrode. Other free-standing probes have been employed for studying chemotaxis¹⁵ and to deliver genetic material¹⁶ in optical microscopy experiments. The open volume flow recirculation principle has also been applied for stimulating brain slices.¹⁷

We have previously reported the concept of a HCF microfluidic pipetting device, constructed by sealing channel grooves with a thin membrane.⁴ This configuration enables recirculation while allowing for angle adjustment and repositioning of the device. It closely resembles the utility of glass micropipettes, which are typically used in microscopy experiments. This

Department of Chemical and Biological Engineering, Chalmers University of Technology, Kemivägen 10, SE-41296 Göteborg, Sweden. E-mail: aldo@chalmers.se; Fax: +46 31 772 6120; Tel: +46 31 772 6112

† Electronic supplementary information (ESI) available. See DOI: 10.1039/c2lc20906c

particular feature strongly influenced the decision to coin our concept a 'pipette'.

Herein we describe the construction and characterization of a multifunctional pipette, developing the initial concept into a research-ready device, optimized to fit into practically any micromanipulation environment. The pipette has been given a sharp elongated shape, facilitating the application within spatially confined microscopy setups, typically found in bioscience environments, where crowding with probes and manipulation equipment is commonplace. We therefore optimized the geometry to reduce the impact on the microscope sample stage, leaving sufficient space for integrating eight on-chip wells, which can store and provide solutions. We have also created a self-aligning holder, designed for robust clamping of the pipette and providing each well with individual pressure control. The pipette and its interfacing have been optimized for both performance and convenience of use by bioscientists without particular microfluidics expertise.

We provide extensive characterization of the pipette performance, and show exemplary circuitry for on-chip switching between three solutions, which we applied to sequentially deliver capsaicin and calcium to single adherent cells in a surface-adhered collective. The concept is highly flexible, novel circuits and functions can be quickly introduced by using new microstructure molds and adapting the control software accordingly. The holder itself is reusable, allowing for rapid adaptation at low cost.

Methods

Fabrication of the microfluidic tip

Devices (Fig. 1A) were fabricated in PDMS (Dow Corning Sylgard 184) using standard soft-lithography techniques. Instrumental procedures and bonding conditions were applied as previously described.⁴ Four pipette tips were simultaneously molded using a polycarbonate form (Hagal Machinery AB, Mölndal, Sweden). To define the pipette shape, reservoir wells and microchannels, a master was fabricated using SU-8 on a 4" silicon wafer, with characteristics summarized in Table 1. The molded PDMS slab was bonded to a 20 μm thin PDMS film, followed by cutting out each tip and punching out the bottom of the wells. The PDMS part was subsequently bonded to a 0.55 mm thick glass substrate (Prazisions Glas & Optik GmbH, Iserlohn, Germany) to increase the structural strength of the tip and rigidify the body of the device. The step-by-step fabrication procedure is depicted in Fig. S1 of the ESI†.

Holder and control interface

The holder (Fig. 1B) was fabricated in stainless steel (Tea-dusmosaiik OÜ, Tartu, Estonia) and constitutes a compromise between aqueous solution compatibility, rigidity and cost. The lower part of the holder provides a self-aligning cavity, into which the pipette tips can slide. A cylindrical 7 mm diameter rod is attached at the rear of the holder, to allow for easy interfacing with common micromanipulators.

The upper part of the holder consists of a hinged manifold, which provides pressure connectivity to each of the wells. The underside of this manifold contains sharp flanges (Fig. 1C), which are pushed against the PDMS pipette, sealing it to the manifold

when the holder is closed. This interface has been tested to withstand pressures in excess of 2 bar, more than double the maximum operation pressure projected. The manifold connects each well individually with the pressure control unit through a 1 m long and 1 mm I.D. length of Nalgene® PVC tubing, which we determined to be optimal to obtain the fastest pressure switching (see Fig. S2†). Supply pressures were controlled with an in-house developed pressure and valve actuation controller (Fig. S3†), allowing vacuum control within the range $0.00\text{--}0.60 \pm 0.01$ bar, and channel pressure control for two channels in the range between 0.00 and 0.90 ± 0.01 bar (at 95% confidence level). Pressure and vacuum controllers were calibrated with a high precision digital manometer LEX1 (Keller AG, Winterthur, Switzerland). Flow switching is achieved through a valve controller, actuating pressure in the wells with the following specifications: electronic time resolution, 1 ms; delay between the electronic signal and valve opening, 23 ± 2 ms; pressure rise time, 6.0 ± 0.7 ms; delay between the electronic signal and valve closing, 6 ms and pressure fall time, 6 ± 1 ms. All experiments were controlled *via* an in-house programmed graphical user interface, developed in Microsoft Visual Studio 2008.NET (C++).

Characterization

Solution switching within the microfluidic channels and at the pipette outlet was characterized using a 100 μM solution of fluorescein (sodium salt) in deionised water. An inverted microscope Leica DM IRB (Leica Microsystems, Wetzlar, Germany) equipped with a fluorescence lamp, a Leica 10×0.3 NA air objective, and a Chameleon USB camera (Point Gray Research Inc., Richmond, Canada) was used for experimentation. Alternate visualization was implemented using water soluble food colour in order to highlight the component flows at the switching junction.

Solution switching near the substrate surface (~ 100 nm) was further characterized using TIRF microscopy with a Leica HCX PL APO 63×1.67 NA oil TIRF objective, utilising 488 nm Sapphire 488-150 CW CDRH laser excitation (Coherent, Santa Clara, USA).

Cell culturing and stimulation

Adherent Chinese hamster ovary (CHO) cells expressing the human transient receptor potential vanilloid 1 (hTRPV1) ion channel were cultured as previously described.⁴ The cells were loaded with calcium sensitive dye, Calcium Green™-1 AM ester (Life Technologies Inc, Carlsbad, USA). At first, a 200 μM stock solution was prepared in DMSO, which was further diluted with Ringer's solution (VWR) to obtain a final concentration of 4 μM . The cells were cultured on Petri dishes equipped with a 0.15 mm thin glass bottom, suitable for confocal imaging. After removing from the incubator, the culture medium was removed and the cells were rinsed twice with Ringer's solution, followed by addition of the dye labelling solution. The cells were exposed to the dye loading solution for 1 h at room temperature, then rinsed twice with Ringer's solution, which was also used as the experimental buffer. 1 μM capsaicin (Sigma-Aldrich) and 10 mM, pH 7.4 calcium chloride solution (VWR) were loaded into the multifunctional pipette, and the microscopy experiment was

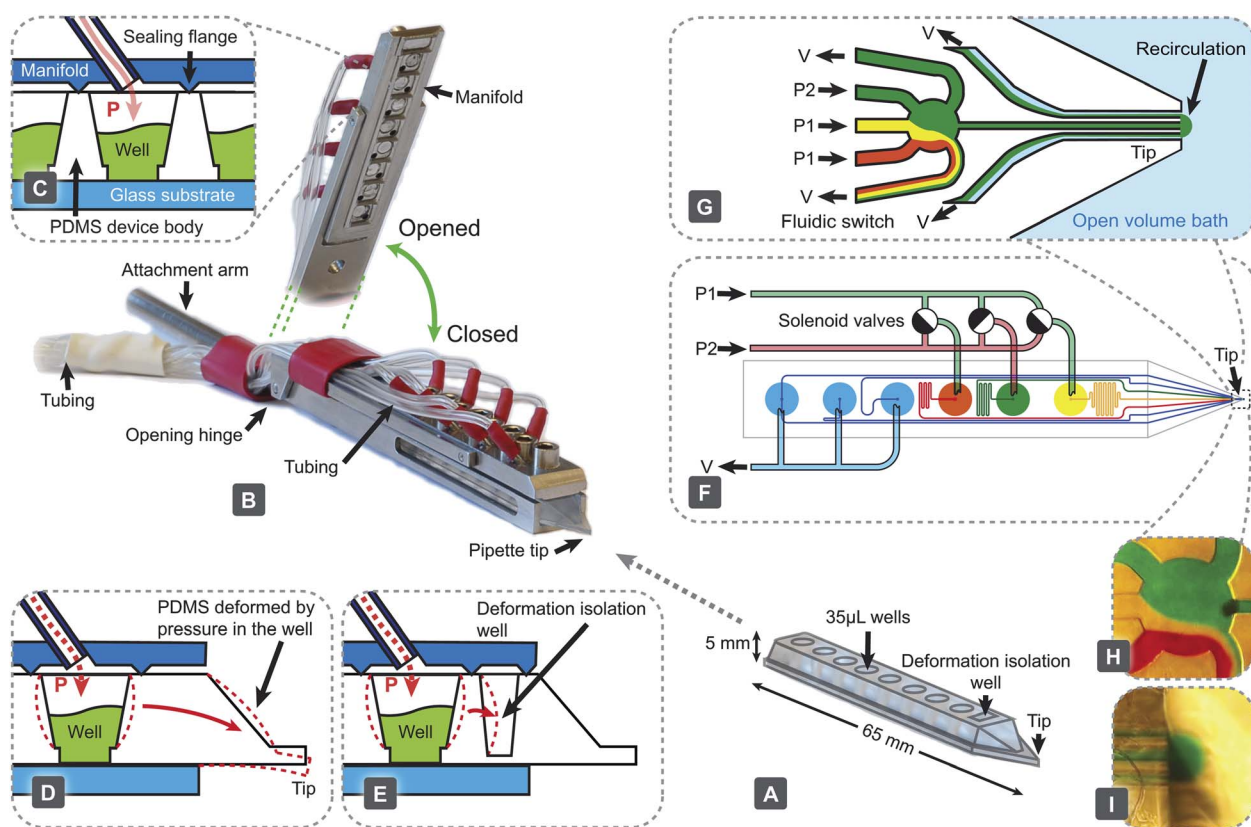


Fig. 1 The multifunctional pipette: components, construction and setup. (A) The PDMS microfluidic pipette tip. (B) The holder, shown in a closed state holding the tip. An elevated angle is also displayed to highlight the manifold's interfacing structure, which contacts the tip. (C) Pneumatic interface between the holder and the tip is formed with sharp flanges protruding from the manifold, which are pushed into the PDMS surrounding the well. Each well has an individual connection, through which pressure can be controlled. (D) Deformation associated with pressure change within the well. (E) Implemented solution to (D), minimising the effects through the use of an isolation well. Exemplary circuitry of a fast 3-solution switch, showing the driving mechanism (F) and the microfluidic switching junction near the tip (G). Microscopy images of a fluidic switching junction (H) and a recirculation volume (I) loaded with coloured water.

performed immediately thereafter. Fluorescence intensity was measured with a Leica DM IRE2 confocal microscope equipped with a Leica TCS SP confocal scanner, an oil-immersion 40× 1.25 NA Leica objective, and Leica Confocal Software (v2.61). Fluorescent intensity was measured from single cells, with excitation at 488 nm and emission collected between 505 and 600 nm.

Simulations

Simulations were performed with COMSOL Multiphysics 4.1, combining models of laminar flow (spf) and transport of dilute species (chds) in stationary and transient 3D models. In the simulations, the mechanical properties used for PDMS were: Young's modulus 1.8 MPa and Poisson's modulus 0.45,¹⁸ the

viscosity of water was 1 mPa s and the diffusivity of fluorescein was $5 \times 10^{-10} \text{ m}^2 \text{ s}^{-1}$.

Results and discussion

Device

In order to demonstrate the multi-functionality of the pipette, we implemented a valveless superfusion device, able to switch between three solutions. Functionally, it is similar to superfusion systems made from glass tubing,¹⁹ but has significantly better reproducibility of geometry and simpler handling. Compared to the valveless switch we have reported previously,⁴ the current device does not have dedicated switching channels, removing the

Table 1 Characteristics of microchannels and fluidic circuitry

Characteristic	Symbol	Value	Unit
Channel height	H	20	μm
Channel widths	W	20 and 40	μm
<i>Flow conductance of channels</i>			
Supply/waste/recirculation (well \rightarrow tip)	G	37	$\text{nL s}^{-1} \text{ bar}^{-1}$
Outlet (switch \rightarrow tip)	G_o	500	$\text{nL s}^{-1} \text{ bar}^{-1}$

restrictions of the resistance of the output channel, connecting the switch to the tip. Switching in our current device occurs when pressures are changed between individually supplied wells (Fig. 1F and G and Movie S1†). A reverse concept has been demonstrated, to sort fractions of a continuous fluid stream, using an inverse flow direction.²⁰

Two levels of pneumatic pressure are supplied by the attached pressure control device, and fast switching is achieved through the use of miniature solenoid valves (Fig. S3†). Two pressure levels are needed to avoid backflow from the switch to any of the supply channels, which would cause unwanted mixing of these solutions. For this switching principle to function properly, the pressures applied need to meet certain conditions. The flow rates in the two inactive (switched off) channels have to be smaller than the flow rates to one of the waste channels. In this case only one solution is directed to the output,

$$2G(P_1 - p) < (p + V)G$$

where P_1 denotes the pressure in the solution wells, which are in the “switched off” state, P_2 is the pressure in the wells in the “switched on” state, G and G_0 are the flow conductances as defined in Table 1, V is the vacuum (negative pressure) applied to waste and recirculation wells, and p is the pressure inside the switch junction,

$$p = \frac{G}{5G + G_0}(P_2 + 2P_1 - 2V)$$

Crucially, there must be no backflow from the switch to the wells in the “switched off” state, requiring $p < P_1$. Finally, for typical recirculation settings, the total inflow has to be twice the outflow, requiring $VG \approx pG_0$.

Considering these conditions, and the physical performance limits of our pressure controller, we can derive a set of suitable operation parameters, which are summarized in Table 2. The number of solutions to be switched can be increased, which in the case of our system is limited to seven, as at least one well has to be reserved for recirculation and waste.

Pressure control in elastic devices, such as PDMS, requires attention to possible elastic deformation, which might compromise positioning precision (Fig. 1D). To mitigate motion of the tip during pressure pulsing, we have added a deformation isolation well to the tip and introduced additional flanges toward the front of the manifold (Fig. 1E). These measures reduce unwanted motion during most operations to less than 4 μm in the axial direction (pressure 0.5 bar) (Fig. S4†).

In an attempt to facilitate a more unified design, both the molding tools and the holder have a universal geometry, while

the internal circuitry of the pipette tip can be re-designed to address specific experimental needs. This allows very rapid customization, requiring only fabrication of a new channel molding master.

Solution exchange

Solution exchange performance was characterized using fluorescence microscopy. As epi-fluorescence can only measure the solution exchange within the bulk volume, we combined it with TIRF microscopy, to probe the solution exchange in a confined volume close to the surface of a coverslip, which should provide a better representation of the efficiency of solution exchange around adherent cells than averaging over the recirculation volume. Using high flow rates, the time constant of concentration increase near the surface was found to be 219 ± 94 ms, while concentration decrease was 154 ± 76 ms (Fig. 2), both are sensitive to the positioning of the pipette. The slightly lower fall time can be due to a diffusional dilution effect caused by the surrounding environment, which contains no fluorescent molecules. The solution exchange time in the bulk volume using epi-fluorescence was measured to be ~ 130 ms.

To elucidate the factors influencing the solution exchange time, we carried out a theoretical evaluation, based on analytical

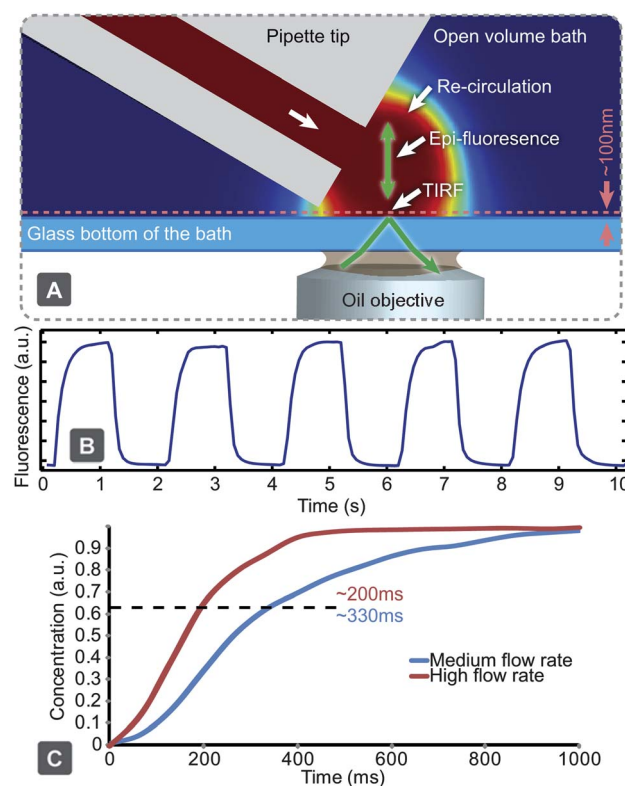


Fig. 2 Characterising solution exchange times. (A) Experimental setup using TIRF microscopy, to monitor solution exchange dynamics near the sample surface. The same setup can be used for epifluorescent measurements of a deeper region, through modification of the excitation angle. (B) Fluorescent intensity measurements of periodic solution exchange near a glass surface using TIRF. (C) Concentration rise time near the surface with high and medium flow rates (~ 10 and ~ 5 nL s^{-1} , respectively).

Table 2 Examples of operation settings

Parameter	High flow rate	Medium flow rate	Low flow rate
P_2/bar	0.9	0.5	0.3
P_1/bar	0.2	0.06	0.035
V/bar	0.4	0.19	0.094
Outflow $I_0/\text{nL s}^{-1}$	13.5	6.5	4.9
Run time/min	16	~ 30	~ 45 to 120

models and finite element simulations (COMSOL). The results are summarized in Table 3, Fig. 3, and in the ESI (Fig. S6–S9†). The largest contribution arose from the flow rate rise time in the supply channel, which is due to the elasticity of PDMS, especially at the end section of the channel, where one of the walls is a thin, unsupported and easily deformable PDMS layer (Fig. S6†). Channel deformability leads to compliance, the hydraulic analogue of capacitance.²¹ When coupling this with hydraulic resistance of the channel, a low-pass RC filter is formed, dampening rapid pressure changes, leading to slower flow rate changes towards the end of the channel (Fig. S7†). Thereafter the concentration pulse passes through the outlet channel, where it is subject to dispersion,²² which broadens the pulse (Fig. S8†).

Once the solution has exited the channel, it has to reach the surface-immobilized cell. Since flow near the surface is restricted due to friction, a short final distance has to be passed mainly by means of diffusion, which occurs at a slower rate (Fig. 3A). Other factors, such as filling the dead volume of the switch, inertia of the liquid and external pressure control, have only minor contributions (Table 3 and Fig. 3B). To improve the switching speed, the outlet channel can be shortened. Enlarging the channel dimensions, which increases the flow rate, would also increase the speed (Fig. S9†). This will reduce the experimental run time as the liquid in the supply wells will be consumed at an accelerated rate. A practical solution in many experiments, since short and long time-scale processes are typically not studied simultaneously, would be to minimize flow rates during setup and positioning (“stand-by mode”), then to only increase supply pressures when high switching speeds are desired. We have implemented such structured modes of operation into the application software. A steeper positioning angle, which would direct the flow closer to the surface, and fabrication in hard materials would be other feasible options to reduce solution exchange times.

The use of a thicker bottom layer for channel sealing can cause opposing effects, reducing, on one hand, the elasticity of the channel, while on the other hand increasing the distance between the channel outlets and surface. Based on simulations and estimations, the exchange speed in this kind of devices could be improved to ~10 to 50 ms (increased flow rates, minimising outlet channel length to the open volume, and use of hard materials for the device). When evaluating fluidic exchange behaviour, it is also necessary to consider the nature of the desired active agent and its diffusivity in solution.

Table 3 Components contributing to the solution exchange time and the dependence of micro-channel geometries l and w , bottom thickness d and flow rate Q (derivations and calculations are supplied in the ESI)

Component	τ /ms	Scaling \propto
Solenoid valves	2	
External tubing	4	
Inertia	0.5	$w^2 l^{-1}$
Supply channel	30	$w^{-1} P d^{-1}$
Dead volume of the switch	2.5	$w^3 Q^{-1}$
Outlet channel	~70	$w^2 P^{0.5...1} Q^{-0.5...-1}$
Outlet to cell	~40	
Sum	~150	

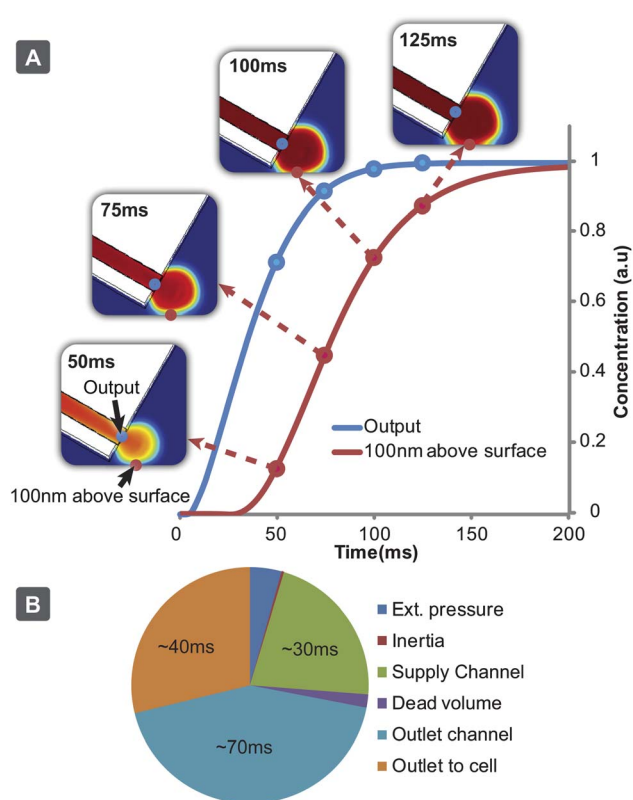


Fig. 3 Results of a computer simulation to model the fluidic exchange times close to the sample surface. (A) Concentration rise time near the surface (100 nm above) and at the channel output. (B) Contributing factors and influence to the solution exchange time, based on experimental results, simulations and calculations.

Application to single cell studies

Delivery of stimuli to individual cells allows for exquisite analysis of cellular function while enabling the mapping of population heterogeneity. However, greater levels of detail can be extracted by simultaneous exposure of small collectives of cells, where individual cell analysis can be made on their response. The multifunctional pipette offers a flexible way to address either situation, through control of recirculation flow and positioning (Fig.S5 and Movie S2†).

An adherent CHO cell culture, expressing hTRPV1, was used to demonstrate the use of the device for chemical stimulation of single cells, through the sequential delivery of active compounds to selected cells from within a collective. The cells were pre-treated with a cell-penetrating, mildly fluorescent species, which upon entering the cell is enzymatically converted into a calcium chelator. In the presence of calcium ions this molecule forms a highly fluorescent complex, which can be readily detected. Using the multifunctional pipette, the dye loaded cells were first treated with a 10 s pulse of capsaicin to activate the hTRPV1 channel, then washed for 5 s and treated with a 10 s pulse of Ca^{2+} . After 50 s, the Ca^{2+} pulse was repeated. Cells that had been exposed to capsaicin became Ca^{2+} permeable, which was observed by their rapid increase in fluorescent intensity, whereas Ca^{2+} applied to cells not treated with capsaicin demonstrated no significant increase. A slight shape change was observed during

the course of the experiment, likely due to a slight osmotic pressure imbalance.

Interestingly, we observed several different types of cellular response, as depicted in Fig. 4C. Some cells exhibited a strong response to the first calcium pulse, but not to the second (Cell 1), while others responded to both pulses (Cell 2). Varied loading efficiencies of the indicator dye within the cell population gave a wide range of initial fluorescence intensity values. One such cell was selected from the background population outside the recirculation zone (Cell 3) and demonstrated no response to the calcium pulses, indicating fluidic isolation from the targeted cells. The observed variable calcium responses may be cell population heterogeneity, or flow velocity dependent, as lateral positioning with respect to the pipette tip will determine the flow rate. Some cells situated within the centre of the recirculation zone (marked with a dashed line) exhibited behaviour similar to an internal calcium release. Capsaicin application and high flow velocities within this region may have contributed to this type of cellular response.

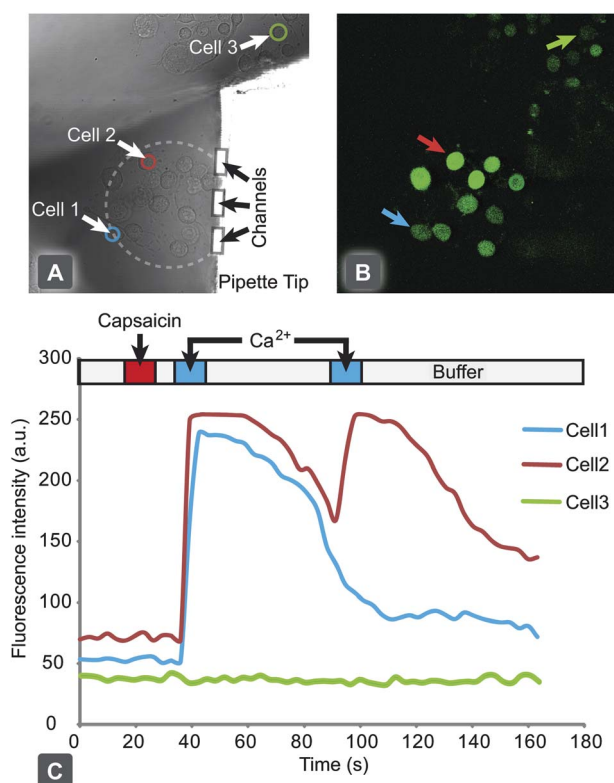


Fig. 4 Chemical stimulation and response of individual *hTRPV1* expressing CHO cells, through activation with capsaicin. (A) Bright field microscopy image of adherent cell culture of *hTRPV1* expressing CHO cells, with the pipette tip targeting a small collective. (B) Confocal fluorescent micrograph of Calcium GreenTM loaded cells after stimulation with capsaicin and subsequent exposure to Ringer's solution, spiked with 10 mM calcium chloride. (C) A graph of individual cellular responses to the application protocol, with the delivery times highlighted above. Cells 1 and 2 are within the recirculation zone and display a positive activation response. Cell 3 is a representative cell from the background outside of the stimulation zone.

Conclusion

We have created a free-standing multifunctional pipette for highly localized perfusion in single cell experiments. It addresses the needs for facile setup, handling, and application. The pipette was developed from an HCF principle, enabling contamination-free confinement of one miscible liquid inside another. Molding in PDMS allows pipette fabrication at low cost and high flexibility, as compared to microfluidic probes made of hard materials,^{3,11} where fabrication requires complex processing equipment such as a mask-aligner, deep reactive ion etching (DRIE), bonder, polishing tools and also a cleanroom environment. Soft-lithography requires only a photolithographically fabricated master, which can be re-used for many cycles, a spin-coater, and an inspection microscope. A plasma chamber was used for bonding our device together, which provides better reproducibility than other attachment techniques. An additional benefit of molded devices is that solution wells can be easily integrated into the same component piece. Apart from easy handling and lower reagent consumption, the use of integrated wells completely overcomes the typical problem of the dead volume of external tubing, which is usually significantly larger than the volume of the microchannels. A major benefit in comparison to other microfluidic HCF devices is the possibility to approach the recirculation volume with other probes, such as patch pipettes, optical fibres, or electrodes. It can be used together with upright microscopes at lower application angles, as the sharp tip produces minimal optical disturbance (shadowing) of a transmission image, which can be minimised using oblique and/or ring illumination.

We have also demonstrated that the internal fluid processing circuitry can be contained within a recirculation device, minimizing on-chip dead volumes and decreasing the solution switching times. Hard material microfluidic probes could offer advantages when very small recirculation volumes are desired, since vertical configuration and circulation in small clefts allow for forcing liquid circulation closer to the surface and to achieve higher Péclet numbers. This is mostly favourable for chemical surface processing, but less applicable for cell cultures and tissue, as high shear stress can move, detach and destroy cellular structures. Moving away from elastomeric materials would also remove device compliance, which will allow faster solution switching.

In summary, we believe that the versatility, simplicity of design, and ease of integration of the multifunctional pipette, either as a primary or supporting device, will impact single cell and tissue culture research, most prominently in neuroscience and pharmacology, where it can amend current superfusion techniques and open new application areas.

Acknowledgements

This research was funded by the European Research Council (ERC grant), Swedish Research Council (VR), the Knut and Alice Wallenberg Foundation, the Swedish Strategic Research Foundation (SSF), and the National Institute of Health (NIH). We thank AstraZeneca R&D CNS&P Södertälje for the cell line stably expressing the human TRPV1 ion channel and Erik T. Jansson and Carolina Boström for maintenance of the cell line.

Notes and references

- 1 S. K. W. Dertinger, D. T. Chiu, N. L. Jeon and G. M. Whitesides, *Anal. Chem.*, 2001, **73**, 1240–1246.
- 2 M. A. Unger, H. P. Chou, T. Thorsen, A. Scherer and S. R. Quake, *Science*, 2000, **288**, 113–116.
- 3 D. Juncker, H. Schmid and E. Delamarche, *Nat. Mater.*, 2005, **4**, 622–628.
- 4 A. Ainla, E. T. Jansson, N. Stepanyants, O. Orwar and A. Jesorka, *Anal. Chem.*, 2010, **82**, 4529–4536.
- 5 K. V. Christ and K. T. Turner, *Lab Chip*, 2011, **11**, 1491–1501.
- 6 J. H. Gaddum, *J. Physiol.*, 1961, **155**, P1.
- 7 S. Kottegoda, I. Shaik and S. A. Shippy, *J. Neurosci. Methods*, 2002, **121**, 93–101.
- 8 N. A. Cellar, S. T. Burns, J. C. Meiners, H. Chen and R. T. Kennedy, *Anal. Chem.*, 2005, **77**, 7067–7073.
- 9 O. Feinerman and E. Moses, *J. Neurosci. Methods*, 2003, **127**, 75–84.
- 10 H. Shiku, T. Yamakawa, Y. Nashimoto, Y. Takahashi, Y.-s. Torisawa, T. Yasukawa, T. Ito-Sasaki, M. Yokoo, H. Abe, H. Kambara and T. Matsue, *Anal. Biochem.*, 2009, **385**, 138–142.
- 11 G. V. Kaigala, R. D. Lovchik, U. Drechsler and E. Delamarche, *Langmuir*, 2011, **27**, 5686–5693.
- 12 R. D. Lovchik, U. Drechsler and E. Delamarche, *J. Micromech. Microeng.*, 2009, **19**, 115006.
- 13 A. Queval, N. R. Ghattamaneni, C. M. Perrault, R. Gill, M. Mirzaei, R. A. McKinney and D. Juncker, *Lab Chip*, 2009, **10**, 326–334.
- 14 D. Momotenko, F. Cortes-Salazar, A. Lesch, G. Wittstock and H. H. Girault, *Anal. Chem.*, 2011, **83**, 5275–5282.
- 15 W. K. Raja, B. Gligorić, J. Wyckoff, J. S. Condeelis and J. Castracane, *Integr. Biol.*, 2010, **2**, 696–706.
- 16 H. Tavana, A. Jovic, B. Mosadegh, Q. Y. Lee, X. Liu, K. E. Luker, G. D. Luker, S. J. Weiss and S. Takayama, *Nat. Mater.*, 2009, **8**, 736–741.
- 17 Y. T. Tang, J. Kim, H. E. Lopez-Valdes, K. C. Brennan and Y. S. Ju, *Lab Chip*, 2011, **11**, 2247–2254.
- 18 F. Schneider, T. Fellner, J. Wilde and U. Wallrabe, *J. Micromech. Microeng.*, 2008, **18**.
- 19 N. S. Veselovsky, F. Engert and H. D. Lux, *Pfluegers Arch.*, 1996, **432**, 351–354.
- 20 C. A. Baker and M. G. Roper, *J. Chromatogr., A*, 2010, **1217**, 4743–4748.
- 21 H. Bruus, *Theoretical Microfluidics*, Oxford University Press, 2007.
- 22 *Physicochemical Hydrodynamics*, ed. R. F. Probstein, John Wiley & Sons, 1995.

A Multifunctional Pipette

Alar Ainla,* Gavin D. M. Jeffries, Ralf Brune, Owe Orwar and Aldo Jesorka

Electronic Supplementary Information (ESI)

Table of contents

Table of contents	1
Supplementary methods	2
Fabrication	2
Supplementary figures.....	3
Fig S2 (Tube optimization)	3
Fig S3 (Pneumatic control system).....	4
Fig S4 (Tip stability)	5
Fig S5 (Single cell solution delivery)	5
Supplementary analysis (Solution exchange times)	6
Inertia	6
Supply channel.....	6
Dead volume of the switch	8
Fluid dispersion in the outlet channel	8
Outlet to cell	9
Scaling	9
Captions of supplementary movies	10
SMovie 1 (Positionable solution exchange)	10
SMovie 2 (Individual cell-targeted delivery)	10

Supplementary methods

Fabrication

Microchannel mold. All microchannel molds were prepared in the ISO100 cleanroom facility MC2 at Chalmers University of Technology. In order to yield $\sim 20\ \mu\text{m}$ thick SU-8 structures, SU-8-10 was dispensed onto 4" wafer and spun for 30 s at 1600 rpm (acceleration: 5 s till 500 rpm and 4 s till 1600 rpm), followed by baking for 2.5 min at $65\ ^\circ\text{C}$ and 6 min at $95\ ^\circ\text{C}$. Thereafter the resist was exposed ($200\ \text{mJ}/\text{cm}^2$) through a chromium mask in a Karl Süss MA6 contact mask aligner (G-line, $5\text{--}6\ \text{mW}/\text{cm}^2$), post baked for 1 min at $65\ ^\circ\text{C}$ and 3 min at $95\ ^\circ\text{C}$ and developed for 4 min in SU-8 developer (1-methoxy-2-propyl acetate). Finally the molds were cleaned by spraying with isopropanol and water, blow dried, ashed in a Plasma Therm Batchtop PE/RIE (oxygen plasma, 1 min, 50 W, 250 mTorr) and hard baked at $200\ ^\circ\text{C}$ for 30 min. Before use all masters were anti-adhesion-treated for 5 min with dichlorodimethylsilane by exposing the surfaces to the vapors under a Petri dish cover. The **Fabrication of polydimethylsiloxane (PDMS) pipettes** is illustrated in figure S1.

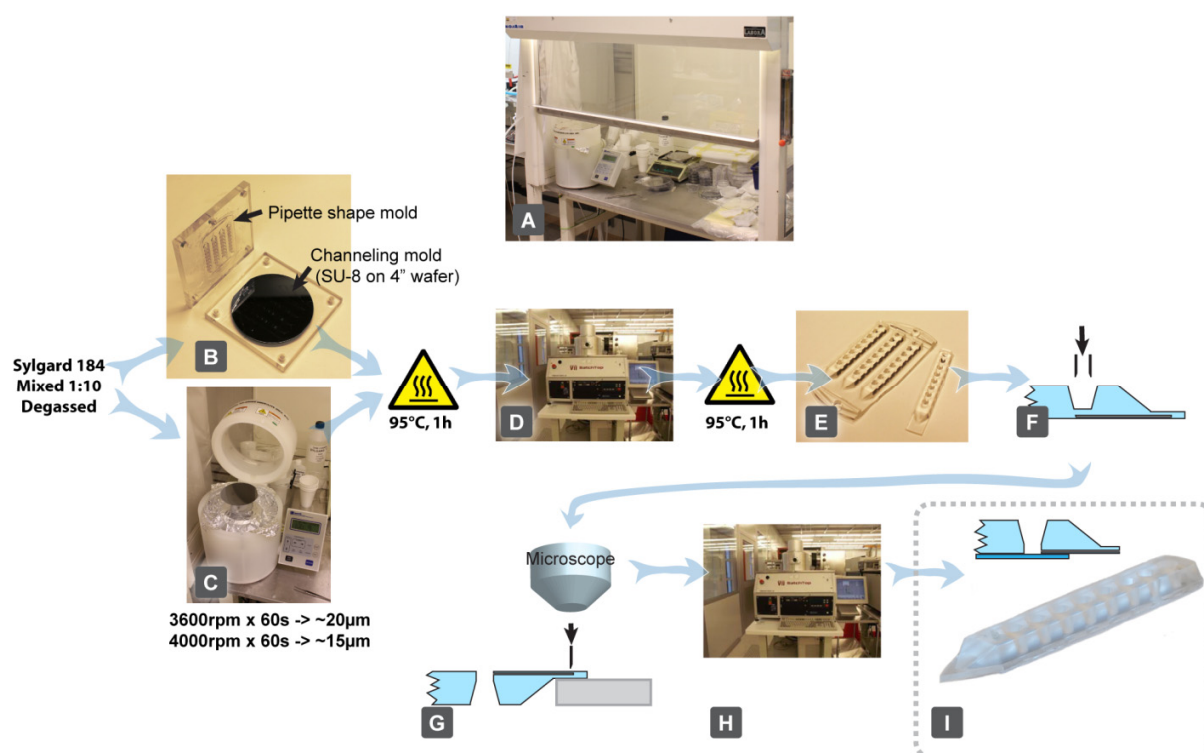


Fig S1. Pipette fabrication by means of replica molding. PDMS casting and curing was performed under a laminar flow hood (A) in a standard laboratory. PDMS pre-polymer (Dow Corning Sylgard 184) was prepared by mixing parts A and B in a ratio 10:1 (wt:wt) and degassed for 15 min in a vacuum desiccator. Subsequently the PDMS mixture was cast into the mold (B). This mold is a combination of a machined polycarbonate upper part, defining the macroscopic shape of the pipettes, and a lower plate supporting a 4" wafer master. The thin PDMS layer was spin-coated onto an unstructured 4" wafer (C). Both parts were cured in an air circulation oven at a temperature of 95°C for 1 h. Thereafter, the slab containing four pipette structures was removed from the mold. Both the slab and the thin PDMS layer, still attached to the wafer, were plasma treated (Plasma Therm Batchtop PE/RIE at 250 mTorr, 85 W, 10 sccm O_2 for 10 s) (D) and bonded to each other, followed by a baking step (95°C for 1h) to strengthen the bonding. The composite slab was then removed from the wafer and the individual pipettes were cut out (E). Subsequently the wells were punched out (F). Honing of the tip shape was performing using a microtome blade while observing the cutting region using a standard inspection microscope (G). Finally, the shaped PDMS part was plasma bonded onto a rectangular glass support (H), resulting in a functional "ready to use" tip (I). The whole process has a high yield and can be easily scaled through the use of larger wafers. Less scalable steps are the manual tip cutting (G), which currently requires individual alignment of the cutting blade and bonding to the glass support (H). It also requires prior alignment of glass and PDMS pieces. However, tools to facilitate or automate these steps are conceivable.

Supplementary figures

Fig S2 (Tube optimization)

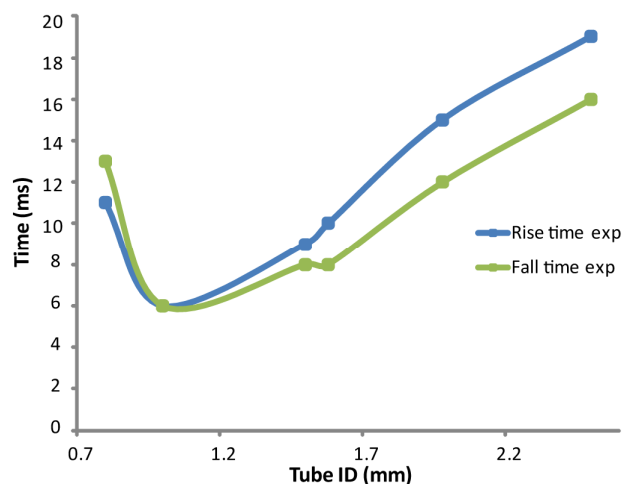


Fig S2. Pressure propagation in supply tubes connecting the valve controller to the manifold, depending on their inner diameter (ID). In order to optimize the fluid switching speed, we compared different tubing materials and internal diameters. All the tubes tested were 1.0 m long. Narrow tubes have higher fluidic resistance hindering gas flow (tube limited), whereas wide tubing has a high volume with lower flow resistance, but needs to be filled (supply limited). For our pump supply, the optimal tube size was found to be 1 mm I.D., exhibiting both exponential rise and fall times of 6 ms. Rise and fall times without tube were measured to be 2 ms, indicating for a 1m section, the tube contributes with 4 ms.

Fig S3 (Pneumatic control system)

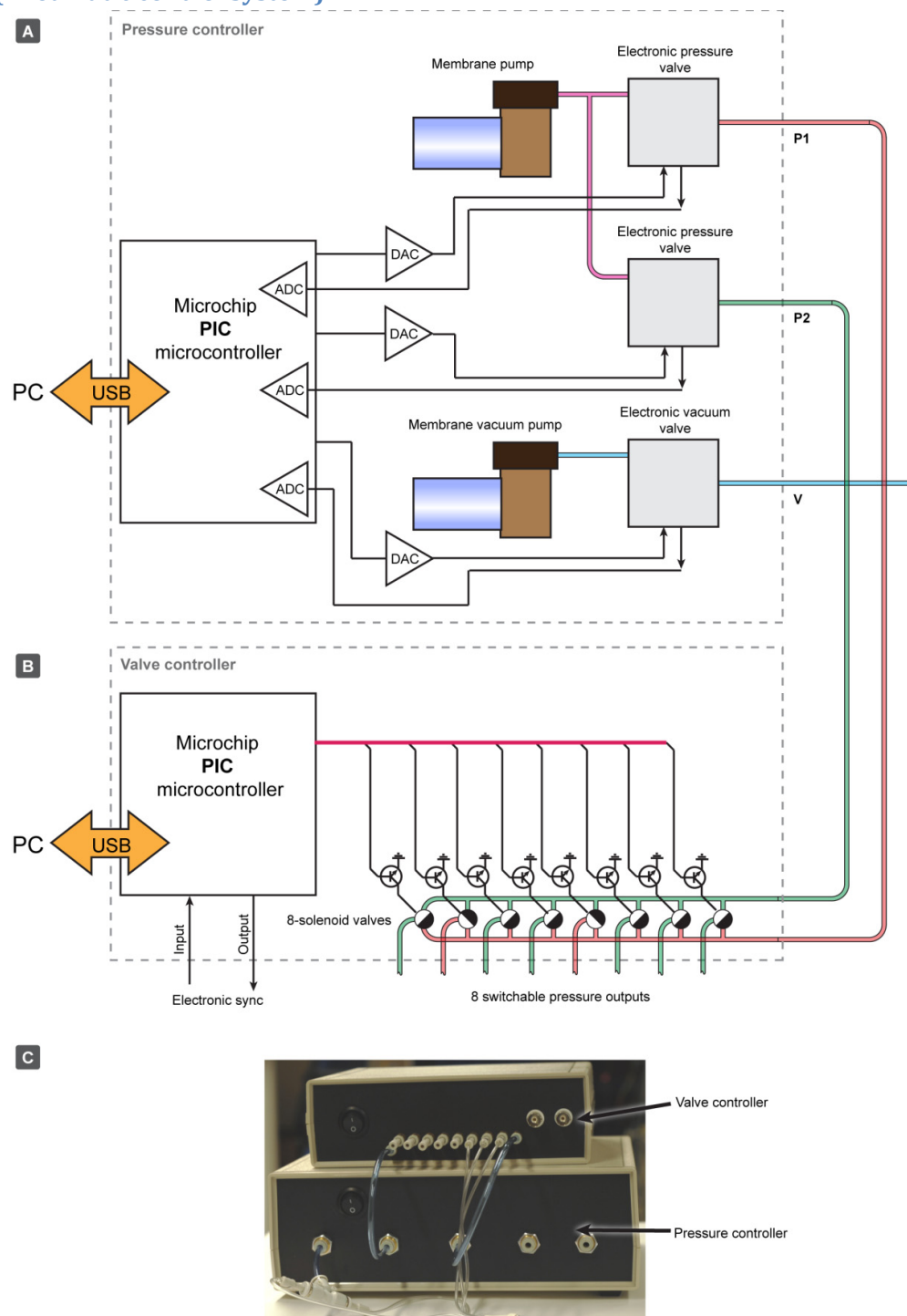


Fig S3. Pneumatic control schematic and assembly. The components were purchased from SMC Sweden (pumps, electronic valves), Pneumadyne Inc. (solenoid valves) and ELFA AB (all other parts). The control unit was divided into two subunits: pressure controller (A) and valve controller (B). The control electronics are based on a PIC18F4550 microcontroller, interfaced to a PC via USB 2.0. Both pneumatic controller subunits (C) were equipped with 4mm push-fit connectors, which allow for quick reconfiguration, depending on the experiment and the type of pipette tip used.

Fig S4 (Tip stability)

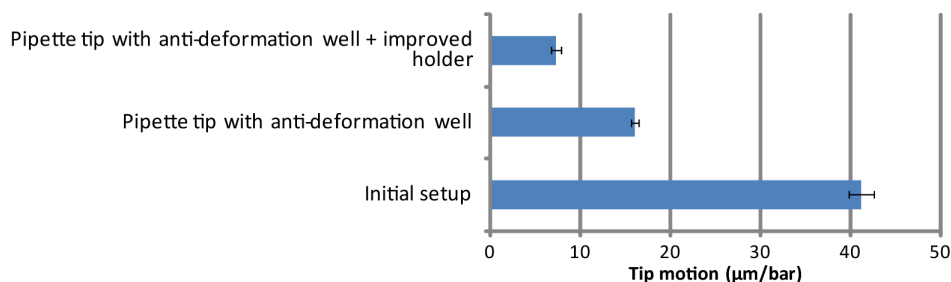


Fig S4. Minimizing tip displacement under operation. Due to material elasticity, the PDMS can deform and cause the pipette tip to change position by several μm when the pressure in the wells is changed. The tip displacement is mostly axial, with respect to the sample. This effect can be comparatively large when the pressure change takes place in the first well, i.e. closest to the tip. In our initial setup we observed elastic displacement of up to $40 \mu\text{m}/\text{bar}$. Tip displacement can be also caused by deformation of a structurally weak tip holder. To reduce tip motion we added a deformation isolation well and upgraded the holder design to improve its structural strength. After these changes the motion was reduced to $\sim 7 \mu\text{m}/\text{bar}$. In typical experiments, the pressure steps are $< 0.5 \text{ bar}$, yielding positional stability better than $4 \mu\text{m}$.

Fig S5 (Single cell solution delivery)

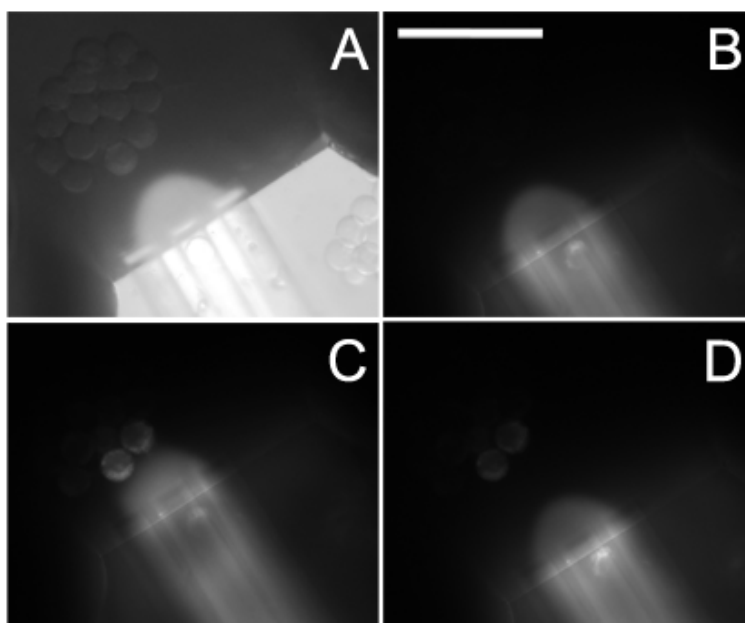


Fig S5. Targeted delivery to individual HEK293 cells by means of the multipurpose pipette. The flow recirculation is maintained throughout the experiment, thus delivery to the cell is controlled through positioning of the pipette tip. A small isolated patch of HEK293 cells adhered to a glass coverslip is approached. Both recirculation volume and cell colony are visible in a combined brightfield and fluorescence image (A). Initially the cells contain no fluorescently labelled species (B). Individual cells from the collective are targeted, and a Rhodamine B solution is delivered to label the cells (C). The label remains inside the cells upon retraction of the pipette. However, progressing photobleaching diminishes the fluorescent signal (D). The scale bar in panel B represents $90 \mu\text{m}$.

Supplementary analysis (Solution exchange times)

Here we provide a breakdown of the components contributing to the solution exchange time. Solenoid valves and external tubes were characterized experimentally (Fig. S2).

Inertia

If we change pressures and therefore the flow rates, the liquid has to be accelerated, which happens not instantaneously.

$$A\Delta p = A(p - QR) = \rho Va$$

Where A is the cross section area, p is applied pressure change, Q is the flow rate, R is the fluidic resistance of the channel, ρ is the density of the liquid, V is the volume of the channel and a is the average acceleration

$$A(p - QR) = \rho \frac{dQ}{dt}$$

$$\frac{-\rho}{AR} \int_0^q \frac{dQ}{Q - \frac{p}{R}} = \int_0^T dt$$

$$\frac{-\rho}{AR} \ln \left(1 - \frac{qR}{p} \right) = T$$

If we consider an exponential rise of the flow rate then $q = (1 - e^{-1}) \frac{p}{R}$ and

$$\tau = \frac{\rho}{AR}$$

In our system: $A = 20 \cdot 40 \cdot 10^{-12} \text{ m}^2 = 8 \cdot 10^{-10} \text{ m}^2$, $R = 2.8 \cdot 10^{15} \frac{\text{m}^3}{\text{s Pa}}$, $\rho = 1000 \frac{\text{kg}}{\text{m}^3}$

$$\tau = 0.45 \text{ ms}$$

Supply channel

Channel deformation was also studied using COMSOL models for structural mechanics coupled with a moving mesh (Arbitrary Lagrangian-Eulerian technique) (Fig. S6). The necessary mechanical parameters of Dow Corning Sylgard 184 PDMS were reported previously (F. Schneider, T. Fellner, J. Wilde, U. Wallrabe, *J. Micromech. Microeng.*, 2008, **18**, 065008). As a result, a roughly linear dependence was found between the applied pressure and a subsequent volume increase (at 1 bar the channel volume increases roughly 40%). This gives a specific fluidic capacitance of channel c

$$c = \frac{dC}{dl} = 3.2 \cdot 10^{-15} \frac{\text{m}^2}{\text{Pa}}$$

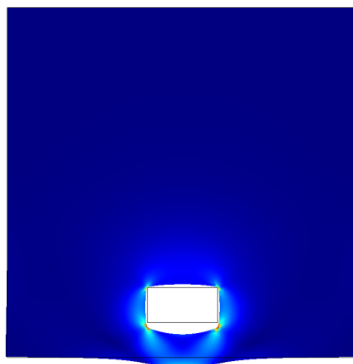


Fig S6. PDMS channel deformation at an applied internal pressure of 1 bar. The largest channel deformation is directed towards the thin bottom layer. PDMS channels extending into the bulk of the device contribute much less, $c \approx 1 \cdot 10^{-15} \frac{m^2}{Pa}$, but this is harder to estimate accurately due to complex device geometry.

Flow rate propagation in a fluidic RC-line

If we look the channel it is a one dimensional conducting line

$$\frac{L}{R} \frac{dp}{dx} = W = \frac{dQ}{dt}$$

$$\frac{dW}{dx} = \frac{cdp}{dt}$$

$$\frac{L}{Rc} \frac{d^2p}{dx^2} = \frac{dp}{dt}$$

Differential equations with this form are known as diffusion or thermal conductance equations. We can solve it for 1D form in COMSOL. For channels, of which 41mm are in supported and 10mm in unsupported PDMS. This yields a rise time of ~30 ms. (Fig. S7)

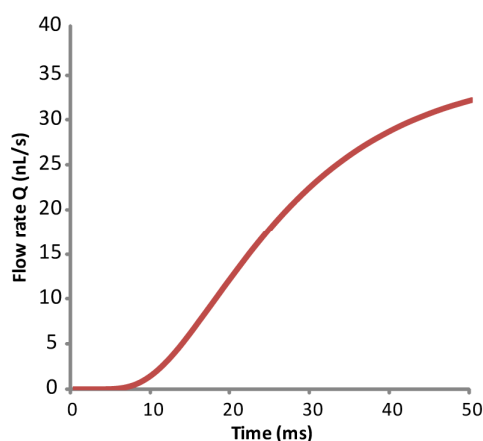


Fig S7. Results of a COMSOL model, estimating the increase of the flow rate at the end of the supply channel after applying a pressure pulse to the entrance to the channel (well).

Dead volume of the switch

For fluid switching to occur, the fluid front has to move over the output channel and a certain volume of the switch cavity has to be filled, requiring fluid flow

$$\tau = \frac{VR}{\Delta p}$$

This volume is ~0.03 nL, which for a pressure step of 0.3 bar results in a contribution to the solution exchange time of ~2.5 ms.

Fluid dispersion in the outlet channel

During the transport of the concentration pulse through the outlet channel, it is subject to dispersion. In our case,

$$Pé \approx \frac{(d/2)v}{D} = 250$$

where $d = 20\mu\text{m}$ is the channel dimension, $r \approx d/2$ is the approximate radius, $v = 12.5\text{ mm/s}$ is the average flow velocity corresponding to a flow rate $Q = 5\text{ nL/s}$ and $D = 5 \cdot 10^{-10}\text{ m}^2/\text{s}$ is molecular diffusivity of fluorescein (a good estimate also for other small molecules). In order to choose a suitable dispersion model, we also evaluate the ratio of channel length and radius.

$$\frac{L}{r} = 100$$

This processes is convection dominated ($Pé > 0$), but since $Pé < 10 \frac{L}{r} = 1000$, diffusion cannot be neglected. The channel length is not sufficient to establish the Taylor regime ($Pé > 0.4 \frac{L}{r} = 40$). The observed more complex regime is located in a transition region on a landscape of dispersion modes, according to R. F. Probstein, *"Physiochemical Hydrodynamics. 2nd Edition, ch. 4.6: Taylor Dispersion in a Capillary Tube"*, John Wiley & Sons, 1995. Therefore, the stepwise propagation of solute concentration through the square channel was modeled in COMSOL Multiphysics using a transient convection-diffusion simulation (Fig. S8). The concentration rise times obtained from this simulation were fitted to a power function.

$$\tau \approx 6.728[s] \cdot (L/[m])^{0.657}$$

We can compare this result with Taylor dispersion on one hand

$$\tau = (1 - e^{-1}) \sqrt{\pi \frac{d^2 L}{48 D v}} = (1 - e^{-1}) \sqrt{\pi \frac{d^4 L}{48 D Q}} \approx 0.16 \cdot d^2 \sqrt{\frac{L}{D Q}}$$

and with pure convective dispersion on another hand.

$$\tau \approx 4.21 \frac{L}{v_{max}}$$

Regime	Scaling	Rise time $L=1\text{mm}$ channel
Taylor dispersion (circular tube)	$\tau \propto d^2 L^{0.5} Q^{-0.5}$	~40 ms
Pure convection (circular tube)	$\tau \propto d^2 L^1 Q^{-1}$	~234 ms
Simulation (square tube)	$\tau \propto L^{0.657}$	70 ms

With respect to both scaling and rise time, the simulated results reside between these two pure regimes, being somewhat closer to the Taylor regime.

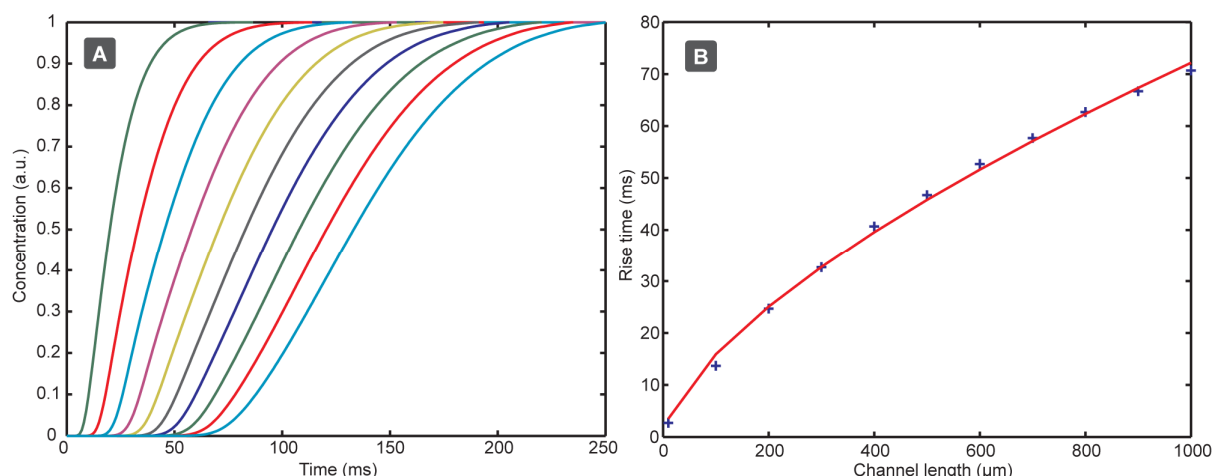


Fig S8. COMSOL Simulation of spreading from a rectangular concentration front, when passing through the output channel. (A) Evaluation for different channel lengths from $L = 100$ - $1000 \mu\text{m}$. Flow rate $Q = 5\text{ nL/s}$. (B) 63 % concentration rise times depending on channel length, fitted with a power function $\tau \approx 6.728[\text{s}] \cdot (L/[\text{m}])^{0.657}$

Outlet to cell

Solution delivery from the device outlet to the cell or surface is the most difficult to describe and to analytically solve or approximate, due to the complex interplay of recirculating flow, geometry and diffusion. Therefore a numerical COMSOL simulation was performed.

Scaling

We evaluate the scaling laws in dependence on the channel size for constant flow and pressure (Fig. S9)

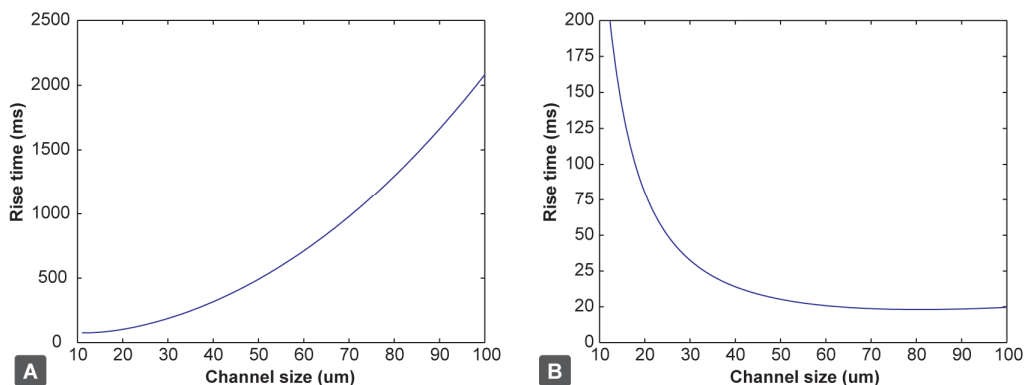


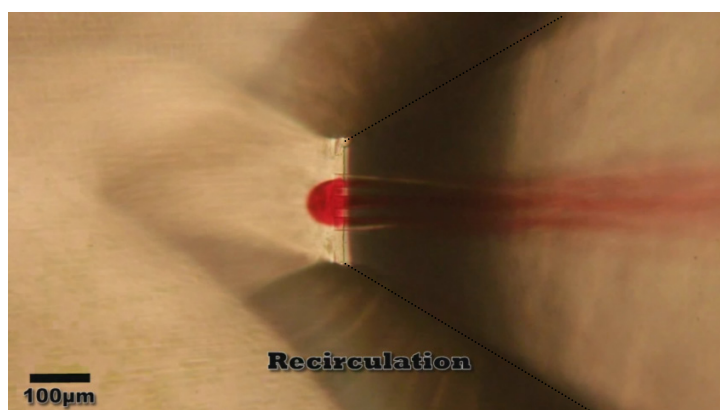
Fig S9. Scale dependence of the rise times (Sum of the components of inertia, dead volume, supply channel and output channel, but without external components) on the channel size, in case of constant flow rates (A) and constant pressures (B).

From this analysis we conclude that at constant flow rates small channels are favourable. However, when considering a constant pressure regime, using the same pressure control, a channel size range around 40 - $60\mu\text{m}$ could be most suitable for high speed switching. This increase implies that the flow rates are significantly larger (20-80x times), indicating that the integrated wells would be depleted in <1 min. However, this could be a suitable option when designing a device for applying rapid, short pulses.

Captions of supplementary movies

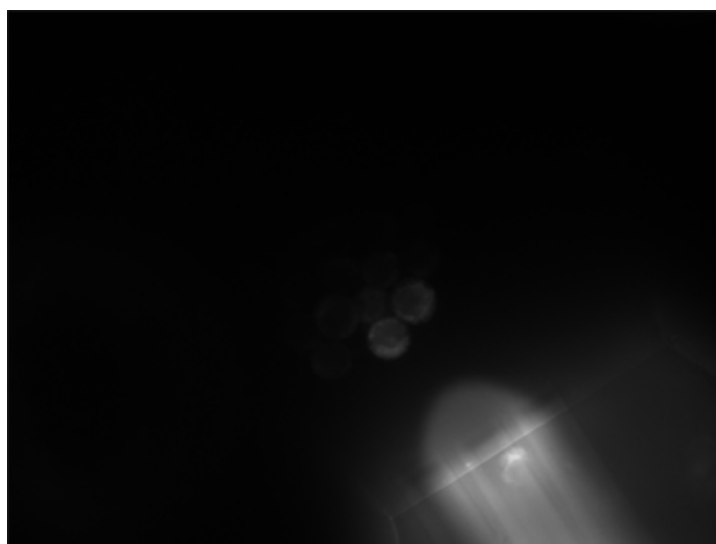
SMovie 1 (Positionable solution exchange)

This movie demonstrates the ability to reposition the flow recirculation zone during solution exchange between three colored liquids (green, yellow and red).



SMovie 2 (Individual cell-targeted delivery)

A small isolated patch of several HEK-293 cells adhered to a glass coverslip are approached by the pipette, and one or two cells are targeted for labeling with a Rhodamine B solution, delivered by the pipette. The recirculation zone is maintained throughout the clip, such that delivery is mediated through positioning. The panels for figure S5 were extracted from this movie.



PAPER

IV

Cite this: *Lab Chip*, 2012, 12, 4605–4609

www.rsc.org/loc

COMMUNICATION

Single-cell electroporation using a multifunctional pipette†

Alar Ainla,^a Shijun Xu,^a Nicolas Sanchez,^b Gavin D. M. Jeffries^a and Aldo Jesorka^{*a}

Received 16th May 2012, Accepted 20th June 2012

DOI: 10.1039/c2lc40563f

We present here a novel platform combination, using a multifunctional pipette to individually electroporate single-cells and to locally deliver an analyte, while in their culture environment. We demonstrate a method to fabricate low-resistance metallic electrodes into a PDMS pipette, followed by characterization of its effectiveness, benefits and limits in comparison with an external carbon microelectrode.

Cellular heterogeneity has been identified as one limiting factor in further understanding how biological cells function within tissues.¹ *In vitro* analysis of cells has shown that individual entities can display considerable variability, particularly stem cells, but primary cells and permanent cell lines display similar behaviour. Treating these populations as an ensemble average infers an unnatural homogeneity to the cellular functions. Individual events occurring infrequently are hidden due to this averaging effect.² The benefits of single cell analysis are driving new investigations, from both biochemical^{3–5} and analytical perspectives.^{6,7}

In order to manipulate and analyze the cellular machinery, access to its content is often required. Electroporation has proven to be a useful technique for this, allowing controllable and reversible permeabilization of the cell membrane, by application of an electric field.^{8,9} Nano-scale membrane pores, which are created in the process, allow transport of a variety of substances from small molecules to DNA and RNA across the membrane.¹⁰ As the effects of electroporation on the membrane can be achieved reversibly, the cells maintain their functions and remain viable. This allows, for example, investigation of gene expression and RNA interference.¹¹ Methods for the targeted electroporation of single-cells have also emerged,¹² utilizing microfluidic technology,^{13–15} glass capillaries^{16,17} or micro electrodes.^{18,19}

In this communication, we present a novel approach for single cell electroporation in combination with highly localized solution delivery, utilising the multifunctional microfluidic pipette.^{20,21} We demonstrated this approach using two electrode configurations; carbon fiber electrodes being externally (with respect to the device) arranged to apply the electroporation field, and fabrication of an electroporation electrode into the pipette. The second strategy has the distinct advantage of enabling solution delivery and targeted field deployment on one device, therefore avoiding the need to

position two separate probes (fluidic and electroporation electrode) near the cell.

We have previously demonstrated the utility of the multifunctional pipette for localized solution delivery and switching.²¹ Here we demonstrate the combination of this device with both on-chip and external electroporation electrodes, suitable for single-cell studies. A schematic of the procedure for the integrated electrode fabrication is shown in Fig. 1, with a detailed description given in the electronic supplementary information (ESI)†. A photograph of the connecting interface is shown in Fig. 1B, and the final fabricated electrode can be seen in Fig. 1C,D.

In a first experimental set, we used the pipette to generate a localized chemical environment (fluorescein solution) around a cell and used a carbon fiber electrode for electroporation (Fig. 2A). This poration scheme takes advantage of the tilted pipette configuration, which provides access to the recirculation zone for external probes. Microfluidic probes featuring a planar apex that covered the surface^{22,23} would not allow for such an arrangement. In a second experimental set we extended the electroporation concept by integrating an electrode into the pipette (Fig. 2B). This not only eliminates the need for two micromanipulators, but most of all simplifies operation, as only one probe needs to be positioned. The risk of damaging the rather fragile carbon fiber microelectrode is also eradicated.

Fabrication of the pipette itself is achieved by soft-lithography in polydimethylsiloxane (PDMS).²⁴ However, integrating electrodes into a PDMS structure is challenging due to the poor adhesion of metals to PDMS, hindering standard photolithographic patterning and vapor deposition of the metal tracks. Previously reported approaches to fabricate electrodes into a PDMS device include rather elaborate procedures: gold implantation from a filtered cathode voltage arc, creating a 50 nm conductive layer ($\sigma \approx 2 \times 10^5 \text{ S m}^{-1}$),²⁵ mixtures of silver particles and PDMS (AgPDMS, $\sigma \approx 2 \times 10^4 \text{ S m}^{-1}$) filled into $40 \mu\text{m} \times 100 \mu\text{m}$ channels,²⁶ mixtures of carbon nanotubes (CNTs) and PDMS ($\sigma \approx 67 \text{ S m}^{-1}$), filled into $200 \mu\text{m} \times 170 \mu\text{m}$ channels.²⁷ Additionally, injection of molten metals and alloys has been used to fabricate electrodes, for example liquid gallium ($\sigma \approx 10^7 \text{ S m}^{-1}$),²⁸ solder,²⁹ and a gallium–indium eutectic.³⁰

We fabricated our electrodes using a metal filling approach, where molten metal is pressure-driven into the channel. The main benefit of this method is ensuing high conductivity of the finished electrode. We chose Field's metal ($\sigma \approx 2.4 \times 10^6 \text{ S m}^{-1}$), a low-melting temperature non-toxic alloy, for our in-channel metal electrodes. This fabrication method is favourable due to the fast

^aDepartment of Chemical and Biological Engineering, Chalmers University of Technology, S-41296 Göteborg, Sweden

^bExploratory Unit, Sanofi-Aventis R&D, 34184, Montpellier, France

† Electronic supplementary information (ESI) available. See DOI: 10.1039/c2lc40563f

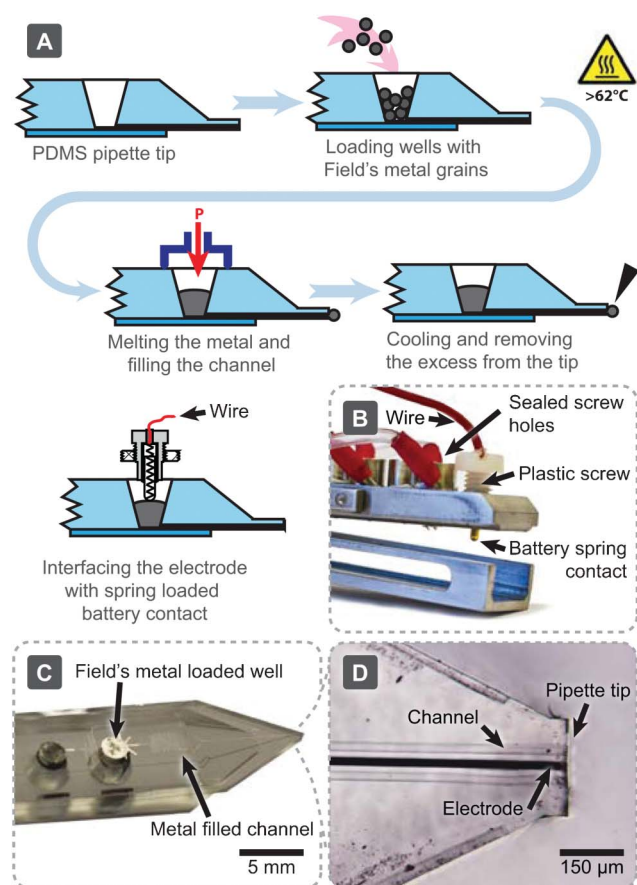


Fig. 1 Integrating electrodes into the multifunctional pipette. (A) A depiction of the fabrication procedure for Field's metal electrodes, using a common laboratory hotplate. The electrodes were electroplated with gold before use; this step is not shown. (B) A photograph of the pipette holder and electrical interface to the internal electrode. (C) Macro- and (D) micro-photographs of a pipette tip, highlighting the integrated electrode.

and simple post-processing of PDMS pipettes, which requires only a few minutes of time. No specific instrumentation or expensive materials are required. A certain disadvantage of utilizing this metal is the brittleness; therefore care has to be taken not to damage the electrode while interfacing it with the external voltage source. Too high mechanic stress applied to the metal plug in the well can break the plug apart from the molded wire in the channel. Field's metal does not wet copper wires, making soldering difficult. We found a reliable and convenient way to interface the electrode by using battery spring contacts, applying only slight pressure. Our electrodes exhibited low-resistance ($40\ \Omega$), but made the otherwise flexible pipette tip more fragile. Nevertheless, the remaining flexibility was sufficient to tolerate accidental surface collisions during micromanipulation, which would be impossible with glass pipettes. We also observed slight electrode degradation and formation of precipitation around the pipette tip during the application of electrical pulses. In order to eliminate this problem, electrochemical gold plating of the Field's metal tip was a sufficient measure. In alternative approaches, we have attempted to use silver particles ($\sim 1\ \mu\text{m}$ diameter) mixed with PDMS, as well as conductive silver pastes and epoxies. We did not succeed to fill the $20\ \mu\text{m} \times 20\ \mu\text{m}$ channels of our device. The particle suspensions penetrated only a few millimeters into the channel, after which

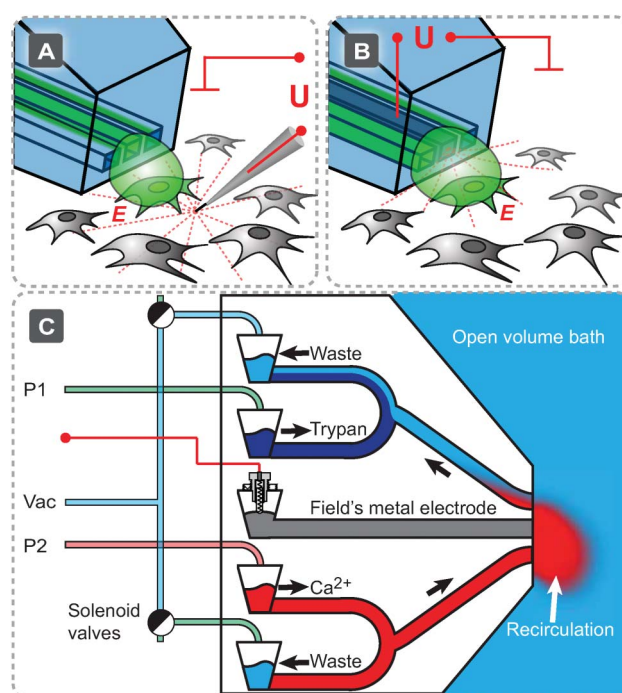


Fig. 2 Pipette configurations. (A) A combination of the multifunctional pipette with an external carbon fiber electrode for single cell electroporation and simultaneous localized solution delivery. The red dotted lines represent the electric field (simplified). (B) The multifunctional pipette with integrated electroporation electrode in the same experimental environment. The counter electrode for both configurations is located in the open bath, represented by a red ground symbol. (C) A schematic representation of a two-channel superfusion pipette, allowing multiplexing between two chemical environments: Ca^{2+} for chemical stimulation and Trypan blue for a subsequent viability test. External supply connections and solution well structures are also depicted, but are not to scale.

particulates formed and prevented further flow of the composites. Channel filling even did not succeed after applying elevated pressures (up to 3 bar) and extended times (hours). This is consistent with previous reports that these filling methods are successful only with significantly larger channels.

The NG-108-15 cells were prepared the same for both experiments, except for the second set, in which the cells were pre-loaded with a Ca^{2+} sensitive dye (Method S2†). Pipette and carbon fiber electrodes were mounted to hydraulic micromanipulators (Narishige MC-35A/MHW-3-course/fine). For superfusion, the pipette wells were loaded either with $25\ \mu\text{M}$ fluorescein solution in PBS or with $1\ \text{mM}$ calcium chloride in PBS, and with a standard Trypan blue solution for cell viability testing (Invitrogen). For electroporation, the electrodes were connected to a Digitimer DS2A flat-top pulse generator ($0\text{--}99\ \text{V}$ with adjustable pulse length and width between $1\text{--}2000\ \text{ms}$), using crocodile clips. All studies were performed using a Leica DM IRE2 confocal microscope with a $40\times\ \text{NA}\ 1.25$ oil immersed objective.

The electric field simulations were performed on COMSOL Multiphysics 4.1 with the electric currents (ec) module. The cell was assumed to be an electrically conductive volume with insulating boundaries. All currents and electric fields were treated as stationary. Detailed simulation parameters can be found in Method S4†.

In both experimental sets, the cell membrane viability was tested after electroporation, using Trypan blue as a live-dead stain. This required the pipette to have the capability to switch between the Ca^{2+} containing PBS solution, and Trypan blue staining solution. This was achieved with the microfluidic circuitry depicted in Fig. 2C. Here, interchanging P1 and P2 and switching vacuum (V) between wells enabled solution switching. Solution exchange

occurred in less than 3 s. Switching parameters for the exchange can be found in Table S5†.

Utilising the fluidic pipette to generate a recirculation zone allowed for the contamination free delivery of the desired analyte, fluorescein or Ca^{2+} , to the cell. The delivered analyte did not penetrate into the cell before application of an electroporation pulse of up to 100 V for 1–10 ms. To discover the critical

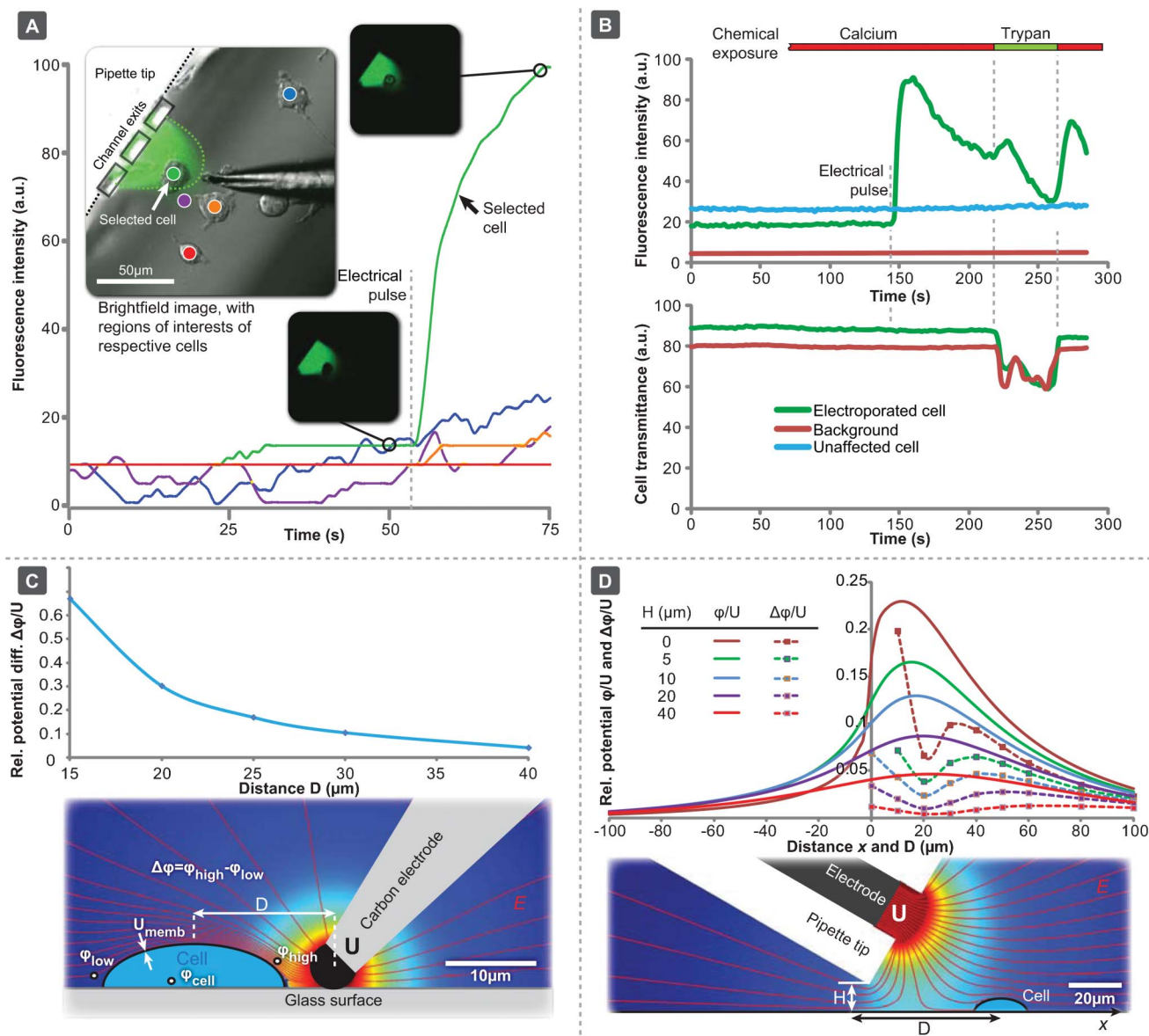


Fig. 3 Targeted single-cell electroporation and fluidic interrogation (A) Single-cell electroporation with an external carbon fiber electrode and simultaneous superfusion with 25 μM fluorescein solution in PBS. The regions of interest and the corresponding intensity graphs are colour coded on the inset image. The superfused cell of interest is represented in green. Fluorescence micrographs of the cell of interest at time points before and after electroporation are displayed as insets on the graph. (B) Single-cell electroporation with the pipette-integrated electrode. The cells were pre-loaded with Calcium-GreenTM, and superfused using the pipette with 1 mM calcium chloride in PBS. Calcium inflow was monitored *via* quantitative fluorescence imaging (upper panel). The cell viability was tested by switching the pipette outflow to Trypan blue and monitoring optical transmission (lower panel). The sequence of chemical exposure is represented by a horizontal top bar. Fluorescence (calcium inflow) and transmission (Trypan blue exposure) micrographs of the targeted cell are shown for different time points in the supporting information. (C) An electric field simulation, close to the tip of a carbon fiber electrode. The graph shows the transmembrane potential dependence on the electrode distance D from the cell. The schematic depicts the electrode arrangement with respect to the cell, overlaid with the electrical potential (coloured using a rainbow LUT). (D) The same simulation for a pipette-integrated electrode, where the electrical potential distribution ϕ (solid lines) and transmembrane potential $\Delta\phi$ (dotted lines) are plotted in relation to pipette height H (distance from device bottom to the glass surface) and distance D from the cell.

electroporation parameters, voltage and pulse duration were gradually increased until permeabilization of the membrane occurred. This was indicated by a rapid increase in intracellular fluorescence in both cases (Fig. 3A, B). During our analysis a sample size of ~ 50 cells was collected, with almost 100% electroporation success rate, tuning the conditions for the individual cells. The viability of each individual addressed cell was not interrogated prior to analysis, and may explain the occasionally observed necrosis upon electroporation. The switching capability of the superfusion pipette allowed for exchange of the Ca^{2+} solution to Trypan blue, which was initiated after ~ 1 min of Ca^{2+} delivery. Within ~ 30 s of constant exposure, Trypan blue was not observed to penetrate the cell membrane, indicating membrane integrity. Some cells however, appeared to show slight response to external calcium changes, as long as 2.5 min after the electroporation pulse. This passage of calcium, but not Trypan blue, suggests that the membrane retains its viability, but may contain small or closing pores.

In order to elucidate the electric field strength around the cells, a COMSOL study was performed (Fig. 3C,D). Since our estimations (Method S4†) indicated that an essential voltage drop occurs only in a small volume around the electrode tip ($> 96\%$), other resistive components of the bath were neglected. To interpret our simulation results and obtain the membrane potential, the electric potential distribution was monitored along the outer surface of the cell in order to find the highest (ϕ_{high}) and lowest (ϕ_{low}) values. Even though we do not know explicitly the potential of the cell interior, we can assume that it is constant, since the cell interior can be considered highly conductive compared to its insulating boundaries. Therefore the transmembrane potential should be at least $\Delta\phi_{\text{membrane}} \geq (\phi_{\text{high}} - \phi_{\text{low}})/2$ at some point along the cell membrane. It is further known that electric potentials across the cell membrane that exceed a critical limit of 0.25–1 V permeabilize the membrane.⁹ Since point electrodes have been used, the electric field in our system is non-homogeneous and heavily dependent on the distance from the electrode (Fig. 3C,D).³¹ The effective electric field strength drops with increasing distance, with the exception when the pipette is positioned exactly over the cell. In this case symmetry causes smaller potential differences along the cell (Fig. 3D). We found that the voltage difference along the cell membrane is at least 0.1 V per 1 V applied electrode potential for the carbon fiber and 0.06 V/V for the integrated electrode. Therefore, voltage pulses in the ranges of 5–20 V and 8–33 V for an external, and an integrated electrode, respectively, should be sufficient for electroporation. In the experiments, comparable voltage pulses (3–10 V for 2–10 ms) were indeed sufficient to electroporate using the carbon fiber microelectrode. However, voltages larger than predicted by the simulations were needed in case of the Field's metal electrode (30–100 V for 1 ms, even longer pulse durations time did not lower the voltage requirement). An explanation could be a larger voltage drop at the interface between the metal electrode and buffer, which is the only unknown parameter of the resistive chain.

Here we have demonstrated a multifunctional pipette with an integrated electrode, suitable for the electroporation and simultaneous superfusion of single-cells. The use of Field's metal with its

low-melting temperature provides a facile bench top method to fabricate low-resistance electrodes in the microfluidic channels, even though it reduces the flexibility of the tip and requires gold plating for chemical stability in some situations. We demonstrated that by combining local superfusion, with single cell electroporation, highly localized sequential delivery of several compounds across the physical boundary of a single cell can be achieved, while eliminating chemical contamination of the surrounding medium, as well as electric field damage of nearby cells. The additional electroporation functionality clearly extends the versatility and performance of the pipette as a multifunctional single-cell manipulation tool. A distinct advantage of this setup is the microfluidic functionality provided by the pipette. Switching between different solutions allows convenient testing of viability and electroporation efficiency during an experiment. Dye penetration could in such a system be utilized as an indicator for, or even feedback of successful electroporation, preceding delivery of active compounds through the pores.

Acknowledgements

We acknowledge the European Research Council, the Swedish Research Council (VR), the Wallenberg Foundation, and the National Institutes of Health (NIH) through grant GM R01-066018. We thank Owe Orwar for support and Erik T. Jansson for helpful discussion. We are grateful to Sanofi-Aventis for supporting Nicolas Sanchez' internship in our laboratory.

References

- N. de Souza, *Nat. Methods*, 2010, **7**, 35–35.
- M. Niepel, S. L. Spencer and P. K. Sorger, *Curr. Opin. Chem. Biol.*, 2009, **13**, 556–561.
- D. Anselmetti, *Single Cell Analysis*, Wiley-VCH Verlag GmbH & Co. KGaA, 2009.
- G. Charvin, *Nat. Methods*, 2010, **7**, 363–363.
- D. G. Spiller, C. D. Wood, D. A. Rand and M. R. H. White, *Nature*, 2010, **465**, 736–745.
- J. Sun, C. C. Stowers, E. M. Boczek and D. Li, *Lab Chip*, 2010, **10**, 2986–2993.
- M. A. Messerli, L. P. Collis and P. J. S. Smith, *Electroanalysis*, 2009, **21**, 1906–1913.
- I. Hapala, *Crit. Rev. Biotechnol.*, 1997, **17**, 105–122.
- J. Olofsson, K. Nolkranz, F. Ryttsen, B. A. Lambie, S. G. Weber and O. Orwar, *Curr. Opin. Biotechnol.*, 2003, **14**, 29–34.
- D. Luo and W. M. Saltzman, *Nat. Biotechnol.*, 2000, **18**, 33–37.
- M. Tanaka, Y. Yanagawa and N. Hirashima, *J. Neurosci. Methods*, 2009, **178**, 80–86.
- M. Wang, O. Orwar, J. Olofsson and S. G. Weber, *Anal. Bioanal. Chem.*, 2010, **397**, 3235–3248.
- C. Ionescu-Zanetti, A. Blatz and M. Khine, *Biomed. Microdevices*, 2008, **10**, 113–116.
- M. Khine, A. Lau, C. Ionescu-Zanetti, J. Seo and L. P. Lee, *Lab Chip*, 2005, **5**, 38–43.
- W. G. Lee, U. Demirci and A. Khademhosseini, *Integr. Biol.*, 2009, **1**, 242–251.
- J. Olofsson, M. Levin, A. Stromberg, S. G. Weber, F. Ryttsen and O. Orwar, *Anal. Chem.*, 2007, **79**, 4410–4418.
- C. Bae and P. J. Butler, *BioTechniques*, 2006, **41**, 399.
- J. A. Lundqvist, F. Sahlin, M. A. I. Aberg, A. Stromberg, P. S. Eriksson and O. Orwar, *Proc. Natl. Acad. Sci. U. S. A.*, 1998, **95**, 10356–10360.
- M. A. I. Aberg, F. Ryttsen, G. Hellgren, K. Lindell, L. E. Rosengren, A. J. MacLennan, B. Carlsson, O. Orwar and P. S. Eriksson, *Mol. Cell. Neurosci.*, 2001, **17**, 426–443.
- A. Ainla, E. T. Jansson, N. Stepanyants, O. Orwar and A. Jesorka, *Anal. Chem.*, 2010, **82**, 4529–4536.
- A. Ainla, G. D. M. Jeffries, R. Brune, O. Orwar and A. Jesorka, *Lab Chip*, 2012, **12**, 1255–1261.

- 22 D. Juncker, H. Schmid and E. Delamarche, *Nat. Mater.*, 2005, **4**, 622–628.
- 23 G. V. Kaigala, R. D. Lovchik, U. Drechsler and E. Delamarche, *Langmuir*, 2011, **27**, 5686–5693.
- 24 Y. N. Xia and G. M. Whitesides, *Angew. Chem., Int. Ed.*, 1998, **37**, 551–575.
- 25 J.-W. Choi, S. Rosset, M. Niklaus, J. R. Adleman, H. Shea and D. Psaltis, *Lab Chip*, 2010, **10**, 783–788.
- 26 N. Lewpiriyawong, C. Yang and Y. C. Lam, *Electrophoresis*, 2010, **31**, 2622–2631.
- 27 A. Pavesi, F. Piraino, G. B. Fiore, K. M. Farino, M. Moretti and M. Rasponi, *Lab Chip*, 2011, **11**, 1593–1595.
- 28 C. Priest, P. J. Gruner, E. J. Szili, S. A. Al-Bataineh, J. W. Bradley, J. Ralston, D. A. Steele and R. D. Short, *Lab Chip*, 2011, **11**, 541–544.
- 29 A. C. Siegel, S. S. Shevkoplyas, D. B. Weibel, D. A. Bruzewicz, A. W. Martinez and G. M. Whitesides, *Angew. Chem., Int. Ed.*, 2006, **45**, 6877–6882.
- 30 J.-H. So and M. D. Dickey, *Lab Chip*, 2011, **11**, 905–911.
- 31 I. Zudans, A. Agarwal, O. Orwar and S. G. Weber, *Biophys. J.*, 2007, **92**, 3696–3705.

Single-Cell Electroporation Using a Multifunctional Pipette

Alar Ainla, Shijun Xu, Nicolas Sanchez, Gavin D. M. Jeffries and Aldo Jesorka

Electronic Supplementary Information (ESI)

Table of contents

Table of contents	1
Supplementary Methods	1
Method S1. Cell preparation.....	1
Method S2. Dye loading of cells.....	1
Method S3. Preparation of carbon fiber electrodes.....	2
Method S4. Electric field simulation	2
Method S5. Fabrication of the Pipette with an integrated electrode	2
Table S1. Simulation settings for the external carbon fiber electrode.....	2
Table S2. Simulation settings for the integrated Field's metal electrode.....	3
Table S3. Geometries of the macroscopic parts of the electroporation setup	3
Table S4. Serial resistance components.....	4
Figure S1. A schematic representation of the electrode setup	5
Figure S2. Fluorescent and brightfield micrographs of pipette electoporated cells	5
Table S5. Characteristic parameters and operation conditions for the microfluidic superfusion pipette.....	6

Supplementary Methods

Method S1. Cell preparation

Adherent NG-108-15 cells were cultured in thin glass bottom (#1 coverslip) petri dishes, suitable for confocal imaging, for 2-6 days in Dulbecco's modified eagle medium (DMEM) supplemented with fetal calf serum (10%).

Method S2. Dye loading of cells

The cells were loaded with the calcium sensitive dye, Calcium-Green™-1 AM ester (Life Technologies Inc, Carlsbad, USA). A 200 μ M stock solution was first prepared using DMSO, which was then diluted with Ringer's solution (VWR) to obtain a final working concentration of 4 μ M. After removing the petri dish from the incubator, the culture medium was removed and the cells were rinsed twice with PBS buffer, followed by the addition of 2ml of the calcium dye loading solution. The cells were exposed to the dye loading solution for 1 h at room temperature, then rinsed twice with phosphate buffered saline (PBS) buffer

(Ca²⁺ free). This buffer had an ionic strength of 60 mM; containing 5 mM Trizma base, 30 mM K₃PO₄, 30 mM KH₂PO₄ and 0.5 mM NaEDTA, NaOH adjusted to pH 7.8, and was also used as the main buffer for all experiments.

Method S3. Preparation of carbon fiber electrodes

Plastic encapsulated ProCFE carbon fibers, with an OD 5 μ m, were obtained from Dagan Corp. and assembled as follows: An OD 1.0 mm borosilicate glass tube was trimmed to 5 cm in length, using a ceramic glass cutter or diamond scribe. A 10 cm long silver wire was inserted such that 1cm protruded from the tube. Conductive silver epoxy (ELFA Electronics, Sweden) was mixed in a 1:1 ratio and a drop of 2-3 mm diameter was applied to the protruding end. The glass rod with the epoxy covered end was quickly inserted into the rear of the plastic covered carbon fiber, such that the epoxy filled the plastic barrel completely. Additional epoxy was applied where necessary, to achieve a complete seal. The carbon fibers were stored vertically, with the tip pointing downwards, for at least 1h before use, to ensure that the silver epoxy had sufficiently hardened.

Method S4. Electric field simulation

Electric field strengths were evaluated in numeric simulations using COMSOL Multiphysics 4.1 employing the electric currents (ec) model. The electrical conductivity of water was set to an initial value of $\sigma = 5.5 \cdot 10^{-6} \text{ S/m}$ (pure water in COMSOL). Our model is, however, insensitive to the exact values of electrical conductivity, as long as the value is used consistently throughout the calculations. Two simulation series were performed: one for the carbon fiber electrode, and another for the integrated Field's metal electrode, using the parameters outlined in tables S1 and S2, respectively. In both cases the "Cell" was modeled to be 5 μ m high, a diameter of 20 μ m, with an insulating membrane and a conducting interior.

Method S5. Fabrication of the Pipette with an integrated electrode

PDMS multifunctional pipettes were fabricated as described earlier²¹. Electrodes were prepared as shown in Figure 1. First, the bottom of the well connecting to the electrode channel was filled with grains of Field's metal (Alloy MCP61, Mindsets Ltd, Waltham Cross, UK). Thereafter, the pipette was heated to ~70-90 °C for 1min on a hot plate. Pressure of up to 2.7 bar was then applied, which caused the molten metal to quickly (<5s) fill the channel, forming a droplet at the pipette tip. The pipette was removed from the hot plate, and left to cool to room temperature. Excess metal was removed from the tip using tweezers. The pipette was inspected under a light microscope to check for air entrapped in the metal filling. Defects were corrected by repeating the filling cycle.

Gold coating. In order to eliminate electrochemical degradation of the Field's metal, we electrodeposited a gold film onto the exposed electrode surface at the pipette tip. For this purpose the tip was immersed into a common commercial KAu(CN)₂ based gold plating solution A3000 (Aurotech, Sweden) with Na₂CO₃ added for pH adjustment. A Pt wire was used as a counter electrode and a potential of -1.6V (relative to the Pt wire) was applied for 10 min to the Field's metal electrode for deposition.

Interfacing. A custom pipette holder was ordered from Teadusmosaik OÜ (Tartu, Estonia). This holder was equipped with M4 screw holes at the top surface of the manifold, which allowed access to the pipette wells. The holes are normally hermetically sealed with Teflon tape tightened screws. The electrode-fitted well was interfaced with a spring loaded battery contact (ordered from ELFA, Sweden), which was fitted into a Nylon™ screw. The spring-loaded contacts ensured good electrical connection without putting strain on the Field's metal plug.

Table S1. Simulation settings for the external carbon fiber electrode

Parameter	Values
Outer dimensions of the simulation volume	100 μ m x 100 μ m
Height of the simulation volume	50 μ m
Radius of the fiber tip	2.5 μ m
Height of the fiber (center)	2.5 μ m
Distance between fiber and center of the cell (series)	10, 15, 20, 25, 30, 35, 40 μ m
Calculated electrical resistance of the simulation volume (R_{sim})	16 G Ω

Table S2. Simulation settings for the integrated Field's metal electrode

Parameter	Values
Bottom dimensions of the simulation volume	300 μm x 200 μm
Height of the simulation volume	150 μm
Width of the pipette tip	200 μm
Electrode size	20 μm x 20 μm
Thickness of the bottom membrane (bottom to electrode distance)	20 μm
Pipette height (distance between pipette bottom and surface) (series)	0, 5, 10, 20, 40 μm
Pipette angle	30°
Pipette position in the middle of sim. volume	
Distance between pipette and center of the cell (series)	10, 20, 30, 40, 50, 60, 80, 100 μm
Calculated electrical resistance of the simulation volume (R_{sim})	9.1 GΩ

The total resistance of the electroporation setup can be calculated as a sum of resistances of electrodes R_e , the interface between the metal and the liquid R_{int} , and the liquid bath R_B . In this particular geometry we can divide the resistance of the liquid bath further into serial components. $R_B = R_{sim} + R_{B1} + R_{B2} + R_{B3}$. R_{sim} describes the resistance of the simulation volume, which is in the immediate vicinity of the electrode, R_{B1} describes a spherical extension of this volume extending to the surface of the bath, R_{B2} describes the resistance of the bath as a thin disk shaped water layer ($r \gg h$), and finally, R_{B3} describes the resistance around the cylindrical gold counter electrode, which is placed as a loop inside the liquid bath. The geometry of the setup and all resistances are shown in figure S1.

The resistances between the spherical surfaces can be calculated from the equation,

$$R = \frac{\rho}{4\pi} \left(\frac{1}{r_1} - \frac{1}{r_2} \right)$$

While for cylindrical and disk shaped volumes it is expressed as,

$$R = \frac{\rho}{2\pi L} \ln \frac{r_2}{r_1}$$

where $\rho = 1/\sigma \approx 1.8 \cdot 10^5 \Omega \cdot m$ stands for the resistivity of water. The geometries of the macroscopic parts are given in table S3.

Table S3. Geometries of the macroscopic parts of the electroporation setup

Parameter	Symbol	Value
Radius of the dish	r	22 mm
Height of water level in the dish	h	~4 mm
Length of Au wire	$l = 2\pi r$	~140 mm
Diameter of Au wire	D_{gw}	0.25 mm
Radius of simulation volume (Carbon fiber electrode)	r_s	50 μm
Radius of simulation volume (Integrated electrode)	r_s	150 μm

In case of the integrated electrode, the geometries of the macroscopic parts remain the same, only the simulation volume changes. The resistance of each component can be calculated for both setups (Table S4).

Table S4. Serial resistance components.

This estimation of resistances justifies the assumption that the entire voltage drop in the bath occurs inside the simulation volume. The error in both case should be < 4 %.

Component	Expression	Value (Carbon fiber)	Value (Integrated electrode)
R_e	<i>measured exp.</i>	--	~40 Ω
R_{int}	<i>unknown</i>	--	--
R_{sim}	<i>simulation</i>	16 G Ω	9.1 G Ω
R_{B1}	$\frac{\rho}{2\pi} \left(\frac{1}{r_s} - \frac{1}{h} \right)$	0.57 G Ω	0.18 G Ω
R_{B2}	$\frac{\rho}{2\pi h} \ln \frac{r}{h}$	12 M Ω	12 M Ω
R_{B3}	$\frac{\rho}{2\pi l} \ln \frac{h}{D_{gw}}$	0.57 M Ω	0.57 M Ω

The actual electric conductivity of the buffer solution can be estimated from the conductivity equation for strong electrolytes (Atkins, *Physical Chemistry 6th ed*, 2000).

$$\Lambda = \sum_i v_i \lambda_i$$

Where v denotes the concentration of a certain ion and λ this ion's molar conductivity. In case of ECB solution, the most prominent ions are Na⁺ (~140 mM, $\lambda = 5.01 \text{ mS m}^2 \text{ mol}^{-1}$) and Cl⁻ (~140 mM, $\lambda = 7.63 \text{ mS m}^2 \text{ mol}^{-1}$), giving $\Lambda \approx 1.8 \text{ S m}^{-1}$, which is ~330,000 times larger than for MilliQ (18 M Ω) water, giving a resistance estimate of the liquid bath to be ~50 k Ω in the case of the carbon fiber system, and ~28 k Ω in the case of the integrated electrode. These values are still significantly larger than, for example, the electrode resistance, which can be neglected.

Figure S1. A schematic representation of the electrode setup

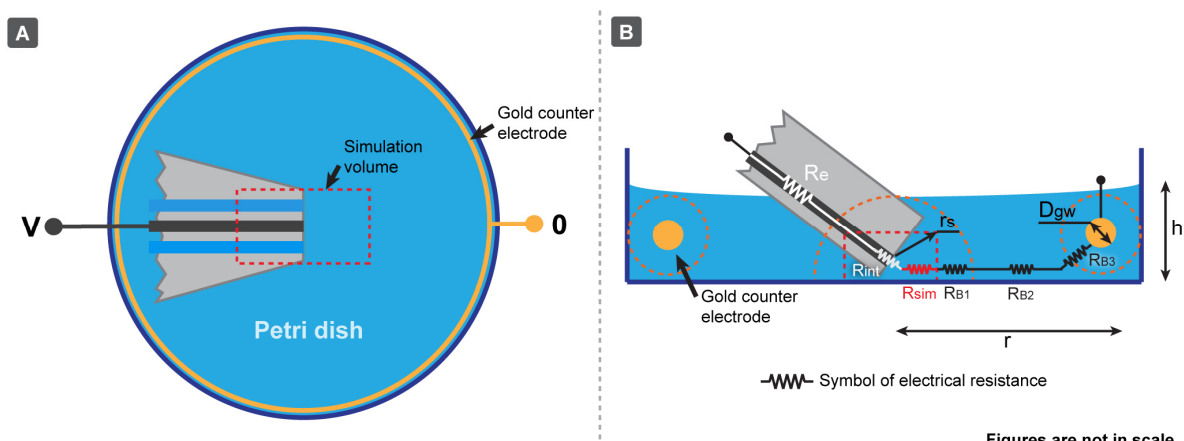


Figure S1. A schematic representation of the electrode setup; (A) plan view, (B) side view. The side view shows the series of resistances used in the simulations. The red dotted lines indicate the calculation regions; the central rectangle was numerically simulated, the circular regions were analytically solved. The dish radius is denoted by “ r ”, the liquid level is denoted by “ h ”. All other parameters are defined in table S3 and S4.

Figure S2. Fluorescent and brightfield micrographs of pipette electroporated cells

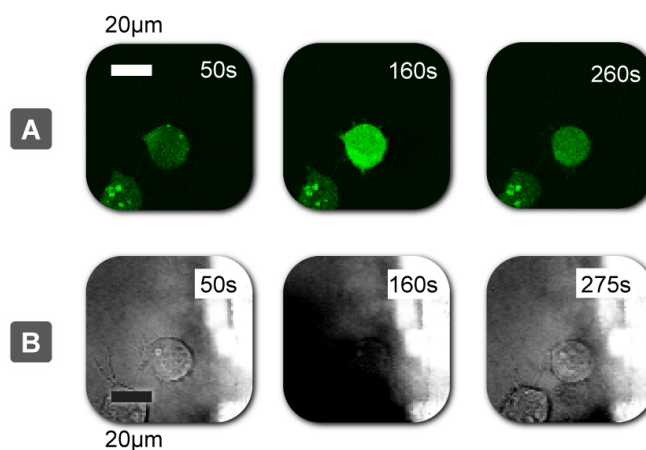


Figure S2. Fluorescent and brightfield micrographs at selected time points, for single cell electroporation using the pipette incorporated electrode, for the graph in figure 3B. (A) Shows the calcium transport through imaging of the calcium green reporter dye. (B) displays the state of the cell prior and post electroporation as well as during calcium exposure. The lack of trypan staining at the end of the experiment was a strong indication of membrane integrity at the end of the experiment.

Table S5. Characteristic parameters and operation conditions for the microfluidic superfusion pipette.

Description	Symbol	Value	Unit
Channel width	w	20	μm
Channel height	h	20	μm
Supply channel length	L_s	30	mm
Outlet channel length	L_o	10	mm
Electrode channel length	L_e	40	mm
Hydraulic conductance			
Supply channel	G_s	19	$\text{nL}/(\text{s} \cdot \text{bar})$
Outlet channel	G_o	56	$\text{nL}/(\text{s} \cdot \text{bar})$
Electrode resistance (calculated)	R_e	40	Ω
Operating settings			
Injection "on" pressure	P_{on}	0.15	Bar
Injection "off" pressure	P_{off}	0	Bar
Vacuum	V	-0.6	Bar
Inflow-Outflow ratio	I/O	4	
Outflow	Q_{out}	1.65	nL/s
Inflow	Q_{in}	6.6	nL/s
Approx. liquid exchange delay	τ	2.4	s

PAPER

V

A multifunctional pipette for localized drug administration to brain slices

Short communication

Aikeremu Ahemaiti^a, Alar Ainla^a, Gavin D. M. Jeffries^a, Holger Wigström^b, Owe Orwar^a, Aldo Jesorka^a, Kent Jardemark^{a,c,*}

^a Department of Chemical and Biological Engineering, Chalmers University of Technology

^b Institute of Neuroscience and Physiology, The Sahlgrenska Academy at University of Gothenburg

^c Department of Physiology and Pharmacology, Karolinska Institutet

*Corresponding author. Tel.: +46 8 52487918.

E-mail address: Kent.Jardemark@ki.se

ABSTRACT

We have developed a superfusion method utilizing an open-volume microfluidic device for administration of pharmacologically active substances to selected areas in brain slices with high spatiotemporal resolution. The method consists of a hydrodynamically confined flow of the active chemical compound, which locally stimulates neurons in brain slices, applied in conjunction with electrophysiological recording techniques to analyze the response. The microfluidic device, which is a novel free-standing multifunctional pipette, allows diverse superfusion experiments, such as testing the effects of different concentrations of drugs or drug candidates on neurons in different cell layers with high positional accuracy, affecting only a small number of cells. We here demonstrate the use of the method in electrophysiological recordings of pyramidal cells in hippocampal and prefrontal brain slices from rats, determine the dependence of electric responses on the distance of the superfusion device from the recording site, and document an approximately 10 fold gain in solution exchange time, as compared to whole slice perfusion. Localized solution delivery by means of open-volume microfluidic technology also reduces reagent consumption and tissue culture expenses significantly, while allowing more data to be collected from a single tissue slice, thus reducing the number of laboratory animals to be sacrificed for a study.

1. Introduction

In vitro brain slices constitute a valuable experimental model system for studying communication between, or the effects of drugs on, neurons and astrocytes in an environment which preserves the cellular network, i.e. the organization in cell layers, processes, and synapses. Unlike *in vivo* studies on brain using live anesthetized animals, experiments on brain slice preparations have the advantage that the influence of anesthetics on cellular functions is eliminated. Single cells are more easily accessible by probes and imaging techniques, which enables precise physiological and pharmacological studies of the functions and properties of the neuronal networks present in these slices.

Microfluidics is emerging as a powerful tool for neuroscientists (Huang et al., 2012), allowing spatiotemporal control over solution delivery to the extracellular environment around neurons and astrocytes in brain tissue preparations. The major ambitions of microfluidics in the context of brain tissue slices are to provide efficient nutrient and oxygen delivery and waste removal, allow spatiotemporal control over the local chemical environment, and to

enable diverse imaging and probing techniques. Examples of device designs which represent solutions to one or more of these problems include microfluidic flow chambers which support interstitial flow for better gas penetration of thick tissue slices (Rambani et al., 2009), or focal perfusion within conventional slice chambers for improved control over the solution environment in a selected slice region (Blake et al., 2007). A new promising approach is the use of hydrodynamically confined flow (HCF) technology for localized microperfusion (Queval et al., 2010). By continuous uptake of the delivered solution, HCF devices produce a confined liquid volume outside the device, i.e., a virtual flow chamber which merely touches a selected area of the tissue slice. This principle is an extension of the many variants of the push-pull arrangement of glass capillaries (Veselovsky et al., 1996). The use of microfabricated devices eliminates disadvantages associated with glass needles, and adds additional benefits such as facilitated interfacing and a broader choice of materials.

A distinct problem with the initially introduced HCF devices is the difficulty to use conventional light microscopes, as the vertical architecture with

perpendicular apertures blocks the optical path. Moreover, it is impossible to use auxiliary probes, such as electrophysiological recording electrodes, in conjunction with this superfusion architecture. We have recently developed a HCF based free-standing multifunctional pipette in polydimethylsiloxane (PDMS) which largely overcomes these disadvantages (Ainla et al., 2010; Ainla et al., 2012). Briefly, the test solution is selected from a set of local reservoirs by an internal fast-acting liquid switch zone and fed to a delivery channel at the tip of the pipette close to the biological specimen. Vacuum channels located on either side of the delivery channel help to form a virtual flow chamber of the test solution. The device is applied at an angle to the microscope table, allowing additional probes to be used in tandem, addressing the same environment at the tip of the pipette. Here, we demonstrate the capabilities and benefits of the multifunctional pipette to administer 2-amino-3-(3-hydroxy-5-methyl-isoxazol-4-yl) ropanoic acid (AMPA) -type glutamate receptor antagonist 6-cyano-7-nitroquinoxaline-2,3-dione (CNQX) and the glutamate receptor agonist AMPA to electrophysiologically recorded pyramidal cells in rat hippocampal and cortical brain slices.

2. Materials and methods

2.2 Preparation of brain slices

2.2.1 Hippocampus

Hippocampal slices were prepared from 12- to 20-day-old Sprague-Dawley rats (Scanbur BK, Sollentuna, Sweden). The procedures conformed to the guidelines of the Swedish Council for Laboratory Animals and were approved by the Gothenburg Ethical Committee for Animal Experimentation. The animals were sacrificed by decapitation after initial isoflurane anesthesia, and the hippocampi were quickly dissected. Transverse slices (400 μ m thick) were prepared by an in-house designed McIlwain-type tissue chopper and placed in a holding chamber containing an oxygenated Ringer's solution at room temperature, composed of (in mM): NaCl 119, KCl 2.5, CaCl₂ 2.0, MgCl₂ 2.0, NaHCO₃ 26, NaH₂PO₄ 1.0, and D-glucose 10, gassed with 95% O₂/5% CO₂. After storage for at least 90 min, the slices were transferred as needed to a recording chamber where they were submerged by a continuously superfusing solution saturated with 95% O₂ and 5% CO₂. The composition of the perfusion solution was the same as in the holding chamber except for using 2.5 mM CaCl₂ and 1.3 mM MgCl₂, with the pH balanced to 7.4. A peristaltic pump (Ismatec, Labinett Lab AB, Sweden) was used to recirculate the solution (1.5-2.0 ml/min), keeping the flow rate constant and avoiding any flow artifacts. Experiments were performed at 31°C

2.2.2 Medial prefrontal cortex

Male Sprague-Dawley rats (Charles River, Germany) were used (80–250 g) for all the experiments. The animals were housed under standard laboratory conditions and maintained on a 12 hour light/dark cycle (lights on at 06:00) with *ad libitum* access to food and water. All experiments at Karolinska Institutet were approved by, and conducted in accordance with, the Stockholm North Committee on Ethics of Animal Experimentation. Procedures for the preparation of rat medial prefrontal cortex (mPFC) slices have been described previously (Arvanov et al., 1997; Arvanov and Wang, 1998; Konradsson et al., 2006). Briefly, the rats were decapitated under halothane anaesthesia. The brains were then rapidly removed and cooled in ice-cold Ringer's solution (pH 7.4) consisting of (in mM): NaCl 126, KCl 2.5, CaCl₂ 2.4, MgCl₂ 1.3, NaH₂PO₄ 1.2, D-glucose 10, NaHCO₃ 18, and oxygenated with 95% O₂/5% CO₂. The brains were then cut coronally, using a Vibroslice (Campden model MA 752, World Precision Instruments, Sarasota, FL, USA) instrument, in order to produce 450 μ m slices. The brain slices were removed from the instrument and kept submerged in oxygenated Ringer's solution at room temperature for at least 1 hour to allow for recovery.

2.3 Electrophysiological recordings

2.3.1 Extracellular recording of field excitatory postsynaptic potentials (fEPSPs) in the hippocampus

The commissural-Schaffer collateral pathway of the hippocampal CA1 area was stimulated using an in-house developed programmable pulse generator. Stimuli consisted of 100 μ s, 20-50 μ A, negative constant-current pulses, delivered via an insulated sharpened tungsten wire (type TM33B01, World Precision Instr., FL, USA) at a rate of 0.1-0.2 Hz. Extracellular field potentials were recorded in the middle of the pyramidal cell dendritic layer (stratum radiatum), 200-500 μ m away from the stimulating electrode, via a glass micropipette filled with 1 M NaCl (resistance 3-5 M Ω ; made from Kwik-Fil borosilicate glass capillaries, World Precision Instr., FL, USA; pulled by a P-97, Sutter Instruments, Novato, CA, USA). Signals were amplified, filtered, digitized and transferred to a computer for analysis, using electronic equipment based on an Eagle Technology (RSA) multifunction board. Off-line data analysis was performed using pCLAMP-Clampfit software (Molecular Devices, CA, USA). The size of the recorded fEPSP, which was dominated by the contribution from AMPA-type glutamate receptors, was estimated as the negative peak amplitude relative to the prestimulus baseline. This measure provides an index of the efficacy of AMPA receptor (AMPA) mediated synaptic transmission (Muller et al., 1988; Muller et al., 1989; Shahi and Baudry, 1992).

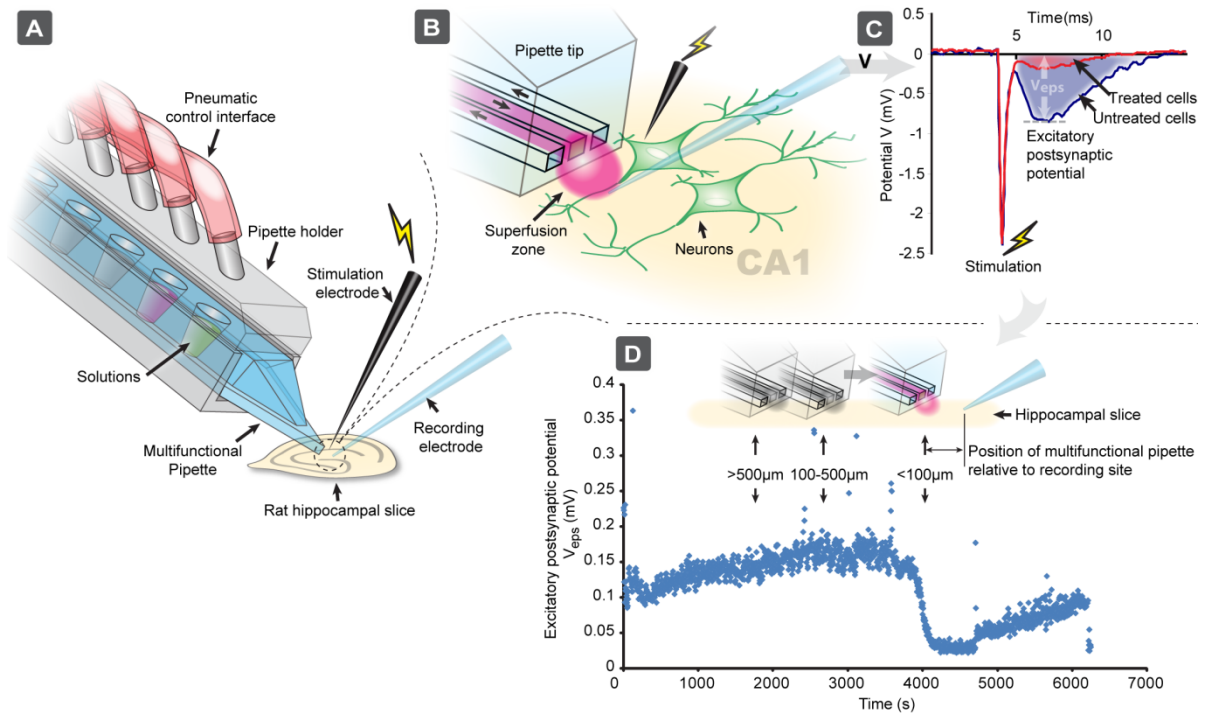


Fig. 1. The microfluidic pipette for local administration of biological active substances to cells in brain slices. **a)** and **b)** The pipette was used to locally deliver CNQX for blocking electrically stimulated fEPSPs in the CA1 region of a hippocampal brain slice, by exposing the surface to the recirculation region at the tip of the pipette (red volume). **c)** and **d)** The electrically stimulated fEPSP was reduced by CNQX with the multifunctional pipette in the CA1 region of rat hippocampal slice. When the multifunction pipette was positioned within 100µm from the recording site, i.e. a distance which was the diameter of the recirculating area of the pipette, the fEPSP was immediately reduced by administered CNQX. The fEPSPs began to recover when the pipette was moved away from the recording electrode.

2.3.2 Intracellular recording of AMPA-induced currents in medial prefrontal cortex

A single slice containing the mPFC was transferred to a recording chamber (32 °C) and was held submerged between two nylon nets. The chamber was continuously perfused with oxygenated Ringer's solution at a flow rate of 1-2 mL/min. A standard intracellular single-electrode technique was used to record from pyramidal cells in layers V and VI of the mPFC slices as described previously (Arvanov et al., 1997; Konradsson et al., 2006). Briefly, electrodes were pulled from borosilicate glass capillaries (Warner Instruments, Hamden, CT, USA) using a horizontal electrode puller (Model P-87, Sutter Instruments, Novato, CA, USA). The electrodes were filled with 2 M potassium acetate and used for intracellular recordings of pyramidal cells of the mPFC with an Axoclamp 2A amplifier (Axon Instruments, Foster City, CA, USA). Voltage-clamp (holding potential: -60 mV) recordings were performed in the discontinuous mode with a sampling rate of 5-6.2 kHz, and acquired using digital/analogue sampling and data acquisition software (Clampex 9, Axon Instruments, Foster City, CA, USA). Tetrodotoxin (TTX; 0.5 µM),

glycine (1 µM), and bicuculline (5 µM) were routinely included in the perfusion solution during the recordings.

2.4 Drugs and Buffers

Potassium chloride, sodium dihydrogen phosphate, calcium chloride dihydrate, sodium hydrogen carbonate and potassium acetate were all obtained from Merck (Darmstadt, Germany). Magnesium chloride hexahydrate, AMPA, glycine, and bicuculline methiodide were purchased from Sigma-Aldrich (St. Louis, MO, USA). Glucose was purchased from VWR international (Leicestershire, UK) and sodium chloride from Riedel deHaen (Seelze, Germany). TTX (citrate buffer) was obtained from Tocris Bioscience (Bristol, UK) and halothane (fluothane) was purchased from Astra Zeneca (Stanhope Gate, London, UK).

2.5 Multifunctional pipette

The multifunctional pipette has been described previously (Ainla et al., 2012), from which operation

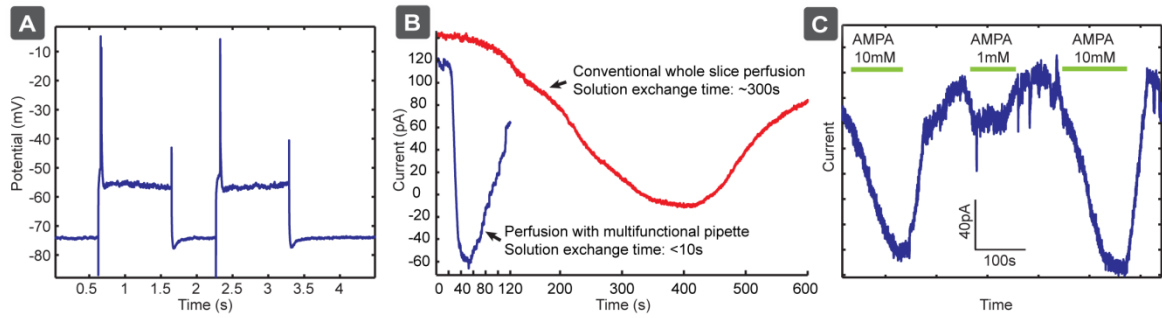


Fig. 2. Local administration of AMPA by the microfluidic pipette to intracellularly recorded pyramidal cells of the rat mPFC. **a)** Electrophysiological characterization of the pyramidal cells. **b)** The temporal resolution of AMPA administration to pyramidal cells in the mPFC was significantly improved when using the microfluidic pipette compared to when conventional whole slice perfusion was used. **c)** The microfluidic pipette contains multiple reservoirs which enabled local administration of different concentrations of AMPA to the pyramidal cells with fast resolution.

parameters, such as air pressure and vacuum and inflow/outflow ratio were extracted. Briefly, an outflow rate of ~ 30 nl/s (Outflow/inflow ration 0.5) was applied forming a recirculation zone at the tip of the pipette. The pipette tip was positioned so that a distance of 10 μ m was maintained from the tissue surface. Prior to loading into the pipette, all solutions were filtered through a 0.2 μ m syringe filter, to prevent blockages within the microfluidic device.

3. Results and Discussion

The present experimental applications were designed to show the ability of the multifunctional pipette to administer biologically active substances to specific parts or spots in brain slices with high spatial resolution. In the first example, electrically stimulated fEPSPs were recorded extracellularly in the CA1 region of rat hippocampal slices *in vitro* (Fig. 1a). The fEPSPs were blocked by the AMPA receptor-antagonist CNQX which was locally delivered to the recording site by the multifunctional pipette (Figs. 1b and 1c). Fig. 1d illustrates the spatial resolution of local administration of CNQX to the slice by the pipette. The pipette was gradually positioned closer the recording site, and when the distance between the pipette tip and the recording site was < 0.1 mm (i.e. the approximate diameter of the superfusion zone, inhibition of the fEPSP was observed, implying that CNQX was able to reach the recorded cells. The electrically stimulated fEPSPs immediately started to recover when the pipette was moved > 0.1 mm from the site of recording in the slice. Thus, by using the multifunctional pipette, biologically active substance can be added to a small extracellular volume, where it can control the pharmacology of the brain slice in a strictly local manner.

In the second example, we have tested the ability of the microfluidic pipette to administer the glutamate receptor agonist AMPA to intracellularly recorded pyramidal cells of the rat mPFC. The electrophysiological criteria for distinguishing

pyramidal from non-pyramidal cells in layers V and VI of the mPFC have been described previously (Arvanov and Wang, 1998; Jardemark et al., 2005). Briefly, the presumed pyramidal cells of the mPFC have relatively long spike duration (1–3 ms at half-maximum spike amplitude) and show a pronounced spike-frequency adaptation in response to constant-current depolarization pulses (see Fig. 2a, illustrating that only single spikes were induced by long pulses). As seen in Fig. 2b, the multifunctional pipette leads to a substantially faster response time (seconds) than conventional whole chamber perfusion (minutes). Since the drug is delivered along with the circulating buffer in the conventional setups, drug concentration in the bath will gradually increase before it reaches a steady state, and gradual decrease will also occur at the end of drug application. Although the response time was faster than with conventional perfusion it is slower than can be achieved with local perfusion of isolated cells (often < 0.1 s). This is because the cells in the slice are embedded in surrounded tissue, which presents a significant diffusion barrier slowing down the applied concentration steps.

The pipette has integrated solution reservoirs which allow for administration of biologically active substances with a markedly reduced reagent use compared to conventional perfusion systems. Moreover, these reservoirs can be preloaded with different drugs, or different concentrations of drugs. The latter allows for easy determination of concentration-response profiles. Here we demonstrate that our multifunctional pipette can deliver AMPA at two different concentrations in the same experiment (Fig. 2c).

There are several examples of other micro-perfusion devices designed for extracellular delivery of biologically active substances in brain slices. For example, glass micropipettes, with the capability of applying substances via a laminar flow through a micro scale aperture, have been widely used (for review see Huang et al., 2012). However, control of flow dynamics

is quite limited with these pipettes because of the poor designability a fabrication construction. There are also more complex microfluidic devices (see e.g. Huang et al., 2012) which, like our pipette, are using recirculation for local administration of chemicals to brain slices. However, these devices are limited in positioning and have to rely on a prearranged alignment of the perfusion ports. Thus, the present pipette allows the top of the slice to be open and the possibility of flexible delivery of different concentrations of biological substances (e.g. drugs or drug candidates) to any area of choice in the brain slice.

4. Conclusions

We demonstrate high spatial and temporal resolution, for delivery of drugs or drug candidates, at different concentrations to brain slices, using the multifunctional pipette. Application in combination with electrophysiological probes was shown, demonstrating the flexibility with other advanced experimental set ups. Through localized administration of AMPA to pyramidal cells, a 30 fold decrease in the time to full response was observed, when using the microfluidic pipette compared to when conventional perfusion to the whole recording chamber was used, allowing kinetics to be probed in greater detail.

References

- Ainla A, Jansson ET, Stepanyants N, Orwar O, Jesorka A. A Microfluidic Pipette for Single-Cell Pharmacology. *Analytical Chemistry*, 2010; 82: 4529-36.
- Ainla A, Jeffries GDM, Brune R, Orwar O, Jesorka A. A multifunctional pipette. *Lab on a Chip*, 2012; 12: 1255-61.
- Arvanov VL, Liang X, Schwartz J, Grossman S, Wang RY. Clozapine and haloperidol modulate N-methyl-D-aspartate- and non-N-methyl-D-aspartate receptor-mediated neurotransmission in rat prefrontal cortical neurons in vitro. *The Journal of pharmacology and experimental therapeutics*, 1997; 283: 226-34.
- Arvanov VL, Wang RY. M100907, a selective 5-HT_{2A} receptor antagonist and a potential antipsychotic drug, facilitates N-methyl-D-aspartate-receptor mediated neurotransmission in the rat medial prefrontal cortical neurons in vitro. *Neuropsychopharmacology*, 1998; 18: 197-209.
- Blake AJ, Pearce TM, Rao NS, Johnson SM, Williams JC. Multilayer PDMS microfluidic chamber for controlling brain slice microenvironment. *Lab on a Chip*, 2007; 7: 842-9.
- Huang Y, Williams JC, Johnson SM. Brain slice on a chip: opportunities and challenges of applying microfluidic technology to intact tissues. *Lab on a Chip*, 2012; 12: 2103-17.
- Jardemark K, Marcus MM, Konradsson A, Svensson TH. The combination of nicotine with the D₂ antagonist raclopride or the weak D₄ antagonist L-745,870 generates a clozapine-like facilitation of NMDA receptor-mediated neurotransmission in pyramidal cells of the rat medial prefrontal cortex. *The international journal of neuropsychopharmacology / official scientific journal of the Collegium Internationale Neuropsychopharmacologicum (CINP)*, 2005; 8: 157-62.
- Konradsson A, Marcus MM, Hertel P, Svensson TH, Jardemark KE. Inhibition of the glycine transporter GlyT-1 potentiates the effect of risperidone, but not clozapine, on glutamatergic transmission in the rat medial prefrontal cortex. *Synapse (New York, N.Y.)*, 2006; 60: 102-8.
- Muller D, Joly M, Lynch G. Contributions of Quisqualate and NMDA Receptors to the Induction and Expression of LTP. *Science*, 1988; 242: 1694-7.
- Muller D, Larson J, Lynch G. The NMDA Receptor-mediated Components of Responses Evoked by Patterned Stimulation are not Increased by Long-Term Potentiation. *Brain Research*, 1989; 477: 396-9.
- Queval A, Ghattamaneni NR, Perrault CM, Gill R, Mirzaei M, McKinney RA, Juncker D. Chamber and microfluidic probe for microperfusion of organotypic brain slices. *Lab on a Chip*, 2010; 10: 326-34.
- Rambani K, Vukasinovic J, Glezer A, Potter SM. Culturing thick brain slices: An interstitial 3D microperfusion system for enhanced viability. *Journal of Neuroscience Methods*, 2009; 180: 243-54.
- Shahi K, Baudry M. Increasing Binding-affinity of Agonists to Glutamate Receptors Increases Synaptic Responses at Glutamatergic Synapses. *Proceedings of the National Academy of Sciences of the United States of America*, 1992; 89: 6881-5.
- Veselovsky NS, Engert F, Lux HD. Fast local superfusion technique. *Pflügers Archiv-European Journal of Physiology*, 1996; 432: 351-4.

PAPER

VI

Article

An optofluidic temperature probe

Ilona Węgrzyn, Alar Ainla, Gavin D. M. Jeffries, and Aldo Jesorka*

Department of Chemical and Biological Engineering, Chalmers University of Technology, Kemivägen 10, SE-412 96 Göteborg, Sweden; E-Mails: ilona.wegrzyn@chalmers.se (I.W.); ainla@chalmers.se (A.A.); jeffries@chalmers.se (G.D.M.J.); aldo@chalmers.se (A.J.)

* Author to whom correspondence should be addressed; E-Mail: aldo@chalmers.se (A.J.); Tel.: +46 31 772 6112; Fax: +46 31 772 6120.

Received: / Accepted: /

Published:

Abstract: We report the application of a microfluidic device for semi-contact temperature measurement in picoliter volumes within aqueous media. Our device, a freely positionable multifunctional pipette, operates by a hydrodynamic confinement principle, i.e. by creating a virtual flow cell of micrometer dimensions within a greater aqueous volume. We utilized two fluorescent rhodamines, with greatly different fluorescent responses with temperature, and made ratiometric intensity measurements. The temperature dependence of the intensity ratio was calibrated and used in a model study of the thermal activation of TRPV1 ion channels expressed in Chinese hamster ovary cells. Our approach represents a practical and robust solution to the specific problem of measuring temperature in biological experiments in vitro, involving highly localized heat generation, for example with an IR laser.

Keywords: Rhodamine B, Rhodamine 6G; Multifunctional pipette; microfluidic device, microthermometer; temperature sensing, semi-contact, optofluidic

1. Introduction

Accurate temperature determination is a key issue in many experimental studies within physics, chemistry and biology. The progressing miniaturization in many experimental methodologies has consequently also affected the instrumentation for thermal measurements. In particular the fast developing research field of microfluidics, which is largely transdisciplinary and adds a strong engineering component to scientific investigations, produced quite a variety of thermometry

implementations within microfluidic chip technology. Many applications involving microfluidic chips depend on temperature measurement and control, mostly performed on flows confined to fluidic channels of micro- to millimeter dimensions. Examples include on-chip PCR amplification of DNA[1], separation methods based on thermal gradients[2-3], and devices enabling the investigation of kinetics and thermodynamics of chemical and biochemical reactions on the microscale [4-5]. However, local temperature measurement of biological samples in aqueous environments not confined to channels is challenging, in particular around single cells in cultures and tissue during microscopy experiments.

The range of techniques for temperature determination is extensive, with their physical foundations in thermoelectricity, temperature dependent resistance changes of electrical conductors, and optical phenomena such as fluorescence [6]. The majority of them, for example thermal imaging and a variety of spectroscopic methods, lack the spatial resolution to be applied in small scale devices. In microdevice technology, common methodologies to measure temperatures at small size scales rely on the application of solid state sensing devices such as thermistors [7], resistance temperature detectors (RTD) [8-9], and thermocouples [10-13]. A number of other methods suitable for the microscopic size scale exist, most notably ion conductometry through a narrow glass capillary [14] or fluorescence based techniques which either use strongly temperature-responsive fluorophores [15-17], or molecular beacons [18]. Thermistors as semiconductor resistance thermometers, and RTDs allow for high precision measurement, excellent stability and repeatability, but require elaborate fabrication. Microthermocouples also offer noteworthy advantages, namely short response time, simple construction and low production cost. They give moderately precise results, but the interface junction potentials require compensation. For integration into the surface of microfluidic chips and flow chambers, where the sensor is isolated from the aqueous flow to be investigated, such sensors can be conveniently obtained from commercial sources, or alternatively, directly fabricated into the device. Apart from the fabrication effort and other difficulties, these assemblies feature only limited positional flexibility, and microheating devices have to be designed so that heat source and sensor are co-localized. If more flexible local measurements are needed, *i.e.* to bring the probe to the heat source, specifically designed microprobes need to be employed, which require custom fabrication, packaging and physical isolation from the aqueous medium. We have previously utilized such microthermocouple probes in combination with micromanipulation in various temperature studies on giant vesicles and in single cell electrophysiology [10].

Measuring the temperature dependence of ion conductivity using microcapillaries is an alternative means to measure the temperature locally in a microscale fluid environment. Glass needles benefit from their small footprint, and from the possibility to be specifically manipulated to a desired location in the sample [17]. A disadvantage is their fragility, which is particularly troublesome when measurements close to the surface, for example in a cell culture or on supported lipid films, need to be performed. They also require calibration individually for each fabricated needle, which is due to small differences in the tip geometry. Moreover, sensitive electronics are required to amplify the small signals generated by this probe, and the capillaries with their tiny orifices are prone to blockage. The benefits of glass needles are the relatively simple preparation, coupled with the ability to make fast and highly localized measurements.

A good substitute for solid state sensors to be applied in microchannels within microfluidics devices, is the semi-invasive approach of utilizing an optical, fluorescence based sensing principle [15-

16,19–20]. The temperature is determined by following the change in fluorescence intensity of the fluorophore via a previously obtained calibration model [21]. Many interesting variants have been reported, for example the use of ratiometric dual-emission-wavelength measurements using molecular beacons in order to create a thermometer whereby the response is independent of the fluorophore concentration, as well as slight run-to-run changes in the experimental setup [18].

Many microscopy experiments in the life sciences utilize fluorescence or confocal imaging as standard techniques, thus the additional fluorescence intensity measurements for such a thermosensor does not pose any additional challenges or expenses. Such systems also exhibit disadvantages, including the absorption of the fluorescent dye by the channel walls, most notable in polydimethylsiloxane (PDMS) based microfluidic devices, which hinders accurate fluorescence measurement, or the degradation of the fluorophore by photobleaching [19,22]. While the primary benefits of the optical readout are striking, with no need for electrical shielding or insulation, and lower fabrication and packaging requirements, it seems apparent that the use of dye solutions is limited to in-channel measurements.

We present here an open-volume and fluorescence based temperature measurement technique utilizing two rhodamine solutions in a hydrodynamically confined flow (HCF) device (Figure 1). By means of the previously reported multifunctional pipette [23], a positionable open volume microfluidic device, we construct an optofluidic semi-contact thermometer which can be readily applied in microscopy experiments of biological and artificial cells, or tissue samples.

The multifunctional pipette primarily re-circulates a solution of the temperature-responsive fluorophores Rhodamine B (RhB) [24–27]. An aqueous solution of this dye is well known to exhibit an inverse dependency of its fluorescence emission intensity on temperature [28]. Using the solution switching capability of the device, we alternate RhB solution with Rhodamine 6G (Rh6G), which does not exhibit a dramatic dependence on temperature in the applicable range for biological systems. By making a comparative analysis of the ratio of fluorescence intensity obtained from either solution as the temperature is changed, we are able to exclude all environmental factors such as pipette position, heating source variances, microscope and detector settings (pinhole, signal gain etc.).

The main advantage of this concept is the avoidance of complex fabrication and interfacing steps, as is required for most solid state sensors, and utilize instead an established, readily available microfluidic device. We essentially redirect the fabrication challenge away from the sensor element, which involves fabrication, packaging, and interfacing, towards the simple replica molding procedure of a PDMS microfluidic chip. This greatly facilitates the construction of a microthermometer, and introduces a number of practical benefits. The device can be freely positioned close to the object of interest, and is at the same time unbreakable upon accidental contact with the surface. Most importantly, the specific features of the multifunctional pipette provide a remedy to some significant issues of fluorescence based temperature sensing: the virtual flow cell is unaffected by absorption of the dye to the device walls [29], and the fast exchange of rhodamine solutions counteracts fluorescence photobleaching, which has a detrimental effect on the intensity measurements. Due to the dual dye, single wavelength intensity ratio measurement, the device needs calibration only once for a given pair of dye concentration values used in the microfluidic devices.

2. Experimental Section

2.1. Multifunctional pipette

The fabrication of the multifunctional pipette was described elsewhere [23]. The key specifications of the pipette were as follows: channel dimensions: 30 x 30 μm , channel separation at the tip: 20 μm , bottom clearance of the channels: 20 μm , solution reservoir volume: 35 μl , on chip switching capability: 4 independent solutions. The device used in the study was purchased from Avalance Biotech AB (Sweden).

2.2. Chemicals

Rhodamine B and Rhodamine 6G were purchased from Sigma-Aldrich (Sweden). Stock solutions were prepared of both rhodamines and the concentrations adjusted so that the fluorescence emission intensities (543/554–604 nm) were approximately equal. Absorption spectra were measured in PBS buffer (pH 7.4), using 10 mm cuvettes. The absorbance values, which are convenient to reproduce the dye solutions (concentration $\sim 80 \mu\text{M}$) used in the experiments, were 0.595675 at $\lambda_{\text{abs_max}} = 554 \text{ nm}$ for RhB, and 0.452295 at $\lambda_{\text{abs_max}} = 527 \text{ nm}$ for Rh6B, respectively (supplementary information). 35 μl of each solution was transferred into the multifunctional pipette.

2.3. Microscopy

A laser scanning confocal microscope Leica IRE2 (Leica Microsystems GmbH, Wetzlar, Germany) equipped with a Leica TCS SP2 confocal scanner, and a long working distance objective 20x, NA 0.7. A HeNe laser provided the 543 nm, and an Ar/ArKr laser the 488 nm excitation wavelength. The 543 nm laser line was used to excite RhB and Rh6G solutions and 488 nm laser to visualize fluorescence of YO-PRO (emission collected 500–535 nm) after activation the human Transient Receptor Potential Vanilloid 1 (TRPV1) channels in Chinese hamster ovary (CHO) cells. Leica Lite (Leica Microsystems), Labview (National Instruments) and Matlab (Mathworks) packages were used to analyze the data.

2.4. Heating systems

2.4.1. Surface printed heaters

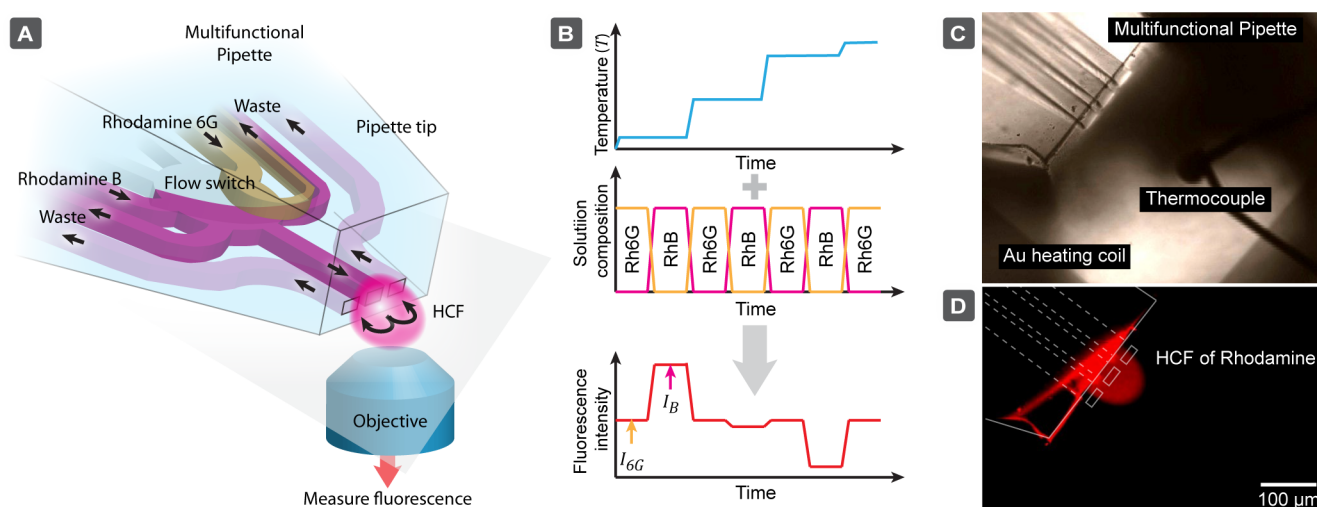
To generate a calibration curve, a non-optical microheating system in combination with a thermocouple reference sensor was used. The microheater consisted of a serpentine-shaped gold film, microfabricated onto a microscopy glass coverslip and coated with a layer of hard-baked SU-8 epoxy. The cover slip was interfaced using custom made microscope-stage contacts. The microfabrication procedures (photolithography, film deposition, and epoxy-coating) have been previously described and applied by Markström et al. [10]. The reference temperatures for calibration have been determined using a Type E (chromel–constantan with 68 $\mu\text{V}/^\circ\text{C}$) microthermocouple (Omega Engineering, UK) connected to an custom built amplifier (10 $\text{mV}/^\circ\text{C}$) with junction compensation, which was positioned

closely to the micropipette channel exits. The thermocouple calibration measurements were performed in the range of 21 – 60 °C. The thermocouple readout was recorded after a stable temperature was achieved, while simultaneously a recording a fluorescence image of the re-circulation zone from the micropipette.

2.4.2. IR laser and optical fiber

In the experiments, a 5W, 1470nm (IR-B) semiconductor diode laser (Seminex HHF-1470-6-95) connected to 8A power supply (4308 LaserSource, Arroyo Instruments) was used as an optical heat source. The laser light was transmitted to the measurement region by a 50 μm core diameter, 0.22NA naked optical fiber (Ocean Optics). The polished end of the fiber was immersed into the aqueous sample solution, and micromanipulated to the region where the experiment was performed.

Figure 1. Concept of the microfluidic temperature probe with optical readout. **(A)** Schematic perspective view of the multifunctional pipette, which generates a hydrodynamically confined flow (HCF) in the environment where the temperature is probed. The content of this virtual flow cell can be quickly multiplexed between the strongly and weakly temperature responsive dyes. **(B)** The fluorescence signal of Rhodamine B (RhB) IB rapidly drops with increasing temperature, while the fluorescence intensity of Rhodamine 6G (Rh6G) I6G is only slightly influenced by temperature change. Outlined within is the concept of coupling the alternation of a change in temperature. **(C)** Micrograph of the multifunctional pipette in the calibration setup on top of a surface printed thin film heater (dark areas in left and right bottom corners) and a type E microthermocouple as a reference sensor. **(D)** Fluorescence image of the rhodamine HCF generated at the tip of the pipette (top down view). The diagonal line observed, is an artifact due to the pipette contacting the surface, which does not interfere with the flow or function.



2.5. COMSOL simulations

All simulations were performed with finite element modeling software COMSOL 4.1 (COMSOL AB, Stockholm, Sweden) running on Intel® Xeon® CPU (4 cores, 2.13GHz) with 16GB of installed memory. The model incorporated the physics of laminar flow (spf), transport of dilute species (chds) and heat transfer (ht/fluid), with approximately 200,000 elements in the mesh.

2.6. Thermal activation of human TRPV1 channels in CHO cells

Cells for expression of TRPV1 with the tetracycline regulated expression system (T-Rex) were received as a kind gift from Astra Zeneca, R&D, CNS & Pain, Södertälje, Sweden. Before use, the cells were cultured for 2-6 days. The TRPV1 channel is a non-selective channel, permeable for cations, which contains six transmembrane domains [30-31]. It can be activated by several stimuli such as capsaicin, protons and temperatures higher than 42 °C [32].

2.6.1. TRPV1 activation

A 1 µM solution of the carbocyanine nucleic acid dye YO-PRO®-1 (purchased from Invitrogen) in extracellular buffer (140 mM NaCl, 5mM KCl, 1mM MgCl₂, 10mM HEPES, 10mM D-glucose, 10 mM Na₄BAPTA, pH 7.4) was added to the culture dish containing the cells prior to the experiment, but could not enter the cell through the TRPV1 channels below activation temperature. The fluorescence intensity of YO-PRO-1 increases significantly when it enters a cell and binds to DNA. For the ion channel activation/dye uptake experiment, the temperature was increased locally stepwise by means of the IR laser heater, and monitored with the pipette thermometer. When a desired temperature value was reached, the fluorescence emission of YO-PRO-1 was recorded for the period of 6 minutes (five different temperature points were measured).

3. Theory and Model

The physics of the pipette thermometer is governed by the convection-diffusion equation. We consider a stationary measurement regime (after equilibration):

$$\vec{v} \cdot \nabla c = D \nabla^2 c \quad (1)$$

where v is the convective flow velocity, D is the diffusivity and c is the concentration of the dye. The concentration distribution depends on the Péclet number, a dimensionless scaling parameter: $Pé = vL/D$. The temperature distribution can be calculated by an equivalent equation, where the concentration is replaced by temperature T , and the diffusion by the thermal diffusivity $D_{therm} = 1.4 \cdot 10^{-7} \text{ m}^2/\text{s}$. The thermal diffusivity is about 380x higher than the molecular diffusivity of small molecules, for example, dye molecules such as rhodamine B or 6G. Another relevant difference between the thermal and molecular diffusivity lies in the boundary conditions. While molecular transport is confined to a liquid environment, the thermal diffusion also occurs at a nearly equal rate in solids, i.e., heat dissipated through the glass bottom of the dish and pipette tip itself. The key to correct pipette function is to use a size scale, and flow parameters, so that $Pé_{mol}$ is sufficiently high to confine the dye and avoid contamination of the open volume, while $Pé_{therm}$ is sufficiently low to allow that the liquid in the confined volume equilibrates thermally with the surrounding, which is necessity for accurate thermal sensing. Another critical aspect is the determination of an operation regime which is

least sensitive to experimental variances which may change from run to run, including the microscope settings, pipette position and angle etc., in order to ensure repeatability and a universally valid calibration. For this we briefly describe how the fluorescence based intensity signal is actually formed. Intensity signal I in microscope can be described as,

$$I = \int_V P \cdot G \cdot A(\vec{r}) c(\vec{r}, \vec{v}, D(T)) f(T(\vec{r}, \vec{v}, T_s)) d\vec{r}^3 \quad (2)$$

where P is the power of the excitation light, G is the sensor gain. $A(\vec{r})$ is the spatial optical response function, describing how efficiently fluorescent light is gathered from different spatial locations. It depends on the pipette position, objective and focus. $c(\vec{r}, \vec{v}, D(T))$ describes the spatial concentration distribution of the dye, which depends on the flow \vec{v} and diffusivity $D(T)$. $f(T(\vec{r}, \vec{v}, T_s))$, describes the molecular fluorescence, which depends on the temperature $T(\vec{r}, \vec{v}, T_s)$, which further depends on the flow and the local temperature T_s , which itself is of interest to be sensed. The fluorescence response is thus depending on a multitude of parameters, nearly impossible to reproduce and take into account fully. In order to simplify this situation, we have taken advantage of the switching function of the pipette, allowing to exchange between two similar fluorescent dyes, having similar diffusivity D . If we also maintain the flow rates \vec{v} during exchange, use the same microscope settings (focus, spot size etc.) and also same excitation and fluorescence measurement parameters, then P , G , A , c and V will be identical. In this case the ratio I_B/I_{6G} becomes

$$\frac{I_B}{I_{6G}} = \frac{\int_V A(\vec{r}) c(\vec{r}, \vec{v}, D(T)) f_B(T(\vec{r}, \vec{v}, T_s)) d\vec{r}^3}{\int_V A(\vec{r}) c(\vec{r}, \vec{v}, D(T)) f_{6G}(T(\vec{r}, \vec{v}, T_s)) d\vec{r}^3} \quad (3)$$

Since the contributions f are having a non-linear dependence on temperature, this equation is still too complex. However, if the flow rates are sufficiently low, such that the hydrodynamically confined volume becomes thermally equilibrated with the surrounding, then $T = T_s \neq f(\vec{r})$, thus most of the integral components cancel out and Eq. 3 becomes

$$\frac{I_B}{I_{6G}} = \frac{f_B(T_s)}{f_{6G}(T_s)} \quad (4)$$

where the ratio $f_B(T_s)/f_{6G}(T_s)$ is solely a molecular property of the dyes, depending only on the temperature, but not on the device, microscope, sensor or illumination settings.

Therefore, this ratio is universal and an easily transferable calibration parameter. The only crucial aspect is to ensure the accuracy of concentration values of both fluorescent dyes, which can be easily determined by absorption spectrometry (Supplementary information). One other assumption has to be made in this model: Only a small fraction of the excitation light is absorbed in the measured volume, i.e., the measured volume is adequately illuminated. If $\varepsilon \approx 10^5 \text{ M}^{-1}\text{cm}^{-1}$ (Supplementary Figure), a maximum possible path length of $l \approx 30 \mu\text{m}$, and a dye concentration $c \approx 100 \mu\text{M}$, then the absorption of excitation light is less than 7%, which can be considered negligible.

3.1. Simulation

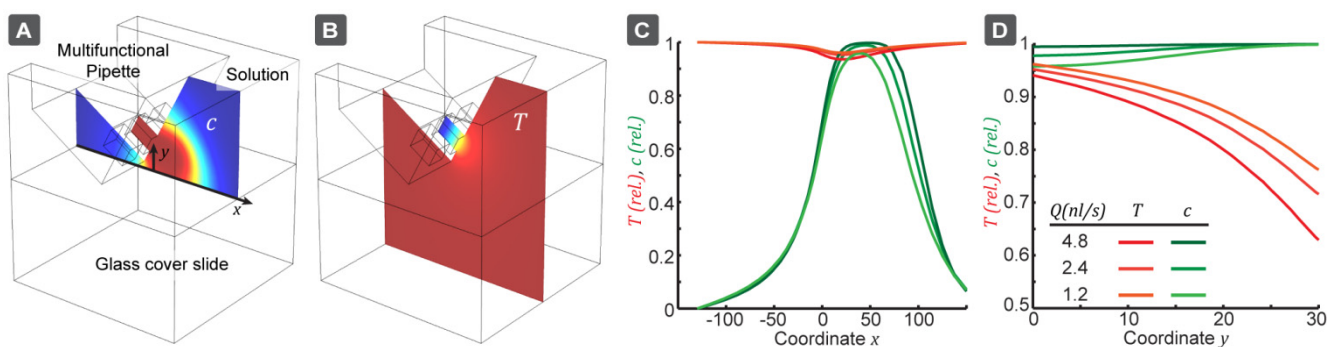
A finite element model has been created to find suitable flow conditions, which would confine the dye molecules, while allowing for sufficient thermal equilibration. These simulations were also used for a simple perturbation analysis of the pipette, in order to determine how the signal can be affected by small deviations in flow rate Q , and outflow-inflow ratio R ,

$$\frac{\Delta I}{I} = \underbrace{\frac{Q}{I} \cdot \frac{\partial I}{\partial Q}}_a \frac{\Delta Q}{Q} + \underbrace{\frac{R}{I} \cdot \frac{\partial I}{\partial R}}_b \frac{\Delta R}{R} \quad (5)$$

We have determined the first order perturbation coefficients a and b , which are important to estimate how slight pressure fluctuations and flow channel imbalances could affect the measurement result.

The pipette has three channels of equal size, with a cross-section of $30 \times 30 \mu\text{m}^2$ separated by a channel wall of $20 \mu\text{m}$, as well as a $20 \mu\text{m}$ bottom membrane. The pipette is positioned at an angle of 30° and positioned $10 \mu\text{m}$ above the glass bottom. The glass bottom layer is $150 \mu\text{m}$ thick (#1 glass). The outflow was set to $Q = 1.2, 2.4$ and 4.8 nl/s and inflow rate such that $Q_{\text{out}}/Q_{\text{in}} = 0.45$, as used in the experiments. The simulation volume was $200 \times 200 \times 200 \mu\text{m}^3$ around the pipette tip. In a first step, the flow-field was calculated and the results were used for evaluation of the concentration profile and the thermal equilibration. The diffusivity of the rhodamines was $D(20^\circ\text{C}) = 4.2 \cdot 10^{-10} \text{ m}^2/\text{s}$ at room temperature, while at $D(60^\circ\text{C}) = 2.4D(20^\circ\text{C})$. [33] The thermal diffusivity, on the other hand, is very little affected by temperature changes in this range (less than 1.1x).

Figure 2. Finite element model of the pipette thermometer. **(A)** Hydrodynamic confinement of the fluorescent dye. **(B)** Thermal equilibration of the out-flowing solution. **(C)** Concentration and thermal equilibration profile along the bottom surface of the chamber (e.g. culture dish) and vertically in front of the pipette tip **(D)**, for different flow rates Q . The graphs are normalized such that 0 corresponds to the surrounding liquid composition (C) and completely non-equilibrated temperature (T), while 1 corresponds to outflow composition and full thermal equilibration.



From our simulations, the perturbation parameters found were $a = 0.18$ and $b = 0.0006$. Thermal equilibration near the surface is around $\sim 95\%$ and through the entire volume $\sim 87\%$ (Supplementary Table 1). However, the actual extent of thermal equilibration must be higher, since the pipette tip itself is also heat conductive (neglected in the above described model). The concentration drop due to diffusion is negligible $\sim 1\%$. These values define the maximum variations, which are possible due to slight changes in the pipette position. The parameters a and b are only weakly dependent on the flow rate and the Q_{out}/Q_{in} ratio, which indicates a stable calibration.

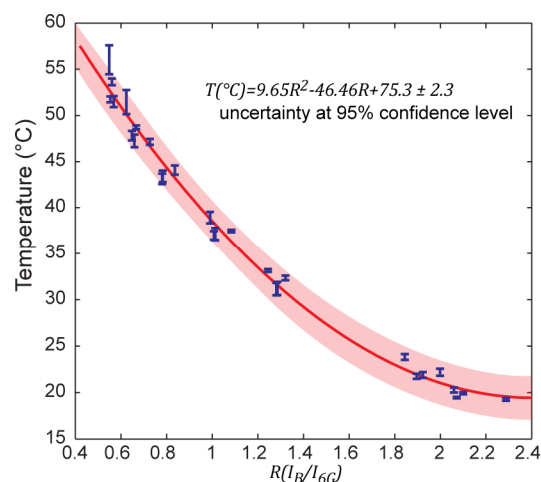
4. Results and Discussion

4.1. Calibration curve

After measuring the fluorescence intensities (single wavelength excited) of both dyes at different temperatures, a series of intensity ratios I_B/I_{6G} could be calculated and plotted vs. temperature. The data points were fitted by a second order polynomial (Figure 3). The temperatures for the calibration model were determined by a calibrated thermocouple (Figure 1). The dynamic range of the sensor does not exceed the temperature range relevant for biological systems. It is likely that different dye pairs can be used to address other desired dynamic ranges and sensitivity.

This calibration curve is universally transferable to other experimental setups and conditions as long as the same dyes and concentration ratios are used in the actual measurements. It is not strictly required to replicate absolute concentrations, as long as the ratio is preserved and the fluorescence intensity change over the temperature range of interest is covered by the dynamic range of the optical fluorescence detector.

Figure 3. Calibration curve of pipette thermometer, showing the relation between fluorescence intensity ratio I_B/I_{6G} and temperature T . Temperature dependent measurements were carried out in both directions (to account for a possible hysteresis), at two different flow rates and at two different distances of the channel outlets from the bottom plane. All error bars are given for the 95% confidence level.



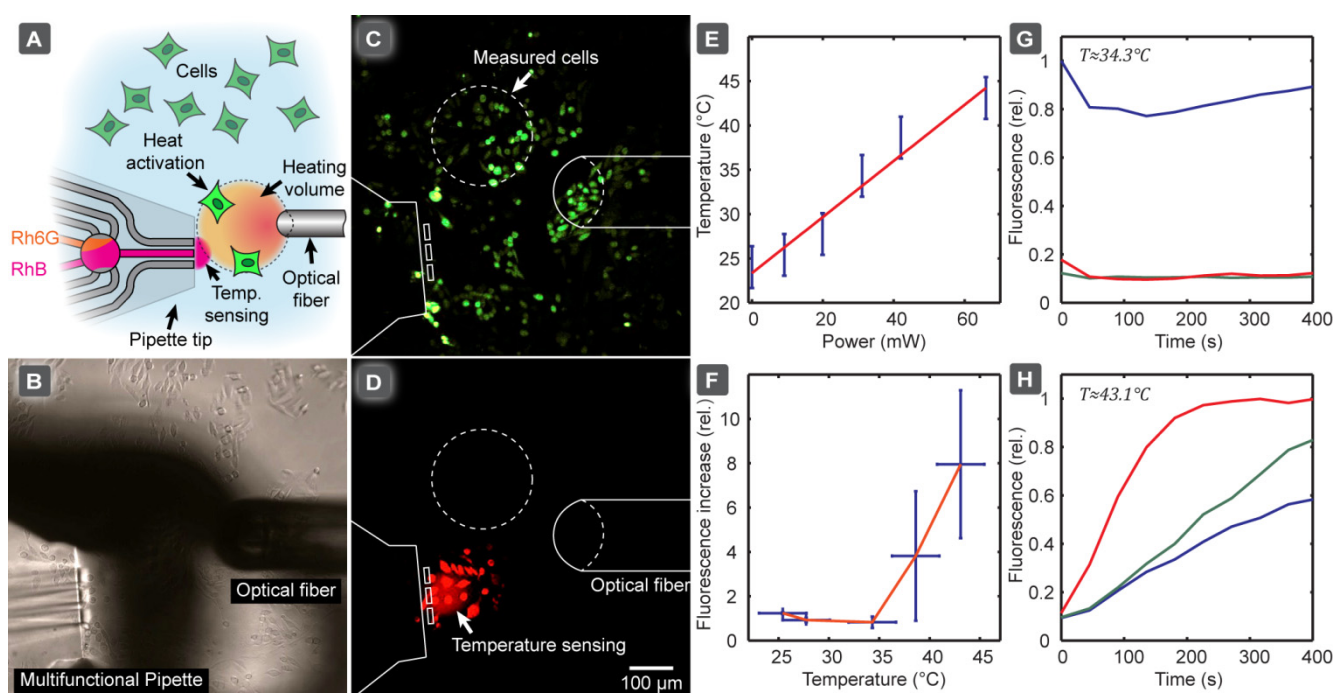
The calibration curve in Figure 3 features 6 discernible groups of data points, each of which corresponds to a set of measurements under varied experimental conditions. In each group alterations

of either a) the channel height above the bottom (0 – 10 μm), or b) the flow rate (2.4 nl/s – 4.8 nl/s), or c) the direction of temperature change (up - down) were made in order to test the measurement repeatability, and thereby the validity of the theoretical model. These quite aggressive variations confirm, on one hand, independency from external influences, but are, on the other hand, the main cause of the somewhat decreased precision of the sensor.

This calibration model, based on a single excitation wavelength ratiometric measurement, is universally transferable. Absolute temperature measurements can thus be performed on samples directly without re-calibration.

4.2. Thermal activation of TRPV1 channels in CHO cells

Figure 4. Heat activation of temperature sensitive ion-channels TRPV1, over-expressed in CHO cells, measured as a YO-PRO-1 uptake assay. **(A)** Schematic drawing of the concept of the experiment. Small groups of cells are activated by localized heating with IR radiation through the optical fiber (50 μm core). Ion-channel activation is characterized by the passage of the prefluorescent dye YO-PRO-1, while temperature is simultaneously probed using the pipette thermometer. **(B)** Brightfield micrograph of the actual experimental setup, showing the pipette and the optical fiber in close vicinity to the cells. **(C)** Fluorescence images of cells, measuring the intracellular fluorescence ($\lambda_{\text{exc}} = 488\text{nm}$) in the region shown in (a). **(D)** Fluorescence image of the same region recorded in the rhodamine channel ($\lambda_{\text{exc}} = 543\text{nm}$). The cells in the vicinity of the HCF zone appear brighter due to membrane absorption of rhodamine. **(E)** The equilibrium temperature depending on laser power. **(F)** The cellular fluorescence response depending on the temperature, measured as relative fluorescence increase. **(G-H)** Time course of the cellular fluorescence, after switching on the laser heater (G) below (34.3 $^{\circ}\text{C}$) and (H) above (43.1 $^{\circ}\text{C}$) the activation temperature. All error bars are given at the 95% confidence level.



We subsequently applied the calibration model in an application example, in which we investigated the thermal activation of heat-sensitive TRPV1 ion channels in single CHO cells. In order to determine the activation temperature of TRPV1 ion channels, which are over-expressed in the specific CHO cell line we employed, we used an IR diode laser coupled to an optical fiber. This served as a localized heat source to activate the ion channel of a selected group of cells, allowing the DNA binding stain YO-PRO-1 to enter the cell, as a reporter of activation (YO-PRO-1 uptake assay). Figure 4 shows the experimental setup (A-B), and the fluorescence image of the activated cells (C). Since the cells readily absorb rhodamine (Figure 4D), a region of interest in-between the cells was defined and used for temperature sensing. In Figure 4D the linear dependency of the equilibrium temperature from the laser power is presented, giving an indication which power range has to be approximately provided to cover the dynamic range of the pipette thermometer. A low power fiber-coupled diode laser is normally sufficient for this kind of investigation, but we note that coupling losses between fibers can significantly reduce the available power, depending on the core diameter of the receiving fiber.

Figure 4 (F) depicts the relative YO-PRO-1 fluorescence increase depending on temperature, indicating that that TRPV1 activation occurred when the temperature exceeded 40 °C, which is in accordance with the literature. The calibration curve in Figure 3 was used to calculate the temperature values shown in (F). A time course of the cellular fluorescence intensity change (relative), determined for three individual cells after switching on the IR laser, is presented before (G) and after (H) the activation temperature was reached. Note that the fluorescence intensities of the three cells are somewhat different, reflecting small differences, such as size, between the individual cells. The cells were selected such that the distance of the cells and the thermometer from the long (horizontal) axis of the laser fiber was approximately the same, in order to ensure that the measured temperature corresponds to the temperature the selected cells experience. Alternatively, the optical fiber can be repositioned for each cell to ensure the same distances selected cells, either by micromanipulating the fiber or translating the stage.

This exemplary study shows that the pipette thermometer can serve as a convenient auxiliary device to probe local temperatures under the conditions of single cell experiments, where closed channel microfluidic thermometers are unsuitable, solid state thermal sensors are less suitable (IR absorption, lack of positionability), and ion conductometry by means of glass capillary is risky (clogging risk by cell debris, proximity to surface). The precision and accuracy of the temperature measurement achieved with the probe are at least sufficient to make semi-quantitative statements (above/below/close to activation temperature), which is often satisfactory.

5. Conclusions

We have demonstrated the possibility of an open volume microfluidic thermometer, using a hydrodynamically confined flow device and optical fluorescence readout generated from a single excitation wavelength. Two fluorescent dyes with different thermal fluorescent responses are sequentially pumped through a virtual flow cell produced by the device. Assuming thermal equilibrium between the flow cell and the surrounding environment, and low enough dye concentrations to ensure adequate illumination of the whole volume, the temperature can be determined directly by measuring the fluorescence intensity ratio between the two dyes in conjunction with an established calibration

model. In contrast to most closed-channel microfluidic thermosensing devices with optical readout, our thermosensor is positionable, meaning that it can be brought very close to objects of interest. This allows for temperature measurements of biological experiments *in vitro* involving highly localized heat generation, for example by IR laser radiation. The optical detection principle is also beneficial in experiments involving sensitive electrical measurements, for example when patch clamp electrophysiology, electrochemical detection or impedance measurements are performed.

The multifunctional microfluidic pipette provides non-conventional opportunities to perform experiments that are otherwise difficult to perform. One example is the direct temperature measurement in the vicinity of a single adherent biological cell. Envisioned application areas are heat- or cold-activated ion channel studies, or other heat-assisted experiments on cells or tissue slices, in conjunction with confocal, or most beneficially, total internal reflection (TIRF) microscopy. We have shown that the calibration model is universally transferable, meaning that absolute temperature measurements are possible, independent from small day-to-day changes in the experimental conditions.

Future opportunities exist to improve some figures of merit, in particular the currently moderate precision (see section 4.1) and the spatial resolution of the thermal sensor. In order to increase spatial resolution, the recirculation volume has to be decreased. This can in principle be achieved by decreasing the channel dimensions, but countermeasures against the increasing cross-boundary diffusion are required. One possible remedy is the use of fluorescent nanoparticles, for example, polymer nanospheres or vesicles loaded with the fluorescent dyes, so that smaller channels can be used at lower $Pé_{therm}$. If such particles are carefully chosen such that they do not bind or otherwise interfere with the objects of interest, and absorb at a suitable wavelength, they might very well be routinely added to MFP superfusion protocols, which would provide a facile means of *in-situ* temperature measurement.

6. Acknowledgments

This research was supported by the Swedish Research Council (VR), the European Research Council (ERC), Nordforsk (Nordic Network for Dynamic Biomembrane Research), and the Carl Tryggers Stiftelse.

7. References and Notes

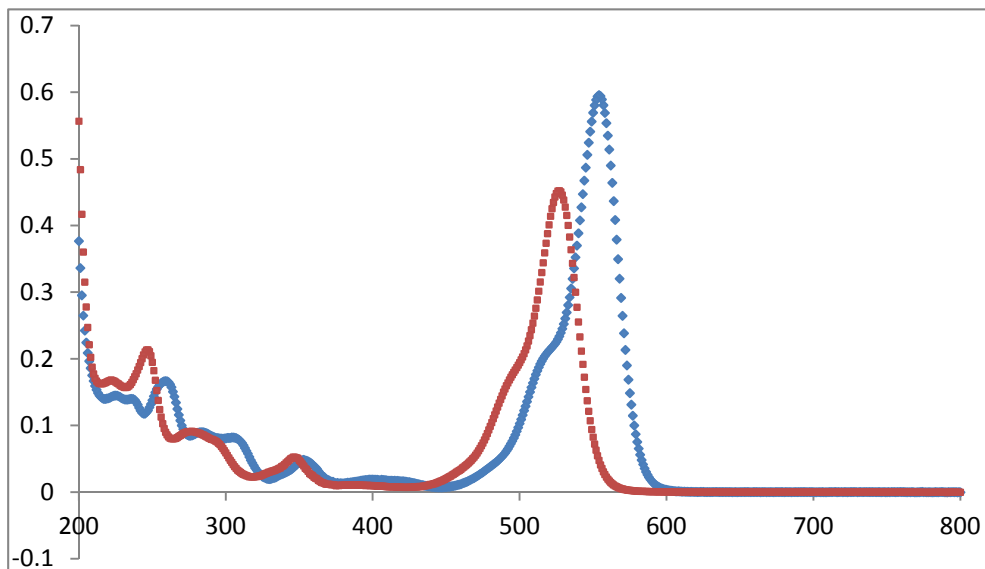
1. Kopp, M.U.; de Mello, A.J.; Manz, A., Chemical amplification: Continuous-flow pcr on a chip. *Science* **1998**, *280*, 1046-1048.
2. Vigolo, D.; Rusconi, R.; Stone, H.A.; Piazza, R., Thermophoresis: Microfluidics characterization and separation. *Soft Matter* **2010**, *6*, 3489-3493.
3. Bargiel, S.; Górecka-Drzazga, A.; Dziuban, J.A., A micromachined system for the separation of molecules using thermal field-flow fractionation method. *Sensors and Actuators A: Physical* **2004**, *110*, 328-335.
4. Hirano, K.; Ishii, R.; Imayou, H.; Nishioka, M.; Matsuzawa, Y.; Katsura, S.; Mizuno, A.; Ieee, *Application of local temperature control for DNA micromanipulation*. I E E E: New York, 1996; p 177-182.

5. Chabala, L.; Sheridan, R.; Hodge, D.; Power, J.; Walsh, M., A microscope stage temperature controller for the study of whole-cell or single-channel currents. *Pflugers Arch.* **1985**, *404*, 374-377.
6. Childs, P.R.N.; Greenwood, J.R.; Long, C.A., Review of temperature measurement. *Review of Scientific Instruments* **2000**, *71*, 2959-2978.
7. Beakley, W.R., The design of thermistor thermometers with linear calibration. *Journal of Scientific Instruments* **1951**, *28*, 176-179.
8. Barber, C.R., Platinum resistance thermometers of small dimensions. *Journal of Scientific Instruments* **1950**, *27*, 47-49.
9. Tsutsui, M.; Kawai, T.; Taniguchi, M., Unsymmetrical hot electron heating in quasi-ballistic nanocontacts. *Sci. Rep.* **2**.
10. Markstrom, M.; Gunnarsson, A.; Orwar, O.; Jesorka, A., Dynamic microcompartmentalization of giant unilamellar vesicles by sol gel transition and temperature induced shrinking/swelling of poly(n-isopropyl acrylamide). *Soft Matter* **2007**, *3*, 587-595.
11. Allen, P.B.; Rodriguez, I.; Kuyper, C.L.; Lorenz, R.M.; Spicar-Mihalic, P.; Kuo, J.S.; Chiu, D.T., Selective electroless and electrolytic deposition of metal for applications in microfluidics: Fabrication of a microthermocouple. *Analytical Chemistry* **2003**, *75*, 1578-1583.
12. Millingen, M.; Bridle, H.; Jesorka, A.; Lincoln, P.; Orwar, O., Ligand-specific temperature-dependent shifts in ec50 values for the gabaa receptor. *Analytical Chemistry* **2007**, *80*, 340-343.
13. Beckman, P.; Roy, R.P.; Velidandla, V.; Capizzani, M., An improved fast-response microthermocouple[sup a)]. *Review of Scientific Instruments* **1995**, *66*, 4731-4733.
14. Yao, J.; Liu, B.; Qin, F., Rapid temperature jump by infrared diode laser irradiation for patch-clamp studies. *Biophysical Journal* **2009**, *96*, 3611-3619.
15. Ross, D.; Locascio, L.E., Fluorescence thermometry in microfluidics. In *Temperature: Its measurement and control in science and industry*, vol 7, pts 1 and 2, Amer Inst Physics: Melville, 2003; Vol. 684, pp 1051-1055.
16. Ross, D.; Gaitan, M.; Locascio, L.E., Temperature measurement in microfluidic systems using a temperature-dependent fluorescent dye. *Analytical Chemistry* **2001**, *73*, 4117-4123.
17. Zeeb, V.; Suzuki, M.; Ishiwata, S., A novel method of thermal activation and temperature measurement in the microscopic region around single living cells. *Journal of Neuroscience Methods* **2004**, *139*, 69-77.
18. Barilero, T.; Le Saux, T.; Gosse, C.; Jullien, L., Fluorescent thermometers for dual-emission-wavelength measurements: Molecular engineering and application to thermal imaging in a microsystem. *Analytical Chemistry* **2009**, *81*, 7988-8000.
19. Glawdel, T.; Almutairi, Z.; Wang, S.; Ren, C., Photobleaching absorbed rhodamine b to improve temperature measurements in pdms microchannels. *Lab Chip* **2009**, *9*, 171-174.
20. Erickson, D.; Sinton, D.; Li, D., Joule heating and heat transfer in poly(dimethylsiloxane) microfluidic systems. *Lab Chip* **2003**, *3*, 141-149.
21. Shah, J.J.; Gaitan, M.; Geist, J., Generalized temperature measurement equations for rhodamine b dye solution and its application to microfluidics. *Analytical Chemistry* **2009**, *81*, 8260-8263.
22. Toepke, M.W.; Beebe, D.J., Pdms absorption of small molecules and consequences in microfluidic applications. *Lab Chip* **2006**, *6*, 1484-1486.
23. Ainla, A.; Jeffries, G.D.M.; Brune, R.; Orwar, O.; Jesorka, A., A multifunctional pipette. *Lab Chip* **2012**, *12*, 1255-1261.
24. Arbeloa, I.L.; Rohatgi-Mukherjee, K.K., Solvent effects on the photophysics of the molecular forms of rhodamine b. Internal conversion mechanism. *Chemical Physics Letters* **1986**, *129*, 607-614.
25. Fu, R.; Xu, B.; Li, D., Study of the temperature field in microchannels of a pdms chip with embedded local heater using temperature-dependent fluorescent dye. *International Journal of Thermal Sciences* **2006**, *45*, 841-847.

26. Gui, L.; Ren, C.L., Temperature measurement in microfluidic chips using photobleaching of a fluorescent thin film. *Applied Physics Letters* **2008**, *92*, 024102-024102-024103.
27. Sakakibara, J.; Hishida, K.; Maeda, M., Measurements of thermally stratified pipe flow using image-processing techniques. *Experiments in Fluids* **1993**, *16*, 82-96.
28. Sakakibara, J.; Adrian, R.J., Whole field measurement of temperature in water using two-color laser induced fluorescence. *Experiments in Fluids* **1999**, *26*, 7-15.
29. Robinson, T.; Schaerli, Y.; Wootton, R.; Hollfelder, F.; Dunsby, C.; Baldwin, G.; Neil, M.; French, P.; Demello, A., Removal of background signals from fluorescence thermometry measurements in pdms microchannels using fluorescence lifetime imaging. *Lab Chip* **2009**, *9*, 3437-3441.
30. Caterina, M.J.; Schumacher, M.A.; Tominaga, M.; Rosen, T.A.; Levine, J.D.; Julius, D., *The capsaicin receptor: A heat-activated ion channel in the pain pathway*. 1997; Vol. 389, p 816-824.
31. Jordt, S.-E.; Tominaga, M.; Julius, D., Acid potentiation of the capsaicin receptor determined by a key extracellular site. *Proceedings of the National Academy of Sciences* **2000**, *97*, 8134-8139.
32. Neelands, T.; Jarvis, M.; Han, P.; Faltynek, C.; Surowy, C., Acidification of rat trpv1 alters the kinetics of capsaicin responses. *Molecular Pain* **2005**, *1*, 28.
33. Holz, M.; Heil, S.R.; Sacco, A., Temperature-dependent self-diffusion coefficients of water and six selected molecular liquids for calibration in accurate 1h nmr pfg measurements. *Physical Chemistry Chemical Physics* **2000**, *2*, 4740-4742.

Supplementary Information

Figure S1. UV-Vis absorption spectra of the RhB (blue) and Rh6G(red) solutions used in the study (sixteen times diluted).



Dye concentrations calculated, using Lambert –Beer’s Law:

RhB: Ext. Coeff. $\epsilon_{\text{mol}} = 106\,000\text{ M}^{-1}\cdot\text{cm}^{-1}$, ($\lambda_{\text{abs, max}} = 554\text{ nm}$, $A = 0.595675$)

Concentration before dilution: $89.9\text{ }\mu\text{M}$

Rh6G: Ext. Coeff. $\epsilon_{\text{mol}} = 116\,000\text{ M}^{-1}\cdot\text{cm}^{-1}$, ($\lambda_{\text{abs, max}} = 527\text{ nm}$, $A = 0.452295$)

Concentration before dilution: $62.4\text{ }\mu\text{M}$

The measurements were performed in water within 10mm quartz cuvettes. The solutions used in the pipette thermometer were 16x diluted before absorption measurement. Note that the absolute concentration values are only approximate, since the literature extinction coefficients used in the calculation were determined in ethanol. Absolute concentrations are not required for calibration and temperature measurement, it is important that the concentration ratio of 1.44 : 1 (RhB/ Rh6G) is established in order to use the calibration model described in the main text.

Table S1. Thermal equilibration and dye concentration depending on flow rate. The flow rate preferentially used in the experiments (2.4 nl/s) is highlighted in blue

$Q\left(\frac{\text{nl}}{\text{s}}\right)$	T_{surface}	T_{average}	T_{min}	c_{surface}
1.2	96 %	89 %	76 %	96 %
2.4	95 %	87 %	71 %	99 %
4.8	94 %	83 %	63 %	99.7 %

PAPER

VII

Lab on a Membrane: a Toolbox for Reconfigurable 2D fluidic networks

Alar Ainla, Irep Gözen, Bodil Hakonen, and Aldo Jesorka*

Supported molecular phospholipid films are versatile model membrane architectures¹, which are valuable to mimic fundamental properties and features of the plasma membrane at reduced complexity^{2-3,4}. Double bilayer⁵⁻⁶, single bilayer⁷⁻¹² as well as monolayer films¹³ can be formed on solid supports, providing enhanced stability and improved accessibility by probing techniques¹⁴. Supported membranes can cover an extensive area homogeneously, which greatly facilitates modification, observation and imaging¹. Two-dimensionality and fluidity allow their utilization in micro-¹⁵⁻¹⁸ and nanofluidic devices¹⁹, which supports functional studies of membrane proteins²⁰⁻²¹, and promotes the development of membrane-based chemistry²², sensing²³⁻²⁴ and separation¹⁵. Here we introduce a microfluidic toolbox to write 2D nanofluidic networks composed of supported phospholipid membranes, and dynamically modify their connectivity, composition, and local function. We demonstrate how such networks are conveniently generated and locally restructured, and show how various design possibilities such as diffusional barriers and hydrodynamic trapping points can be used in a “lab on a membrane” to directly address biomembrane functions and properties, or to perform membrane-assisted studies of molecular interactions.

Our open volume approach is fundamentally different from the miniaturized technologies currently used to assemble artificial bilayer systems¹⁸. Microfluidic devices that operate in the “open space”, i.e., outside the confinement imposed by channels and chambers, provide unique opportunities for interacting with biological samples. Using a hydrodynamically confined flow device (a multifunctional pipette²⁵) for dispensing suspensions of small unilamellar vesicles (SUVs, 25-50 nm in diameter) in close proximity to a planar surface, we assemble a molecular film locally by means of vesicle adhesion, and subsequent fusion. Hydrodynamic flow confinement limits the exposed area on the surface to 50-100 μm in diameter, and rapid switching between different vesicle types and auxiliary solutions allows dynamic spatiotemporal control over film composition. Figure 1 presents the four main components of the toolbox: *Writing* (Fig. 1a), *Dynamic control of composition* (Fig. 1b), *Erasing* (Fig. 1c), and *Localized lipid film modification and decoration* (Fig. 1d). 2D-networks are directly written by providing liposomes through the pipette, while simultaneously translating the substrate

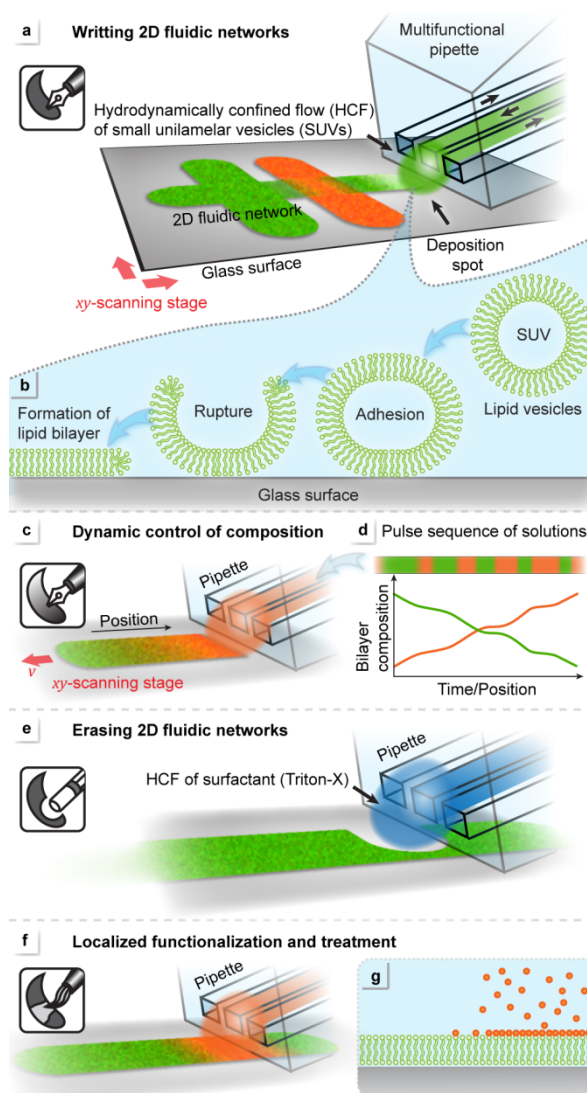


Figure 1| Processing tool box for the “lab on a membrane”, using a virtual flow chamber at the tip of the multifunctional pipette. Up to four process steps can be consecutively applied with the device. a) Writing 2D fluidic networks of a phospholipid bilayer by dispensing small unilamellar vesicles to a confined region on a glass surface. Sequential vesicle adhesion, rupture and fusion lead to a continuous bilayer patch. b) Dynamic control of composition. The composition of the molecular film can be changed during writing by means of the multifunctional pipette, which draws vesicles from the on-chip reservoirs and blends them according to the desired film composition, using a pulse code. The left panel schematically shows the transition from one lipid type to another, the panel on the right shows film composition depending on the position along the writing trajectory. c) Site-selective removal (erasing) of membrane area from the previously written patches by dispensing

a detergent from the multifunctional pipette. d) Localized functionalization or treatment of previously written membrane patches with reactive compounds.

by means of a motorized stage. The maximal writing speed is generally restricted by the kinetics of film formation. Diffusively continuous fluidic networks can be produced in this way, where the topology is defined by the x,y scanning sequence, and the composition depends on the lipids supplied by the pipette. The device allows multiplexing between several different lipid (e.g. SUV) types. The formation mechanism of supported lipid bilayers from small vesicles, which is schematically depicted in Fig. 1b, has been elucidated previously²⁶⁻²⁷. Vesicles adhere to the surface, rupture, and eventually transform into a continuous bilayer. Vesicle rupture occurs either immediately upon contact with the substrate or, alternatively, after a critical concentration of surface adhered vesicles is reached. The bilayer composition can be dynamically altered during the writing process (Fig. 1c,d), owing to the on-chip multiplexing capability. A writing protocol defines lipid type and order of administration, as well as writing time and stage position. Brief exposure bursts sequentially co-deposit vesicles prepared from different lipids in a pulse width modulation (PWM) like manner²⁸ (Fig. 1d), where the final composition is determined by sequence and length of the individual bursts. Since the networks are diffusively connected, the compositional diversity will be lost over time. In order to preserve the composition of a particular membrane lane, it can be temporarily or permanently cut off by means of an “eraser” tool (Fig. 1e). Hydrodynamically confined flow of a detergent solution (e.g. Triton X) from the pipette is used to locally dissolve and thus remove a part of the previously written lipid film. The eraser restores the surface, which can be overwritten with a new lipid layer at a later time. In addition to creating and removing lipid material, lanes and patches can be modified by exposure to various reagents (Fig. 1f-g).

Writing Tool: Figure 2a-h depicts the lipid film deposition. Depending on the lipid used, we observed two different regimes of adding lipid material to the forming film: non-spreading and spreading deposition. Non-spreading deposition occurs when lipid vesicles adhere to the exposed surface, rupture and fuse into a continuous lipid film (Fig. 2a). Deposition ceases upon full coverage, and the formed membrane does not grow beyond the exposed surface region. This means that overwriting of patches in the non-spreading regime is not possible. We demonstrate non-spreading deposition by using SUVs composed of 1-Palmitoyl-2-oleoylphosphatidylcholine (POPC) in Fig. 2b-c, and supplementary figure S4. The size of the generated membrane patch is largely time independent (Fig. 2d). In contrast, spreading deposition involves fusion of vesicles to an existing, previously assembled film²⁷ (Fig. 2e), and

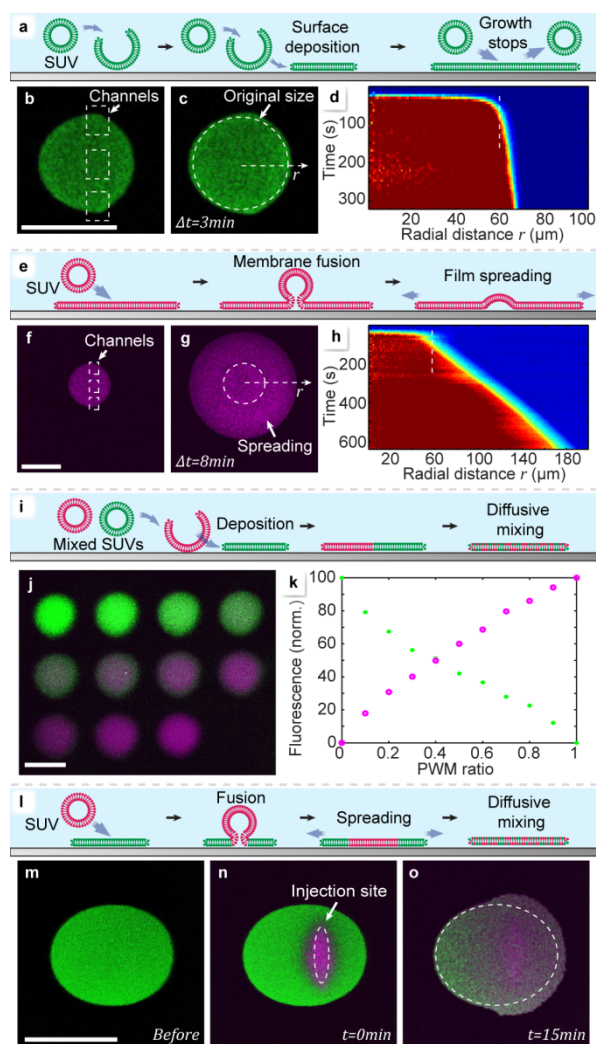


Figure 2 | Deposition. Scale bars: 100 μ m. a) Schematic view of the vesicle adhesion-rupture mechanism, leading to continuous bilayers (*Non-Spreading Regime*). Assembled films cannot be modified by overwriting, as excess lipid material is not inserted into the film. b) Fluorescence micrograph of a deposited POPC-488 membrane patch immediately after deposition and c) after three minutes. The channel positions are marked by white rectangles in (b), and the initial patch perimeter ($t=0$ min) by a white circle in (c). d) Fluorescence intensity depending on time and radial distance, showing no significant area gain. The intensity is color coded from red (highest) to blue (lowest). e) Schematic view of vesicle adhesion-fusion mechanism, leading to continuous bilayers (*Spreading Regime*). The surface area covered by the patch is steadily growing, as excess lipid material is inserted into the film. f) Confocal fluorescence micrograph of a deposited DOTAP patch immediately after deposition and g) after 8 minutes. The channel positions are marked by white rectangles in (f), and the initial patch perimeter by a white circle in (g). h) Fluorescence intensity depending on time and radial distance. The intensity is color coded from red (highest) to blue (lowest). i) Deposition of mixed lipid films by dispensing two vesicle suspensions sequentially by PWM-like switching (schematic view). j) Fluorescence micrograph of eleven sequentially deposited membrane patches of gradually (10% per step) changing composition (POPC-488 (green)/POPC-655 (purple)). k) Fluorescence intensities of the 2 fluorescent labels present in the patches. Each pair of data points (green/red)

represents one individual patch in (j). l) Fusion of SUVs with a previously deposited membrane patch, causing diffusional lipid mixing and spreading. m) Fluorescence micrographs of a POPC-488 patch immediately after deposition, and n) of the same patch after deposition of DOTAP-SUVs onto the center of the patch. The white line marks the injection site. o) Fluorescence micrograph of the binary patch at $t=15$ min after deposition. The white line marks the initial size of the POPC-488 patch.

the deposited membrane expands by surface spreading as long as new vesicles are supplied. Spreading deposition is achieved by using SUVs composed of L- α -phosphatidylcholine (Soy) and the cationic transfection lipid 1,2-dioleoyl-3-trimethylammonium-propane (DOTAP) (1:1 mixture, Fig. 2 f-g). Here, the radius of the membrane patch increases continuously over time for at least 600 seconds (Fig. 2h). In fig. 2i-k we demonstrate how to change the composition of the patches dynamically during deposition (Fig. 2i). By means of the solution switching function of the pipette, two POPC vesicle suspensions, each carrying a different fluorescent label, were consecutively dispensed. In Fig. 2j, a series of 11 patches was deposited from the binary source, with the PWM ratio, i.e composition, changing in steps of 10%. In Fig. 2k the observed fluorescence intensity of the two labels is displayed for each patch. The spreading regime of deposition can be utilized to insert membrane material into an existing patch (Fig. 2l-o). Vesicle fusion merges the supplied SUVs with a previously written membrane, first displacing the original membrane, followed by spreading and diffusional mixing (Fig. 2l). We wrote a POPC membrane patch, and subsequently exposed the center of the patch to DOTAP vesicles. Initially, the DOTAP vesicles displaced the POPC entirely from the surface, as is evident from the complete extinction of their fluorescence emission, and a slight increase of the intensity in the remaining patch. After 15 min, diffusive mixing and spreading have transformed the patch, and spreading has caused the area to increase by $\sim 15\%$ (Fig. 2m-o). In order to write extended two-dimensional lipid membrane structures, the deposition is combined with translation of the substrate to generate lanes. Lane writing protocols (denoted P1, P2...) for each experiment are listed in the Supplementary section S5. In Fig. 3 we demonstrate the application of the writing tool to create loops (Fig. 3a), linear arrays (Fig. 3b) and networks (Fig. 3c), consisting of one or two different lipid components. The network displayed in Fig. 3c consists of POPC with two different fluorescent labels (POPC-488, POPC-655), written sequentially from two lipid sources. It is cohesive, i.e., diffusively fully connected. Fig. 3d-e demonstrates this connectivity on a pair of overlapping lanes, which diffuse into each other within ~ 14 minutes. The progression of the diffusion is quantified in Fig. 3e. For comparison, Fig. 3f shows the same analysis for an incohesive film. The writing operation in combination with solution exchange was then used to create a compositional gradient along a lane

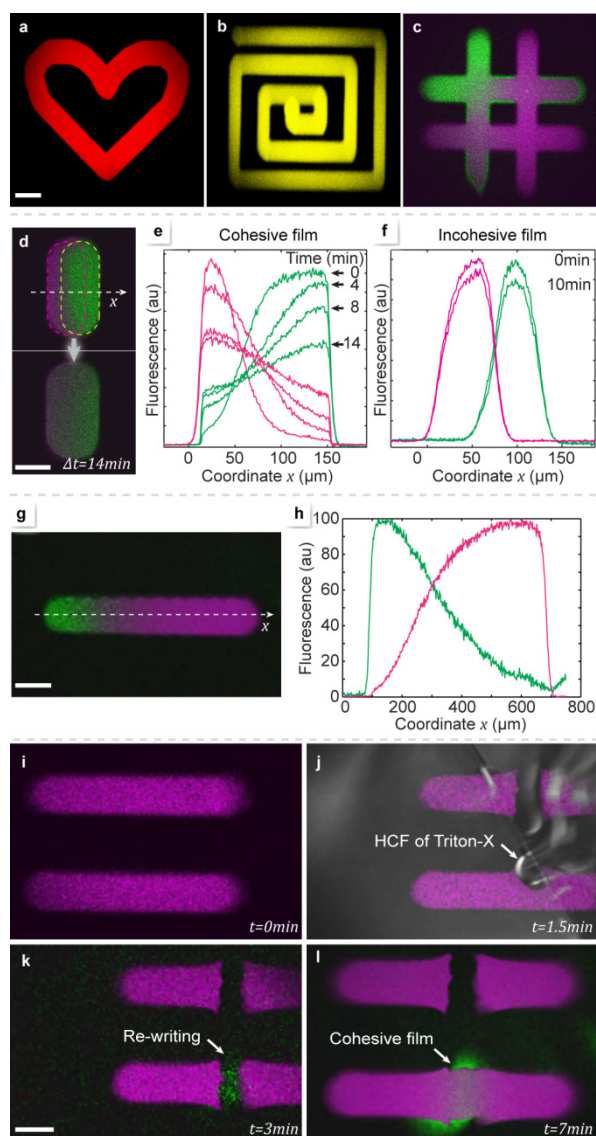


Figure 3| Writing, erasing, and re-writing. Scale bars: 100 μm . Confocal micrographs of a loop (a) and a connected linear array (b), which were written using POPC-655 SUVs. c) A binary network which was written sequentially, utilizing POPC488 (green) and POPC-655 (purple), respectively. d) Confocal micrographs of a pair of lanes, sequentially written with an offset, and composed of POPC488 (green) and POPC-655 (purple), respectively. The upper image was taken immediately after writing, the lower image after 14 min. The red and white lines in the upper picture mark the outlines of the individual lanes. e) Fluorescence intensity profile along a coordinate across the two lanes in (d), presented for four consecutive time points after deposition. The deposited membranes are cohesive, i.e., lipids can freely diffuse between both lanes. f) The same intensity profile for an incohesive film, where the SUV deposition time is so short that the deposited vesicles are not sufficiently dense to form a continuous bilayer membrane. g) Confocal micrograph of lane featuring a binary composition gradient, obtained by flow switching between POPC488 (green) and POPC-655 (purple) during the writing. h) Fluorescence intensity graph along the lane. The colors are in accordance with the image in (g). i-l) Lane cutting and re-writing using the erasing and writing tools. i) Confocal micrograph of two parallel lanes written with POPC-655 (purple) SUVs. j) Overlay of

the confocal transmission and fluorescence images, showing the lane cutting operation by means of the detergent Triton-X. The hydrodynamically confined flow (HCF) is clearly visible due to the higher refractive index of the triton solution. k) Confocal micrograph depicting re-writing of the erased lower lane section with a POPC488 (green) bridge, closing the gap. l) POPC-655 diffusion into the bridge confirms that a cohesive film is restored.

of $\sim 600 \mu\text{m}$ length (Fig. 3g). The position dependent fluorescence emission depicted in Fig. 3h gives a good estimation of the film composition, but is distorted due to apparent energy transfer between the two fluorescent labels.

Eraser tool: The writing of lipid films is irreversible, since the transition from membrane to vesicles is energetically unfavorable, and lipid loss from a bilayer film is negligible. However, by applying a detergent to the membrane locally, it can be dissolved and permanently removed from the exposed region. Fig. 3i shows two labeled POPC lanes, which are cut perpendicularly by Triton-X exposure. In Fig. 3j the erasing has proceeded through the upper lane. The cutting edges appear sharp, only the corners of the remaining membrane are slightly deformed. After erasing, the surface appears clean and is available for re-writing. Fig. 3k is a snapshot obtained during deposition of POPC with an alternate label (green color) directly into the gap in the lower lane. After completed re-writing, the gap is repaired by a cohesive lipid film, indicated by the diffusion of the original label (red color) into the gap region (Fig. 3l).

Functionalization tool: We here demonstrate how the writing methodology is applied to already deposited membrane lanes and networks, and describe a series of experiments involving biotin antibody recognition²⁹ as an example for multistep functionalization (Fig. 4a). POPC vesicles were modified to contain 1 % biotin-lipid conjugate, and utilized to write a $100 \mu\text{m}$ composite membrane lane, one half of its area fluorescently labeled. The central part of the lane was then decorated with IgG goat anti biotin antibodies (primary). After 4 minutes, which allows the antibody patch to diffusively broaden, donkey anti goat antibodies (secondary) were written over exactly the same area. We observed that the diffusion of both primary and secondary antibody is arrested. This development is shown individually for each channel in Fig. 4b-e, and quantified in the associated charts (Fig. 4f-i). The analysis shows that the functionalized region does not hinder diffusion of the fluorescent label, but collects, or “captures” anti biotin antibodies that have previously been diffusing out (grey arrows in Fig. 4i, Supplementary figure S13). When the second antibody is instead applied immediately after the first, avoiding diffusion, the first antibody is efficiently retained by the functionalized region (Supplementary figures S12 and S13).

Application examples: If the deposition sequence of the experiment shown in Fig. 2m, in which a POPC patch was overwritten by DOTAP vesicles, is reversed, POPC vesicles do not fuse with the DOTAP patch, but adhere to its surface and maintain some diffusional mobility (Fig. 5a). If the injection flow from the middle channel of the pipette is reversed to a high aspiration rate, vesicles are collected in a stagnation point on the membrane surface beneath the channel exit (Fig. 5b-e). This previously reported hydrodynamic trapping of membrane components³⁰ is possible because the particles experience the forces exerted by the aspiration flow and move laterally, but are restricted in perpendicular direction. A brief analysis of the trapping parameters is included in the supplementary section S12. Another prospective application area is directed transport of lipid film and associated molecules¹⁶⁻¹⁷, using patterned surfaces. We have created spreading lanes by covering the substrate with a hydrophobic polymer, where we defined accessible substrate areas photolithographically. Fig. 5f shows schematically how a circular deposition area, which is connected to a spreading lane, is accessed by the pipette. Figure 5h-j are fluorescence recordings from a 10 minute deposition experiment with fluorescently labeled DOTAP vesicles on a surface pre-coated with POPC, demonstrating that the lipid front propagates only in the spreading lane. The sharp boundary in the distance plot of the emission intensity displayed in Fig. 5g indicates that the transport of lipid on the surface occurs through spreading, rather than by diffusion into the POPC film. This is analogous to capillary driven convective flow in 3D microfluidics³¹.

In conclusion, we have developed a versatile and convenient toolbox for the generation and manipulation of molecular phospholipid film patches and networks on solid supports. These networks are directly written, and do not require patterning^{2,16-18}, or printing³². This technology greatly expands the experimental possibilities in research on supported biomembranes.

Methods| The preparation of plain and patterned glass surfaces is described in supplementary section S1, the preparation of lipids, vesicles and solutions in section S2. Details on design and function of the multifunctional pipette are provided in section S3. Section S4 describes the experimental setup and the microscopic methods used. Section S5 gives an overview over the control algorithm, and section S6 lists the protocols for the individual experiments. Supplementary sections S7-S12 contain additional data and experimental details for: the deposition of lipid films from single (S7) and multiple components (S8), writing (S9), diffusion measurements (S10), membrane functionalization (S11), and hydrodynamic trapping (S12). Four supplementary videos, corresponding to figures 2-5, are also supplied. Descriptions of the videos are located at the end of the supporting section.

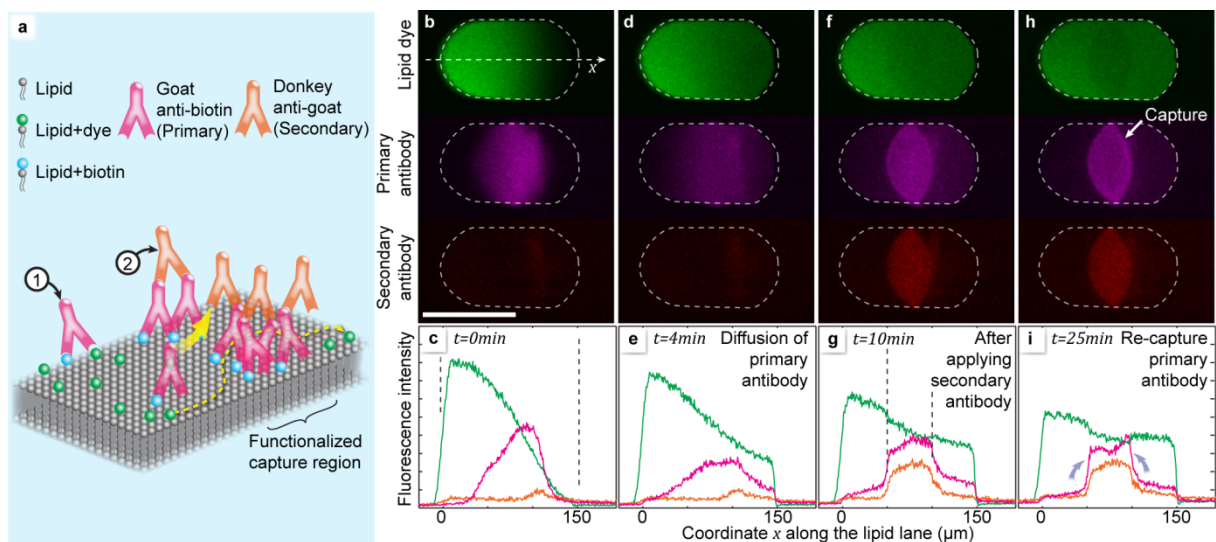


Figure 4| Surface functionalization. Scale bars: 100 μm . a-i) Creation of a diffusional filter for lipid attached molecules. a) Artist's view of the molecular arrangements the two different antibodies, each binding to two antigens, effectively cross-linking the biotinylated lipid molecules in the film. b-e) Confocal fluorescence micrographs of the writing sequence (false-colored). Initially, a binary lipid membrane lane is sequentially written, the first half using biotin/fluorescent dye labeled POPC-488B, the second half using the non-fluorescent POPC-B. A lane of a fluorescently labeled primary antibody (goat anti-biotin) is then written perpendicularly over the center of the composite lane. Subsequently, this antibody lane is overwritten by a secondary, differently labeled anti-goat antibody, locking the primary antibodies in place. White arrows depict the writing sequence. The three fluorescent labels are simultaneously imaged in different emission channels. f-i) Lateral fluorescence intensity profiles for the three labeled species. Green: labeled lipids, red: primary, orange: secondary antibody. Grey arrows in (j) point to an increase in the fluorescence intensity of the anti-biotin fluorophore at the borders of the central region, indicating that the primary antibody diffuses into the barrier and is being trapped there.

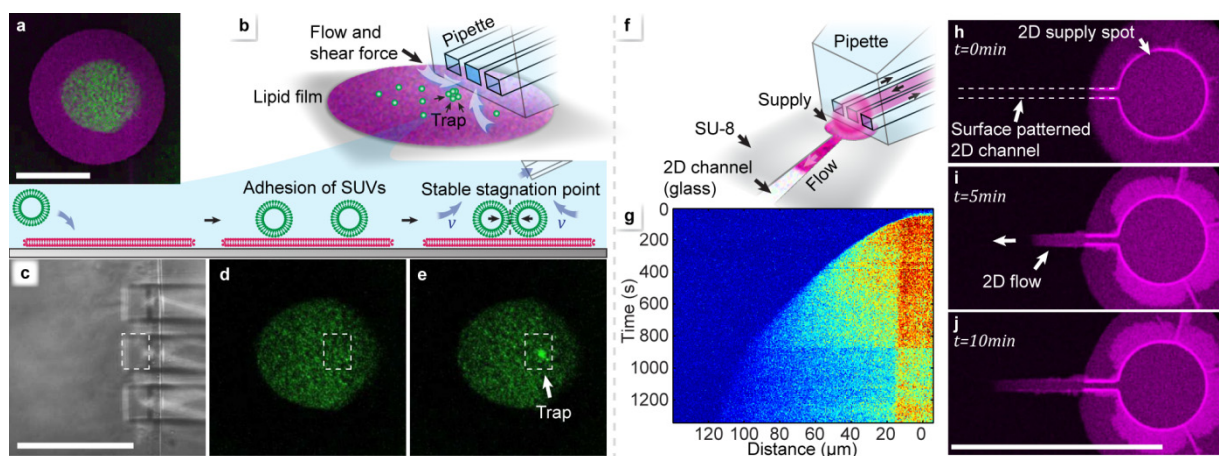


Figure 5| Lab on a membrane - application examples for the toolbox Scale bars: 100 μm . a-e) Hydrodynamic trapping of surface-associated SUVs. a) Sequential deposition of DOTAP, followed by POPC-488 vesicles, which adhere, but do not fuse with the film. b) Switching the middle channel of the multifunctional pipette from injection to aspiration, the vesicles are drawn to the channel opening by the hydrodynamic forces (schematic view). The free in-plane, but restricted perpendicular mobility concentrates the vesicles in a stable stagnation point at the pipette tip. White arrows depict the liquid inflow. c-e) Confocal micrographs of the trapping region. c) Transmission image showing the pipette tip, and fluorescence images showing d) the deposited vesicles, and e) collection of vesicles in the stagnation point. The position of the middle channel is visualized in each image by a white rectangle. f-j) Directed lipid spreading in 2D channels on a patterned surface. f) Schematic view of deposition and the spreading process on a SU-8 photoresist surface, featuring a microfabricated lane which promotes lipid adhesion. The deposition device is dispensing vesicles to a circular deposition region, from where the film flows into the channel. g) Fluorescence intensity profile depending on distance and time. The intensity is color coded from red (highest) to blue (lowest). h-j) Confocal fluorescence micrographs showing in-lane spreading at three consecutive points in time.

Acknowledgements:

This work was financially supported by the Swedish Research Council (VR), the European Research Commission (ERC), and the Nordic Council of Ministers (Nordforsk). The authors thank the Chalmers Area of Advance for Nanoscience and Technology for supporting the development of the multifunctional pipette.

References:

- 1 Sackmann, E. Supported membranes: Scientific and practical applications. *Science* **271**, 43-48, doi:10.1126/science.271.5245.43 (1996).
- 2 Tanaka, M. & Sackmann, E. Polymer-supported membranes as models of the cell surface. *Nature* **437**, 656-663, doi:10.1038/nature04164 (2005).
- 3 Berti, D., Caminati, G. & Baglioni, P. Functional liposomes and supported lipid bilayers: towards the complexity of biological archetypes. *Physical Chemistry Chemical Physics* **13**, 8769-8782 (2011).
- 4 Dietrich, C. *et al.* Lipid rafts reconstituted in model membranes. *Biophys. J.* **80**, 1417-1428 (2001).
- 5 Gözen, I. *et al.* Fractal avalanche ruptures in biological membranes. *Nat Mater* **9**, 908-912, doi:http://www.nature.com/nmat/journal/v9/n11/abs/nmat2854.html#supplementary-information (2010).
- 6 Han, X. J. *et al.* A Self-assembly Route for Double Bilayer Lipid Membrane Formation. *ChemPhysChem* **11**, 569-574, doi:10.1002/cphc.200900798 (2010).
- 7 Keller, C. A., Glasmastar, K., Zhdanov, V. P. & Kasemo, B. Formation of supported membranes from vesicles. *Phys. Rev. Lett.* **84**, 5443-5446, doi:10.1103/PhysRevLett.84.5443 (2000).
- 8 Reimhult, E., Hook, F. & Kasemo, B. Intact vesicle adsorption and supported biomembrane formation from vesicles in solution: Influence of surface chemistry, vesicle size, temperature, and osmotic pressure. *Langmuir* **19**, 1681-1691, doi:10.1021/la0263920 (2003).
- 9 Cremer, P. S. & Boxer, S. G. Formation and spreading of lipid bilayers on planar glass supports. *J. Phys. Chem. B* **103**, 2554-2559, doi:10.1021/jp983996x (1999).
- 10 Richter, R. P., Berat, R. & Brisson, A. R. Formation of solid-supported lipid bilayers: An integrated view. *Langmuir* **22**, 3497-3505, doi:10.1021/la052687c (2006).
- 11 Castellana, E. T. & Cremer, P. S. Solid supported lipid bilayers: From biophysical studies to sensor design. *Surf. Sci. Rep.* **61**, 429-444, doi:10.1016/j.surfrep.2006.06.001 (2006).
- 12 Reviakine, I. & Brisson, A. Formation of supported phospholipid bilayers from unilamellar vesicles investigated by atomic force microscopy. *Langmuir* **16**, 1806-1815, doi:10.1021/la9903043 (2000).
- 13 Woodward, J. T. & Meuse, C. W. Mechanism of formation of vesicle fused phospholipid monolayers on alkanethiol self-assembled monolayer supports. *J. Colloid Interface Sci.* **334**, 139-145, doi:10.1016/j.jcis.2009.03.007 (2009).
- 14 Chan, Y. H. M. & Boxer, S. G. Model membrane systems and their applications. *Curr. Opin. Chem. Biol.* **11**, 581-587, doi:10.1016/j.cbpa.2007.09.020 (2007).
- 15 Kam, L. & Boxer, S. G. Spatially selective manipulation of supported lipid bilayers by laminar flow: Steps toward biomembrane microfluidics. *Langmuir* **19**, 1624-1631, doi:10.1021/la0263413 (2003).
- 16 Groves, J. T. & Boxer, S. G. Micropattern formation in supported lipid membranes. *Accounts Chem. Res.* **35**, 149-157, doi:10.1021/ar950039m (2002).
- 17 Jonsson, P., Gunnarsson, A. & Hook, F. Accumulation and Separation of Membrane-Bound Proteins Using Hydrodynamic Forces. *Anal. Chem.* **83**, 604-611, doi:10.1021/ac102979b (2011).
- 18 Zagnoni, M. Miniaturised technologies for the development of artificial lipid bilayer systems. *Lab Chip* **12**, 1026-1039, doi:10.1039/c2lc20991h (2012).
- 19 Lenhart, S. *et al.* Lipid multilayer gratings. *Nat. Nanotechnol.* **5**, 275-279, doi:10.1038/nnano.2010.17 (2010).
- 20 Salafsky, J., Groves, J. T. & Boxer, S. G. Architecture and function of membrane proteins in planar supported bilayers: A study with photosynthetic reaction centers. *Biochemistry* **35**, 14773-14781, doi:10.1021/bi961432i (1996).
- 21 Nair, P. M., Salaita, K., Petit, R. S. & Groves, J. T. Using patterned supported lipid membranes to investigate the role of receptor organization in intercellular signaling. *Nat. Protoc.* **6**, 523-539, doi:10.1038/nprot.2011.302 (2011).
- 22 Chan, Y. H. M., Lenz, P. & Boxer, S. G. Kinetics of DNA-mediated docking reactions between vesicles tethered to supported lipid bilayers. *Proc. Natl. Acad. Sci. U. S. A.* **104**, 18913-18918, doi:10.1073/pnas.0706114104 (2007).
- 23 Nielsen, C. H. Biomimetic membranes for sensor and separation applications. *Anal. Bioanal. Chem.* **395**, 697-718, doi:10.1007/s00216-009-2960-0 (2009).
- 24 Bally, M. *et al.* Liposome and Lipid Bilayer Arrays Towards Biosensing Applications. *Small* **6**, 2481-2497, doi:10.1002/sml.201000644 (2010).
- 25 Ainla, A., Jeffries, G. D. M., Brune, R., Orwar, O. & Jesorka, A. A multifunctional pipette. *Lab Chip* **12**, 1255-1261, doi:10.1039/c2lc20906c (2012).
- 26 Richter, R., Mukhopadhyay, A. & Brisson, A. Pathways of lipid vesicle deposition on solid surfaces: A combined QCM-D and AFM study. *Biophys. J.* **85**, 3035-3047 (2003).
- 27 Schonherr, H., Johnson, J. M., Lenz, P., Frank, C. W. & Boxer, S. G. Vesicle adsorption and lipid bilayer formation on glass studied by atomic force microscopy. *Langmuir* **20**, 11600-11606, doi:10.1021/la049302v (2004).
- 28 Azizi, F. & Mastrangelo, C. H. Generation of dynamic chemical signals with pulse code modulators. *Lab Chip* **8**, 907-912, doi:10.1039/b716634f (2008).
- 29 Nguyen, T. T., Sly, C. L. & Conboy, J. C. Comparison of the Energetics of Avidin, Streptavidin, NeutrAvidin, and Anti-Biotin Antibody Binding to Biotinylated Lipid Bilayer Examined by Second-Harmonic Generation. *Anal. Chem.* **84**, 201-208, doi:10.1021/ac202375n (2012).
- 30 Jonsson, P. *et al.* Hydrodynamic trapping of molecules in lipid bilayers. *Proc. Natl. Acad. Sci. U. S. A.* **109**, 10328-10333, doi:10.1073/pnas.1202858109 (2012).
- 31 Juncker, D. *et al.* Autonomous microfluidic capillary system. *Anal. Chem.* **74**, 6139-6144, doi:10.1021/ac0261449 (2002).
- 32 Kaufmann, S., Sobek, J., Textor, M. & Reimhult, E. Supported lipid bilayer microarrays created by non-contact printing. *Lab Chip* **11**, 2403-2410, doi:10.1039/c1lc20073a (2011).

Lab on a Membrane: a Toolbox for Reconfigurable 2D Nanofluidic Networks

Alar Ainla, Irep Gözen, Bodil Hakonen and Aldo Jesorka

Supplementary Information

Table of contents

Table of contents	1
Supplementary Methods	2
S1. Preparation of surfaces	2
S2. Preparation of lipids and solutions	2
S3. Multifunctional pipette	3
S4. Experimental setup	4
S5. Control algorithm	4
S6. Protocols	5
Supplementary Data	7
S7. Basic deposition process	7
S8. Deposition of multiple components	8
S9. Writing.....	10
S10. Diffusion measurement and reference	11
S11. Functionalization	12
S12. Trapping	13
Supplementary Videos	14

Supplementary Methods

S1. Preparation of surfaces

Glass surfaces. Circular microscope cover glasses #1.5 (Menzel-Gläser, 47mm diameter) were obtained from Thermo Scientific (Sweden). Before use, the glass surfaces were cleaned in the MC2 process laboratory at Chalmers University of Technology (class 100 semiconductor clean room), using the processing facilities, chemicals and materials provided there. First, the slides were immersed in freshly prepared piranha solution (3:1 v/v mixture of concentrated H₂SO₄ and 30% H₂O₂, heated to 100-110 °C) for 10 min, followed by rinsing with deionised water and blow drying with nitrogen. Thereafter the glass slices were mounted to a Willco Wells® dish frame using a dedicated double sided tape and assembly kit (Willco Wells B. V., Amsterdam, Netherlands) and stored in a sealed plastic bag until use. **Critical:** smooth and homogeneous surfaces are essential for the function of the 2D fluidic network. For example, sputtered silicon dioxide surfaces can be readily covered with lipids, but the forming films are not diffusively conductive and do not support transport of material.

SU-8 surfaces. The cleaned cover glasses were coated with ~2 µm high SU-8 patterns using the procedure provided by Microchem Corporation. SU-8 2002 (Microchem Corp, Massachusetts, USA) was spin-coated at 3000 rpm for 30 s, followed by soft baking for 2 min at 95 °C on a hot-plate. The SU-8 film was exposed with a dose of 120 mJ/cm² on a Karl-Süss contact mask aligner MA6 (G-line, 5-6 mW/cm²), using the "Low-Vac" mode with a bright-field chromium mask. The substrates were then post-exposure-baked for 2 min at 95 °C on a hot-plate. Thereafter, the SU-8 was developed in SU-8 Developer (Microchem) for 1 min using two sequential bathes, rinsed by spraying with clean developer, and blow dried with nitrogen, yielding a SU-8 coated cover glass where the channels are formed by the exposed glass. The surfaces were plasma cleaned briefly in a Plasma Therm BatchTop RIE (50 W, 250 mTorr, 1 min) plasma chamber, and hard baked for 10 min at 200 °C on a hot plate with slow heating and cooling to prevent crack formation. The so prepared glass slides were mounted to dish frames like the plain glass slides described in the previous section.

S2. Preparation of lipids and solutions

Vesicle preparation

The compositions of the six lipid mixtures (wt%) used in the experiment are summarized in the table S1.

Table S1. Lipid mixtures used in experiments.

Denomination	POPC	PC	DOTAP	ATTO 488-DOPE	ATTO 655-DOPE	Biotin-PE
POPC-488	99%	-	-	1%	-	-
POPC-655	99%	-	-	-	1%	-
POPC-B	99%	-	-	-	-	1%
POPC-488B	98%	-	-	1%	-	1%
POPC-655B	98%	-	-	-	1%	1%
DOTAP-655	-	49%	50%	-	1%	-

1-Palmitoyl-2-oleoyl-*sn*-glycero-3-phosphocholine (POPC), Soy L- α -phosphatidylcholine (PC), 1,2-dioleoyl-3-trimethyl-ammonium-propane (DOTAP), 1,2-dioleoyl-*sn*-glycero-3-phosphoethanolamine-N-(cap biotinyl) (Biotin-PE) were obtained from Avanti Polar Lipids (USA). ATTO 488 1,2-dioleoyl-*sn*-glycero-3-phosphoethanolamine (ATTO 488-DOPE) and ATTO 655 1,2-dioleoyl-*sn*-glycero-3-phosphoethanolamine (ATTO 655-DOPE) were provided by ATTO-TEC GmbH (Germany).

A two-step procedure was followed for vesicle preparation: (I) Preparation of stock vesicle suspensions, (II) Preparation of small unilamellar vesicles. De-ionized water from a Milli-Q system (Millipore) was used for all preparations.

(I) Stock vesicle suspensions: For each recipe, a designated amount (see table) of lipids and lipid conjugates in chloroform were mixed and diluted with chloroform to a total concentration of 10 mg/ml. 300 µl of this solution was placed in a 10 ml round bottom flask, and the chloroform was removed in a rotary evaporator at reduced pressure (-80 kPa) over a period of 6 hours. The dry lipid film at the walls of the flask was rehydrated with 3 ml of PBS buffer containing 5mM Trisna Base (Sigma Aldrich), 30 mM K₃PO₄ (Sigma Aldrich), 30 mM KH₂PO₄ (Sigma Aldrich), 3 mM MgSO₄*7H₂O (Merck) and 0.5 mM Na₂EDTA (Sigma Aldrich). The pH was adjusted to 7.4 with H₃PO₄ (Sigma Aldrich). The rehydrated lipid cake was placed in the fridge (4°C) overnight. In the final step the

lipid cake was sonicated at 120W/35kHz (Bandelin Sonorex, Germany) at room temperature for 15-30 s, to induce the formation of giant vesicles of varying, mainly multiple lamellarity.

(II) Small unilamellar vesicles: Small unilamellar vesicles were prepared on the day the experiments were conducted. 100 μ l of the desired vesicle stock solutions were diluted (1:10) with TRIS buffer [125 mM NaCl (Sigma Aldrich), 10 mM TRIS (VWR), 1 mM Na₂EDTA (Sigma Aldrich), adjusted to pH=7.4 and sonicated using a Sonics & Materials Vibra Cell™ High Intensity Ultrasonic Liquid Processor (Model 501, CIAB, Chemical Instruments AB, Sweden) at 15 °C for 10 minutes. The sonicated samples were subsequently ultracentrifuged at 40,000 rpm at 15 °C for 30 minutes to separate multilamellar aggregates and tip debris (Beckman TL-100 Ultracentrifuge, USA). The small unilamellar vesicles in the supernatant were transferred to a separate tube. **Critical:** For high quality membrane fabrication, the vesicle suspensions must be freshly prepared. Upon prolonged storage, vesicle preparations form agglomerates.

Triton X was obtained from Sigma Aldrich and diluted 1:10 with TRIS buffer.

Antibodies were obtained from Agrisera (Sweden). **Goat anti-biotin antibody conjugated to DyLight 650** ("Goat anti-biotin"): 0.2 mg of goat anti-biotin antibody was dissolved in 1 ml of 10 mM TRIS buffer. **Donkey anti-Goat IgG antibody conjugated to DyLight 594** ("Anti-goat"): 0.2 mg of donkey anti-goat antibody was dissolved in 1 ml of 10 mM TRIS buffer. All antibody solutions were prepared instantly prior to the experiments, at room temperature.

S3. Multifunctional pipette

A detailed description of the multifunctional pipette has been reported elsewhere [Ainla *et al*, *Lab Chip*, 2012, **12**, 1255-1261 and Xu *et al*, *manuscript in press*]. In the following (Fig S1. and Table S2), only key parameters are summarized together with operation settings used in the experiments. The multifunctional pipette was controlled by an in-house build pneumatic control unit. This control unit interfaces with a PC computer via USB 2.0. It supports valve-less switching between four solutions, allows controlling the flow rates and adjusting the size of the hydrodynamically confined flow (HCF) volume, i.e. the extent of the region to which solutions are delivered.

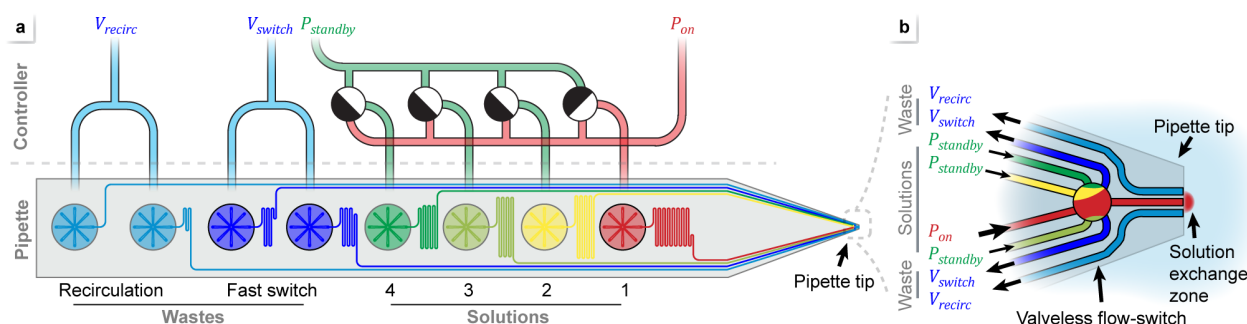


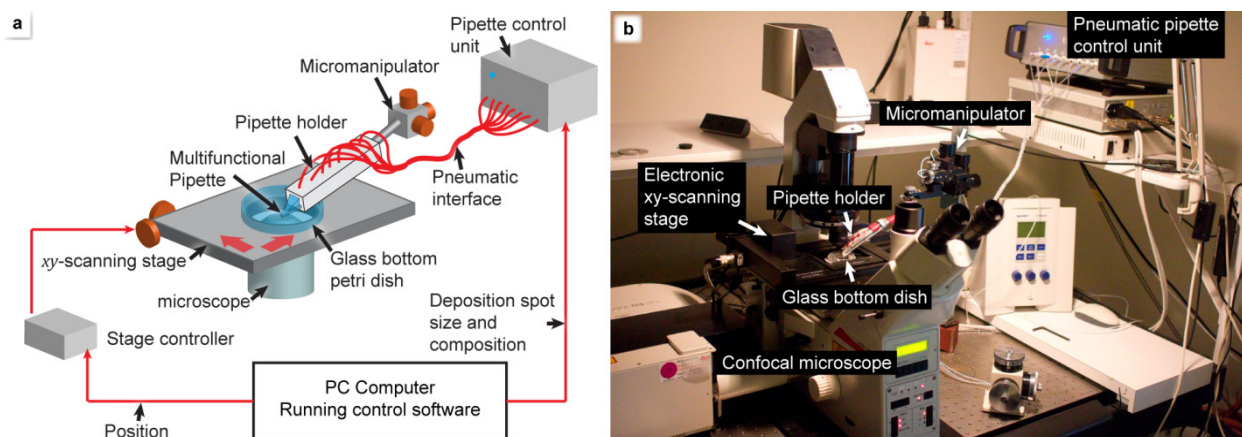
Fig S1. Layout of the multifunctional pipette. Schematics and control circuitry: (a) multifunctional pipette layout and external connections, and (b) magnification of the flow switch and pipette tip. Pressures used for operation: $V_{recirc}=V_{switch}=-100$ mbar, $P_{standby}=20$ mbar, $P_{on}=200$ mbar.

Table S2. Essential parameters of the pipette and its operation.

Parameter	Value
Channel size	30 μm x 30 μm
Channel-channel separation at the tip	20 μm
Channel-bottom separation at the tip	20 μm
Solution reservoirs	35 μL
Flow conductance of supply channels	53 nL/(s*bar)
Outflow	3.2 nL/s
Inflow (from 2 channels)	10.6 nL/s
Ratio (outflow/inflow)	0.3
Run-time	55-110 min
Solution exchange time	~100 ms

S4. Experimental setup

The experimental setup (Fig. S2) comprised the multifunctional pipette, a laser scanning confocal microscope Leica IRE2 (Leica Microsystems GmbH, Wetzlar, Germany) equipped with Leica TCS SP2 confocal scanner with AOBST[™] and Ar/ArKr and HeNe lasers to provide excitation wavelength 488, 594 and 633 nm. Objectives used were HC PL APO CS 20x 0.70 UV and HCX PL APO CS 40x 1.25 OIL UV. The sample position was controlled by a scanning stage SCAN IM 120x100 (Märzhäuser Wetzlar GmbH & Co. KG, Wetzlar, Germany), equipped with a Corvus stage controller (Märzhäuser). Both scanning stage and pipette control unit were connected to a PC computer via USB port. Custom software, written in Microsoft Visual C++ (.NET), allowed simultaneous control of stage position and pipette control unit, through which the liquid composition and deposition spot size were controlled. The pipette was held and positioned in the beginning of an experiment by a 3-axis water hydraulic micromanipulator Narishige MH-5 (Japan). During the experiment, the pipette tip was positioned about ~10-20 μm above the surface, so that materials could be delivered to the surface, while avoiding direct contact, which would damage the lipid film.

**Fig S2.** Experimental setup. Schematic drawing (a) and a photograph (b).

S5. Control algorithm

The algorithm used to control the writing and subsequent processing of 2D fluidic networks is illustrated in figure S3. The translation of the motorized stage, i.e., the substrate surface, occurred step-wise from one point to the next with step length L_{step} , where deposition time $t_{deposition}$ was allowed in each point to process the surface. In order to achieve a diffusively connected lane, the step length is chosen to be smaller than the spot size ($L_{step} < L_{spot}$), where L_{spot} is the diameter of the hydrodynamically confined flow

(HCF) volume. If the step length is decreased, the edges of the lane become accordingly smoother. To move between unconnected parts of a network, i.e., to translate without writing, the outflow is switched off ($t_{switching} = 2 - 5$ s). Different parts of a network can thus be created or processed with different solutions. There are up to four different solutions possible with the current system, but the number of individual solutions can be greater, depending on the pipette design.

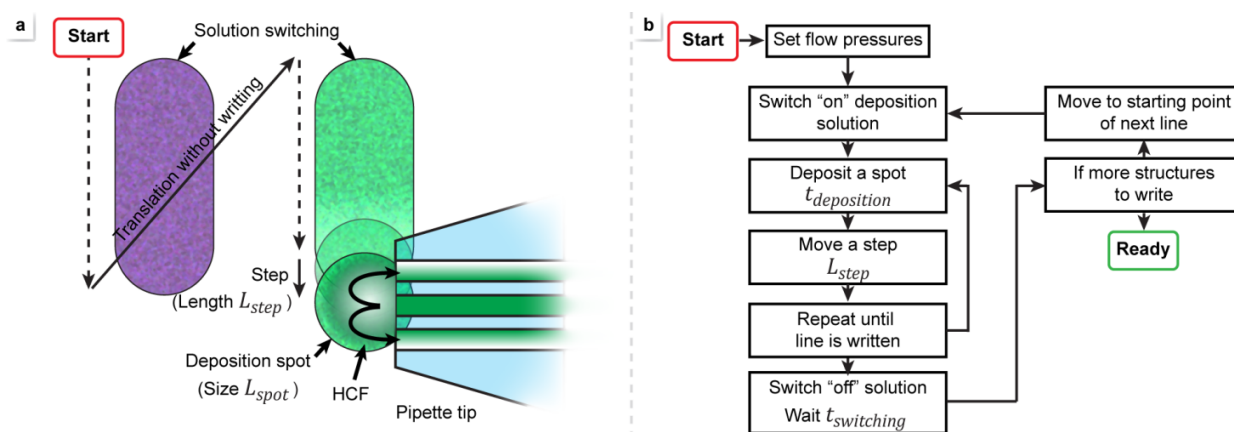


Fig S3. Control algorithm for writing and processing 2D fluidic networks. (a) Concept of writing two independent lanes with different lipid composition. (b) Block diagram of the control algorithm.

S6. Protocols

The protocols which were used in the experiments are listed in table S3.

Table S3. Experimental protocols.

Protocol	Experimental description
P1	Deposition of a POPC spot. The pipette was positioned and the flow of lipid vesicle suspension (POPC-488) was switched-on. Density and size evolution of the spot were analysed.
P2	Deposition kinetics and density of the POPC spot. The pipette was positioned and the flow of lipid vesicle suspension (POPC-655) was switched-on. Kinetics of the density change was analyzed.
P3	Deposition of a DOTAP spot. The pipette was positioned and the flow of lipid vesicle suspension (DOTAP-655) was switched on. Density and size evolution of the deposition spot were analysed.
P4	On-surface dilution series of POPC with different labels. The pipette was loaded with two different types of lipid vesicles (POPC-488 and POPC-655). Dilutions were created using the pulse width modulation (PWM) principle on the surface. For this, the deposition was multiplexed between the two sources, where the PWM period was 10 s. Each spot was deposited for 30 s, thus each spot deposition contained three periods. In total 11 spots were created with the duty cycle changing in 1 second steps (e.g. 10:0, 9:1, 8:2, 0:10 seconds). The spots with a diameter of 100 μm were created as a 3 x 4 grid with a pitch of 300 μm . The stage movement between the spots was controlled by the protocol software.
P5	Fusion of DOTAP into a POPC spot. The pipette was loaded with two types of lipid vesicles (POPC-488 and DOTAP-655). Thereafter the pipette was positioned, and the flow of POPC-488 vesicle suspension was switched on for 60s to deposit a POPC spot. Thereafter, the flow was switched off and the pressure conditions were set such that the outflow rate would be about half the previous rate, to ensure that the size of the hydrodynamically confined flow (HCF) volume is reduced and the DOTAP is deposited within the boundaries of the already existing POPC film. Thereafter DOTAP-655 deposition was switched-on.
P6	Overlapping DOTAP-on-POPC spot. This experiment was performed in a manner similar to the previous one, except that the flow-conditions were not adjusted between the different lipid spots. However, the pipette position was moved slightly by ~30 μm to create two partly overlapping films.
P7	Deposition of POPC onto a DOTAP spot. This experiment was performed similarly to P5, but the deposition sequence was exchanged. First DOTAP-655 was deposited for 60s, followed by POPC-488 for 90s. Since the area of the initially deposited DOTAP-655 film grows due to spreading, there was no need to reduce the size of the HCF volume between different lipid types.

P8	Overlapping POPC-on-DOTAP spot. This experiment was performed similarly to P6 , but the deposition sequence was exchanged, such that a DOTAP-655 spot was deposited first. Subsequently, after the pipette was positioned to the edge of the spot, POPC-488 was deposited.
P9	Writing a loop. The pipette was positioned and the flow of lipid vesicles (POPC-655) was switched-on. A "heart" shaped closed loop was written using step length $L_{step} = 13 - 18 \mu\text{m}$ and step deposition time $t_{deposition} = 7 \text{ s}$. Since the spot diameter was about $100 \mu\text{m}$, the line area becomes deposited in about 30 s. Total writing: 200 steps, corresponding to ~24 min writing time.
P10	Writing a "Labyrinth". Similar to P9 , with $L_{step} = 13 \mu\text{m}$ and $t_{deposition} = 3 \text{ s}$. Total: 560 steps and a writing time of ~28 min.
P11	Writing a two-component network 1 (grid). The pipette was loaded with two types of lipid vesicles (POPC-488 and POPC-655). Four lines, two vertical and two horizontal, were sequentially written, out of which one vertical and one horizontal line were written from POPC-488, and the other two from POPC-655. $L_{step} = 50 \mu\text{m}$ and $t_{deposition} = 10 \text{ s}$. Total writing time was ~15 min, followed by 15 min time for diffusion.
P12	Writing a two-component network 2 (cross). This experiment was performed similarly to P11 , using a different cross geometry, composed of two lines, a vertical (POPC-488) and a horizontal (POPC-655) one.
P13	Diffusion of two dyes in a POPC film 1. The pipette was loaded with two types of lipid vesicles (POPC-488 and POPC-655) and positioned. Two $300 \mu\text{m}$ long and $100 \mu\text{m}$ wide lanes were written ($L_{step} = 25 \mu\text{m}$ and $t_{deposition} = 10 \text{ s}$). First POPC-488 was written, followed by POPC-655. The lanes were offset by $50 \mu\text{m}$ and were overlapping partially. After writing, the diffusion was monitored for 15 min.
P14	Diffusion of two dyes in a POPC film 2. This experiment was performed similarly to P13 , but the offset distance between the lanes was increased to $120 \mu\text{m}$. The diffusion was monitored for 8 min.
P15	Writing a gradient. This experiment was performed similarly to P4 , but instead of depositing individual spots, the lipid vesicles were deposited gradually on a single lane in $80 \mu\text{m}$ steps, creating a smooth gradient.
P16	Erasing. The pipette was loaded with three solutions: two types of lipid vesicles (POPC-488 and POPC-655) and a solution of dilute Triton-X. Two parallel lanes of $150 \mu\text{m}$ length were written, using POPC-655. Thereafter the outflow was switched off and the supply pressure P_{on} was increased from 200 mbar to 250 mbar, since Triton-X is more viscous. Thereafter Triton-X solution was switched on. The HCF volume is easily visible in the transmission channel of the microscope, due to a higher refractive index (Triton-X has a refractive index of $n = 1.49$ vs. $n = 1.33$ for water). Triton-X was scanned perpendicularly over the lower lane. Thereafter the outflow was switched off again, P_{on} was set to its initial value, and the pipette was positioned onto the cutting point of the lane. A spot of POPC-488 was deposited in order to reconnect the lane. The first (upper) lane served as a reference.
P17	Diffusion of a dye. The pipette was loaded with two types of lipid vesicles (POPC-488B and POPC-B) and positioned. A $200 \mu\text{m}$ lane was written ($L_{step} = 10 \mu\text{m}$ and $t_{deposition} = 5 \text{ s}$), such that during the first half of the deposition (0-100 μm) POPC-488B was deposited, and during the second half (100-200 μm) POPC-B. Thereafter the diffusion was monitored for about 15min. Note that due to the round lane ends, $200 \mu\text{m}$ scanning length results in a $300 \mu\text{m}$ lane.
P18	Functionalization Sequence 1. The pipette was loaded with two types of lipid vesicles (POPC-488B and POPC-B) and two antibody solutions: goat anti-biotin, and anti-goat. The pipette was positioned and a $200 \mu\text{m}$ lane was written ($L_{step} = 10 \mu\text{m}$ and $t_{deposition} = 5 \text{ s}$), such that first $100 \mu\text{m}$ were composed of POPC-488B, followed by $100 \mu\text{m}$ of POPC-B. Thereafter the pipette was moved $100 \mu\text{m}$ backwards onto the middle point of the lane, and goat anti-biotin was applied for 5 s, followed by 10 min diffusion time. Thereafter anti-goat was applied for 5 s onto the same spot, after which re-distribution of molecular species was monitored for about 15 min.
P19	Functionalization Sequence 2. This experiment was performed similarly to P18 , but the 10 min diffusion time after functionalization with goat anti-biotin was omitted, and anti-goat was applied directly after goat anti-biotin.
P20	Trap. This experiment was started as described in P7 , by depositing POPC vesicles onto a DOTAP film. After POPC vesicles were deposited onto a DOTAP film, the supply pressures were adjusted ($V_{recirc}=0 \text{ mbar}$, $V_{switch}=-350 \text{ mbar}$, $P_{standby}=P_{on}=20 \text{ mbar}$) for maximal inflow ($Q \approx 33 \text{ nl/s}$) through the middle channel. Trap formation and collection of vesicles under the middle channel were monitored.
P21	Flow in patterned 2D channels. The pipette was loaded with two types of lipid vesicles (POPC-488 and DOTAP-655) and positioned onto the patterned area. First, the surface of the patterned channel was covered with POPC-488, thereafter DOTAP-655 was deposited onto the circular supply area, and transport of fluorescently labelled lipid from the supply area into the channel was monitored for about 25 min.

In each experiment the response was recorded as a series of fluorescent confocal microscopy images, collected in up to three different fluorescence emission channels corresponding to the fluorophores used (Table S4). A brightfield transmission image was also recorded.

Table S4. Dyes and wavelengths used for excitation and collection of fluorescence.

Compound(s)	Excitation (nm)	Collected emission (nm)
POPC-488, POPC-488B	488	496-586
Donkey anti-goat (DyLight 594)	594	610-620
POPC-655, POPC-655B, DOTAP-655, Goat anti-biotin (DyLight 650)	633	650-800

Supplementary Data

All microscopy images presented in following section are false coloured. The actual collection ranges of emitted light, controlled by the confocal microscope, are given in Table S4 above.

S7. Basic deposition process

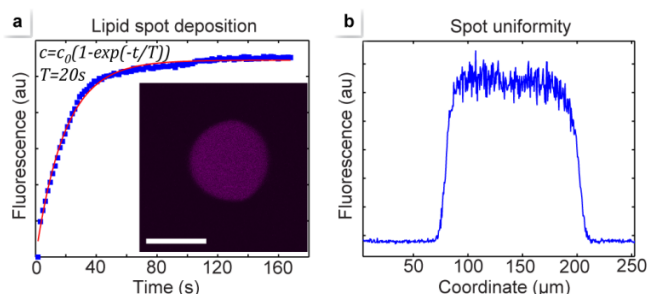


Fig S4. Spot deposition of lipid film according to protocol **P2**. **(a)** Exponential surface coverage kinetics with a time constant of about 20s. **(b)** Spot uniformity. When the surface becomes covered it forms eventually a uniform film. We observed neither deposition of multiple layers, nor further significant adhesion of lipid vesicles to the membrane.

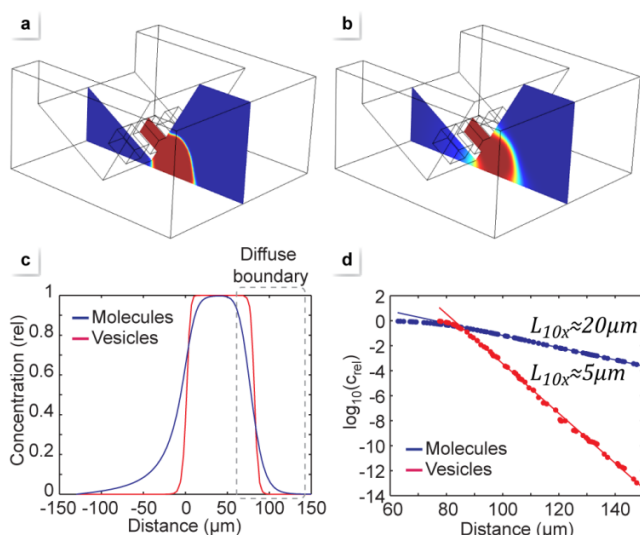


Fig S5. Simulation of diffusion for the deposition of lipid films and film functionalization. Comparison of vesicles (the size of the SUVs is about 20-50 nm in diameter) $D \approx 2 \cdot 10^{-11} \text{ m}^2/\text{s}$ **(a)** and small molecules, like fluorescent dyes, $D \approx 5 \cdot 10^{-10} \text{ m}^2/\text{s}$ **(b)**, which gives a 25 fold difference in Péclet number. Vesicles are confined with a much sharper boundary than small molecules at the same flow rate and HCF volume size **(c)**. In a diffuse boundary the concentration drops exponentially **(d)**. 10-fold reduction in concentration occurs over characteristic length scales: $L_{10x} \approx 5 \mu\text{m}$ and $L_{10x} \approx 20 \mu\text{m}$, for lipid vesicles and small molecules, respectively. The flow rates used for the simulations are the same as for the experiments (Table S1). Simulations were performed with COMSOL Multiphysics 4.1, combining models of laminar flow (spf) and transport of dilute species (chds) in stationary 3D models. The viscosity of water was $1 \text{ mP}\cdot\text{s}$. The pipette was positioned $10 \mu\text{m}$ above the surface at an angle of 30° . Due to a sharp chemical boundary at high $P\acute{e}$, an about 10x finer mesh was used for the diffusion calculation compared to the flow calculation.

S8. Deposition of multiple components

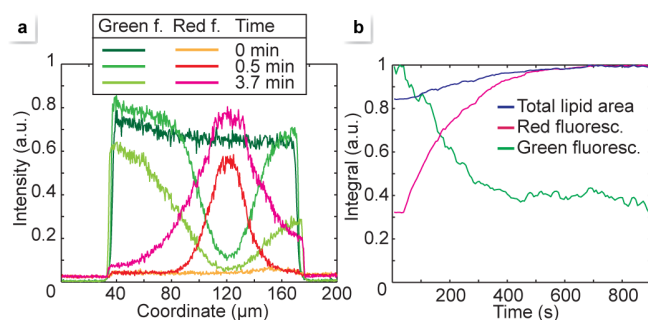


Fig S6. Depositing DOTAP on top of a POPC film (Protocol P5). Intensity profiles before and after injection of DOTAP (a). Integrals of total film area and fluorescence in two channels (b). Microscopy images are provided in Fig. 2 of the main text. Already a small scale injection of DOTAP-655 (area increase only about ~15%) causes significant quenching of green (POPC-488) fluorescence (about ~60%). However, a local fluorescence increase of the green fluorescence can be observed outside the injection site directly after injection. This can be due to an initial compression of the film. The net decrease of the fluorescence is due to energy transfer from the green (488) to the red (655) dye. We speculate that the dyes are forming a molecular assembly, where energy from many green fluorophores is efficiently funnelled to a single red fluorophore, since small amounts of Atto-655 dye quench the fluorescence of many Atto-488 dye molecules. Alternatively, it could be possible that the film remains compressed and the amount of actually incorporated DOTAP is higher than predicted by the total area increase of the lipid film.

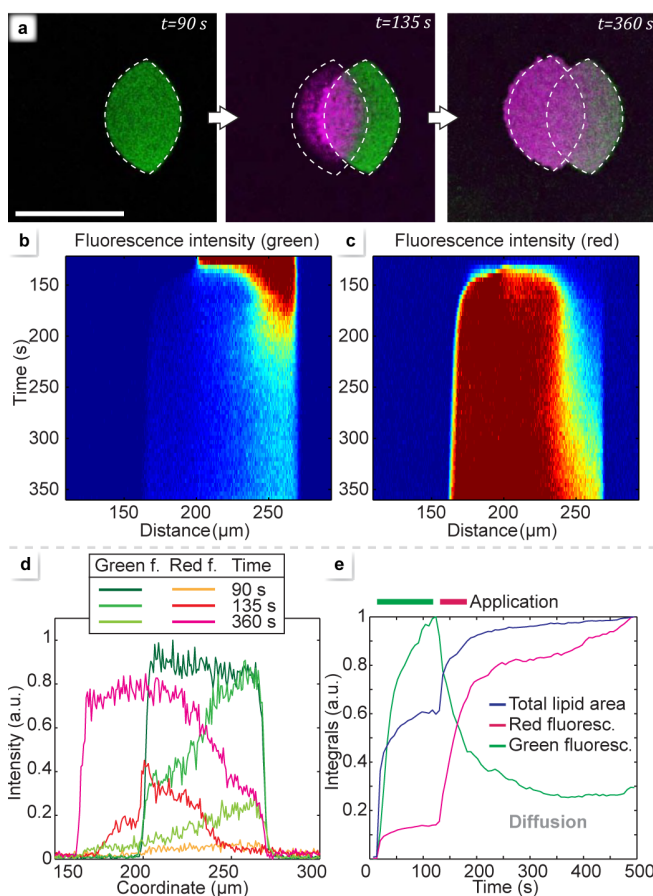


Fig S7. Overlapping DOTAP spot on a POPC spot (Protocol P6). Confocal microscopy images (a), time evolution of the fluorescence profile across the membrane patches (b-d), as well as the integrals of the total film area and fluorescence in both channels (e). DOTAP is readily depositing on the glass surface and fusing into a POPC film. Immediately after DOTAP-655 deposition has started ($t=135$ s), the red (655) fluorescence increases more rapidly on top of the POPC-488 film near its boundary, while the green (488) fluorescence is decreasing there. This supports the hypothesis of energy transfer between these dyes. The mixing is most efficient directly on the edge, where a sharp spike can be seen. Further evidence for energy transfer is provided by the integrals. After applying DOTAP, mixing between DOTAP-655 and POPC-488 occurs, which results in rapid decrease in green and increase in red fluorescence. Even after switching off the deposition, the membrane area increases slightly along with increasing red fluorescence. This can be due to on-going spreading and diffusion. Evaluating the areas, the membrane should be composed of 60% of POPC-488 (green) and 40% of DOTAP-655 (red) lipids. However, mixing with the red dye results in quenching of about 70% of the green fluorescence.

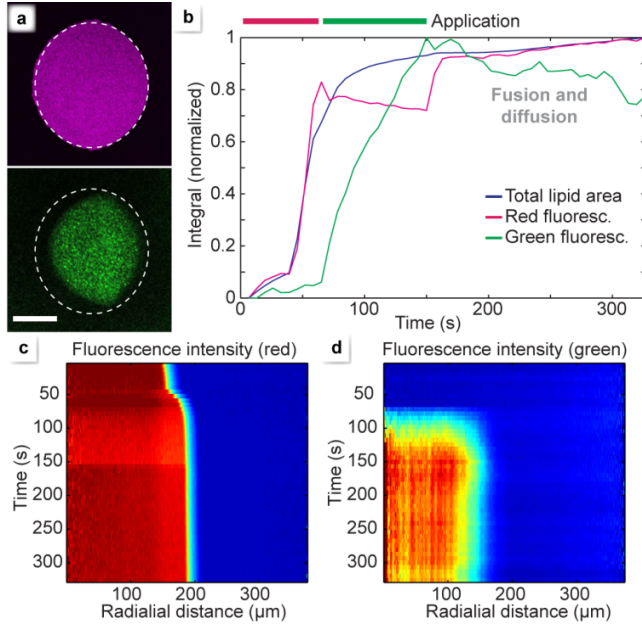


Fig S8. Deposition of POPC on the DOTAP spot (Protocol P7). Confocal microscopy images (a), integrals of total film area and fluorescence in the two channels (b), and time evolution of the profile of fluorescence intensities (c-d). These experiments indicate that POPC vesicles are adhering to the DOTAP film, but do not fuse readily, which should result in an area increase, or at least in diffusion and energy transfer. Instead, deposition of POPC results in a very small area increase ($<20\%$), which could be also due to ongoing spreading of DOTAP. There is almost no energy transfer discernible. Note that the step in the red channel between 50 and 150 s during the application of POPC-488 is an artefact caused by mechanical interaction of the pipette and the dish, as well as slight mechanical motion caused by switching. Minor fusion is distinguishable by a slight area increase, as well as an increase in red, and decrease in green fluorescence ($<10\%$).

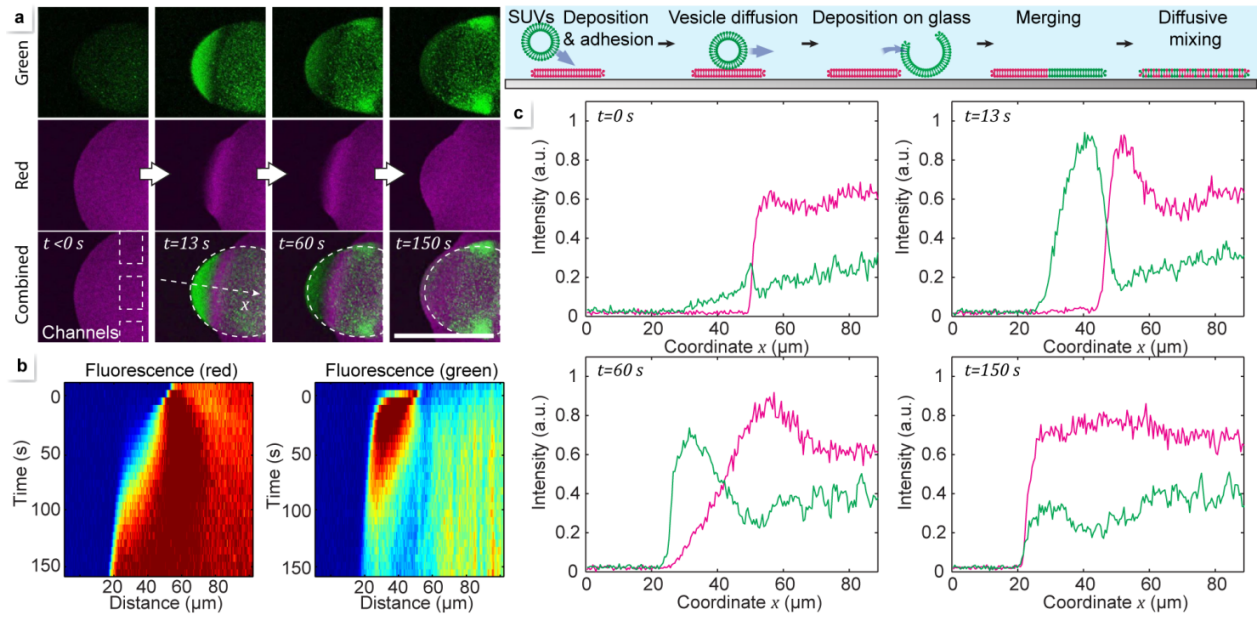


Fig S9. Overlapping POPC-on-DOTAP spot (Protocol P8). Confocal microscopy images (a), and the evolution of the fluorescence profile (b-c). Directly after the deposition of POPC-488 was started ($t=0$ s), a sharp increase in the green (488) fluorescence channel can be observed on the glass side of the boundary of the lipid films, as POPC vesicles immediately adhere and fuse there. This forming POPC film is diffusively connected to the DOTAP patch. This results in energy transfer and a sharp increase in red (655) fluorescence on the edge of the DOTAP patch ($t=13$ s). As diffusion progresses, the green fluorescence is reduced ($t=60$ s), and eventually both parts of the film are homogeneously mixed ($t=150$ s). In contrast, a darker rim is visible in the green channel on the lipid side of the boundary, indicating a loss of vesicles after deposition. POPC vesicles do not fuse with the DOTAP membrane, but maintain mobility after adhering. They are rapidly affected by the pipette inflow and removed from the patch perimeter. The accumulation of green vesicles on both sides under the inlet channels are indicators for a hydrodynamic trap, a phenomenon which was further investigated in another experiment (see P20, S12).

S9. Writing

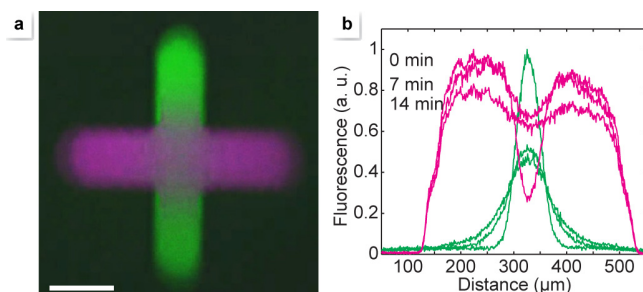


Fig S10. Writing a two-component network (Protocol **P12**). Confocal microscopy image after deposition and diffusion (**a**), and fluorescent intensity profile along the red axis of the cross (**b**). First the green (POPC-488) lane is written, which is then crossed by the red (POPC-655) lane. Since POPC films cannot be overwritten, the green lane initially causes a break in the red lane, but as they are diffusively connected, mixing occurs over time.

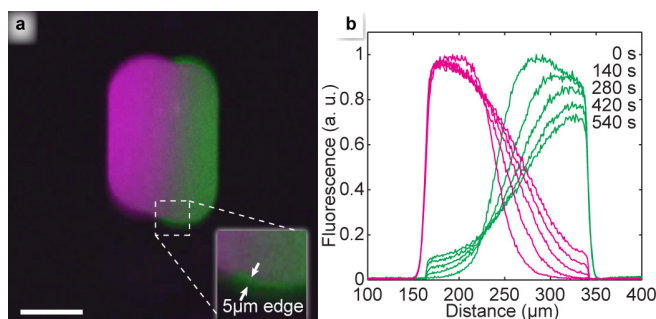


Fig S11. Diffusion of two dyes in a POPC film (Protocol **P14**). Confocal microscopy image after diffusion (**a**) and fluorescent intensity profiles across the lanes at different time points (**b**). The diffusive mixing of two lipid-anchored dyes (488 and 655) can be monitored. However, a closer look reveals that a narrow (about 5 μm) stripe at the edge of the patch is not diffusively connected (inset of panel **a**, and lower left and right corners in the graph in **b**). This is explained by the diffusive boundary of the HCF volume, where a 5 μm distance would correspond to about one order of magnitude in concentration drop (Fig. S5). While this lower vesicle concentration is sufficient to create a visible coverage with nanoscopic lipid patches, the density is too low to form a connected and cohesive film which would support diffusive transport.

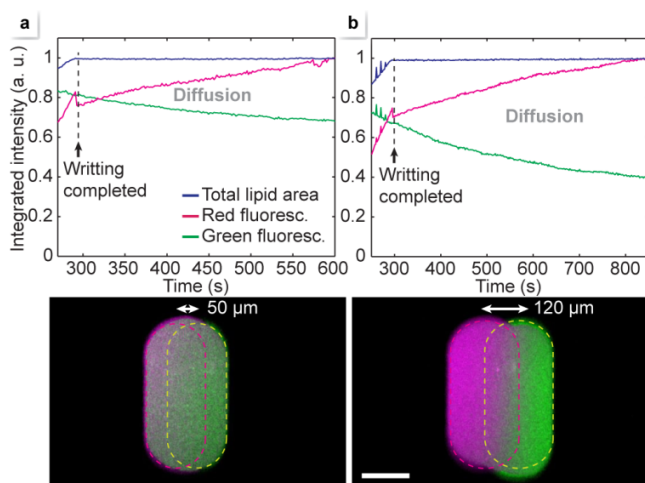


Fig S12. Integrated fluorescence intensities and normalized lipid film areas. (**a**) 50 μm offset between two lanes, in which case the film is composed of 80% of green lipid and 20% of red lipid. (**b**) 120 μm offset between two lanes, in which case the film is composed of 55% of green lipid and 45% of red lipid. During mixing there is no further deposition of lipids and the area is preserved (no spreading). However, the integrated intensities are changing such that the intensity of the green fluorescence drops while that of the red increases. This can be explained by energy transfer from the green absorbing (488 nm) to the red absorbing (655 nm) dye.

S10. Diffusion measurement and reference

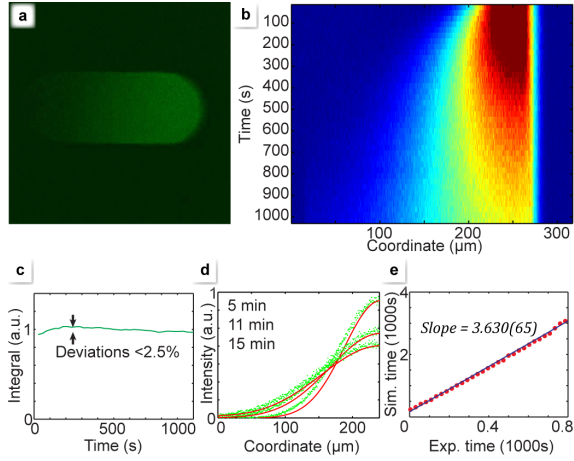


Fig S13. Diffusion of one dye (Protocol P17). Microscopy image (a). Evolution of the fluorescence intensity along the lane (b). Integrated fluorescence intensity over the total area of the lane (c). Fitting simulation (red line) and experiment (green dots) (d). Correlation of time required in simulation and experiment for the same dye distribution (e). In case of a single dye, where there is no possibility for energy transfer, the integral of fluorescence intensity is well preserved with small drifts of $<2.5\%$ (std), which are caused by a combination of the stability of the microscope focus, laser intensity, detector gain and photobleaching, which is most significant in case of the low wavelength (488 nm) dye. This stability for a single dye clearly suggests that the observed large changes in other cases are due to the interactions between fluorophores. This allows us to assume that fluorescence intensity is directly proportional to fluorophore concentration and can be used to characterize diffusion. The diffusion constant was estimated using a numerical analysis. The lane was considered as a one dimensional system and a respective model was constructed in COMSOL. The initial concentration distribution was taken from the experiment and a transient simulation was used with $D_{sim} = 1 \mu m^2/s$. The output (time series of concentration profiles) was transferred to MATLAB. Since the solution of the diffusion equation depends on the parameter Dt , the output of the simulations can be fitted to the experimental results (d). The observed slight deviations are most likely due to the fact that the lane, having round corners, is not perfectly one dimensional. When the best fitting simulation time is plotted against the experimental time, a linear relation is formed, in which the slope contains the actual diffusion constant. Since $c(D_{sim}t_{sim}) = c(D_{exp}t_{exp})$, $D_{exp} = D_{sim}t_{sim}/t_{exp} = D_{sim} \cdot Slope$. In this case $D_{exp} = 3.630(65) \mu m^2/s$.

S11. Functionalization

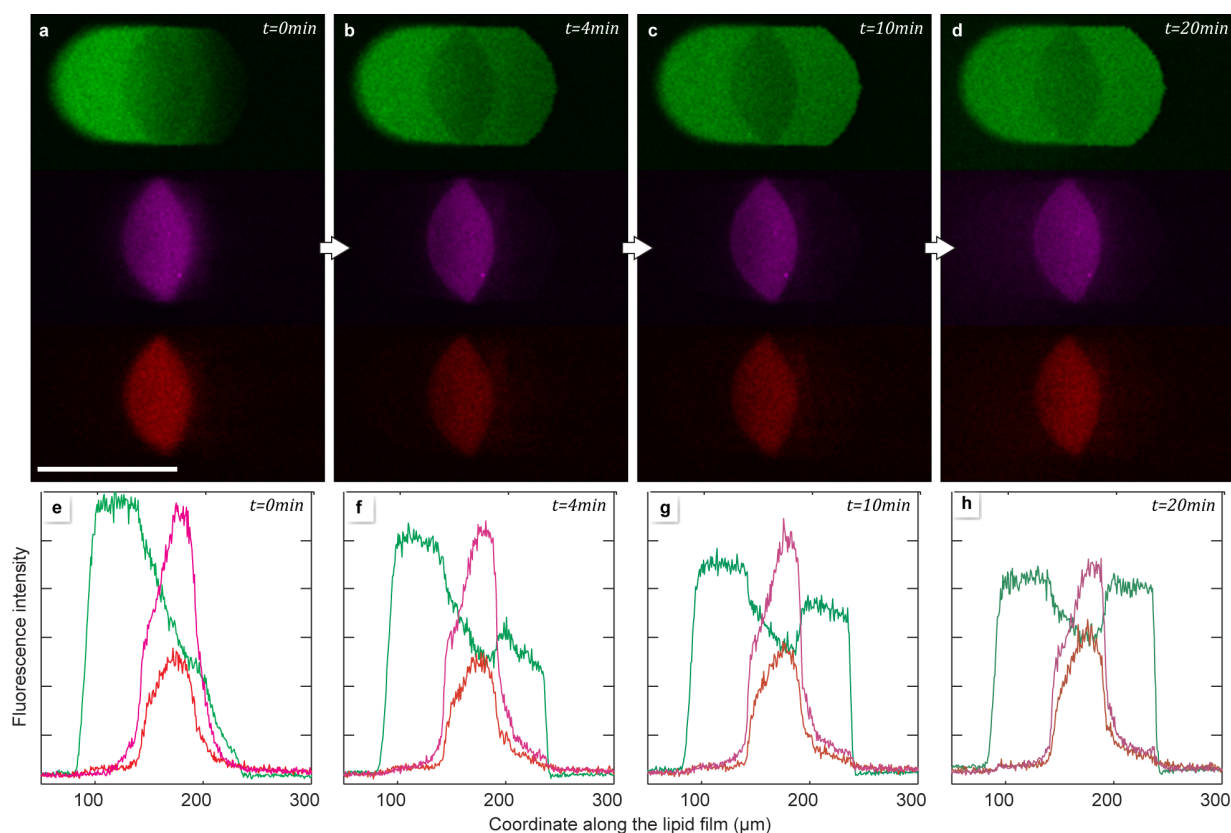


Fig S14. Functionalization (Protocol P19). When a secondary antibody (anti-goat) is applied directly after the primary (anti-biotin), there is essentially no diffusion of the primary antibody observable, and the distribution of both antibodies remains constant, with only minor diffusion around the edges. However, the antibody functionalized region is permeable for the lipid dye (488), which diffuses freely through the barrier. Reduced intensity of the fluorescence of POPC-488B is due to energy transfer to the antibody-conjugated dye. The graph colors correspond to the colors in the confocal micrograph. Green: POPC-488B; purple: goat anti-biotin; red: anti-goat.

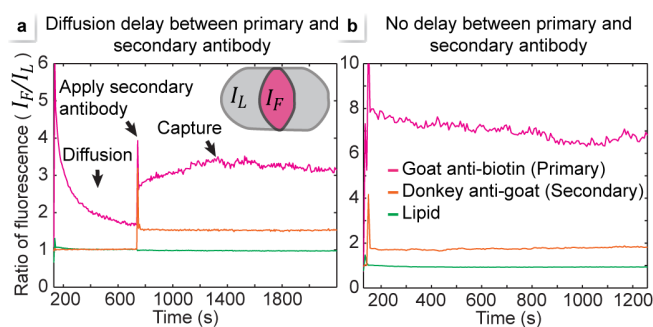


Fig S15. Ratios of average fluorescent intensities (I_F/I_L) measured on the entire lipid lane, where I_F is the fluorescence intensity measured on the functionalized region, and I_L on the remaining lane area. This ratio is a good indicator of diffusion and capture of material in the functionalized region. (a) Initially, a 600 s diffusion time was used in between the deposition steps of the two antibodies. During this time the primary antibody diffused out of the functionalized region, and intensity differences were equilibrating (from $I_F/I_L = 4.5$ to 1.5). The fluorescent intensity corresponding to the primary antibody started to gradually increase after functionalization with the secondary antibody, indicating that the anti-biotin is captured in the functionalized region. An abrupt change of the fluorescent intensity is due to cross-talk between channels. If the channel cross-talk is subtracted, the fluorescence intensity ratio was found to increase ~41%. The average intensity ratio of the secondary antibody remains constant, indicating no diffusion. Even though diffusing, the intensity ratio of the lipid remains constant due to the symmetrical deposition of the lane. (b) In a second experiment, the diffusion time between primary and secondary antibody was omitted. In this case the primary antibody was bound immediately, and no significant diffusion was observed. During this time, the intensity ratio decreased only by 16%.

S12. Trapping

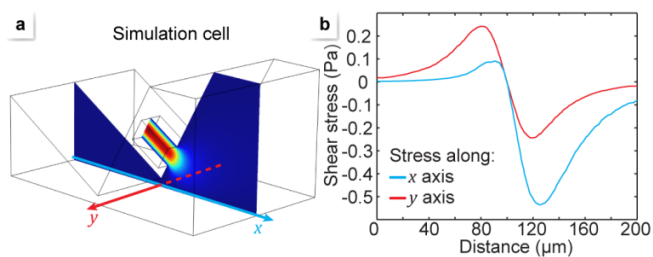
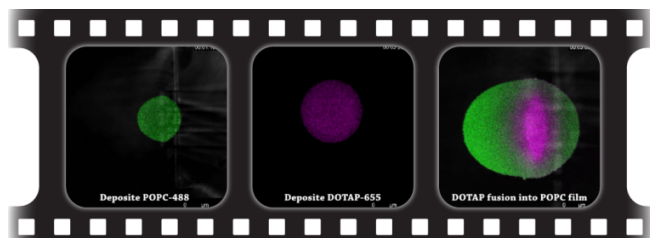
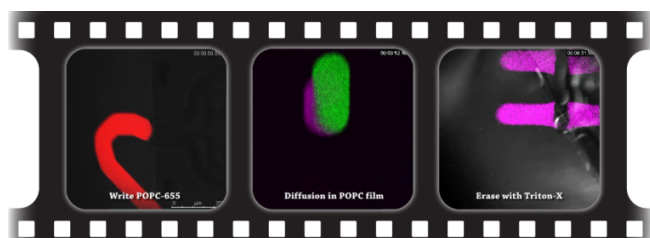


Fig S16. Hydrodynamic trap simulation to estimate the trapping force. The simulation cell (a) and the hydrodynamically generated stress profile on the surface (b). In this simulation, the pipette was positioned 10 μm above the surface at a 30° angle. A flow rate of ~33 nl/s was applied. For 20 to 50 nm vesicles, the estimated trapping force is in the range of 0.5 to 5 fN, at a maximum shear stress of ~0.5 Pa. The trapping force scales $\propto Q$ and $\propto d^2$, where Q is the flow rate and d is the vesicle/particle size.

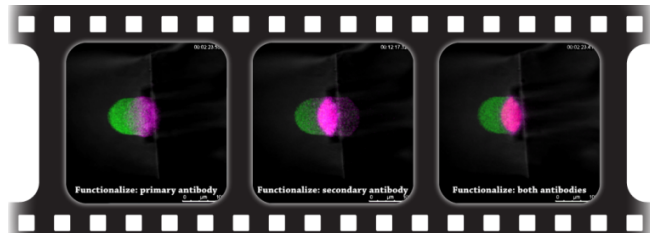
Supplementary Videos



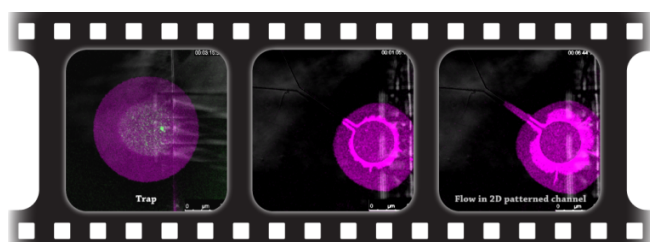
Video 1. Deposition. This is the supplementary video for figure 2 in the main text. This time-lapsed video shows deposition of POPC and DOTAP films, on-surface dilution of lipid, and fusion of DOTAP into a POPC film.



Video 2. Writing and erasing. This is the supplementary video for figure 3 in the main text. This time-lapsed video shows writing of single and multiple component membrane structures and 2D fluidic networks, further 2D diffusion in a membrane, and erasing and rewriting.



Video 3. Functionalization. This is the supplementary video for figure 4 in the main text. This time-lapsed video shows functionalization of membrane structures with a primary antibody (goat anti-biotin) and further functionalization with a secondary antibody (donkey anti-goat).



Video 4. Other examples. This is the supplementary video for figure 5 in the main text. This time-lapsed video shows hydrodynamic trapping of lipid vesicles from POPC adhered to a DOTAP film, and lipid flow on a surface patterned channel.